Design of Percutaneous Dual Propeller Pump to assist Patients with Single Functional Ventricle

Jakin Nitin Jagani

Thesis submitted to the Faculty of the
Virginia Polytechnic Institute and State University
in partial fulfillment of the requirements for the degree of

Master of Science
in
Mechanical Engineering

Alexandrina Untaroiu, Chair
Walter F. O'Brien
Pablo A. Tarazaga

February 15, 2018
Blacksburg, Virginia

Keywords: Cavopulmonary Assist Device, Dual Propeller Pump, Computational Fluid Dynamics, Hemodynamics, Blood Damage, Experimental Testing

Design of Percutaneous Dual Propeller Pump to assist Patients with Single Functional Ventricle

Jakin Nitin Jagani

ABSTRACT

Various congenital heart defects (CHDs) are characterized by the existence of a single functional ventricle, which perfuses both the systemic and pulmonary circulation in parallel. A three-stage palliation procedure, including the final Fontan Completion, is often adopted by surgeons to treat patients with such CHDs. However, the most common outcome of this surgery, an extra-cardiac total cavopulmonary connection (TCPC), formed by suturing the inferior vena cava (IVC) and superior vena cava (SVC) to the pulmonary arteries (PAs), results in non-physiological flow conditions, systemic venous hypertension, reduced cardiac output, and pressure losses, which ultimately calls for a heart transplantation. A modest pressure rise of 5-6 mm Hg would correct the abnormal flow dynamics in these patients. To achieve this, a novel conceptual design of a percutaneous dual propeller pump inserted and mounted inside the TCPC is developed and studied.

The designed blood pump is percutaneously inserted via the Femoral vein and deployed at the center of Total Cavopulmonary Connection (TCPC). The two propellers, each placed in the Superior Vena Cava (SVC) and the Inferior Vena Cava (IVC) are connected by a single shaft and motor, and thus rotate at same speed. The device is supported with the help of a self-expanding stent which would be anchored to the walls of the IVC and the SVC. An inverse design methodology implementing Blade Element Momentum theory and Goldstein's radial momentum loss theory was employed to generate the blade profiles for the studied propeller pumps. The propeller blade profiles generated from the inverse design optimization code were examined for hydraulic performance, blood flow pattern and potential for hemolysis inside the TCPC using 3-D computational fluid dynamics (CFD) analysis. The Lagrangian particle tracking approach in conjunction with a non-linear mathematical power law model was used for predicting the blood damage potential of the analysed blood pump designs by calculating the scalar shear stress history sustained by the red blood cells (RBC).

The study demonstrated that the IVC and SVC propeller pumps could provide a pressure rise of 1-20 mm Hg at flow rates ranging from 0.5 to 5 lpm while rotating at speeds of 6,000-12,000 rpm. Moreover, the average Blood Damage Index (BDI), quantifying the level of blood trauma sustained by the RBCs for the analyzed propeller pump designs, was found to be around 3e-04% to 4e-04% which is within the acceptable limits for an axial flow heart assist device. Thus, such a dual propeller blood pump configuration could potentially provide assistance to Fontan patients by unloading the single functional ventricle thereby acting as a bridge to transplantation and recovery until a donor heart is available.

Design of Percutaneous Dual Propeller Pump to assist Patients with Single Functional Ventricle

Jakin Nitin Jagani

GENERAL AUDIENCE ABSTRACT

A single functional ventricle is a type of congenital heart defect, where either left or right ventricle is underdeveloped, resulting in a single ventricular chamber to pump blood to both the body as well as lungs. A three-stage surgical procedure called the Fontan procedure, is often adopted by the surgeons to treat this defect by disconnecting the inferior(IVC) and superior vena cava(SVC), the two main veins carrying de-oxygenated blood from the body to the heart, and connecting them to the pulmonary arteries(PAs), the vessels carrying de-oxygenated blood from heart to the lungs. This helps to bypass the underdeveloped ventricle and allows blood to flow directly from the body to the lungs. However, the absence of a pumping chamber in the newly developed blood portal system causes an increase in pressure inside the vena cava and pressure losses inside the pulmonary arteries, which results in vena cava hypertension, reduced cardiac output. A modest pressure rise of 5-6 mm Hg across the vena cava or pulmonary artery should correct the abnormal flow dynamics and should bring the cardiac output of such patients back to normal. To achieve this, a conceptual design of a dual propeller mechanical circulatory support device has been designed and developed in this thesis.

Dedication

To my Parents
And
To my Uncle and Aunt

Acknowledgments

I would like to extend my sincere gratitude to my advisor Dr. Alexandrina Untaroiu for providing me such a multidisciplinary, interesting and meaningful research topic to work on. Her constant guidance and motivation helped me push myself and work harder at each stage of this research to achieve the targets on time be it for paper/poster presentation, journal paper submission or thesis writing. It was because of her support, knowledge, enthusiasm, and patience that provided me a platform to develop skills required for conducting numerical and experimental studies for this research. I appreciate her providing me this opportunity and guiding me as an advisor during my stint as a Masters student.

Besides my advisor, I would also like to sincerely thank Dr. Walter O'Brien and Dr. Pablo Tarazaga for being in my thesis committee and for their immense knowledge that I gained from their courses and their encouragement and insightful comments on my research and findings.

I would like to greatly thank, Dr. Mihai Bleiziffer, a dear colleague, and a former Ph.D. student of Dr. Untaroiu, for his guidance to develop the propeller design code. His willingness to help and guide me whenever I asked for, despite being in Germany, by taking time off his busy schedule helped me meet the research targets on time. I couldn't imagine myself completing this thesis on time without your timely guidance on the subject matter.

I would like to take this opportunity to thank my fellow labmates, Dr. Gen Fu, Dr. Ssu Ying (Armani) Chien, Dr. Hanxiang Jin and Dr. Elizabeth Mack for their unselfish dedication to help me whenever I asked for and answering my numerous technical questions over the last two years. I really appreciate your coordination, help, and understanding to use your ANSYS licenses to run multiple simulations in parallel during the need of the hour.

I would also like to thank Mr. Darrell Link, the Laboratory Instrument Maker from the BEAM Machine Shop, for timely completing the numerous machining job requests during the last nine months and for his insightful ideas on modifying the design to solve the problems faced in the experimental setup. I am thankful to all the members of the 3D Design Studio at Virginia Tech, especially, Mr. Nick Gazzillo, for helping me 3D print hundreds of propeller prototypes and experimental parts on time and for his guidance on designing to get better quality 3D prints for the prototypes. I would also like to thank my dearest friend Mr. Rohan Devgekar for helping me when I needed an extra pair of hands to assemble the experimental setup, for giving me frequent rides to the hardware store to buy urgent supplies for the experimental setup, and for proof-reading the

critical parts of my thesis and suggesting important changes to improve the flow.

I would also like to take this opportunity to thank my dearest cousin, Mr. Neel Ghodasara for being a fatherly figure to me, guiding and directing me to take the correct decisions in life and for financially supporting me during my Masters. Finally, I would like to extend my sincere and deepest gratitude to my parents, my uncle and aunt, and my siblings for their emotional, spiritual and financial support throughout my life without which I wouldn't have got an opportunity to study at Virginia Tech and achieve what I have today.

Contents

List of Figures

List of Tables

Chapter 1

Introduction

The field of pharmacy, biotechnology, medical science, and devices has seen a rapid growth and development in the past few decades. The advancements in the medical technology have provided physicians and doctors a whole new platform to diagnose and treat their patients and increase their chances of survival. These advancements have led to a cumulative decline of 67% in the mortality rate over the twentieth century in the United States [14]. However, the innovations in medical technology and science have yet to find the elixir or cure for major congenital heart defects and congestive heart diseases. Heart disease is the leading cause of death not only in the United States but throughout the world with more than half of the deaths occurring worldwide attributed to heart diseases [15]. This thesis makes an attempt to look at one such cardiovascular defect and introduces a new conceptual design to provide temporary assistance to such patients.

1.1 Motivation

Congenital Heart Defects (CHD) refers to cardiovascular malformations that an infant can be born with. These malformations usually occur during early weeks of pregnancy due to incomplete or abnormal development of the fetal heart [16]. The CHD could occur in different parts of the heart during its formation, and based on its severity, some patients receive immediate treatment while patients with a very critical condition require long-term medical assistance and/or heart transplantation. The most common parts of the heart that can be underdeveloped during fetus development, include the septum (the wall separating the right and the left side of the heart), heart valves, and the arteries and veins carrying blood to and from the heart.

CHDs are the most common types of birth defects in newborn infants with 8 to 10 per 1,000 live birth being diagnosed with CHDs in the United States. Around 1% of the 4 million births, i.e., 40,000 children are born each year in the United States with some form of CHD and it is the leading cause of death in newborn infants [17,18]. Out of these, around 25% of the babies affected by Critical Congenital Heart Defects (CCHDs) require some form of corrective surgical invasion or

life-saving diagnosis and treatment. According to a study done in 2010, around 2.4 million people, which included 1.4 million adults and remaining 1 million children, were living with some form of congenital heart defects [17]. The surgical invasions have helped to treat most of the less severe forms of CHD but the CCHDs are the ones that are difficult to treat and has resulted in short and long-term mortality. The motivation of this project is to develop a blood pump to assist patients with one such CHD of single functional ventricle until a donor heart is available.

A Single Ventricle physiology is a type of congenital heart defect affecting around 2,000 infants per year [19]. This is a relatively rare type of CHD, however, it is classified as a critical form of CHD since it is one of the most complex type of heart defects. The children born with single ventricle physiology have only one of the ventricles properly performing the function of pumping blood to lungs and other parts of the body. In order to understand this clearly, the normal physiology of the heart and the blood circulation network in a human body is discussed briefly in the next section.

1.2 Normal Circulation

The normal human heart is the main pumping mechanism inside a human body which continuously supplies oxygen rich blood to the organs and cells of the body. An adult heart on an average pumps or circulates around 2000 gallons of blood per day [20]. The normal network of a human circulatory system and the human heart anatomy is shown in Figure 1.1.

The human heart as depicted in Figure 1.2(b) is divided into four main chambers, consisting of four valves and is connected to a network of arteries and veins to carry blood into and out of the heart. Each of the part of the heart and its function during a cardiac cycle is described in detail below:

- **Left Atrium**: This chamber is present above the left ventricle and receives oxygenated blood from the lungs during diastole (relaxation of heart muscles) from the two pulmonary veins. The oxygenated blood inside the left atrium is then emptied into the left ventricle via mitral valve when the atrium contracts.
- **Left Ventricle**: This is the largest chamber of the heart, which receives oxygenated blood from the left atrium via the bicuspid or mitral valve. During systole (contraction of heart muscles), the left ventricle contracts and forces the aortic valve to open, thereby pumping the oxygen-rich blood to the body via the aorta.
- **Pulmonary Veins**: These are the two blood vessels carrying oxygenated blood from the lungs to the left atrium.
- **Aorta**: This is the biggest and the thickest blood vessel in the human body which carries oxygenated blood from the left ventricle to the body.

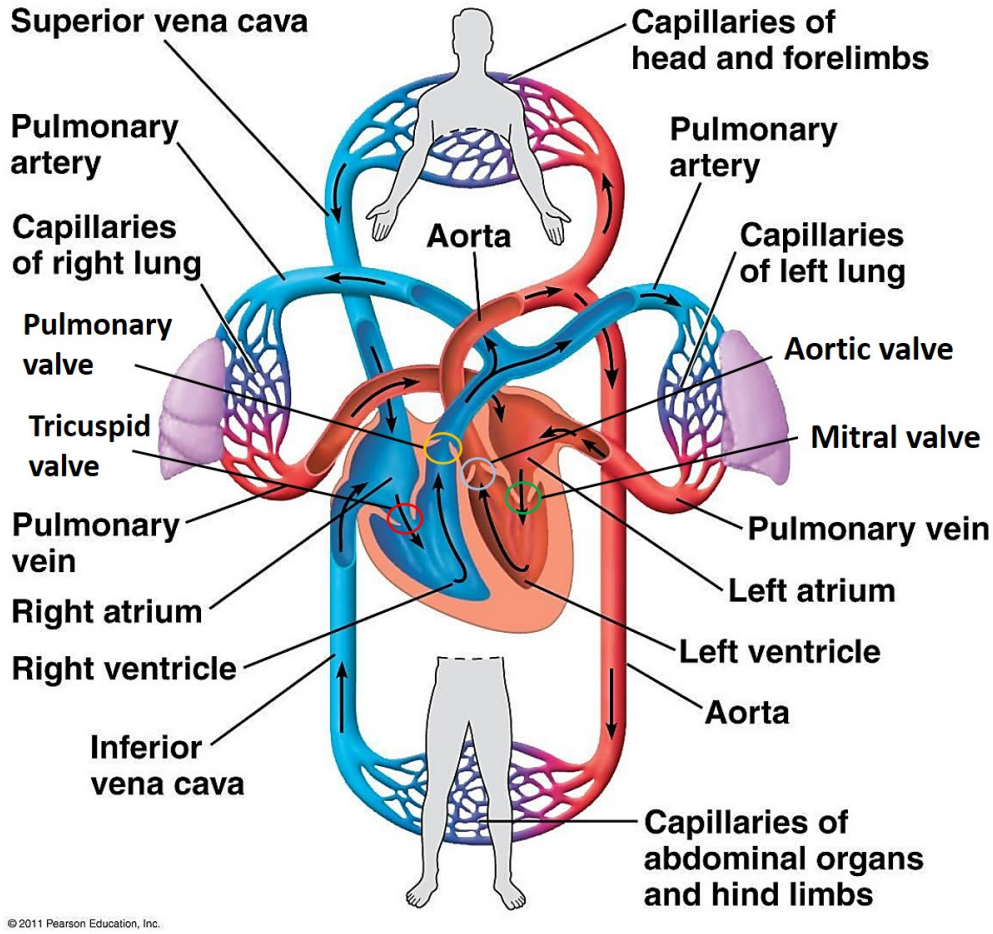

Figure 1.1: Normal Human Circulatory System [1]

- **Inferior Vena Cava** and **Superior Vena Cava**: The deoxygenated blood from the body is delivered to the right atrium by these two main blood vessels. The Inferior Vena Cava (IVC) carries blood from the lower part while the Superior Vena Cava (SVC) carries blood from the upper part of the body.
- **Right Atrium**: This chamber receives all the deoxygenated blood from the body via the IVC and the SVC during diastole. This deoxygenated blood is then emptied into the right ventricle via tricuspid valve when the atrium contracts.
- **Right Ventricle**: This chamber is located below the right atrium is responsible for pumping all the deoxygenated blood to the lungs. During systole, the pulmonary valve is forced to open and the deoxygenated blood is pushed to the lungs via pulmonary arteries.
- **Pulmonary Arteries**: The left and right pulmonary arteries (LPA and RPA) originate from the main pulmonary artery connecting the right ventricle to the lungs, and carry deoxygenated blood to the lungs for oxygenation. The oxygenated blood then reaches the right

atrium via pulmonary veins and the cardiac cycle repeats itself.

- **Septum**: This is the middle thick wall which separates the left side of the heart from the right side, thereby preventing the mixing of the oxygenated and deoxygenated blood.

In a human circulatory system, the lungs are another vital organ containing a vast bed of capillaries performing the function of exchanging carbon-dioxide released from blood with oxygen inhaled by the body. In the following text, the systemic circulation refers to the part of the cardiovascular system which carries oxygenated blood from the heart to the body and organ cells and returns the deoxygenated blood back into the heart. The pulmonary circulation refers to the portion of the cardiovascular system which carries deoxygenated blood from the heart to the lungs and returns the oxygenated blood from the lungs back to the heart. In this way, the Inferior Vena Cava, the Superior Vena Cava, and the Aorta form the part of the systemic circulation while the Pulmonary Arteries and Pulmonary Veins form the part of the pulmonary circulatory system. This section laid the basis for understanding the anatomy of the heart and the functions of various parts of the heart. The next section will look over the malformations of a normal heart, leading to a congenital defect of single ventricle physiology.

1.3 Congenital Heart Defects leading to Single Ventricle Physiology

As discussed earlier, the single ventricular physiology refers to a condition wherein only one ventricle is deemed to perform the work of pumping blood to both the lungs and the body in conjunction. This CHD can occur naturally wherein one of the ventricles, either left or right is underdeveloped and is incapable of pumping the blood as effectively, as in a normal human heart. Whereas in other cases, the heart defect could be associated with underdevelopment of the valves or of the septal wall. These conditions are more critical than an under-formed ventricle since in these cases either the systemic or the pulmonary circulation is almost completely blocked. Thus, invasive surgeries are performed in such infants just a few weeks after the birth to get a more stable single ventricular physiology. The Single Ventricle Physiology (SVP) of the heart is then treated in stages to achieve an adequate heart function. The congenital heart defects leading to SVP are discussed in detail below:

1.3.1 Tricuspid Atresia

Tricuspid Atresia is a CHD where the tricuspid valve, which is the gateway between the right atrium and ventricle isn't formed or is completely absent. This restricts the flow of blood to the right ventricle and hence, in most of the cases, leads to an underdeveloped right ventricle as compared to the normal heart as shown in the Figure 1.2(a). The patients with Tricuspid Atresia are

also diagnosed with Atrial Septal Defect (ASD) and Ventricular Septal Defect (VSD). Both atrial and ventricular septal defects provide a secondary blood flow pathway from the right atrium and ventricle toward left atrium and ventricle respectively.

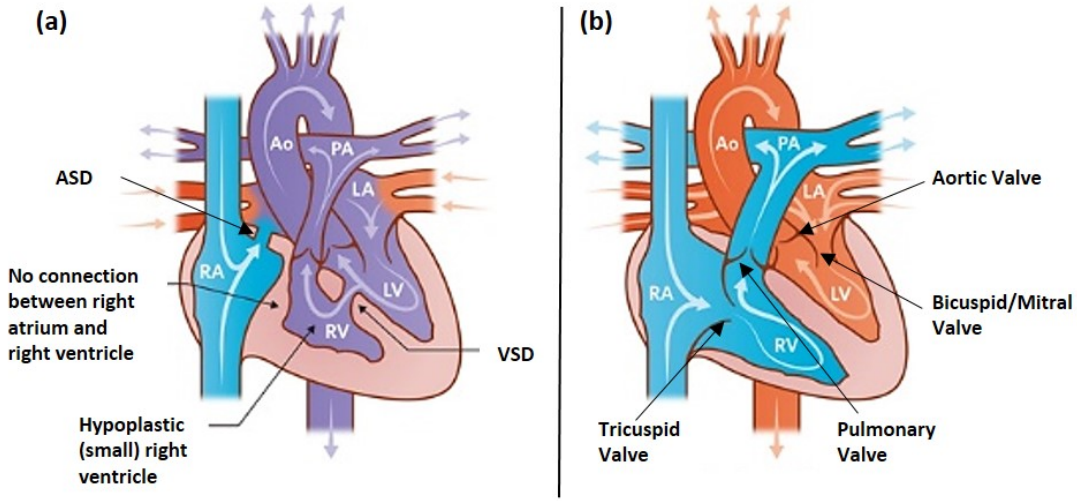

Figure 1.2: (a) Heart physiology with Tricuspid Atresia, (b) Normal human heart physiology [2]

1.3.2 Pulmonary Atresia

Patients born with Pulmonary Atresia, have a complete obstruction between the right ventricle and the pulmonary artery due to an absent or underdeveloped pulmonary valve as shown in Figure 1.3(a). This defect obstructs the direct passage of blood to the lungs from the right ventricle. However, in most of the cases, newborn babies with this defect are also diagnosed with patent ductus arteriosus, which refers to a small duct or passage connecting the pulmonary arteries to the aorta. This duct is open when the infants are in their mother's womb since there is no need for blood oxygenation, but it is naturally closed once the child is born. In addition to this, the deoxygenated blood from the right ventricle flows into the left ventricle via ventricular septal hole which is also present in such patients in most cases, as depicted in Figure 1.3(a)

1.3.3 Hypoplastic Left Heart Syndrome (HLHS)

Hypoplastic left heart syndrome is one of the most complex and surgically challenging of all the CHDs. In this defect, the left side of the heart which pumps the oxygenated blood to the body is severely underdeveloped. This is clearly depicted in Figure 1.3(b), where the left ventricle and the aorta are very small in size, while the aortic valve is completely closed with an underdeveloped mitral valve. In this case, the left side of the heart lacks the power to pump the blood to the body and hence the blood is forced to follow a secondary path. The blood has to traverse from the left

to the right atrium via atrial septal hole, then to the right ventricle via the tricuspid valve, and finally, after systole, the blood has to enter the aortic arch from pulmonary artery via patent ductus arteriosus. This large flow path for the blood from the left atrium to the aorta acts as a serious source of pressure loss resulting in a dangerously low blood flow to the organs.

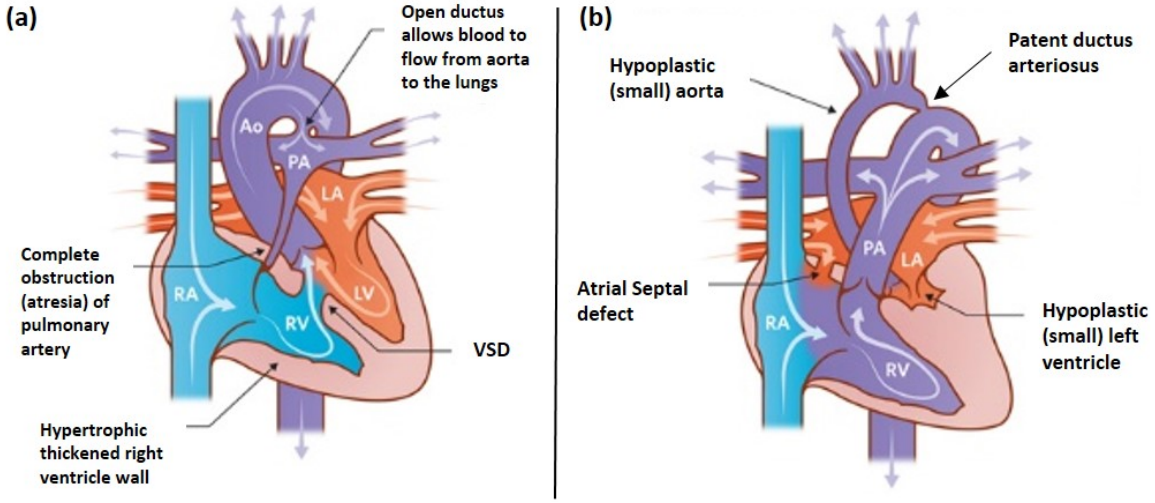

Figure 1.3: (a) Heart physiology with Pulmonary Atresia, (b) Heart Physiology with Hypoplastic Left Ventricle [3, 4]

1.3.4 Double Inlet Left Ventricle (DILV)

In this CHD, the right ventricle is very small or underdeveloped, and hence this defect could also be called as Hypoplastic Right Heart Syndrome (HRHS). In this case, both, the right as well as the left atrium drain blood into the left ventricle, and during systole the blood is pumped both to the lungs and the body. Another unusual phenomenon seen in such patients in comparison to a normal heart is that there is a transposition of the aorta and pulmonary arteries opening in the right and the left ventricle respectively as opposed to opening in their morphological ventricles as illustrated in Figure 1.4(a).

1.3.5 Double Outlet Right Ventricle (DORV)

This congenital heart defect is similar to DILV, where the two great arteries, the aorta and the pulmonary artery, both open into the right ventricle as shown in Figure 1.4(b). There are several sub-types of this defect based on the position of the ventricular septal hole. However, in all the cases the blood from the underdeveloped or small left ventricle passes across the VSD to the right ventricle, from which it is pumped into the great arteries simultaneously during ventricular systole.

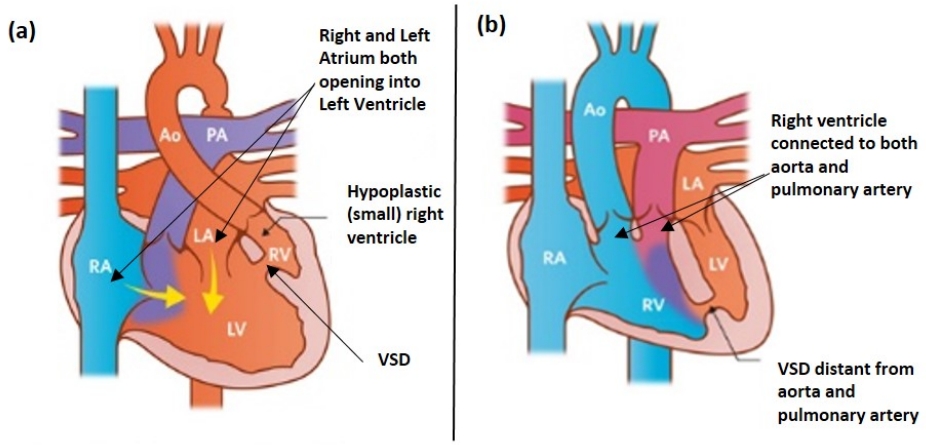

Figure 1.4: (a) Heart physiology with Double Inlet Left Ventricle, (b) Heart Physiology with Double Outlet Right Ventricle [5, 6]

In all of the above cases, there is only one ventricle performing the function of delivering the blood to the systemic and the pulmonary circulation. The major complication common to all of the above mentioned cases is that due to the presence of a VSD or ASD, the oxygenated and the deoxygenated blood mix together inside the single ventricle before being pumped to the lungs and the body organs. Thus, the organs do not receive the required oxygenation and consequently, such babies are cyanotic or have bluish skin tint, have lower cardiac output, chronic volume overload on the single ventricle and require immediate surgical intervention after birth to avoid fatality [21]. The next section will discuss, the surgical procedure carried out to treat such defects and the physiological impairment and complications that could occur after such an operation.

1.4 Fontan Physiology

Before the 1970s, the most common surgical procedure to treat these patients was to connect the right atrium to the pulmonary arteries via an artificial graft forming an atrio-pulmonary shunt. During this procedure, the tricuspid valve and the atrial septal hole are closed if they were initially open. This allows the deoxygenated blood to flow from the right atrium to the lungs. However, there were many post-operative complications from this procedure leading to early mortality of patients, until in 1971, when an improved surgical procedure was introduced by a French surgeon named Dr. Francis Fontan [22, 23]. The improved procedure is usually performed in three stages at different periods within the first 5-6 years after birth. The aim of the Fontan procedure is to relieve the single ventricle of performing dual pumping job and balance the blood flow between the lungs and the body, thereby achieving stable oxygen saturation levels and adequate heart functioning.

Operative Stages of Fontan Surgical Palliative Procedure:

1.4.1 Blalock Taussig (BT) Shunt or Norwood Procedure

The first stage of the surgical intervention is performed within first 4 to 6 week of the birth and the procedure has variations based on the type of CHD [21]. Most of the cases involve suturing of a Gore-Tex tubular graft (Blalock Taussig shunt) between the left subclavian artery (artery carrying blood to the left arm) and the pulmonary artery. This provides a well-balanced and limited flow of blood to the lungs. In certain cases, such as in HLHS, where the aorta and the left ventricle are underdeveloped, the Norwood surgical procedure is performed to reconstruct the aorta to increase its size where the initially open patent ductus arteriosus is closed. The Norwood procedure also has a Gore-Tex shunt placed between the pulmonary and the subclavian artery as shown in Figure 1.5(a).

1.4.2 Glenn Shunt or Partial Cavopulmonary Connection (PCPC)

Once the child grows and the pulmonary vasculature has developed, the second stage of the surgery called the Glenn surgery or the Hemi-Fontan surgery is performed, usually around 4 to 12 months of age [21]. During this procedure, the Superior Vena Cava is disconnected from the right atrium and is sutured directly to the pulmonary artery as shown in Figure 1.5(b). The BT shunt is also removed if existing previously. After this stage, the single ventricle is slightly relieved since the blood from the upper part of the body is now directly channelled to the lungs.

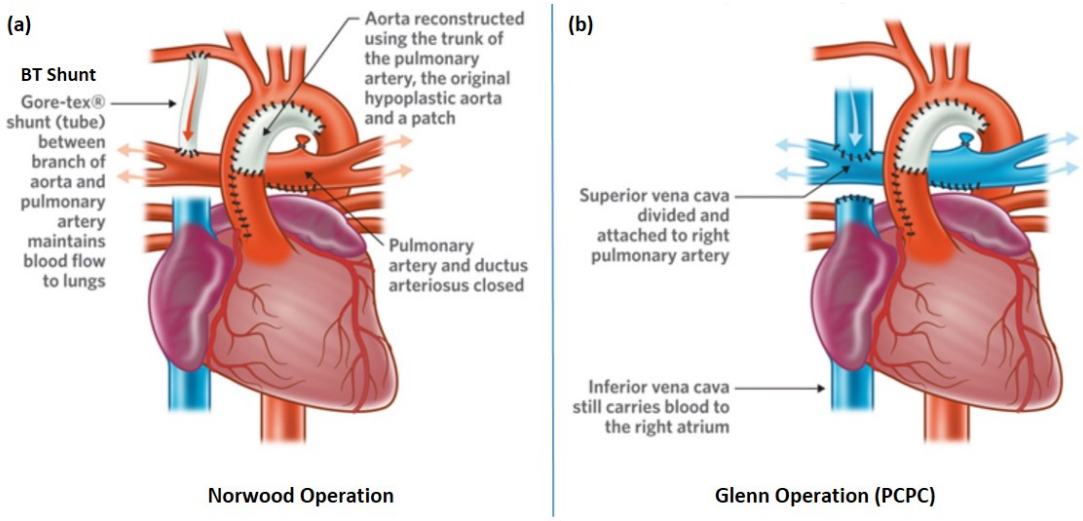

Figure 1.5: (a) Norwood Operation with BT shunt performed for patients with HLHS, (b) Glenn Operation or Hemi-Fontan operation performed 2-3 months after the first stage of Fontan procedure [4, 7]

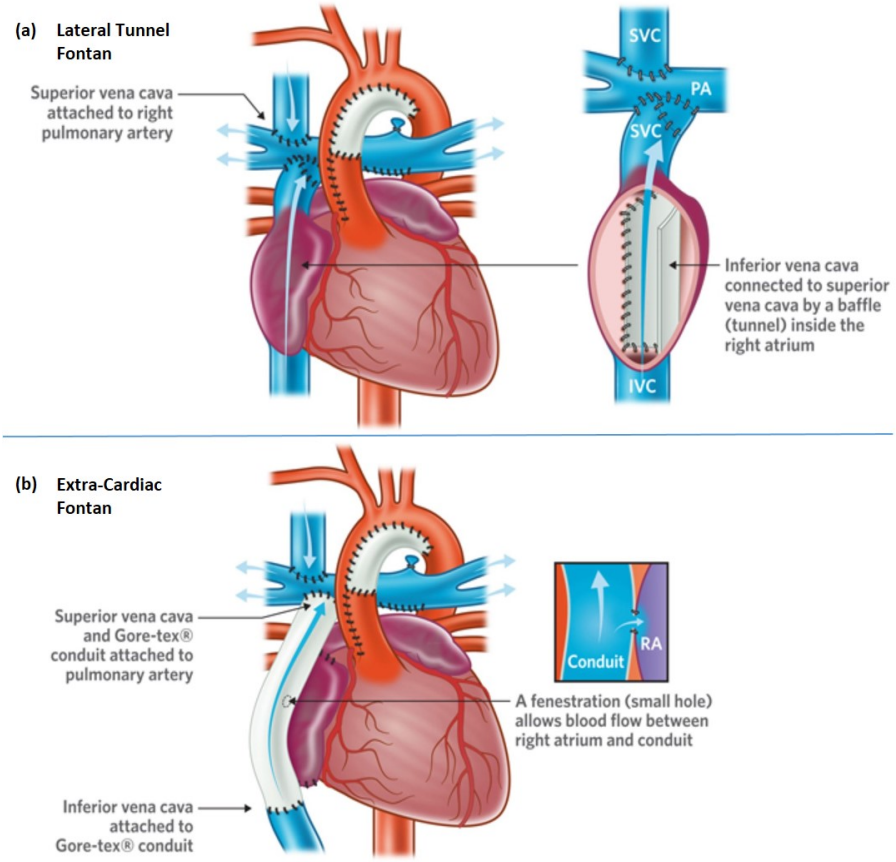

Figure 1.6: Fontan Completion stage variations: (a) Lateral Tunnel Fontan, (b) Extra-Cardiac Fontan [7]

1.4.3 Fontan Completion or Total Cavopulmonary Connection (TCPC)

Each and every patient is different and depending on the growth of patient's vascular structure, the cardiac output, and the blood oxygen saturation level, this final stage is performed anytime between 2 to 5 years of age [21]. In this stage, the second systemic vein, i.e., the Inferior Vena Cava (IVC) is disconnected from the right atrium and is connected to the pulmonary artery. Thus, all of the deoxygenated blood from the body flows to the lungs bypassing the single ventricle which is now only dedicated to pump the blood to the body. Figure 1.6 highlights the two ways in which the IVC could be connected to the pulmonary artery.

The lateral tunnel is the older of the two surgical procedures, introduced in the mid-1980s, where a tubular prosthetic baffle is sutured inside the right atrium to connect the IVC to the SVC ,and then the other side of the right atrium is connected to the pulmonary artery. The Extra-Cardiac Fontan procedure, introduced by de Leval in 1990, involves direct connection of the IVC to SVC via an external Gore-Tex tube graft [24]. A Fenestration or a small hole is usually provided in either case between the graft and the right atrium to act as a buffer for the blood flow in case of

excessive central venous pressure build up.

The Fontan completion allows for near-normalization of arterial oxygen saturation and also helps to drastically reduce the chronic volume overload on the single ventricle thereby prolonging the life of the patients with single ventricle physiology. This surgical intervention creates a new circulatory portal system void of a pumping chamber to push the blood towards the lungs. In such patients, the blood flow to the lungs is governed by the post-capillary transit energy. The unnatural physiology created by the Fontan surgery has two major drawbacks of reduced cardiac output and an elevated systemic venous pressure. These symptoms are caused due to the absence of a sub-pulmonary ventricle and large hindrance posed by the pulmonary vasculature against the blood coming from the vena cave. This causes serious systemic venous hypertension, reduced single ventricular filling, and preload and reduction in cardiac output both at rest and during exercise leading to physiological impairment of the functional ventricle. There is around 20-30% reduction in the Cardiac Output (CO) of Fontan patients while resting and during exercise, the CO is further reduced to 65% of the normal [21]. In most of the cases, the ejection fraction of the single functional ventricle is reduced below 50% post Fontan surgery indicative of impaired systolic ventricular function [25]. Most of the Fontan patients treated with the older technique of atriopulmonary shunt are diagnosed with heart arrhythmia. Such patients also face the problem of protein losing enteropathy where an excessive loss of protein occurs in the intestinal tract mucosa and if not treated soon could lead to early mortality [26–31]. The chronic venous congestion could lead to development of liver cirrhosis or hepatic dysfunction in almost 25% of the patients undergoing Fontan operation [32, 33]. The lungs of the Fontan patients don't receive the required level of perfusion due to the pulmonary vascular impedance to the blood flow. Also, the new vascular physiology developed by the TCPC doesn't divide the blood containing hepatic fluid from the liver equally to both the lungs. The unequal hepatic fluid distribution and reduced lung perfusion are one of the major factors to cause arteriovenous and hepatic venous malformations in Fontan patients [34–38].

The various post-operative complications and impairments after Fontan surgery increases the chances of morbidity and mortality in such patients. The advancement in the surgical procedure and techniques together with an improved perioperative management has resulted in decrement in early mortality of Fontan patients from 20% to between 2-7% over the last couple of decades [25]. Most of these patients suffer from heart failure due to systolic or diastolic ventricular failure, arrhythmia, thromboembolic complications, PLE and plastic bronchitis [21]. In 2010, an approximate 10,000 to 20,000 adults in the United States had undergone Fontan palliation [17]. Mayo Clinic had conducted a 40-year long-term follow up study of 1052 Fontan patients who had undergone Fontan surgery between 1973 and 2012. Of the 1052 Fontan patients, the 10-year, 20-year and 30-year survival after the Fontan completion was 74%, 61%, and 43% respectively. The study also showed that the survival rates improved with the advancements in Fontan surgery techniques [28].

Since it's introduction in 1971, the Fontan procedure has tried to improve the survival chances of the patients with the improved surgical methods like the extra-cardiac TCPC. However, over the years the surgical advancement has reached its summit and yet the long-term survival beyond 30 to 40 years for such patients seems to be bleak. In order to improve the hemodynamics of the

blood flow inside the TCPC to obtain reduced pressure losses and equal distribution of the blood to the lungs, various scientists and doctors have developed different TCPC configurations and grafts. The changes in the TCPC geometry has shown some promising results in terms of effective blood flow to the lungs, but the lack of pumping mechanism to overcome the pulmonary vascular resistance and the trailing problem of systemic venous hypertension has always been a challenge to tackle [38–41]. Heart transplantation has been accepted as the best option to provide definitive therapy for such defects, however, the lack of availability of donor hearts, the unique physiological needs of the child, and the mismatch of size between the donor and recipient would mean the patients would have to wait for a long period of time. In 2015, there were 2,000 children waiting for heart transplantation but the number of available hearts was only 968. Approximately, 17% of the children on the heart transplantation wait list die every year [42]. Over the last one decade, various new ventricular assist devices have been developed and introduced in the market and have proven to increase 1-year survival during the waiting period by 90% in the adult population [42]. This has inspired various researchers and cardiac surgeons to develop a pediatric mechanical circulatory support device to maintain the blood flow hemodynamics through the TCPC and assist the single ventricle until a donor heart is available for transplantation [43–49]. The number of VAD transplantation in adult population had increased almost 10 times from 2006 to 2010 [50]. In comparison to the adult population, there are quite few incidents of VAD implantation in the paediatric patients. Besides, there are only a handful of ventricular assist devices (VADs) commercially available in the market due to the small body size and vascular structure of the kids making it challenging to design. The next section introduces the currently existing cardiac assist devices and technologies and the limitations of the same to assist a child with single functional ventricle physiology.

1.5 Mechanical Circulatory Support Devices for Fontan Patients

- **Berlin Heart Excor**: Berlin Heart GmbH (Berlin, Germany) is the only company in the world producing cardiovascular assist device for all the age groups of patients [8]. Moreover, the Berlin Excor for pediatric patients is the only pump approved by the FDA in the United States. It is a pulsatile pump comprising of an inlet and an outlet cannula, and a central chamber divided by a polyurethane membrane to house blood and air on its either side. To maintain the pulsatile flow, it requires an external pneumatic system to supply time varying pressure similar to that of the heart as shown in Figure 1.7. This extracorporeal device (sits outside the body), can be used for uni- or bi-ventricular support and is designed for medium to long-term mechanical assistance. Due to its small size, it is easy to implant the cannula inside younger children as compared to other existing Ventricular assist devices (VADs) and hence it is most widely used in the clinical trials on patients with CHD of Single Ventricle Physiology. However, since this device is designed specifically for ventricular dysfunctions, the success rate is poor when it comes to supporting Fontan patients. The major

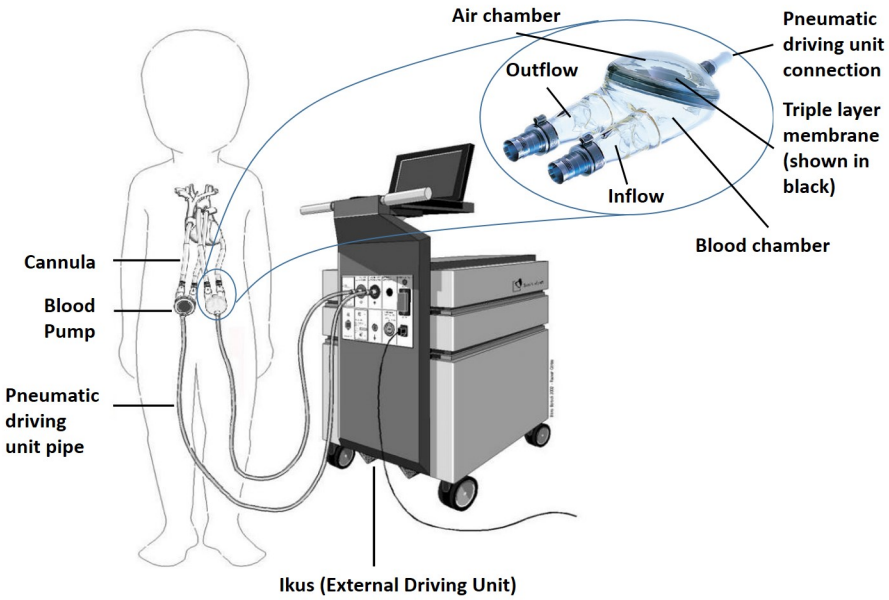

Figure 1.7: Berlin Excor Heart Pump for Pediatric Patients and its components [8]

post-implantation issues faced with Berlin Excor are hepatic dysfunction, venous hypertension, thromboembolism, and respiratory failures. According to Weinstein et al., the survival of patients with SVF supported with Berlin Excor was only 42% which was far less than 73% survival for patients with Biventricular support [51]. The children supported with this device have to carry the large external air pump machine call Ikus making mobility difficult.

- **Thoratec PVAD and IVAD**: Similar to Berlin Excor, the Thoratec PVAD (Paracorporeal VAD) and IVAD (Implantable VAD), are pulsatile pumps used for either pulmonary, systemic, or dual ventricular support. These VADs developed by the Thoratec Corporation (Pleasanton, CA, USA) is widely used for adults and there are very few records of their usage in the pediatric population. The Thoratec PVAD looks similar to the Berlin Excor and also requires an external pulsatile pneumatic pump and is used for short to mid-term cardiovascular support. The only difference between the PVAD and the IVAD is that the latter is implanted inside the chest cavity of the patient instead of keeping the device external to the body. There has been little published data on the usage of Thoratec device for patients with single ventricular physiology. The post-operation complications of this device overlap with those of Berlin Excor, due to same nature of the two devices.

- **HeartWare LVAD**: The Heartware VAD is a centrifugal blood pumping device developed by Heartware Inc., now taken over by Medtronic Inc. (Minneapolis, MN, USA) and is the most widely used device for left ventricular assistance [52]. Due to its small size, it can be easily accommodated inside the pericardial space with inflow and outflow cannula attached to the left ventricle and aorta respectively, as shown in Figure 1.8. This is a continuous flow device, which as compared to the previously discussed devices, removes the pulsatile sensation of

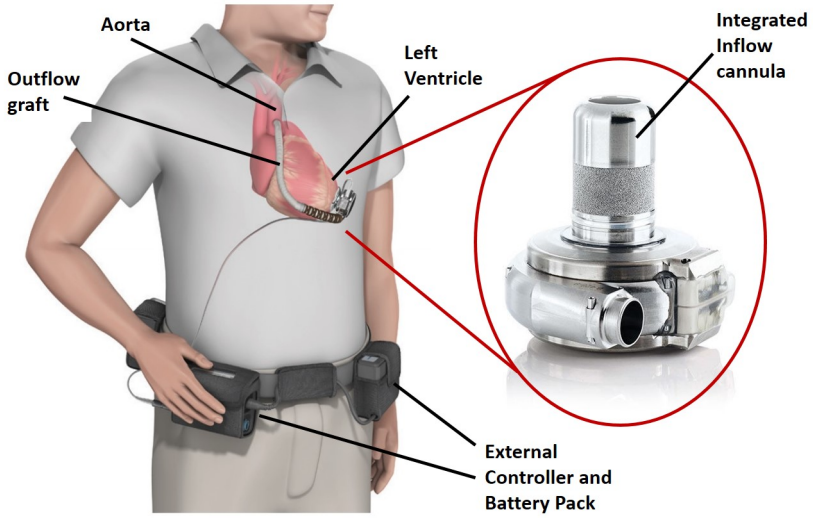

Figure 1.8: Heartware LVAD Centrifugal pump and its accessories [9]

the blood flow through the veins. Researchers have found that there are no adverse effects of the continuous flow of blood on the body and the end organ functioning. This device has seen more clinical trials to support Fontan patients than Thoratec PVAD, and has shown promising results as a Bridge to Transplantation (BTT) device, at least in its small sample of published trials, with only one fatality till now. According to the study done by Niebler and colleagues as well as that done by Arnaoutakis and group, the Heartware provided successful assistance to patients with failing Fontan physiology [53, 54]. Both the studies mention various complications encountered post-implantation, some of which include high central venous pressure, inflow cannula obstruction requiring adjustment in the VAD positioning from ventricle to atrium and high risk of bleeding and thromboembolism [53, 54]. In the midst of the successful transplantation of this device, these complications clearly depict the need for a Fontan specific ventricular assist device designed to meet the missing sub-pulmonary ventricular hemodynamic needs.

- **Impella RP**: Abiomed Inc. (Danvers, MA, USA) produces Impella pumps for right and left ventricular assistance and Impella RP is specifically developed for right ventricular assistance. Impella is the world's smallest heart pump with a diameter ranging from 3mm to 7mm (9Fr to 21Fr) [10]. It is a percutaneous catheter mounted heart pump which is inserted in the body via Femoral artery near the right thigh, into the right atrium, following through the tricuspid and pulmonary valves, and finally rested inside the pulmonary artery as depicted in Figure 1.9. This device works on the Archimedes screw principal to pump the blood. Despite its small size it provide a flow rate of around 2.5 l/min to 5 l/min, however, to maintain such flow rates for very small diameter pump, its speed has to be increased to around 33,000 rpm [55]. The small diameter of the pump in comparison to the vessel diameter (around 12 to 15 mm) provides a large annular space for backward blood recircu-

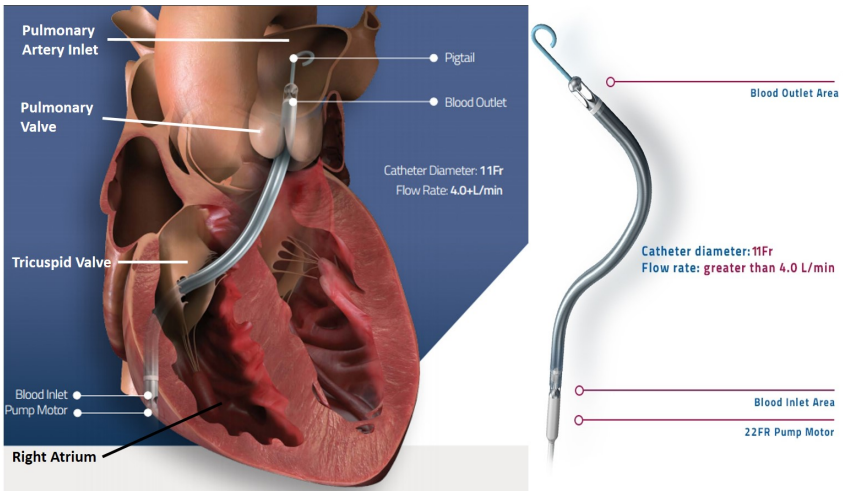

Figure 1.9: Impella RP Catheter Pump and its placement inside the Right Ventricle and Pulmonary Artery [10]

lation. There have been few incidents were Impella pump was used for single ventricular assistance in Fontan patients; according to the study done by Morray et al. in 2017, out of 10 patients with SV anatomy supported on Impella pump, there were 2 fatalities and 4 cases of adverse side effects in the patients that did survive [56]. The high speed of the pump has been the main cause of hemolysis while using this device. Besides, such a device would require an occlusive mechanism just upstream of the outlet to prevent the flow recirculation as investigated and explained by Christopher and his colleagues [55].

- **Reitan Catheter Pump**: Reitan catheter pump is the only foldable axial flow propeller pump commercially manufactured and sold by Cardiobridge Inc. (Hechingen, Germany). Developed and patented by Dr. Oyvind Reitan in 1998, this intra-aortic blood pump is used to treat patients with acute decompensation heart failure by reducing left ventricular afterload, and enhancing end organ perfusion [57]. The diameter of the pump in the folded state is only 10F (where 3F = 1 mm) which increases to 21 mm when deployed inside the aorta. The pump is inserted in closed or folded state via the femoral artery and is unfolded or deployed inside the descending aorta just below the aortic arch as shown in Figure 1.10. The pump consists of an internal sliding mechanism similar to that of an umbrella which facilitates its easy opening and closing. This pump is able to produce a flow rate of 4-5 lpm, with rotational speeds ranging from 1,000 rpm to 13,000 rpm [58]. Such a type of foldable pump has various advantages, including, easy insertion, reduced chances of thrombus formation due to a small exposed foreign surface area, lesser anti-coagulation requirements, and lower potential for blood damage due to reduced shearing. The success of this device due to its hemodynamic design is also evident from the study done by Smith and his group, showing, all the 10 patients who had undergone percutaneous coronary intervention with this device survived without any risk of hemolysis, platelet activation or renal impairment [59].

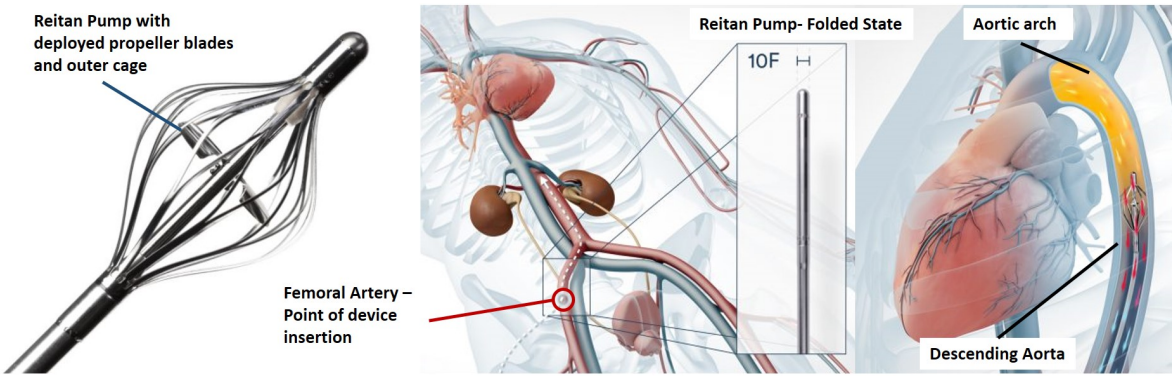

Figure 1.10: Retian Catheter Pump with its foldable blade and cage inserted via Femoral artery [11]

1.6 Development of a unique percutaneous cavopulmonary assist device

The advent of mechanical circulatory devices has reduced the mortality in patients with CHDs, however, as seen in Section 1.5, there is no device specifically developed to assist patients with single ventricle physiology. To address this issue, a unique and novel concept of developing a dual-propeller intravascular percutaneous pump is introduced in this thesis. Such a pump consists of two 2-bladed propellers, one resting inside the IVC, and the other inside the SVC, both connected to the same central shaft as shown in Figure 1.12. This allows both the propellers to rotate at the same speed while augmenting the blood flow from the upper and lower part of the body to the lungs. Such a design allows for a single insertion of the pump. Similar to the Reitan propeller pump, the blades and the stent body of this pump is foldable as shown in Figure 1.11, and will be made out of shape memory alloy called Nitinol.

Nitinol is sensitive to the temperature variations and changes from Martensitic state at low temperatures to Austenitic state at high temperatures. This transition from martensite to austenite occurs at a transition temperature which can be uniquely set for each material. In the current case, the propeller blades and the stent can be programmed to have a transition temperature equal to that of the body temperature. This pump can be inserted inside the body either via Femoral vein near the right thigh or via Jugular Vein near the neck region and guided to the TCPC site via catheter. At the time of insertion, the pump will be covered by a protective sheath and will be cooled to temperatures below that of the body ($26\,^{\circ}C$). Once the pump reaches the desired site, the outer sheath is removed and the blades and the stent are allowed to come in contact with the surrounding blood. The increase in temperature of the stent and the blades triggers them to self-deploy, due to the state change from martensitic to austenitic. The motor placed upstream of the IVC propeller is powered via a battery pack and a controller placed external to the body. The connection is established using a catheter carrying wire from battery to the motor. The power required by the motor is a mere 0.5 W, which could energize the pump to generate a flow rate of 0.5 to 4.5 l/min, while rotating within the speed range of 6,000 rpm to 12000 rpm. Under such conditions, this

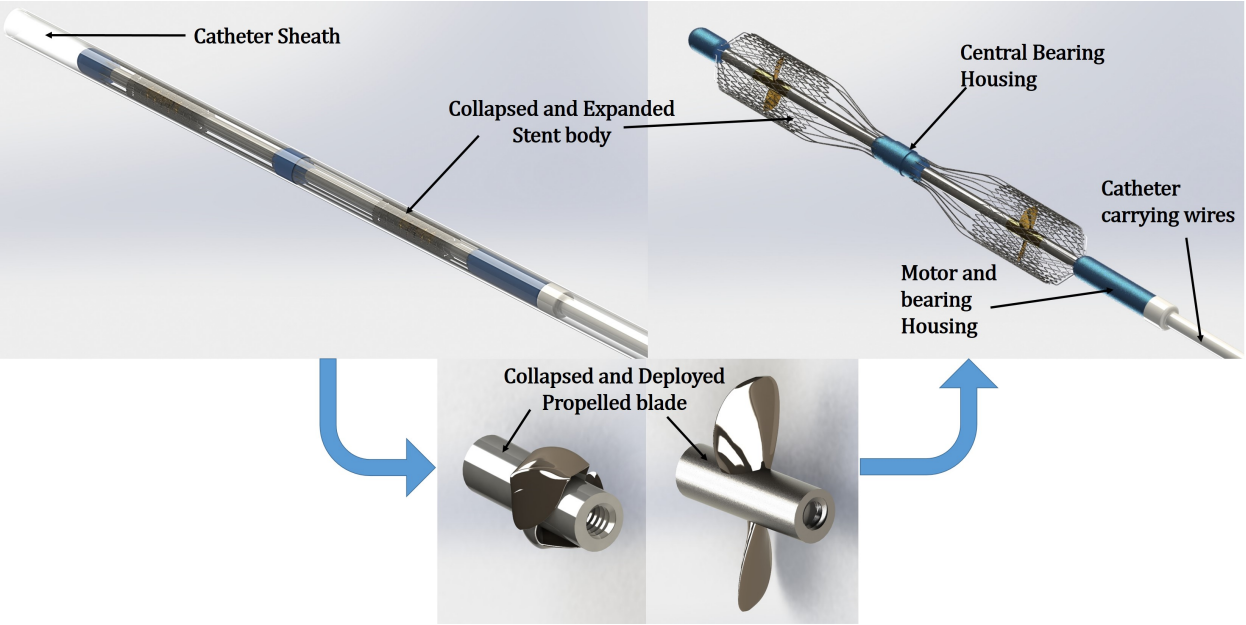

Figure 1.11: Dual Propeller Pump in Folded and Deployed state

pump would generate a pressure rise of 2 to 20 mm Hg which will help reduce the work load of the single ventricle, and at the same time reduce the central venous pressure to more physiological values. It also helps to eliminate the threat of venous hypertension in superior vena cava as it has been experienced in other pumps. The features like small size and few operating parts would mean there will be less high shear stress exerting area on the blood which would consequently lower the risk of hemolysis. Another advantage of such a device is that it occupies a small volume of the blood vessel so that it is non-obstructive in the event of device shutdown. The airfoil shaped blades provide a streamlined blood flow path ensuring minimum evidence of irregular flow patterns to avoid initiation of blood clotting.

Development of a VAD is a time consuming process and even after successful trials, there are lots of FDA (Food and Drug Administration) requirements that need to be fulfilled to obtain its final approval, for introduction of the device into the market. The first step, like in any other pump development process, is to design the blades that would generate the required pressure rise. This is most widely done by using the standard empirical formulas and relations developed over the years to get the required hydraulic performance. The initial pump design is then manufactured and tested to check if it provides the required performance. If the pump fails to meet the requirements, the design parameters are adjusted until the specification targets are met. This trial and error procedure requires a few iterations before obtaining the final design and has been widely used and adopted. However, by adopting an inverse design method one can still obtain a similar outcome. The inverse design method uses classical turbomachinery, fluid mechanics, and continuity equations to develop a non-linear system of equations which when solved iteratively, gives the final pump design parameters such as blade angles, chord length, camber, etc., that determines the

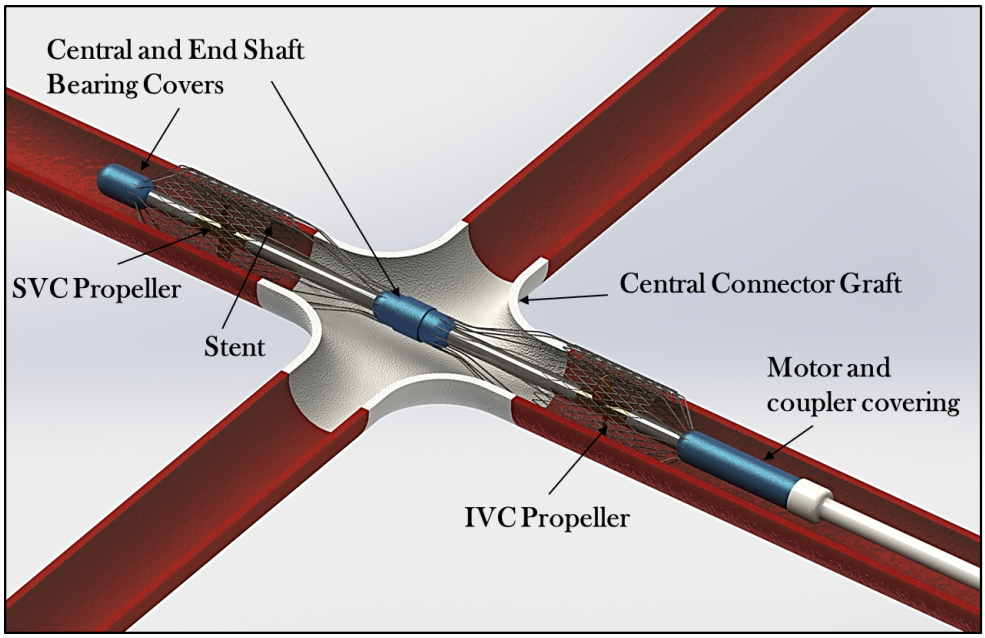

Figure 1.12: Dual Propeller Pump assembly inside sectional Flared TCPC

pump performance characteristics [60]. This method helps to avoid the time invested in multiple trials and testing. Developing a VAD is more challenging than a hydraulic pump since it involves biological operating fluid, i.e. blood, whose behaviour and properties are different as compared to water. One of the main objectives of VAD design is to prevent the damage to the red blood cells while the pump operates. Thus, obtaining the final pump design is just the first step, the next step being conducting an in-vitro test (test performed outside the human body) using blood bag (bovine blood) to determine the blood damage potential of such a pump. If the hemolysis index for the designed pump is within acceptable limits, it is tested in-vivo, inside an animal body (usually sheep or cow). If the device operates successfully with minimal complications, it is given a green light to proceed with clinical trials on patients with CHDs. Since the early 1980s, various numerical analysis packages have been introduced to perform advanced mathematical analysis like computational fluid dynamics (CFD), finite element analysis (FEA), and design optimization. The CFD is a handy tool to quickly analyse the pumps for its hydraulic performance and to determine the blood damage potential of the pump by analysing the shear stress distribution and blood flow path. With the invention of faster computers and processors, the time required for computation has drastically reduced and a designer could evaluate his multiple designs with a matter of few hours or days. The dual-propeller pump introduced here employs an inverse design approach to obtain the blade geometry which is imported inside ANSYS CFX (ANSYS Inc., Canonsburg, Pennsylvania) software (widely used for VAD design and analysis) to evaluate the pump's hydraulic performance and blood damage potential.

1.7 Thesis Goals and Objectives

The overall objective of the current thesis is to design and develop an initial percutaneous dual propeller pump prototype to be used for assisting patients with single ventricle physiology. The inverse design approach incorporated here makes use of the classical marine propeller airfoil data as the input to produce the propeller blade for blood pumping application. The current thesis outlines the classical blade design theory and the methodology adopted to quantify blood damage incurred by a blood pump along with numerical and experimental results quantifying the performance of the proposed dual propeller pump in terms of pressure augmentation and blood damage. The corresponding details of the objectives are given below:

- To select a target age group of Fontan patients and determine the average anatomical and physiological parameters as inputs for the pump design.
- To study four different TCPC geometries to analyze their effect on blood flow distribution to the lungs, and fluid energy losses to select the most favorable TCPC graft geometry.
- To develop and validate an inverse design method to generate propeller blade geometry based on blade element momentum theory and Goldstein's radial loss function.
- To develop and verify a blood damage index model to determine the hemolysis index of a VAD or blood pump.
- To design the IVC and SVC propellers with the proposed method and perform CFD analysis to evaluate their hydraulic performance and blood damage potential.
- To design a test rig to evaluate the hydraulic performance of the pump prototype and the energy losses inside the TCPC.
- To analyze the dual propeller assembly inside the selected optimal TCPC geometry for a reduction in central venous pressure and blood flow distribution to lungs and the power requirement for the pump operation.
- To evaluate the effect of the propeller pump stent support on the hemodynamic performance of the pump and the blood damage potential and select the most favorable stent geometry.

Chapter 2

Design Considerations for a Percutaneous Cavopulmonary Assist Device

This chapter introduces the fluid flowing through the circulatory system, i.e. blood, its composition, its properties, and the factors affecting those properties. The latter part of the chapter discusses a patient's anatomical and physiological parameters to be considered while designing a blood pump, followed by the evaluation of design speed of the pump based on the selected duty point on the Cordier diagram.

2.1 Blood and its properties

Blood is the main carrier of oxygen, carbon di-oxide, nutrients, minerals, and wastes to and from the cells of the body. An average adult human body consists of around $5\,l$ of blood which make up around 8% of the body weight [61]. The blood consists of Red Blood Cells (RBCs) or erythrocytes, White Blood Cells (WBCs) or leucocytes, platelets or thrombocytes, and plasma. The major part of blood is made up of plasma, constituting around 55% of blood volume, and is in turn composed 90% of water and remaining 10% of proteins, ions, nutrients, wastes and dissolved gases. Out of the remaining 45% of blood volume, around 43% is made up of RBCs while platelets and WBCs constitute around 2% and 0.05% of the total volume respectively [61]. Most of the RBC volume is filled with Hemoglobin, which is a critical protein that helps in the transportation of oxygen and carbon-di-oxide between the lungs and the tissue cells. The blood platelets or thrombocytes are involved in blood clotting thereby preventing blood loss in an event of skin rupture whereas the WBCs determine the immunity response of the body by fighting the bacteria and viruses.

As compared to water, the average density of blood is $1050\,kg/m^3$ and its average kinematic viscosity coefficient is $3.5\,cP\,(centipoise)$. The viscosity of the blood is dependent on a number of factors such as the blood hematocrit level, blood temperature, shear rate acting on blood, and the pathological conditions of blood plasma. By definition, blood is non-Newtonian, however, it could

behave as a Newtonian fluid under specific conditions. A Newtonian fluid is one whose viscosity is independent of the applied shear stress at a fixed temperature and pressure. Any material that deforms continuously under the action of an external shear force is classified as fluid and the viscosity (μ) of any fluid is dependent on the rate of deformation $(\frac{\partial u}{\partial y})$ and the applied shear stress (τ). For a 2-dimensional unidirectional flow along the x-direction, the relation between the shear stress, shear rate, and the viscosity is given by Equation 2.1.

$$\tau = \mu \frac{\partial u}{\partial y} \tag{2.1}$$

One of the major factors affecting the blood viscosity is the rate of shear. It has been demonstrated by Whitmore and group that the blood viscosity decreases with an increase in shear rate and becomes constant or independent of it above a value of $100\, sec^{-1}$ [12]. Another factor affecting blood viscosity is Hematocrit which is the measure of the percentage of RBCs in blood volume and as depicted in Figure 2.1, Whitmore et al. has experimentally proved that the blood viscosity is directly proportional to the blood Hematocrit [12]. Moreover, the number of RBCs in the blood reduces, due to their rupture when acted upon by a shear stress above a critical value. This causes a relative increase in plasma content of the blood which is mainly composed of water. This has also been experimentally proven by Cokelet et al., who showed that at low hematocrit levels, the blood plasma demonstrates a linear relationship between shear stress and shear strain rate [62, 63].

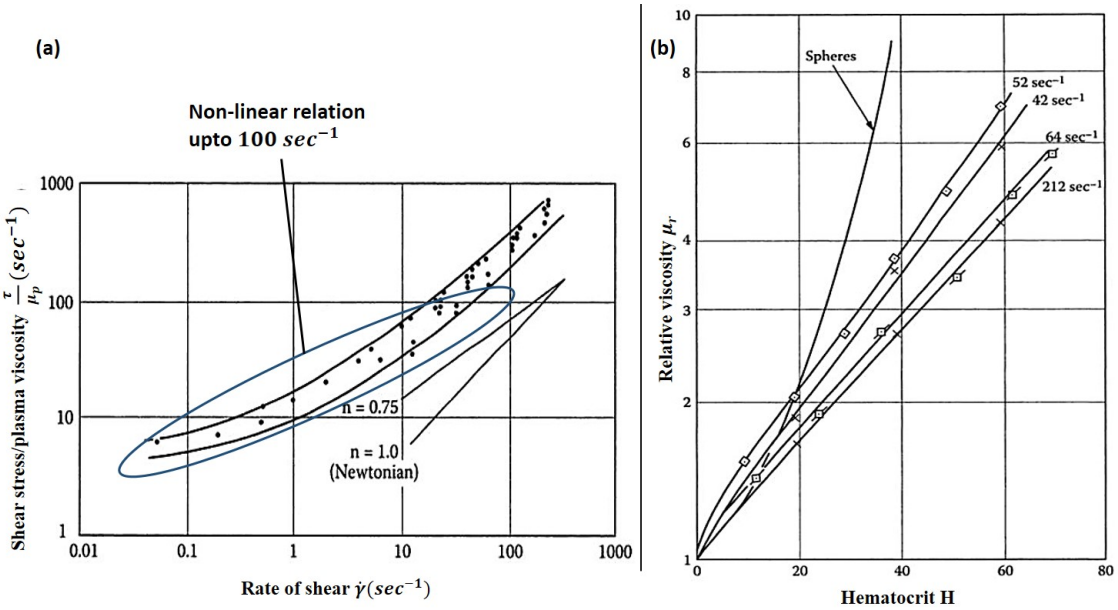

Figure 2.1: (a)Variation of shear stress normalized to the plasma viscosity with shear rate, (b) Effect of hematocrit on the relative viscosity of blood [12]

Most of the patients diagnosed with congenital heart defects, and undergoing invasive surgeries are injected with anticoagulants like heparin to prevent blood clotting at the site of artificial valve

transplantation or near the site of stitches [64]. These anticoagulants or blood thinners have been found to reduce the blood viscosity below the normal values [61]. Moreover, a ventricular assist device rotating at high speeds to pump the blood often exerts a shear rate higher than the critical value of $100\,sec^{-1}$ on the blood thereby making blood behaviour Newtonian during its operation [65]. As a result, most of the researchers developing ventricular assist devices assume blood to be Newtonian while modeling the flow through the device [43, 44, 46]. Based on this background, the blood has been considered as a Newtonian fluid throughout this research with density (ρ) and kinematic viscosity (μ) equal to $1050\,kg/m^3$ and $3.5\,cP$ (or $0.0035Nsec/m^2$) respectively.

2.2 Anatomic and Hemodynamic Parameters for design considerations

In order to develop a ventricular assist device, it is necessary to evaluate the anatomical and physiological parameters of the heart to determine the pump sizing and its design point. The target of such a device should be to revive the single ventricle towards its normal functioning by augmenting the blood flow to the lungs and unloading the single functional ventricle. There have been quite a few studies done to evaluate the complete anatomical and hemodynamic parameters of a Fontan patient. Here the hemodynamic parameters refer to blood pressure in the arteries and veins, cardiac output, and the systolic and diastolic pressure of the left and right ventricle of the heart. To enhance the effectiveness of the blood flow to the lungs and to reduce the flow energy losses, it was necessary to determine an ideal TCPC (Total Cavopulmonary Connection) configuration. Based on the available values in the literature, the required parameters of healthy children within an age group of 11-15 years were determined. These values are used for the design considerations since they are the target values to be achieved. The average diameter of the left and right pulmonary artery was selected from the statistical study done by Knobel, Z. and her group [66]. Similarly, the clinical investigation done by Kutty, S. et al. helped to decide the average IVC and SVC diameters [67]. It is worth noting that the diameters of the arteries and veins inside the human body change during a physiological cycle including the cardiac cycle and lung breathing cycle, i.e. while inhaling and exhaling. However, to reduce the complexity level of the geometry, a fixed value of $14.3\,mm$ is selected as the diameter for all the four blood vessels namely the IVC, SVC, LPA, and RPA.

The mean cardiac output for healthy children in the age group of 11–15 years is around $4.5\,l/min$ and the mean blood flow through the LPA and RPA is around 45% and 55% of the cardiac output respectively as found from the measurements taken by Christopher et al. [68]. Similarly, Mubadda and his colleagues performed a Doppler Echocardiogram study to determine the average blood flow rate through the IVC and SVC for children which came out to be around 63% and 37% of the cardiac output respectively [69]. The average blood pressure inside the LPA and RPA is around $12.8\,mm\,Hg$ for children which is determined based on the review done by Kovacs et al. [70]. These are the flow conditions experienced during the major part of the physiological cycle of a normal child without any heart defects in the age group of 11-15 years. These anatomical

and physiological parameters are tabulated in Table 2.1 and will be used throughout this thesis. The reason for selecting the physiological parameters for design consideration of the proposed blood pump is that the final pump design should correct the defective circulation within a Fontan patient and mimic that experienced by a normal child.

Table 2.1: Hemodynamic and Anatomical parameters of children within age group of 11-15 years

Physiological Parameter	**Value**
Target Age group	$11 - 15\, years$
Diameter of blood Vessels (IVC, SVC, LPA and RPA)	$14.3\, mm$
Cardiac Output (CO)	$4.5\, l/min$
Average Left and Right Pulmonary Artery Pressures	$12.8\, mm\, Hg$
Blood Flow Rate Through IVC	$2.82\, l/min\ (63\%\ CO)$
Blood Flow Rate Through SVC	$1.68\, l/min\ (37\%\ CO)$
Density of Blood	$1050\, kg/m^3$
Viscosity of Blood	$3.5\, cP$

The hemodynamic parameters are sufficient to design the TCPC geometry but it is still necessary to determine the amount of pressure rise required to regain the normal flow physiology in children. In order to understand this clearly, the variation in circulatory pressure in a normal child as compared to a Fontan child is explained and illustrated in Figure 2.2. The Figure 2.2(a) shows the circulatory pressure variation in healthy children, with the values found from the study done by Krovetz et al. on 29 healthy children under 20 years of age (mean age 8.7 ± 5.8) [71]. It could be seen that the systemic ventricle generates high-pressure flow through the aorta which dissipates along its path to the organ cells and furthermore during its return to the systemic veins. As a result, the average pressure values found in the IVC and SVC were around 5-6 mm Hg. The sub-pulmonary atrium and ventricle (RA and RV) takes in this venous return during diastole and pumps it towards the lungs during systole via pulmonary arteries. The pressure inside the PAs was found to be around 12.4 mm Hg for the studied age group of children which is sufficient to preload the left ventricle. Now consider the case of Fontan patients with hypoplastic right ventricle, having only the left ventricle to maintain both systemic and pulmonary circulation. In this case, the central venous pressure increases drastically while the pulmonary arterial pressure reduces due to the pulmonary vascular resistance as it was discussed in the Introduction to the Fontan physiology in Chapter 1. In this case, the extra-cardiac conduit connects the IVC and SVC to the pulmonary arteries as depicted in Figure 2.2(b). The values of CVP and the PAP are determined from a study done by Satoshi et al. on 30 Fontan patients with a median age of 8.6 years [72]. It could be seen that, in the absence of a sub-pulmonary ventricle, to overcome the PVR, the central venous pressure is increased to around 11 mm Hg while the pressure in the pulmonary artery is reduced to 10.3 mm Hg. Such low PA pressures result in reduced lung perfusion, resulting in reduced blood oxygen saturation, reduced ventricular pre-load, and filling which ultimately results in lower cardiac output and increases the risk of mortality in such patients. Dr. Rodefeld, who has studied the Fontan circulation in depth since many years mentions that a modest pressure rise of 5-6 mm Hg should be sufficient to regain the normal transpulmonary flow by overcoming the vascular hin-

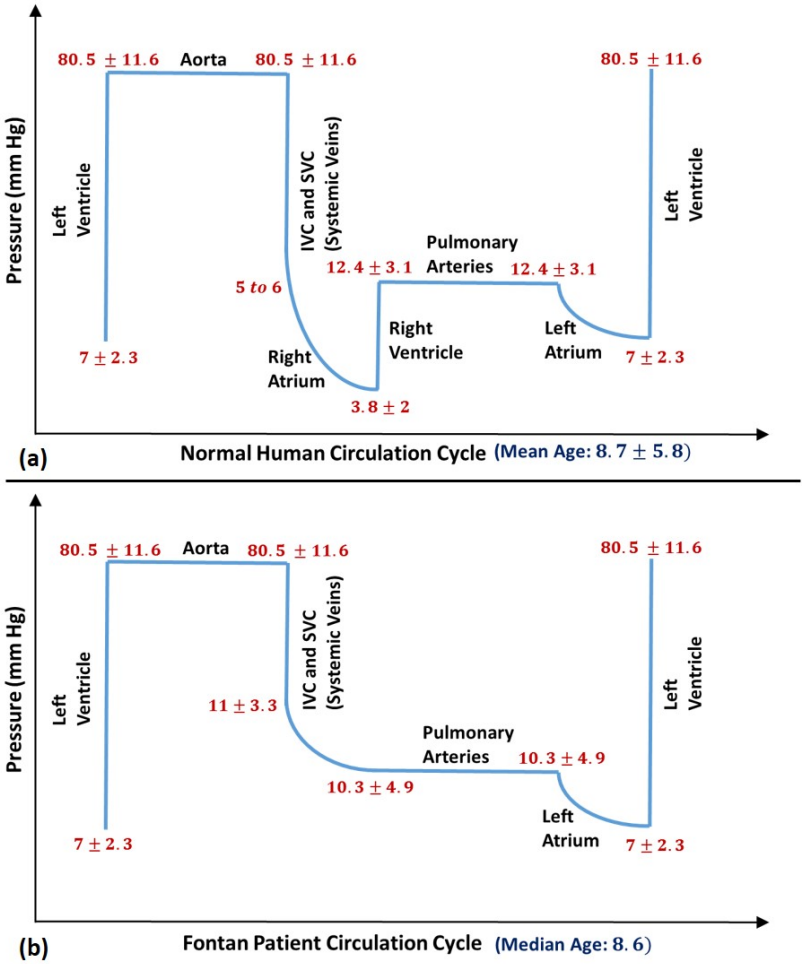

Figure 2.2: (a) Pressure variation in Normal Human Circulatory cycle, (b) Pressure variation in Fontan specific circulatory cycle

drance to ventricular filling [44, 45]. A pressure rise of 5-6 mm Hg would ensure that the pressure inside the IVC and SVC is reduced to a more physiological value of around 6-7 mm Hg.

2.3 Pump selection and its Head characteristics

In 1953, Dr. Cordier found by extensively testing different pumps that a particular group of pumps lied along a definable curve when plotted with their values of specific speed (N_s) and specific diameter (D_s) [73]. A pump whose operating point or duty point lies close to this curve would function efficiently. This plot is known as Cordier Diagram which is widely used by pump designers as an initial point to select the pump type based on the requirements or to determine the pump specifications based on the specific speed and specific diameter. The specific speed and diameter

are dimensionless quantities used to determine the characteristics of a pump and the formula for the same is given by Equation 2.2.

$$\begin{aligned} Specific\,Speed\,(N_s) &= \frac{Q^{1/2} \times N \times \rho^{3/4}}{(\Delta P)^{3/4}} \\ Specific\,Diameter\,(D_s) &= \frac{(\Delta P)^{1/4} \times D}{Q^{1/2} \times \rho^{1/4}} \end{aligned} \tag{2.2}$$

where all the parameters are in SI units

It could be seen that both N_s and D_s are dependent on the flow rate, pressure rise, pump operating speed, and the pump diameter which are all necessary parameters to design a pump. In the present scenario, the operating conditions for the pump are fixed by the physiological and anatomical parameters of a patient as listed in Table 2.1. For both the IVC and SVC pump, the outer diameter or the blade tip diameter is selected as $13\,mm$ giving a clearance of $0.65\,mm$ between the blade tip and the blood vessel wall. The required pressure rise (ΔP) is also fixed to around $5\,mm\,Hg$ while the average flow through IVC (Q_{IVC}) and SVC (Q_{SVC}) of $2.82\,l/min$ and $1.68\,l/min$ is considered as the design flow for the IVC and SVC pumps. The only parameter to be selected is the pump operating speed, which is determined by selecting the duty point from the Cordier Diagram. It could be seen that the centrifugal and radial flow pumps have relatively lower specific speed since they generate higher pressure rise and lower flow rates while the axial flow pumps and fans generate large flows against low pressure heads and hence they have relatively higher specific speed values. For the current application, it was decided to use propeller pump, a member of axial flow pump family, considering its advantages as described in Chapter 1, Section 1.6. However, selecting a duty point within axial flow pump domain would result in higher operating speed to get the required pressure rise thereby increasing the chances of hemolysis like that experienced by Impella pumps. Thus, it was decided to select the operating point to lie within the mixed flow region of the Cordier diagram. After a few trial and errors, it was found that a pump speed of $8000rpm$ would allow both IVC and SVC pump to marginally lie within the mixed flow region and close to the best efficiency curve. Plugging the above mentioned values in Equation 2.2, we get for the IVC propeller, the value of N_s and D_s equal to 1.285 and 1.693 respectively, while for the SVC propeller, the corresponding values are 1 and 2.193. This is depicted in Figure 2.3 where operating points for both the IVC and the SVC propeller lie within the mixed flow region denoted by the dotted line. Making an axial flow pump to operate within a mixed flow region for hemodynamic reasons would, however, reduce the efficiency from the hydraulic point of view. These would be addressed and discussed in Chapter 7.

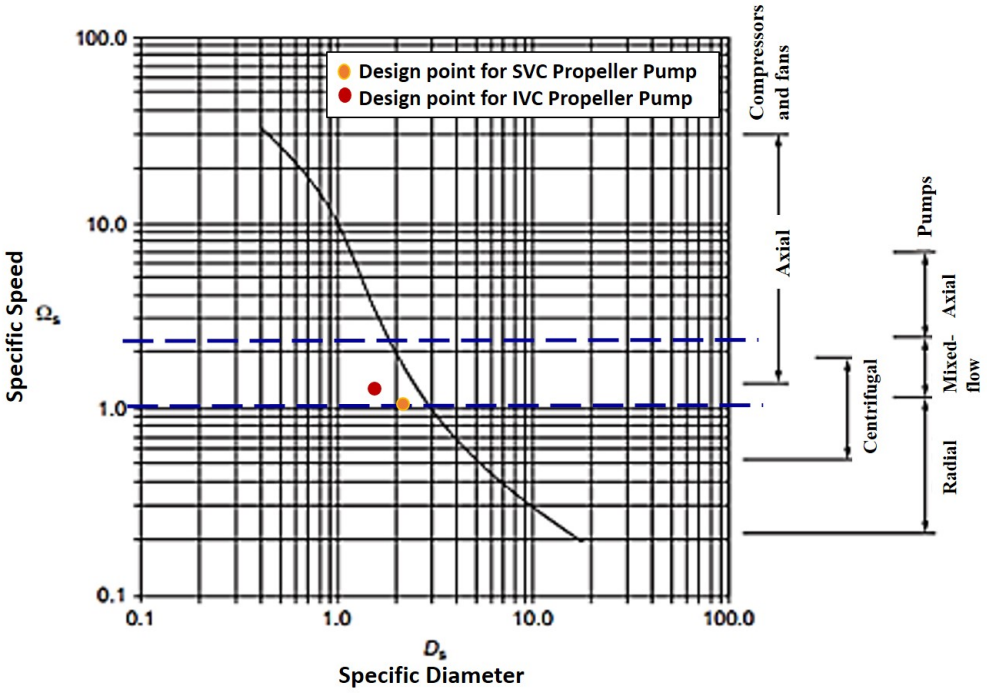

Figure 2.3: Cordier Diagram showing IVC and SVC propeller design point

In this chapter, the arguments for the assumption of the Newtonian behavior of blood in patients with a congenital heart defect were laid followed by the evaluation of anatomical and physiological parameters to be used for designing a propeller pump for single ventricle assistance. The last part of the chapter showed a comparison between the normal and Fontan circulation to determine the pressure rise required inside the cavopulmonary tract and how Cordier diagram was leveraged to determine the operating speed of the pump.

Chapter 3

Blood Damage Modelling

Ventricular Assist Devices (VADs) have helped the patients to provide temporary assistance to their dysfunctional heart, however, the problem of blood damage encountered in these devices still remains a major concern for the VAD designers and researchers. Here, the term blood damage refers to events leading to hemolysis, platelet activation, thrombosis, and emboli formation. To predict the blood damage potential of a VAD inside a human body, an engineer is required to perform in-vivo tests inside an animal to monitor the changes in free plasma hemoglobin level in the blood. Despite years of efforts, researchers have failed to develop an ideal in-vivo or animal model to accurately predict the Hemolysis potential of a VAD when implanted inside a human [74]. Experimental in-vitro tests, consisting of methods like Particle Image Velocimetry and Laser Doppler Velocimetry, to estimate the blood damage have also been developed and performed, however, the difficulty of blood handling and the inability to apply a time varying shear stress makes result interpretation and comparison a tedious job. As a result, various mathematical and numerical models to predict the hemolysis index of a VAD have been developed. This chapter introduces the concept of blood damage and a suitable mathematical model to be used to predict the blood damage incurred by a VAD.

3.1 Blood Damage Introduction

Blood damage in presence of a VAD mainly occurs due to Hemolysis and Thrombosis. Hemolysis refers to a reduction in the RBC count in the blood due to cell skin rupture. Red Blood Cells have an elastic limit and when stressed above it, they rupture, thereby releasing the hemoglobin inside it into the surrounding blood plasma. The time duration of exposure to a particular shear stress is also a deciding factor for RBC rupture. For example, a red blood cell exposed to a low shearing load for a very long period of time or a very high shear stress for a very short duration of time could trigger hemolysis. Thus the amount of hemolysis is directly proportional to the amount of shear stress acting on the blood particles and the exposure time to that stress as shown in Figure

3.1. The mathematical models describing this relation will be discussed in detail in section 3.3.

Thrombosis refers to localized clotting or coagulation of blood inside the circulatory system and is initiated by body's hemostatic mechanism to prevent bleeding and blood loss at the site of blood vessel rupture. This physiological hemostatic mechanism is started by the virtue of platelet activation. Blood platelets which are one of the smallest and the sparsest cells inside the blood consist of alpha and dense cell granules which are composed of proteins like ADP, vWF, thrombin, serotonin and thromboxane A2. These are the same proteins that act as agonists during an event of platelet-lysis to trigger platelet activation [65]. The release of these proteins during platelet-lysis activates a chain reaction where the platelets change their shape from a crisp discoid shape to a more amorphous form with projecting fingers. These activated platelets adhere to each other and to the collagen found in the endothelium of the blood vessel to form a platelet plug. These activated platelets are also responsible for converting the inactive protein called prothrombin to thrombin which triggers blood coagulation and finally formation of a clot. In case of VADs, the shear stress acting on the blood platelets has been found to activate the platelets to form blood clot or thrombus by a possible hypothesis of platelet rupture under high shear stress and has been experimentally proven by Hellums et al. [75]. Since platelet activation and thrombosis is a vast topic in itself, it won't be studied further in this thesis, however, it is a potential topic to look upon while optimizing the proposed propeller pump.

Besides, hemolysis and thrombosis, the doctors often diagnose infections at the site of VAD implantation in patients post operation. Even in these cases, the shear stress acting on white blood cells has been found to be culprit to reduce the effective functioning of WBCs to fight pathogens and bacterias leading to functional impairment of the heart [65]

The current thesis only looks at the blood damage due to hemolysis or RBC rupture as it has been the most common symptom seen in patients implanted with a VAD.

3.2 Computational Methods for Blood Damage Index Prediction

The limitations of the in-vivo and the in-vitro experimental test to predict blood damage have paved way for the development of blood damage predicting mathematical models in conjunction with Computational Fluid Dynamics (CFD). The use of CFD allows for a complete visualization of flow field and the localized and bulk distribution of volumes with critical shear stress. It also provides the liberty to track the blood particles and determine the traveling time of each particle inside the domain along with its stress and strain history. There are two computational methods by which the Blood Damage can be predicted namely: Eulerian and Lagrangian method.

- **Eulerian Method**: In this method, a scalar transport equation quantifying the rate of change of plasma free hemoglobin with time and space is introduced and solved along with the

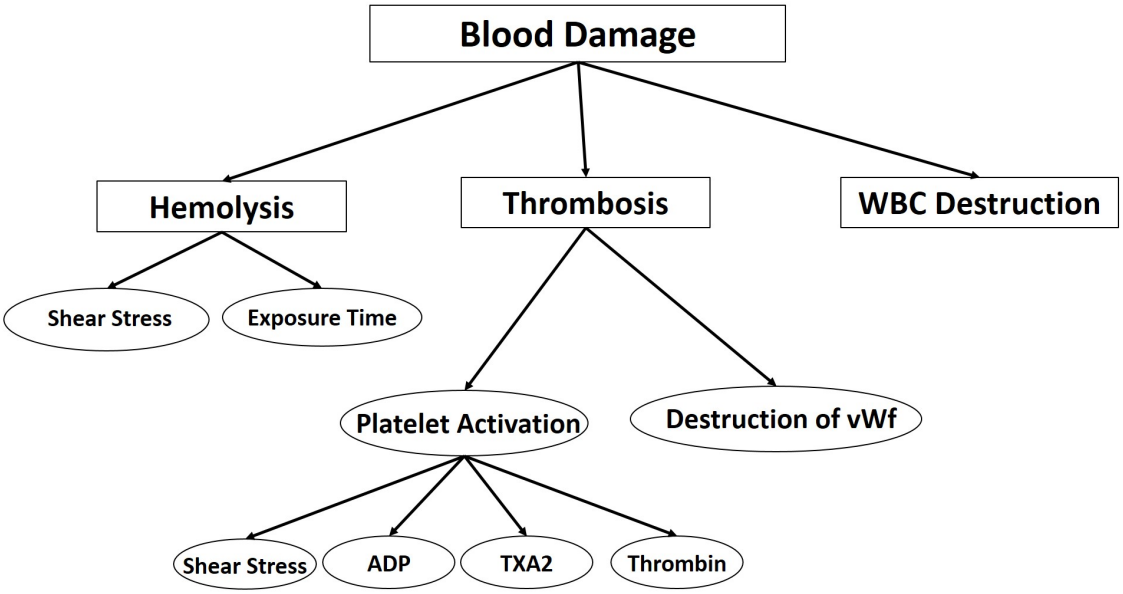

Figure 3.1: Blood Damage Classification and its affecting factors

basic Navier-Stokes equations. The equation is in integral form and hence it is solved for the entire computational domain. The scalar transport equation, as introduced by Taskin et al. is expressed by Equation 3.1 [76].

$$\frac{\mathrm{d}(\Delta Hb')}{\mathrm{d}t} + v\rho.\boldsymbol{\nabla}\cdot(\Delta Hb') = \rho(Hb.C.\tau^{b})^{1/a} \tag{3.1}$$

The expression on the right-hand side of the Equation 3.1 acts as a source term where Hb represents the total hemoglobin content and $\Delta Hb'$ represents the increase in plasma free hemoglobin content in the blood. This equation is solved along with the Navier-Stokes equation and is monitored for convergence. In this way, the Hemolysis Index (HI) values are solved for each and every cell in the computational domain and the overall value is obtained by taking a mass-weighted average of the HI values for all the cells. This method is widely used by various researchers, however, this method does not represent the exposure time to shear stress and it is computationally expensive since one extra equation has to be solved for each element and at each time step.

- **Lagrangian Method**: In this method, the total blood damage sustained by a single particle moving along its designated path is computed by integrating the BDI at discrete points along that path line. To understand this, as shown in Figure 3.2, consider a blood particle traveling along a fixed trajectory, starting from the inlet of the pipe, passing through the pump and exiting from the outlet. Now, if we consider this path line to be divided into n discrete points or n-1 smaller elemental paths, then the cumulative blood damage for that particle would be equal to the sum of the blood damage incurred by the particle while traversing through each elemental path, starting from the inlet to the outlet.

In this way, the Lagrangian approach provides an ability to determine the shear stress history of a particle, the exposure time and its total traversing time. The assumption made while discretizing a blood particle trajectory into infinitesimally smaller paths is that the shear stress acting for the individual elemental path remains constant for that path. To evaluate the blood damage using CFD, a Lagrangian particle tracking employing forward Euler method is used. After the solution is obtained, the particle tracks are obtained for the inserted particles by post-processing the solution. The scalar shear stress and the residence time values at each point along the streak line of a red blood cell are exported and are summed to get the cumulative BDI for that particle. The similar procedure is followed for all the particles to finally determine the average BDI. This is relatively less time-consuming process since all the BDI computation work is performed once the solution is obtained. However, the accuracy of this method depends on the number of particles injected from the inlet and it has been determined by Taskin et al. that a minimum of 500 particles is required to obtain an accurate solution.

Thus, considering the advantages and simplicity of using the Lagrangian approach, it has been implemented in this thesis for BDI prediction of the proposed dual propeller pump.

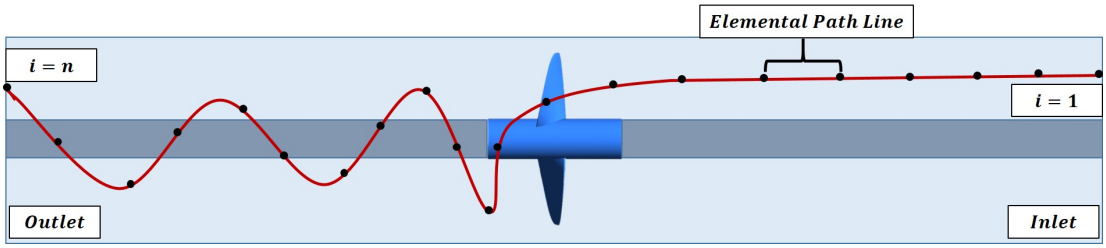

Figure 3.2: RBC Streakline discretized into elemental paths from $i = 1$ to $i = n$

3.3 Hemolysis Mathematical Modelling

A power-law mathematical model, relating the plasma free hemoglobin content with the shear stress magnitude and the exposure time was first developed by Blackshear et al., 1965 and Giersiepen et al, 1990 [77, 78]. The factor to determine the reduction in hemoglobin content is known as Hemolysis Index (HI) which is the measure of the increase in free plasma hemoglobin content after shear loading to the total hemoglobin content of the blood. The Hemolysis Index (HI) is coined with the power law expression given by Equation 3.2

$$Hemolysis\ Index\ (HI)(\%) = \left(\frac{\Delta PH_b}{H_b}\right) \times 100 \ = C\, t^a\, \tau^b \tag{3.2}$$

In the above equation, the constants C, $a\,and\,b$ are determined from experimental tests by regression analysis. The most widely used constant values classified according to the shear

stress magnitude and exposure time are shown in Table 3.1. The GW, HO, and TZ constants have been determined by in vitro experimental tests performed under various conditions with a Couette shearing device (viscometer) by *Giersiepen et al.*, *Heuser and Opitz et al.*, and *Zhang et al.* respectively. The GW constant was most widely used to predict HI, however, it overpredicted the values. In 2015, Taskin et. al performed a series of numerical evaluation to compare the three mentioned constants to determine the HI and she found that the HO constant outperformed the other two with lowest percentage error and the best correlation factor. Thus, backing up on this data, the HO model constants ($C = 1.8 \times 10^{-6}$, $a = 0.7650$ and $b = 1.9910$) were used for the HI prediction in this thesis.

Since Lagrangian approach requires the equation in discrete form, the power law model is discretized into elemental form as in Equation 3.3 and the cumulative blood damage is then given by Equation 3.4.

Table 3.1: Power Law Equation Constants developed by Giersiepen et al., Heuser and Opitz et al. and Zhang et al.

	Range				
	Shear Stress	Exposure Time			
Model	(Pa)	(msec)	C	a	b
GW	< 255	< 700	3.62×10^{-5}	0.785	2.416
HO	< 700	< 700	1.8×10^{-6}	0.765	1.991
TZ	$50 - 320$	< 1500	1.228×10^{-5}	0.6606	1.9918

$$\Delta(BDI)_i = C.\tau_i^b.\Delta t_i^a \tag{3.3}$$

$$BDI = \sum_{i=1}^{N=n-1} C.\tau_i^b.\Delta t_i^a \tag{3.4}$$

The above-developed power law model by Giersiepen, however, has a major drawback in that it doesn't account for the load history sustained by the blood cells as they move along their respective trajectories as pointed out by Grigioni et al [74]. For instance, if two particles moving along different paths, have sustained different mechanical loading in the previous time steps, but are acted upon by same stress or load in the current time step then, the elemental blood damage in the current time step should be different. However, Giersiepen's power law model fails to predict so and gives same elemental blood damage for both the particles in the above-mentioned case. In an attempt to consider the blood damage accumulation, Zimmer et al. in 2000 and Lim et al. in 2000, took derivative of Equation 3.2 to determine the elemental blood damage and took its sum to get the overall BDI value as shown in Equation 3.5. This approach provides an improvisation over the Giersiepen's

Model but would still lack in considering the blood damage history.

$$BDI = C \cdot a \sum_{i=1}^{N=n-1} t_i^{a-1} \tau_i^b \Delta t_i \tag{3.5}$$

A modified Power Law model considering the shear stress history, was then developed by Grigioni et al. in 2005 and is given by equations 3.6 and 3.7.

$$\Delta(BDI)_i = C\, a \left[\sum_{j=1}^{i} \tau(t_j)^{\frac{b}{a}} \, \Delta t_j + D(t_0) \right]^{a-1} \tau(t_i)^{\frac{b}{a}} \, \Delta t_i \tag{3.6}$$

$$BDI = \sum_{i=1}^{N=n-1} C\, a \left[\sum_{j=1}^{i} \tau(t_j)^{\frac{b}{a}} \, \Delta t_j + D(t_0) \right]^{a-1} \tau(t_i)^{\frac{b}{a}} \, \Delta t_i \tag{3.7}$$

In equations 3.6 and 3.7, the term $D(t_0)$ denotes the blood damage at the start of the analysis which is unknown and hence it is assumed as zero in most of the cases. The term inside the square brackets indicates the total blood damage dose sustained by the blood particle from the starting point $(t = 0)$ to the current i^{th} point, whereas the terms outside the square brackets indicates the elementary mechanical damage dose sustained during the i^{th} time interval $(t = t_{i-1}$ to $t = t_i)$. Another important characteristic of this modified power law model is that it doesn't obey the causality principle where the blood damage sustained would reduce in presence of decreasing shear stress along a particle path line. As a result, the blood damage along a trajectory would always increase and add to the initial value.

3.4 Scalar Shear Stress

In order to determine the Blood Damage Index for the injected particles in the computational domain, it is necessary to define shear stress expression during the post-processing step. In order to derive these equations, consider an infinitesimal fluid element moving in space. The continuity and momentum equations in differential form for this element are given by equation 3.8 and 3.9 as adopted from Apel et al. [79]. Here, since we are dealing with blood which is considered as an incompressible fluid, there is no change in density with time and space.

$$\boldsymbol{\nabla} \cdot V = 0 \tag{3.8}$$

$$\rho \left(V.\boldsymbol{\nabla} \right) V = -\boldsymbol{\nabla} p + \boldsymbol{\nabla} \cdot \bar{\bar{\tau}} + \rho.f \tag{3.9}$$

In the above given momentum equation, the stress tensor $\bar{\bar{\tau}}$ comprises of the normal as well as tangential shear stresses which form the part of the surface forces acting on a fluid element while the term f denotes the body force per unit mass. The six-component symmetric stress tensor $\bar{\bar{\tau}}$ is represented in matrix form as:

$$\bar{\bar{\tau}} = \begin{bmatrix} \tau_{xx} & \tau_{xy} & \tau_{xz} \\ \tau_{yx} & \tau_{yy} & \tau_{yz} \\ \tau_{zx} & \tau_{zy} & \tau_{zz} \end{bmatrix} \quad \text{here,} \tau_{ij} = \tau_{ji} \tag{3.10}$$

According to Newton's law of viscosity, the viscous stress acting on a fluid is directly proportional to the velocity gradient and is given by:

$$\begin{aligned} Normal\ Stress\,(\tau_{ii}) &= 2\mu \frac{\partial u_i}{\partial x_i} + \lambda(\boldsymbol{\nabla} \cdot V) \\ Shear\ Stress\,(\tau_{ij}) &= \mu \left(\frac{\partial u_i}{\partial x_j} + \frac{\partial u_j}{\partial x_i} \right) \end{aligned} \tag{3.11}$$

In the above set of viscous stress equations, the term μ denotes the dynamic viscosity while λ denotes the second coefficient of viscosity which is given by Stoke's hypothesis as: $\lambda = -\frac{2}{3}\mu$. This is an approximate relation, however, since the fluid is incompressible the divergence of velocity is zero and hence the term associated with λ vanishes.

Substituting the expression of normal and shear viscous stresses in stress matrix $(\bar{\bar{\tau}})$ we get:

$$\bar{\bar{\tau}} = \mu \begin{bmatrix} 2\dfrac{\partial u}{\partial x} & \dfrac{\partial u}{\partial y} + \dfrac{\partial v}{\partial x} & \dfrac{\partial u}{\partial z} + \dfrac{\partial w}{\partial x} \\ \dfrac{\partial v}{\partial x} + \dfrac{\partial u}{\partial y} & 2\dfrac{\partial v}{\partial y} & \dfrac{\partial v}{\partial z} + \dfrac{\partial w}{\partial y} \\ \dfrac{\partial w}{\partial x} + \dfrac{\partial u}{\partial z} & \dfrac{\partial w}{\partial y} + \dfrac{\partial v}{\partial z} & 2\dfrac{\partial w}{\partial z} \end{bmatrix} \tag{3.12}$$

In some cases, the Reynolds stresses induced by turbulent fluctuations in fluid velocity is added to the discussed shear stress tensor, however, it has been found that its addition results in overestimation of hemolysis index and hence it has been neglected in this work [80].

All the shear stress equations are combined into a single scalar expression for stress by an approach developed by Bludszuweit et al., where the work done for deforming an element in plain shear flow is equated with the work done for 3-D deformation of the same element [81]. This scalar shear stress equation is derived from Von Mises yield criterion and is expressed as:

$$Scalar\ Shear\ Stress\,(\tau_v) = \sqrt{\frac{1}{6}\left[\sum(\tau_{ii} - \tau_{jj})^2 + 6\sum \tau_{ij}^2\right]} \tag{3.13}$$

$$\text{where, } i = x, y, z \ , \ j = x, y, z \ and \ i \neq j$$

This is further expanded to

$$\tau_v = \frac{1}{\sqrt{3}} \sqrt{\tau_{xx}^2 + \tau_{yy}^2 + \tau_{zz}^2 - \tau_{xx}\tau_{yy} - \tau_{yy}\tau_{zz} - \tau_{zz}\tau_{xx} + 3(\tau_{xy}^2 + \tau_{yz}^2 + \tau_{zx}^2)} \tag{3.14}$$

In the scalar shear stress equation 3.14, the normal and viscous shear stresses indicated in shear stress matrix 3.12 are substituted to obtain a scalar value of shear stress for an infinitesimal fluid element in the computational domain. The critical value of scalar shear stress to trigger hemolysis is found to vary with application and the pump type (axial or centrifugal), however, a value above $150\ Pa$ is considered high enough to rupture RBCs [65].

3.5 Blood Damage Model Consistency Check

In this section, the three blood damage prediction models, developed by Giersiepen, Zimmer and Lim, and Grigioni, discussed in section 3.3 are checked for their consistency and accuracy by comparing the values of Blood Damage predicted by the models with the experimental data. The experimental Hemolysis data is obtained from the piston-cup time-varying mechanical blood damage experiment done by Yeleswarapu et al. in 1995 [82].

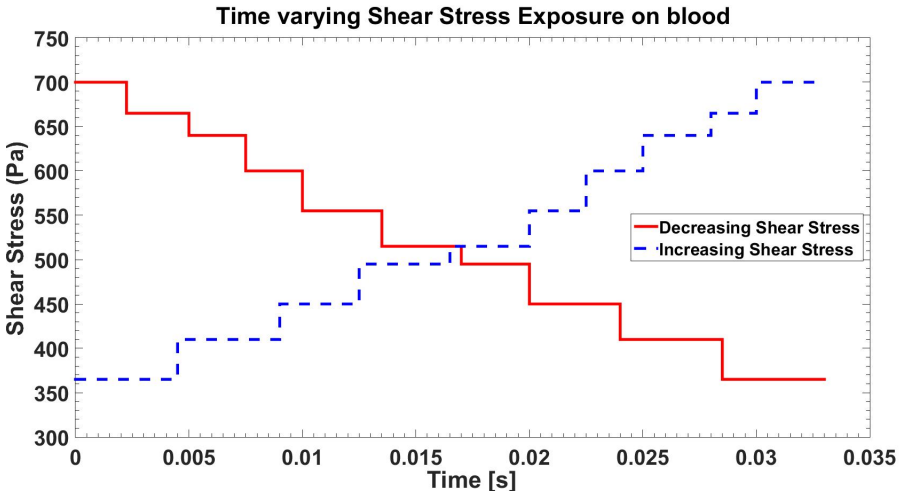

Figure 3.3: Increasing and Decreasing Time-Varying Shear Stress curves exported from Yeleswarapu et al. Hemolysis experiment

In this test, two time-varying shear stresses, decreasing and increasing with time, is separately applied to blood and is graphically depicted in Figure 3.3. Here, the area under increasing and decreasing shear stress over time is same, suggesting the same amount of total shearing work done on the blood during both stress exposures. The shear stress and exposure

time data from this experiment is exported and is used as an input for the three blood damage models represented in equations 3.4, 3.5 and 3.7. The blood damage calculation for all the models is performed in MATLAB (MathWorks, Inc., MA, USA) and the corresponding output is shown in Figure 3.4. For the convenience of comparison, the Giersiepen Constants (GW) shown in Table 3.1 are used in all the Blood Damage Models.

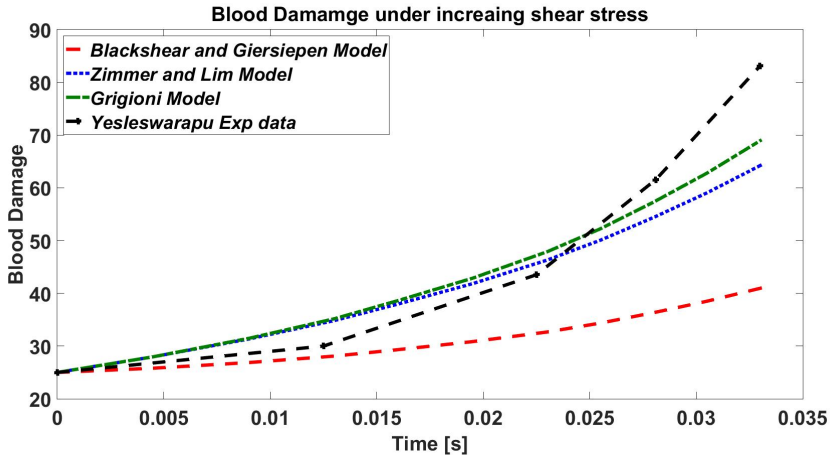

(a) Increasing Shear Stress Blood Damage Prediction

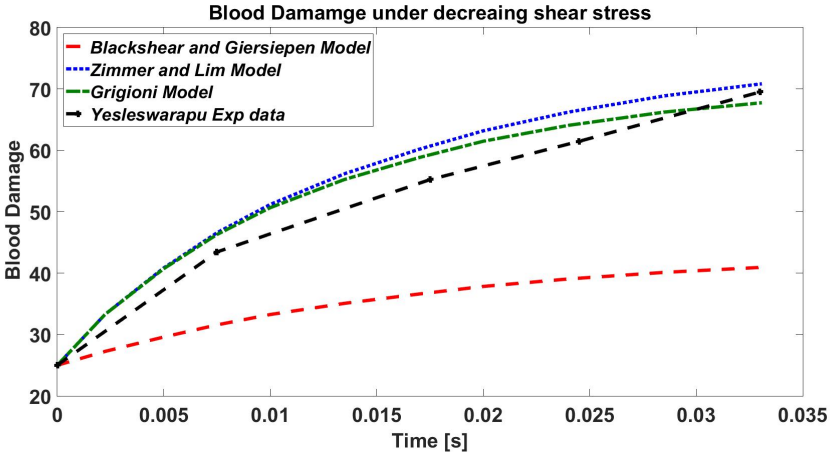

(b) Decreasing Shear Stress Blood Damage Prediction

Figure 3.4: Blood Damage prediction from the three mathematical models as compared to the experimental values

It could be seen from the figure that the Model developed by Giersiepen underpredicts the total blood damage at the end of the test by a huge margin for both increasing and decreasing shear stress study since it doesn't account for the blood damage accumulation. The same shearing work during the two stress cycles would mean that the blood should theoretically have same blood damage at the end of the process. Even though Zimmer and Lim's model gives a comparable performance to Grigioni's model is fails to give equal blood damage

Table 3.2: Root Mean Square Error of Blood Damage Index Prediction from Giersiepen, Zimmer and Lim, and Grigioni Model as compared to the experimental values obtained from Yeleswarapu Hemolysis test

	Giersiepen Model	**Zimmer and Lim Model**	**Grigioni Model**
Blood Damage Prediction Error	[% RMS Error] **Eq 3.4**	[% RMS Error] **Eq 3.5**	[% RMS Error] **Eq 3.7**
Increasing Shear Stress	31.356	13.805	12.137
Decreasing Shear Stress	31.3186	6.258	4.691

values for both the processes. Moreover, the total BDI values for the increasing and decreasing stress cycle are under and over predicted respectively. The Grigioni's Modified Power law model, which accounts for the shear stress history, shows the best performance and the least total blood damage error as compared to the two other models. For better clarification, the final blood damage values for each model and the corresponding error percentage with respect to the experimental blood damage value is shown in Table 3.2. Considering the superior performance of the Blood Damage Model developed by Grigioni et al., it is used for Hemolysis prediction of the proposed dual propeller pump in this thesis.

In this chapter, the concept of blood damage was introduced, followed by the methods of mathematical models used, their advantages and disadvantages. The latter part of the chapter introduced the power law mathematical model to predict blood damage and development of a modified power law model to overcome the drawback of the original power law model. The last part of the chapter discussed the derivation of scalar shear stress expression used to estimate the elemental and total Blood Damage Index for a computational domain.

Chapter 4

Numerical methods to solve governing equations of Fluid Dynamics

This chapter will give a brief introduction of the governing equations used to describe a fluid flow and the numerical methods used to obtain an approximate solution to the system of coupled equations. The latter part of the chapter discusses different turbulence models and their significance.

4.1 Governing equations of Fluid Dynamics

While modeling any fluid flow, the three physical fundamental equations used are the conservation of mass, momentum, and energy. These governing equations could be derived either in differential form or integral form depending on whether the flow domain is modeled as a finite control volume or an infinitesimally small volume. The equations could be further classified as conservative or non-conservative form depending on whether the fluid element under consideration is fixed or moving in space. In this section, for simplicity, only the partial differential form of the governing equations are presented for an infinitesimal small fluid element moving in space.

According to the law of conservation of mass, the continuity equation is given as:

$$\begin{gathered} \frac{D\rho}{Dt} + \rho \boldsymbol{\nabla} \cdot V = 0 \\ \text{where, } V = ui + vj + wk \end{gathered} \tag{4.1}$$

In equation 4.1, the term $\dfrac{D}{Dt}$ represents the substantial derivative or total derivative and is equal to the sum of local derivative $\left(\dfrac{\partial}{\partial t}\right)$ and convective derivative $(V.\boldsymbol{\nabla})$. The term $(\boldsymbol{\nabla} \cdot V)$

represents divergence of velocity vector, where the symbol ($\boldsymbol{\nabla}$) represents the divergence vector given by:

$$\boldsymbol{\nabla} = i\frac{\partial}{\partial x} + j\frac{\partial}{\partial y} + k\frac{\partial}{\partial z} \tag{4.2}$$

Since the fluid under consideration here is blood, which is incompressible, there is no variation in density of the fluid element in both spatial and temporal domain. As a result, Equation 4.1 is reduced to:

$$\begin{aligned} \boldsymbol{\nabla} \cdot V &= 0 \\ or \quad \frac{\partial u}{\partial x} + \frac{\partial v}{\partial y} + \frac{\partial w}{\partial z} &= 0 \end{aligned} \tag{4.3}$$

The second governing equation called the momentum equation is derived from the Newton's second law of motion, which is given as:

$$F = ma \tag{4.4}$$

In the above equation, the term F represents the summation of all the forces acting on a fluid element which can be classified as Body and Surface forces. The Body forces comprise of the gravitational, electric, and magnetic forces while the Surface forces include the elemental surface pressure distribution and the viscous stresses. The viscous stresses are further classified as either normal or shear stress depending on its direction of action with respect to the surface normal. The momentum equation in tensor form can be represented as:

$$\rho\frac{\partial U_i}{\partial t} + \rho V \cdot \boldsymbol{\nabla} U_i = -\frac{\partial P}{\partial x_i} + \boldsymbol{\nabla} \cdot \tau_{ij} + \rho f_i \tag{4.5}$$

Where, the term f_i represents the body force (gravitational force) per unit mass, P denotes the surface pressure on each elemental face, and τ_{ij} represents the viscous stress tensor which, according to Newton's law of viscosity, is linearly proportional to the velocity gradient or rate of shear strain. The general form of viscous stress tensor is given as:

$$\tau_{ij} = \mu\left[\frac{\partial U_i}{\partial x_j} + \frac{\partial U_j}{\partial x_i}\right] + \delta_{ij}\lambda\boldsymbol{\nabla} \cdot V \tag{4.6}$$

where, δ_{ij} represents the Kronecker delta function
$\because \quad \delta_{ij} = 1$ for $i = j$,
and $\quad \delta_{ij} = 0$ for $i \neq j$

In the above equation, the term μ is called the dynamic viscosity while the term λ represents the second coefficient of viscosity, which is related to the bulk viscosity (K) and dynamic viscosity (μ) as $K = \lambda + \frac{2}{3}\mu$

According to Stoke's hypothesis, for an incompressible fluid, the bulk viscosity is equal to zero, considering which we get $\lambda = -\frac{2}{3}\mu$. However, from the continuity equation 4.3, the second part of the right-hand side of the equation 4.6 vanishes since the divergence of velocity is equal to zero. Substituting this relation in equation 4.6, the viscous stress tensor could be represented as:

$$\tau_{ij} = \mu \left[\frac{\partial U_i}{\partial x_j} + \frac{\partial U_j}{\partial x_i} \right] \tag{4.7}$$

The final set of governing equations called the energy equation is derived from the first law of thermodynamics, which relates the internal energy inside a fluid element with the amount of heat transferred to the surrounding and the work done on the element. In this current case, there is no source of heat present in the fluid domain and hence there is no temperature variation with time and space. As a result, the energy equation isn't discussed and solved for.

The equations 4.3 and 4.5 represents the Navier-Stokes equation. However, these equations don't account for the fluctuations and disturbances in the flow variables ($P,\ u,\ v, and\ w$) and hence won't give an accurate solution. These disturbances are representative of the presence of flow turbulence and to describe them time-averaged equations called Reynolds-averaged Navier–Stokes equations are used and discussed in the next section.

4.2 Flow Turbulence

A turbulent flow, in general, is characterized by the perturbations in primary variables introduced due to disturbances such as surface roughness, discontinuities, flow separation, mechanical vibrations, large flow velocities or Reynolds numbers. For instance, consider a general variable (a) at any point in the flow domain whose value is fluctuating with respect to time as shown in Figure 4.1. The value of this variable (a) at any point in time will be equal to the time-averaged value ($\bar{a}$) plus the fluctuating value (a') at that point and time represented as:

$$a(t) = \bar{a}(t) + a'(t) \tag{4.8}$$

The time averaged value of this general variable is given as:

$$\bar{a}(t) = \frac{1}{T} \int_0^T a(\tau) d\tau \tag{4.9}$$

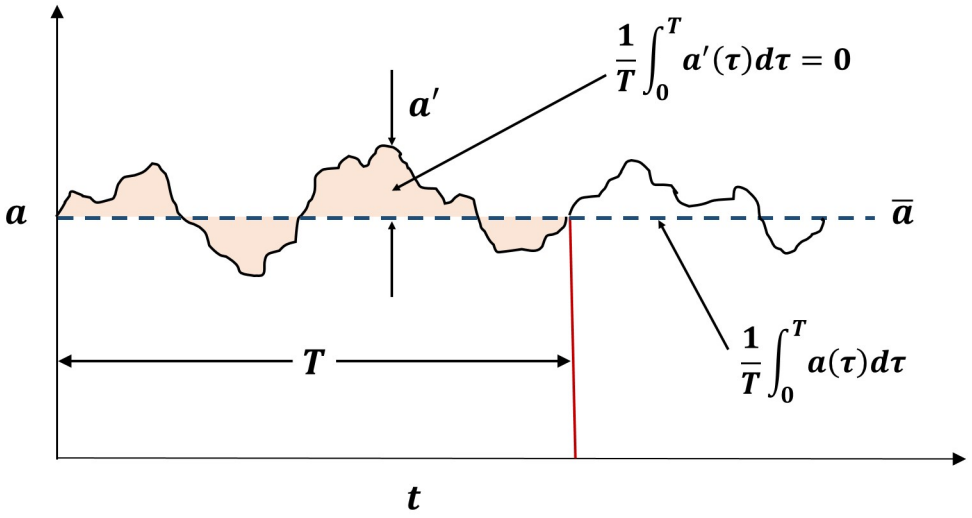

Figure 4.1: Fluctuations of general variable (a) about a mean value ($\overline{a}$)

Here, the time period (T) is long enough to reduce the integral of the fluctuating quantity (a') to zero, but not long enough to change the average value ($\bar{a}$). Thus averaging the fluctuating quantities over time will help to eliminate or dampen the fluctuations.

Applying time averaging principle to the differential form of conservation equations 4.3 and 4.5 we get:

$$\begin{aligned} \overline{\boldsymbol{\nabla} \cdot V} &= 0 \\ \text{which can be written as,} \quad \boldsymbol{\nabla} \cdot \overline{V} &= 0 \end{aligned} \tag{4.10}$$

Similarly, for the momentum conservation equation we get:

$$\rho\left(\overline{\frac{\partial V}{\partial t} + V \cdot \boldsymbol{\nabla} V}\right) = -\overline{\boldsymbol{\nabla} P} + \overline{\mu \boldsymbol{\nabla}^2 V} + \rho f_i$$

$$\text{which can be expanded as,} \tag{4.11}$$

$$\rho\left(\frac{\partial \overline{V}}{\partial t} + \overline{(\overline{V} + V') \cdot \boldsymbol{\nabla}\left(\overline{V} + V'\right)}\right) = -\boldsymbol{\nabla}\overline{P} + \mu \boldsymbol{\nabla}^2 \overline{V} + \rho f_i$$

Here, the square of the fluctuating quantity cannot be equal to zero, thus equation 4.11 can be simplified as:

$$\rho\left(\frac{\partial \overline{V}}{\partial t} + (\overline{V} \cdot \boldsymbol{\nabla}\overline{V}) + (\overline{\boldsymbol{\nabla} \cdot V'V'})\right) = -\boldsymbol{\nabla}\overline{P} + \mu \boldsymbol{\nabla}^2 \overline{V} + \rho f_i \tag{4.12}$$

The above equation can be again expressed in tensor form as:

$$\rho\left(\frac{\partial\overline{U_i}}{\partial t}+(\overline{V}\cdot\boldsymbol{\nabla}\overline{U_i})\right)=\rho f_i-\frac{\partial\overline{P}}{\partial x_i}+\boldsymbol{\nabla}\cdot\left[\mu\left(\frac{\partial\overline{U_i}}{\partial x_j}+\frac{\partial\overline{U_j}}{\partial x_i}\right)\right]-(\overline{\boldsymbol{\nabla}\cdot\rho U_i'U_j'}) \quad (4.13)$$

The equations 4.10 and 4.13 form the Reynolds-Average Navier-Stokes (RANS) equation which can be used to solve the flow involving turbulence. The additional term added to the right-hand side of the equation ($\overline{\boldsymbol{\nabla}\cdot\rho U_i'U_j'}$) is called the **Reynolds Shear Stress** (RSS) term. This Reynolds Shear Stress term is responsible for convective momentum transportation by means of eddies whereas the viscous shear stress introduced earlier is responsible for momentum transfer via conduction by means of molecular interaction. The RSS equation 4.14 can be related to the eddy viscosity or turbulent viscosity and mean velocity gradients by using the gradient diffusion hypothesis as postulated by Boussinesq in 1877 [83].

$$RSS=\overline{\boldsymbol{\nabla}\cdot\rho U_i'U_j'}=\mu_t\left(\frac{\partial\overline{U_i}}{\partial x_j}+\frac{\partial\overline{U_j}}{\partial x_i}\right) \quad (4.14)$$

The formulation method for the eddy viscosity in the above given Reynolds Shear Stress equation classifies the different types of turbulence models and will be discussed briefly in the next section.

4.3 Turbulence Models

In order to solve the Reynolds shear stress term in the RANS equation, the turbulent or eddy viscosity is modeled as the product of turbulent velocity and length scale which are solved using two separate Reynolds Transport equations [84]. The most commonly used two-equation turbulence models in the industry and for various other fundamental engineering problems are $k-\varepsilon$ and $k-\omega$ turbulence model.

4.3.1 K-epsilon Model

In case of $k-\varepsilon$ model, the first and the second transport variable are kinetic energy (k) and turbulence eddy dissipation (ε) which determines the energy and the scale of the turbulence respectively. For $k-\varepsilon$ model, the eddy viscosity is represented as:

$$\mu_t=C_\mu\rho\frac{k^2}{\varepsilon} \quad (4.15)$$

Where C_μ is a constant equal to 0.09 [84]. The Standard K-epsilon model developed by Launder and Sharma solves for the two transport variables and is most widely used [85]. This

model is mainly used for very high Reynolds number flows with small pressure gradients since this model fails to accurately predict the onset of separation in high-pressure gradient flows and consequently under-predicts the amount of separation. In order to overcome this deficiency, damping effects are introduced to the transport equations to form a low-Reynolds number $k - \varepsilon$ model [84].

4.3.2 K-omega Model

The $k - \omega$ model was developed to overcome the drawbacks of $k - \varepsilon$ for low-Reynolds number flows. In case of the $k - \omega$ model, the first and the second transport variables, i.e., the turbulent kinetic energy and the turbulent frequency are related to the eddy viscosity as shown in equation 4.16 and are solved using the method formulated by Wilcox [86].

$$\mu_t = \rho \frac{k}{\omega} \tag{4.16}$$

Even though the $k - \omega$ model provides accurate solution near the wall by precisely resolving the point of flow separation at adverse pressure gradients, it is highly sensitive to the free flow conditions existing far-field from the wall [87].

4.3.3 SST k-omega model

SST k-omega model is a blend of the above discussed two turbulence models and was developed by Menter et al. in 1993. The SST model combines the advantages of both the $k - \varepsilon$ model to accurately resolve the freestream flow away from the wall and that of the $k - \omega$ model to provide a highly accurate prediction of flow separation. As a result, the SST model provides high accuracy for low-Reynolds number flows requiring precise resolution of the boundary layer. In this way, the SST model switches from the $k - \omega$ model near the wall to the $k - \varepsilon$ model when solving for free shear flow far from the wall. Bardina et al. proved this superior behavior of SST model by performing a large number of validation studies [88]. Similarly, Fraser et al. had studied the use of SST model by various investigators and researchers for VAD analysis and justified its use given the dominant existence of laminar to transitional flow regimes in a maximum number of VADs [89]. Thus, the SST model is used for analyzing the blood flow through the dual propeller pump given its high accuracy to model low-Reynolds number flows, robustness and computational economy.

In addition to the above-mentioned Turbulence models, there have been various other models developed to meet the specific requirements of an application or to overcome the drawbacks of basic Turbulence models. The two-equation turbulent models discussed above fall under the RANS models, however, there are more sophisticated computational models like Large Eddy Simulation (LES), Detached Eddy Simulation (DES) and Direct Numerical Simulation (DNS) model which do not use any turbulence model. Instead, these models directly solve

for the spatial and temporal scales of the turbulence numerically with the Navier Stokes equations. Since there are no approximations of turbulence, these models, accurately resolve the eddies in the flow. However, these models have very fine grid requirements to accurately resolve large and detached eddies and hence computationally very expensive and are seldom used by the computational fluid dynamicists.

4.4 Turbulence Model Wall Functions

In case of laminar or low-Reynolds number flows, the flow near the wall or a boundary experiences large velocity gradients and to capture these effects accurately, a very fine mesh and hence long computational time is required to resolve the flow near the wall. To circumvent this need for very fine grid near the wall, a wall function method providing an empirical relation of the flow velocity near the wall as a function of distance from the wall was proposed by Launder and Spalding [85]. If the boundary layer developed near the wall is zoomed in, then it could be seen to be divided into three layers namely the viscous sublayer, the buffer layer and the log-law region as shown in Figure 4.2.

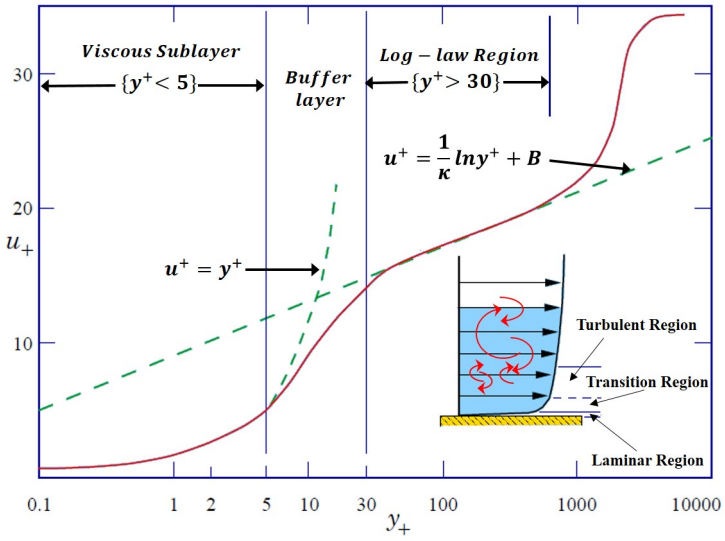

Figure 4.2: Wall functions defining the velocity profile near the wall for a turbulent flow

The wall function, given by equation 4.17, defines the approximate near wall velocity profile

and is dependent on the distance of the near wall mesh node and the wall shear stress.

$$\begin{aligned} u^+ &= \frac{1}{\kappa}\log\left(y^+\right) + C; \quad for\ y^+ > 30 \\ &\text{and for layers within the viscous sublayer:} \\ u^+ &= y^+; \quad for\ y+ < 5 \\ where, \quad u^+ &= \frac{u}{u_t} \\ \kappa = &\ von\ Karman\ constant\ = 0.41 \\ and \quad C = &\ log\ layer\ constant\ = 5\ for\ smooth\ wall. \end{aligned} \tag{4.17}$$

Where, $y+$ denotes the dimensionless wall distance given by:

$$y^+ = \frac{\Delta y\sqrt{\tau_w \rho}}{\mu} \tag{4.18}$$

In the above two equations, the term u_t is the friction velocity near the wall and u is the required tangential velocity to be computed near the wall at a distance Δy which represents the distance of first mesh node from the wall and is in turn dependent on the wall shear stress τ_w.

In the viscous sublayer, which is the region right next to the wall, the viscous effects dominate strongly over the turbulent convective effects and hence the fluctuations could be considered to be zero giving more laminar-like flow behavior. Thus this region, with $y^+ < 5$, is often called as Laminar sublayer where the dimensionless velocity and wall distance have 1:1 correlation as described in equation 4.17. The next region located between $5 < y^+ < 30$ is called the transition region or the buffer region where both the conductive viscous effects and the convective eddies co-exist with comparable magnitudes. It can be seen from Figure 4.2 that this region is not accurately modeled by the wall function. The final region, with $y+ > 30$ is called the turbulent core region where the momentum transport by convective means dominates over the conductive molecular momentum transfer. Here, the dimensionless variables, u^+ and y^+ have a logarithmic relation as shown in equation 4.17, and hence this region is also termed as the log-law region. The wall functions correlate fairly with the actual flow behavior as shown in Figure 4.2, where, the green dotted line represents the approximate wall functions while the red line represents the actual flow behavior. One of the major shortcomings of wall functions is that it doesn't resolve the flow in the buffer region accurately and the numerical results give unbounded errors under refined mesh with $y^+ <$ 15.

In order to solve this problem, most of the commercial CFD packages like ANSYS Fluent or CFX incorporates an automatic wall function approach for the low-Re number flows. While using the automatic wall function, the solver resolves the flow near the boundary numerically within the viscous sublayer which experiences the maximum velocity gradient and in the regions outside the buffer region with $y+ > 15$ the solver switches to the log-law

wall function to approximately resolve the flow and hence save some computational time. Thus, while implementing this method, it is necessary to at least have 10 mesh inflation layers near the wall to ensure a wall y^+ value at most equal to 10. In the current thesis, the commercial CFD software ANSYS CFX has been used which employs finite volume method to numerically solve the two-equation turbulence models and RANS equations.

In this chapter, a brief theory behind the Navier-stokes governing equations and the RANS equation to model turbulent flows was presented. The chapter also discussed various turbulence models used, their advantages and disadvantages and in the last part, the wall functions used to approximate the velocity profile in the boundary layer were introduced along with highlighting the mesh refinement requirements near the wall.

Chapter 5

Propeller Design Methodology

The 'Screw pump' developed by the Greek scientist Archimedes in 250 B.C. was the first pump ever developed to pump fluid from low lying bodies of water to higher lands mainly for irrigation purposes. The design was later adopted by Leonardo Da Vinci in 1500's for propulsion of helicopters depicted in his drawing [13]. Moreover, it wasn't until the later half of the nineteenth century that a major development in propeller design methods for efficient pumping and propulsion applications was witnessed. The Momentum Theory (1865) and the Blade Element Theory (1878) served as major breakthroughs for the scientific community to develop advanced propeller design methods. This brought scientists like Kutta-Joukowski, Lanchester, and Prandtl to develop classical lifting line theory in the early 20h century, which in turn led to advanced computational methods like Vortex Lattice Method, Vortex Panel Method, and the Navier Stokes Equations being developed in the 1950's, facilitating a more accurate analysis of propeller geometry. In this thesis, the Blade Element Momentum theory along with the Betz-Prandtl and Goldstein Radial loss function is used for the design of propeller geometry. This chapter gives a brief introduction of propeller blade designation and geometrical parameters followed by the explanation of momentum and blade element theory. The final part of the chapter describes the propeller design framework and shows verification of the proposed method with the Vortex Lattice method.

5.1 Propeller Blade Geometry Definition

Before introducing the propeller design theory, it is necessary to get familiar with the important propeller geometrical parameters that govern its performance. Consider a propeller located at the origin of a coordinate system shown in Figure 5.1, where the propeller is free to rotate about the shaft axis or the principal axis OX. The axis OZ is often referred to as spindle axis or propeller reference axis because the propeller blade is defined about this line [13]. Finally, OY acts as the horizontal axis about which the propeller pitch angles are most frequently defined. Here, the base of the propeller blade in contact with the shaft is

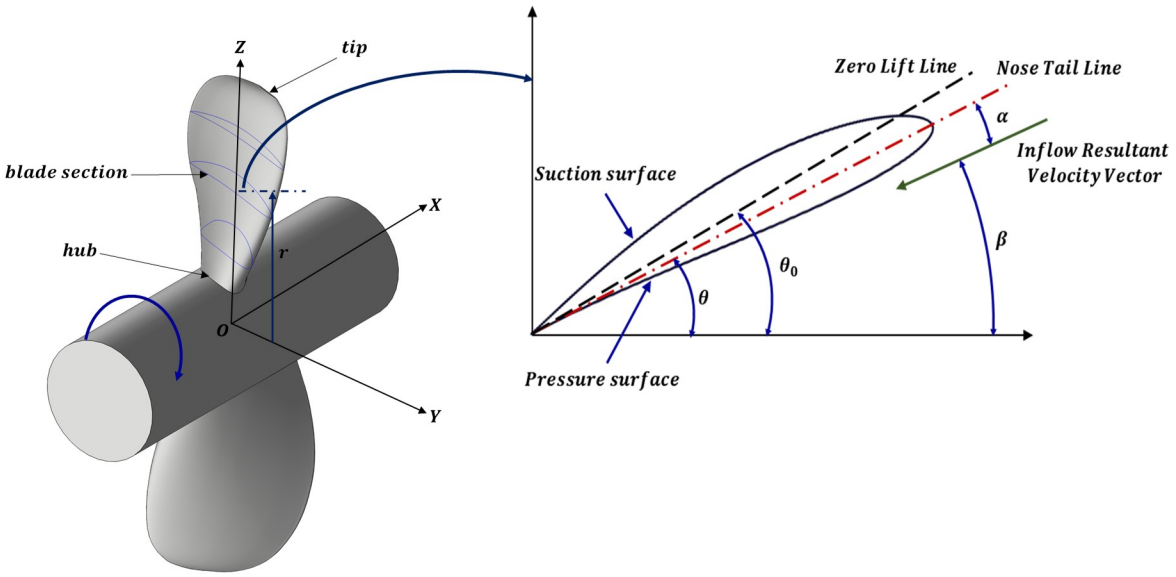

Figure 5.1: Propeller Pitch Angles

called the hub while its other end is called the tip and the corresponding radii are called the hub and the tip radius. One of the most important parameters defining the propeller blade angles is the pitch of the propeller. It is defined as the horizontal distance traversed by a point on the propeller blade at radius 'r' along OX direction during one complete revolution and is give by Equation 5.1

$$\begin{aligned} p &= 2\pi r \tan(\theta) \\ \therefore \quad \theta &= \tan^{-1}\left(\frac{p}{2\pi r}\right) \end{aligned} \tag{5.1}$$

Different types of pitch angles could be defined for a blade section at any arbitrary radius 'r' as shown in Figure 5.1. Here the angle denoted by 'θ' represents the nose-tail pitch or the propeller pitch, which is the angle made by the line joining the leading and the trailing edge of the propeller airfoil section with the horizontal. The effective or the no lift pitch angle denoted by 'θ_0' represents the angle made by the zero lift line with the horizontal. The zero lift line corresponds to the line along which incident flow and resultingly the lift generated on/by the blade section will be zero. The angle of attack (α) or the incidence angle is the angle made by the incident flow with the nose-tail line or the section chord while the same inflow makes an angle 'β' called the hydrodynamic pitch angle with the horizontal. The two angles, θ and θ_0, are associated with the propeller geometry with nose tail pitch most widely used to define a blade section while the remaining two angles are defined from the hydrodynamic point of view. The propeller pitch, the angle of attack and the hydrodynamic

pitch angle are related as shown in Equation 5.2.

$$\theta = \alpha + \beta \tag{5.2}$$

In addition to the above-mentioned parameters, there are few additional parameters called the rake and the skew which are used to define marine propeller, however, the propeller designs used in this thesis have zero rake and skew and hence these parameters aren't discussed further.

5.2 Blade Section Geometry Definition

The propeller performance is dependent on the geometry of the section, shaped as an airfoil, affecting the performance parameters like the lift, drag, thrust, and circulation to name a few. The National Advisory Committee for Aeronautics (NACA) has developed a comprehensive directory containing various airfoil series by performing extensive experimental testing to classify airfoils based on flow Reynolds number, camber and thickness. Figure 5.2 shows a general airfoil section depicting all its characteristic parameters. Here, the Camber line or the Mean line is developed by the locus of midpoints between the upper and the lower surface of the airfoil when measured perpendicular to the mean line. Many airfoil section properties are a primary function of the mean line [90]. The chord line or the nose-tail line is the line joining the leading and the trailing edge and the length of this line is called the chord of the airfoil section. Another important parameter, the airfoil camber, is the maximum perpendicular distance between the chord and the mean line. The airfoil thickness usually varies along the chord, being minimum at the extremities and maximum in the middle. However, at any point along the mean line, the thickness (t) is measured as the perpendicular distance between the upper and the lower surface when measured from the mean line. Moreover, the airfoil surface coordinates (x_u, y_u, x_l, y_l) measured about a point on the mean line can be determined from the mean line coordinates (x_c, y_c), mean line slope (ψ) and the section thickness (t) at that point as shown in equations 5.3a and 5.3b

Coordinates for the upper airfoil surface:

$$\begin{aligned} x_u &= x_c - \frac{t}{2}\sin(\psi) \\ y_u &= y_c + \frac{t}{2}\cos(\psi) \end{aligned} \tag{5.3a}$$

Coordinates for the lower airfoil surface:

$$\begin{aligned} x_l &= x_c + \frac{t}{2}\sin(\psi) \\ y_l &= y_c - \frac{t}{2}\cos(\psi) \end{aligned} \tag{5.3b}$$

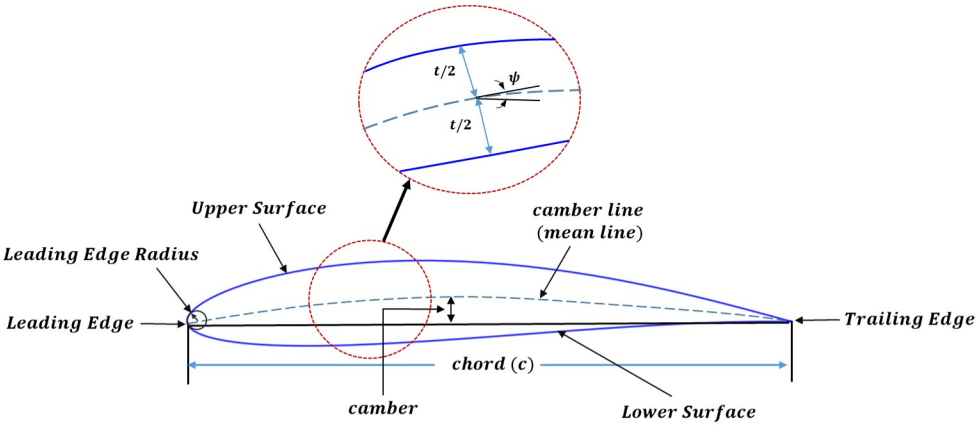

Figure 5.2: Parameters defining an aifoil blade section

All the airfoil families developed and presented by NACA uses meanline centering method in which the mean line is calculated first and then the thickness is distributed around the derived mean line. Thin airfoil theory developed by Munk and modified by Glauert and Theodorsen is widely adopted to determine the mean line coordinates and its slope [90]. This theory assumes the load distribution around an airfoil section as a function of velocity difference between the upper and lower surfaces. Besides, each airfoil series has a naming convention which is related to the airfoil camber, thickness and the lift coefficients. For NACA 6 series airfoils which are widely used for marine applications, the mean lines are computed by assuming a uniform load distribution from $x/c = 0$ to $x/c = a$ and thereafter a linearly decreasing load to zero at $x/c = 1$ [90]. The ordinates of these mean lines are defined by the following expressions:

$$\frac{y}{c} = \frac{c_{l_i}}{2\pi(a+1)}\left\{\frac{1}{1-a}\left[\frac{1}{2}\left(a-\frac{x}{c}\right)^2 \ln\left|a-\frac{x}{c}\right| - \frac{1}{2}\left(1-\frac{x}{c}\right)^2 \ln\left(1-\frac{x}{c}\right) + \frac{1}{4}\left(1-\frac{x}{c}\right)^2 - \frac{1}{4}\left(a-\frac{x}{c}\right)^2\right] - \frac{x}{c}\ln\left(\frac{x}{c}\right) + g - h\frac{x}{c}\right\} \quad (5.4)$$

where,

$$g = \frac{-1}{1-a}\left[a^2\left(\frac{1}{2}\ln a - \frac{1}{4}\right) + \frac{1}{4}\right],$$

$$h = \frac{1}{1-a}\left[\frac{1}{2}(1-a)^2\ln(1-a) - \frac{1}{4}(1-a)^2\right] + g$$

The ideal angle of attack for thee mean lines is give by:

$$\alpha_i = \frac{c_{l_i} h}{2\pi(a+1)} \tag{5.5}$$

In the two equations given above, the angle of attack as well as the mean line coordinates are directly proportional to the ideal lift coefficient (c_{l_i}) which is taken as unity [90]. The NACA airfoil series from 2 to 5 failed to achieve the desired airfoil performance which led to development of NACA 6 series derived by using improved theoretical methods. The aim was to design an airfoil which would allow laminar flow over wide range of flow types, as indicated by their Reynold's number, thereby helping to increase the airfoil lift and substantially reducing the drag coefficient [90]. Further more, Kerwin et al. observed via experiments that NACA 6 series gave more accurate lift predictions as compared to the NACA 4 and 5 series and subsequently NACA 65 series was proposed for the design of Marine propellers [91]. Having learned about the propeller and blade section geometry and terminologies associated with it, we will review the propeller design theory adopted to achieve the required hydrodynamic performance, in the next section.

5.3 Rankine-Froude Momentum Theory

The momentum theory developed by Rankine (1865) and R.E. Froude (1887) was one of the first attempts to evaluate propeller action on fluid flow. This theory does not consider the effect of propeller geometry and in fact, assumes an actuator disk in place of a propeller having the same diameter as the propeller tip. The theory also assumes that the working fluid is an ideal fluid and that the propeller does not experience any frictional drag. The original theory by Rankine had the third assumption of the propeller imparting no rotation to the fluid in the slipstream, which was later removed by R.E. Froude in his subsequent work to get a realistic representation of propeller action [13]. As shown in Figure 5.3, the theory assumes an infinitesimally thin actuator disk located in the propeller plane imparting a sudden pressure rise across it. The actuator disk divides the system or the stream tube into 2 domains: pre and post actuator and we would define the fluid parameters like pressure and velocity at the three points stationed at the inlet , the actuator disk and the outlet. The theory also assumes that the velocity and pressure is uniform at all the cross sections of the stream tube and at the disk.

Let V be the velocity of the fluid flowing from the inlet which increases by a factor of $(1+a)$ as it approaches the disk, where a is the axial interference factor. The fluid velocity in the post actuator domain is further increased to a value of $V(1+b)$ at the exit due to the momentum imparted by the actuator, where b refers to the axial slipstream factor. Therefore, the thrust produced by the blade by applying the law of conservation of momentum between

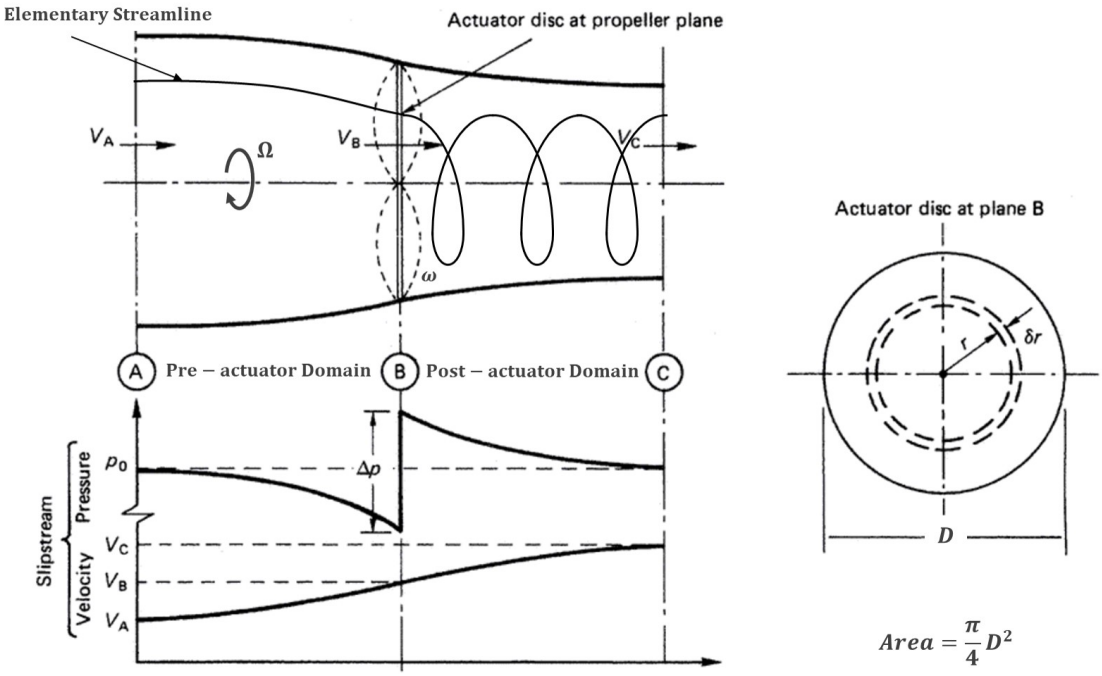

Figure 5.3: Momentum Theory considering both axial and angular velocity for an elementary streamline before and after the actuator disk. [adopted from [13]]

inlet and exit is given by:

$$T = \dot{m}(V(1+b) - V) = \dot{m}Vb \tag{5.6}$$

where, $\dot{m}$ represents the mass flow rate through the disk of diameter 'D' given by:

$$\dot{m} = \frac{\pi}{4}\rho D^2 V(1+a) \tag{5.7}$$

The relation between the pressure and the velocities at the inlet and outlet can be obtained by applying Bernoulli's theorem to the pre- and post-actuator domain as shown below:

$$p + \frac{1}{2}\rho V^2 = p_d + \frac{1}{2}\rho(V(1+a))^2 \tag{5.8a}$$

$$p_d + \Delta p + \frac{1}{2}\rho(V(1+a))^2 = p + \frac{1}{2}\rho(V(1+b))^2 \tag{5.8b}$$

Subtracting equation 5.8a and 5.8b we get the pressure rise across the actuator disk as:

$$\Delta p = \frac{1}{2}\rho V^2 b(2+b) \tag{5.9}$$

Moreover, the amount of thrust imparted is related to the pressure rise given by:

$$T = \Delta p A_{disk} = \frac{\pi}{4} D^2 \Delta p \tag{5.10}$$

Relating equations 5.6 and 5.10, we can prove that 'b' is 2 times that of 'a' as follows:

$$\frac{\pi}{4}\rho D^2 V^2 b(1+a) = \frac{\pi}{4} D^2 \left[\frac{1}{2}\rho V^2 b(2+b)\right] \tag{5.11}$$

$$\therefore \quad b = 2a$$

The energy or the power input required by the disk to impart the derived thrust is given as:

$$Power_{in} = TV(1+a) \tag{5.12}$$

The total power output is also derived from the thrust imparted by the disk but is related to the inlet velocity as: $P_{out} = TV$. Thus we can define the actuator disk efficiency as:

$$\eta_{ideal} = \frac{1}{1+a} \tag{5.13}$$

The above equation gives the expression for ideal efficiency and thus an upper limit on the performance achieved by a propeller.However, this expression, which is a result of Rankine's theory, does not consider the torque and the corresponding rotational velocity imparted by the disk in the slipstream which would affect the propeller's performance. As proposed by R.E. Froude, an angular momentum conservation theory is applied within the same streamtube [13]. His theory assumes that the flow upstream of the disk remains purely axial and uniform while the flow past actuator possesses some angular velocity. Let 'Ω' represent the rotational velocity of the disk, and as proposed by Galuert, let the angular velocity imparted to the fluid be given by 'ω' [92]. This angular velocity is lower in magnitude as compared to the disk rotational velocity and is related to it as:

$$\omega = 2a'\Omega \tag{5.14}$$

where a' angular interference factor. Applying conservation of angular momentum, the elemental torque developed by a differential annular element is given by:

$$dQ = \dot{m}\omega r^2 \tag{5.15}$$

For the annular ring, the mass flow rate ($\dot{m}$) is given as: $2\pi r\rho V(1+a)dr$. Substituting this in the above equation and replacing ω with $2a'\Omega$, we get:

$$dQ = 4\pi\rho V(1+a)a'\Omega r^3 dr \tag{5.16}$$

Furthermore, following Glauert's method, the relative angular velocity immediately behind and front of the disk will be Ω and $\Omega - \omega$. Thus, the pressure rise across an annular element of the disk at radius 'r' by the virtue of angular momentum imparted to the liquid can be derived by applying Bernoulli's theorem and is given by:

$$\Delta p = \frac{1}{2}\rho\Omega^2 r^2 - \frac{1}{2}\rho(\Omega - \omega)^2 r^2 \tag{5.17a}$$

The above equation is reduced to

$$\Delta p = 2\rho\omega\left(\Omega - \frac{\omega}{2}\right) r^2 \tag{5.17b}$$

Again, substituting $\omega = 2a'\Omega$ we get

$$\Delta p = 2\rho a'\Omega^2(1 - a')r^2 \tag{5.17c}$$

Applying thrust and pressure rise relation across the elementary annular area of the disk we get:

$$\begin{aligned} dT &= \Delta p(2\pi r dr) \\ &= 4\pi\rho a'\Omega^2(1 - a')r^3 dr \end{aligned} \tag{5.18}$$

Knowing the expressions for the elemental torque (dT) and thrust (dQ) we could express the disk efficiency as:

$$\eta = \frac{dTV}{dQ\Omega} \tag{5.19}$$

Substituting the values of dT and dQ from equations 5.18 and 5.16 into 5.19 we get:

$$\eta = \frac{4\pi\rho V a'\Omega^2(1 - a')r^3 dr}{4\pi\rho V(1 + a)a'\Omega^2 r^3 dr}$$

which can be reduced to

$$\eta = \frac{1 - a'}{1 + a} \tag{5.20}$$

The above equation gives the expression of actual efficiency determined by considering the angular momentum transferred to the fluid. It can be seen that if the rotational effect in the slipstream is absent (i.e. $a' = 0$), the expression for efficiency becomes equal to the ideal efficiency developed by Rankine (Equation 5.13).

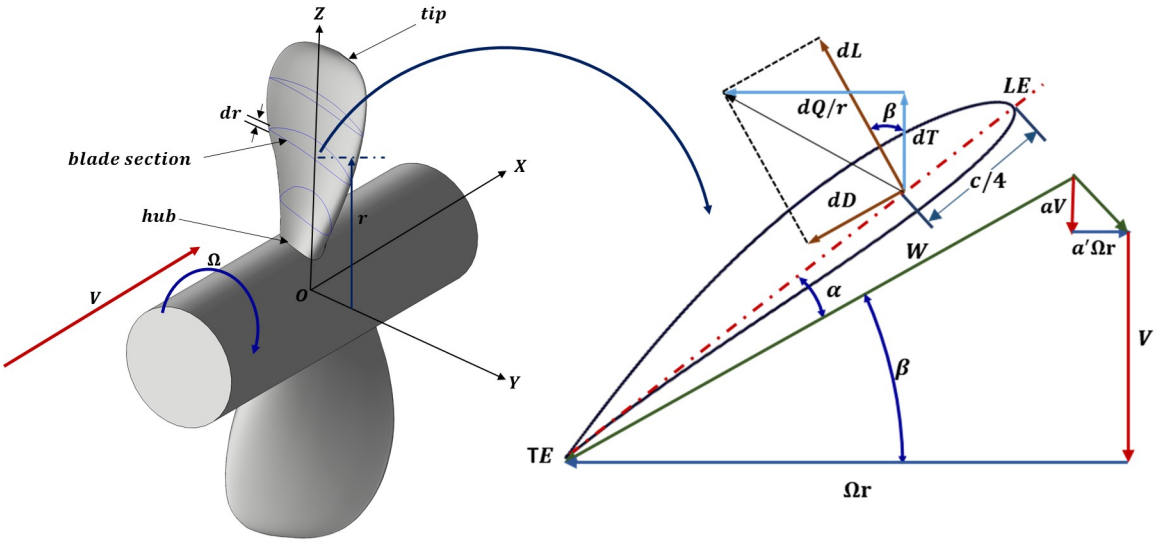

Figure 5.4: Blade Element theory applied to an arbitrary blade section

5.4 Blade Element Theory

The momentum theory by Ranking and R.E. Froude discussed in the previous section provides information regarding the variation in streamtube velocity, the thrust and the theoretical limit of power that could be generated by a pump, however, it doesn't provide the crucial information regarding the effect of pump geometrical parameters on its performance. To consider this effect, William Froude in 1878 developed Blade Element Theory which involved dividing a blade into a large number of elementary strips, as shown in Figure 5.4 and determining the Thrust and Torque acting on each elementary airfoil. The corresponding elementary forces are integrated along the spanwise direction from hub to tip to obtain the expression for the net thrust developed by the blade. The theory involves balancing of the forces acting on an airfoil section whose direction of action can be determined from the velocity diagram at each section. In his original theory, W. Froude did not consider the axial and angular interference factors introduced by the virtue of induced flow acceleration and rotation by the propeller [13]. The solution to this was published in Glauert's work in 1926 where he related the Rankine-Froude's Momentum Theory with Froude's Blade Element Theory which eventually came to be known as Blade Element Momentum Theory [92].

As shown in Figure 5.4, consider an elementary blade strip of infinitesimal thickness 'dr' taken at an arbitrary radius 'r' between the hub and the tip of the blade. Consider the blade to be rotating in clocking wise direction, with angular speed 'Ω'. Let the tangential velocity acting on this section be 'Ωr'. Let 'V' be the free stream velocity which denotes the flow velocity in the axial direction at the inlet. Both the tangential and the axial components of the velocity are corrected to include the induced axial (a) and tangential (a') interference factors

introduced to the flow approaching the blade. The resultant velocity ('W') incident on the blade section can be obtained by closing the velocity diagram. As discussed in section 5.2, the hydrodynamic pitch angle, the propeller pitch and the angle of incidence are denoted by 'β', 'θ', and 'α' as shown in Figure 5.1. The elementary lift (dL) and drag force (dD) will be acting at the aerodynamic center ($1/4^{th}$ of chord length (c) from the leading edge) of the blade perpendicular to and along the direction of the incident velocity respectively.

If 'c_l' and 'c_d' are the lift and drag coefficients of the blade section, then the corresponding elementary lift and drag forces are given by:

$$dL = \frac{1}{2} B \rho c_l W^2 c dr \tag{5.21a}$$

$$dD = \frac{1}{2} B \rho c_d W^2 c dr \tag{5.21b}$$

Where B represents the number of propeller blades. Consequently, the elementary thrust (dT) and torque (dQ) acting on the blade in the axial and tangential direction can be calculated from the elementary lift and drag as given by:

$$dT = \frac{1}{2} B \rho c W^2 (c_l \cos(\beta) - c_d \sin(\beta)) dr \tag{5.22a}$$

$$dQ \frac{1}{r} = \frac{1}{2} B \rho c W^2 (c_l \sin(\beta) + c_d \cos(\beta)) dr \tag{5.22b}$$

Here, the hydrodynamic pitch angle (β) can be directly calculated from the velocity triangle as:

$$\tan(\beta) = \frac{V(1+a)}{\Omega r(1-a')} \tag{5.23}$$

Reapplying the efficiency equation 5.19 from the momentum theory, we get:

$$\eta = \frac{V dT}{\Omega dQ} \tag{5.24}$$

Further, substitution of dT and dQ computed in equations 5.22a and 5.22b in the above efficiency expression, results in:

$$\eta = \frac{V(c_l \cos(\beta) - c_d \sin(\beta))}{\Omega r(c_l \sin(\beta) + c_d \cos(\beta))} \tag{5.25}$$

On combining equations 5.23 and 5.25, and with further simplification we get the final efficiency expression as given below:

$$\eta = \frac{(1 - a')\tan(\beta)}{(1 + a)\tan(\beta + \tan^{-1}(\varepsilon))} \tag{5.26}$$

In the above equation, the term 'ε' represents the sectional drag to lift ratio $\left(\frac{c_d}{c_l}\right)$. Thus, by comparing the efficiency expressions obtained from Rankine and W. Froude's theory, it is seen that the latter one considers the effect of blade sectional properties. The equation 5.26 further complies with the equation 5.20 when the flow losses are neglected i.e. if $\varepsilon = 0$.

This methodology is adopted in the current thesis to design propeller blades. The next section will focus on discussing the blade optimization theory incorporated in this thesis to get the desired propeller performance based on the requirements.

5.5 Betz-Prandtl Radial Loss Model

Lanchester and Prandtl were the first ones to figure out that the lift force at each blade section was related to the bound circulation around that section and that helical vortices are shed aft of the blade along the downstream direction from all the infinitesimal radial sections from hub to tip [93]. These induced vortices increase the kinetic energy of the flow in the slipstream and are the main cause of induced flow losses apart from the flow losses introduced by profile drag (c_d). Betz in 1919, [94] put forth a condition stating: 'to minimize the induced drag, the vortex sheets have to be a regular screw surface having constant pitch radially' which is expressed as:

$$2\pi r \tan(\beta_s) = constant \tag{5.27}$$

Since the vortex sheet is moving in the direction of the flow the helix angle of the sheet is assumed to be same as the hydrodynamic pitch angle.

$$i.e. \quad \beta_s \approx \beta \tag{5.28}$$

This theory was originally developed by Betz for light to moderately loaded propellers with infinite number of blades thereby forming a disk, which was corrected by Prandtl by replacing the vortex sheet with parallel helical filaments shed from radial sections of a propeller with finite number of blades. This assumption reduces the values of induced velocities as

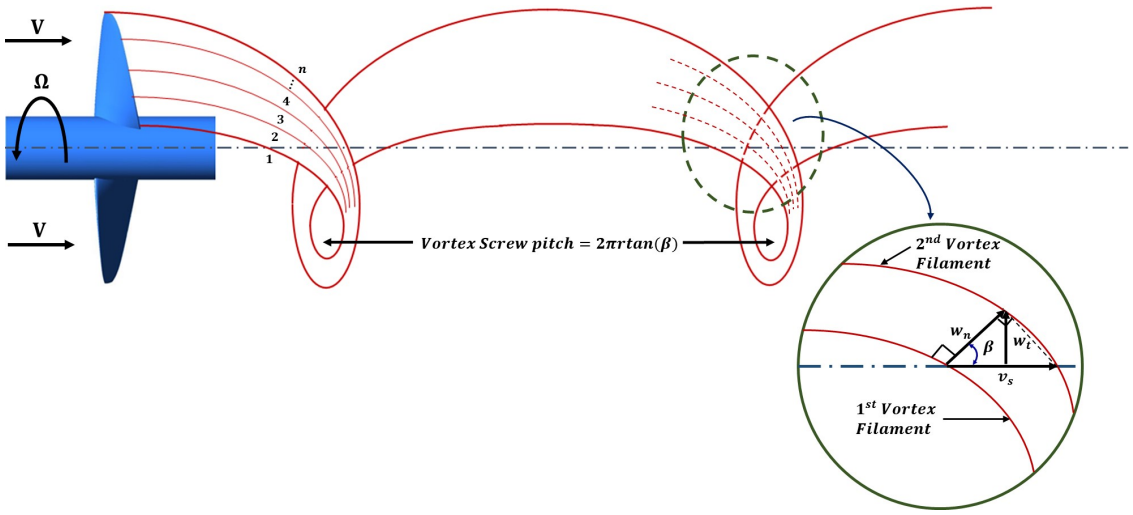

Figure 5.5: Vortex filaments shed from radial sections of one of the blades of the propeller from hub to tip along the downstream

compared to those computed for a disk, and to account for the same, Prandtl introduced a loss factor(F) which in simplified form is given by:

$$F = \frac{2}{\pi}\cos^{-1}(\exp(-f)) \qquad \text{where,} \qquad f = \frac{B}{2}\left(\frac{1-\xi}{\lambda}\right)\sqrt{1+\lambda^2} \tag{5.29}$$

In the above equation, the dimensionless parameters ξ and λ are represented as:

$$\xi = \text{Dimensionless Radius} = \frac{r}{R} \tag{5.30a}$$

and

$$\lambda = \text{Advance Ratio} = \frac{V}{\Omega r} \tag{5.30b}$$

Betz also neglected the contraction of the vortex sheet which was corrected by Theodorsen by showing, that for a contracted wake, the vortex sheet emanating from a propeller blade must eventually become a regular screw surface at large distances downstream of the propeller to fulfil the condition for minimum induced drag losses [95].

To understand this clearly, consider n vortex filaments leaving the propeller blade at different sections from hub to the tip in the downstream direction. Let these filaments be numbered as

1 to n from hub to tip. Let w_t be the tangential component of velocity of the 1^{st} vortex filament, giving us the circulation corresponding to this vortex filament shed at its corresponding radius r as:

$$B\Gamma = 2\pi r F w_t \tag{5.31}$$

Moreover, the blade section itself will have a bound vortex responsible for providing lift as explained by Prandtl and derived by Kutta-Joukowski [92]. This lift per unit radius is given by:

$$\frac{\mathrm{d}L}{\mathrm{d}r} = B\rho W\Gamma \tag{5.32}$$

Equating above two equations we get:

$$\frac{\mathrm{d}L}{\mathrm{d}r} = 2\pi\rho r W F w_t \tag{5.33}$$

As shown in Figure 5.5, the tangential component is related to the normal component as:

$$w_t = w_n \sin(\beta) \tag{5.34}$$

Let v_s be the velocity with which the vortex filament is moving forward in the axial direction which is related to the normal velocity as:

$$v_s = w_n / \cos(\beta) \tag{5.35}$$

For convenience, the displacement velocity (v_s) can be related to the axial inflow velocity (V) by defining a dimensionless parameter, displacement ratio as:

$$\zeta = \frac{v_s}{V} \tag{5.36}$$

Combining equations 5.34, 5.35 and 5.36 with 5.33 we get:

$$\frac{\mathrm{d}L}{\mathrm{d}r} = 2\pi\rho r W F \zeta V \sin(\beta)\cos(\beta) \tag{5.37}$$

By introducing Goldstein factor ($G = Fx\sin(\beta)\cos(\beta)$) and speed ratio ($x = \Omega r/V$) into equations 5.32 and 5.37, the expression for gradient of lift and blade section circulation can be expressed as:

$$\frac{\mathrm{d}L}{\mathrm{d}r} = 2\pi\rho W\zeta V^2\frac{G}{\Omega} \tag{5.38}$$

$$\Gamma = 2\pi\zeta V^2 \frac{G}{B\Omega} \tag{5.39}$$

This gives the final equation for circulation relating the blade properties with the shed vortex filament. The next step is to determine the induced velocity factors ($a,\ a'$) in relation to blade properties. In order to do that, recall the elementary thrust and torque equations 5.6 and 5.16 derived in the momentum theory. Introducing the Prandtl loss factor to the induced velocities, the elementary thrust and torque can be rewritten as:

$$\frac{dT}{dr} = 4\pi\rho r V^2 (1+a) F a \tag{5.40a}$$

$$\frac{1}{r}\frac{dQ}{dr} = 4\pi\rho V (1+a) F a' \Omega r^2 \tag{5.40b}$$

Finally, equating the above two equations with the elementary thrust and torque equations 5.22a, 5.22b derived for an elementary blade section in Blade Element Theory and using the expression 5.23 for hydrodynamic pitch angle, we get:

$$a = \frac{\zeta}{2}\cos^2(\beta)(1 - \varepsilon\tan(\beta)) \tag{5.41a}$$

$$a' = \frac{\zeta}{2}\cos(\beta)\sin(\beta)\left(1 + \frac{\varepsilon}{\tan(\beta)}\right) \tag{5.41b}$$

The expression for the hydrodynamic pitch angle 5.23 can be rewritten by including the expressions for induced velocities derived above, as:

$$\tan(\beta) = \frac{\lambda}{\xi}\left(1 + \frac{\zeta}{2}\right) \tag{5.42}$$

Now, according to Betz's condition for minimum loss the vortex screw pitch given by $r\tan(\beta)$ should be constant, which when introduced into the above expression, we get:

$$r\tan(\beta) = \frac{V}{\Omega}\left(1 + \frac{\zeta}{2}\right) = constant \tag{5.43}$$

It is known that the inflow velocity (V) and the propeller rotational speed (Ω) are constant, thus, the displacement velocity ratio and hence the displacement velocity, has to be constant (i.e. $\zeta = v_s =$ constant) and independent of radius. This is the condition for minimum energy loss introduced by Adkins and Liebeck (1994) in their paper 'Design of Optimum Propellers' which has been adopted in this thesis [96].

Before proceeding with the constraints for the blade optimization procedure, it is necessary to mention another radial loss factor (K) developed by Goldstein in 1929 to provide a more accurate prediction of momentum losses in the slipstream [97]. The original Goldstein's data was in tabular format which was later fitted by Batten et. al. [98] and is given as :

$$K = \frac{2}{\pi} \arccos\left(\frac{\cosh(\xi f)}{\cosh(f)}\right) \tag{5.44}$$

where f is given by:

$$f = \frac{B}{2\xi \tan(\beta)} - \frac{1}{2} \tag{5.45}$$

Adkins showed that using Goldstein's factor, the prediction for momentum loss was more accurate as compared to Prandtl's loss coefficient, especially for less number of blades. Since in the current thesis, the propeller is considered to have only 2 blades, Goldstein's loss function is implemented for blade design given its more precise assumption for lower blade numbers [96].

Like any optimization code, Adkins specified constraints to the values of displacement velocity ratio by correlating it with the required thrust or power from the propeller. In order to do so the thrust and power equations are converted into non-dimensional form as:

$$C_T = \frac{2T}{\rho V^2 \pi R^2} \tag{5.46a}$$

$$C_P = \frac{2Q\Omega}{\rho V^3 \pi R^2} \tag{5.46b}$$

In the above equations, R represents the tip radius of the propeller. In order to use the elementary thrust and torque equations 5.40a and 5.40b derived earlier, we take the derivative of the thrust and power coefficients with respect to non-dimensional radius ξ to get:

$$\frac{dC_T}{d\xi} = I_1'\zeta - I_2'\zeta^2 \tag{5.47a}$$

$$\frac{dC_P}{d\xi} = J_1'\zeta + J_2'\zeta^2 \tag{5.47b}$$

The expression for all the coefficients with primes is given by:

$$I_1' = 4\xi G(1 - \varepsilon \tan(\beta)) \tag{5.48a}$$

$$I_2' = \lambda \left(\frac{I_1'}{2\xi}\right) \left(1 + \frac{\varepsilon}{\tan(\beta)}\right) \sin(\beta)\cos(\beta) \tag{5.48b}$$

$$J_1' = 4\xi G \left(1 - \frac{\varepsilon}{\tan(\beta)}\right) \tag{5.48c}$$

$$J_2' = \left(\frac{J_1'}{2}\right) (1 + \varepsilon \tan(\beta)) \cos^2(\beta) \tag{5.48d}$$

The equations for elementary coefficient of thrust and power are integrated from hub to tip ($\xi = 0 \rightarrow \ \xi = 1$) to get the overall thrust and power developed by the propeller. Here since the value of ζ was found to be constant to obey Betz optimum design condition, we can determine its value from either the specified thrust or power. Let's say the required thrust to be produced by the propeller is specified, then the constraint equation for ζ is given by:

$$\zeta = \frac{I_1}{2I_2} - \sqrt{\left(\frac{I_1}{2I_2}\right)^2 - \frac{C_T}{I_2}} \tag{5.49}$$

With the known value of ζ, the power coefficient and hence the power can be calculated as:

$$C_P = J_1\zeta + J_2\zeta^2 \tag{5.50}$$

In the similar sense, if power is specified then the thrust can be determined using the equations given below:

$$\zeta = -\frac{J_1}{2J_2} + \sqrt{\left(\frac{J_1}{2J_2}\right)^2 + \frac{C_P}{J_2}} \tag{5.51}$$

$$C_T = I_1\zeta - I_2\zeta^2 \tag{5.52}$$

Having introduced the theory, conditions and constraints for designing optimum propeller blades, the following section discusses the design procedure and framework for the same.

5.6 Design Procedure for Optimum Propellers

The Prandtl-Betz-Goldstein propeller design theory discussed in the previous section based on the Blade Element Momentum theory form the basis for the design procedure. A MATLAB script implementing the procedure discussed by Adkins and Liebeck is generated to design the propellers for the heart assist device [96].

The design procedure is started by specifying the propeller geometrical parameters like hub diameter, tip diameter, number of blades, rotational speed, the performance requirements like thrust or pressure rise or power, the lift and the drag coefficient for each section if not constant throughout the span and the fluid properties like density, viscosity, inlet mass flow rate or inlet velocity. It is preferred that the user specifies the number of radial and sectional points to discretize the blade and blade section mean line. If no input is received, a default value of 10 and 100 is considered, signifying the blade will be divided into 10 parts along the spanwise direction from hub to tip and at each section, and the airfoil will be divided into 100 points along the camber line. This procedure developed by Adkins and Liebeck iterates through the values of displacement velocity ratio ζ until the required torque or power coefficient is obtained [96]. The steps followed in each iteration are listed below:

1. The first step is to select an arbitrary value of ζ as an initial guess. If nothing is specified then $\zeta = 0$ by default.
2. Using equations 5.42, 5.29 and 5.44 determine the hydrodynamic pitch angle (β) and the Loss Factors. The user will have an option to select either Prandtl (F) or Goldstein Loss factor (G). If nothing is specified then Goldstein's factor is selected by default given its better accuracy for a lower number of blades.
3. Determine the Reynolds Number at the section using the formula:

$$Re = \frac{\rho W c}{\mu} \tag{5.53}$$

   Here the expression for Wc can be obtained by equating expression for circulation (5.32) and elementary lift (5.21a) and substituting the elementary circulation from equation 5.39 as shown below:

$$Wc = 4\pi\zeta V^2 \frac{G}{\Omega c_l} \tag{5.54}$$

4. If the airfoil data for the selected airfoil series is available for the calculated Reynolds number, then by lookup table feature, the lift to drag ratio (ε) and angle of attack (α) is determined. If the data is unavailable select the ideal values of α and ε for the desired airfoil series.
5. Next, the induced axial and tangential interference factors (a and a') are determined using equations 5.41a and 5.41b
6. With the known values of interference factors, and hydrodynamic pitch angle, determine the blade pitch ($\theta = \alpha + \beta$) and the resultant incident velocity (W) as:

$$W = \frac{V(1+a)}{\sin(\beta)} \tag{5.55}$$

   The computed value of W is then used to determine the blade section chord c from equation 5.54.

7. Determine the primes or derivatives of all the coefficients of C_T and C_P given in equation 5.48. These are integrated from hib to tip ($\xi = 0 \rightarrow \xi = 1$) to obtain the values of I_1, I_2, J_1, and J_2.
8. Depending whether the thrust or power is specified by the user, the value of ζ is determined from 5.49 or 5.51, and the corresponding values of C_P or C_T is determined.
9. If the new value of ζ calculated in the previous step is close to the old value within a tolerable limit of around 0.01% then the iterations are stopped. Otherwise, the new value is used as the input for step 1 of the next loop.
10. Once the iterations are completed, the efficiency of the propeller and the load or circulation distribution along the radial direction can be calculated.
11. If the chord to diameter distribution for a specific airfoil series is specified by the user, then the value of c_l is scaled such that the product cc_l remains constant to maintain the same optimum circulation at each radial section given by:

$$\Gamma = \frac{cc_l W}{2B} \tag{5.56}$$

12. Once the value of lift coefficient for each radial section is determined, the ordinates for the camber line, its slope and the angle of attack can be determined using the equations 5.4 and 5.5. A cosine distribution is considered for the abscissa to determine the camber line coordinates.
13. The next step would be to add thickness perpendicular to the camber line in order to get the upper and lower surface co-ordinates using the equations 5.3a and 5.3b. These 2D coordinates are transformed into 3D coordinates by including the propeller pitch. This way the coordinates for all the sections of the airfoil can be determined and are exported as two different text files in a format that could be read by ANSYS TurboGrid (.curve) for fluid mesh generation, and by SOLIDWORKS or any other CAD software for propeller geometry generation.
14. The propeller mesh thus generated can then be analyzed by importing it into ANSYS CFX to evaluate and verify the propeller performance using CFD. Whereas, the propeller geometry generated from SOLIDWORKS or other CAD software can be 3D printed and then be tested experimentally to validate the design.

The design framework for a propeller is schematically represented in Figure 5.6. The number of iterations required to obtain convergence is usually around 7-8. The graphical output from the code representing the radial variation of all the computed parameters is shown in Figure 5.7. The figure also depicts the 2D blade sections generated from the code which are later transformed into 3D coordinates. In the present thesis, the mean line or the camber line used is NACA 6 series with a=0.8, which has been previously used for Marine applications by Kerwin and has been verified by Miclea-Bleiziffer et al. as a suitable NACA series for axial flow blood pumps [91, 99]. The Naval Propeller 4148 is used as the base propeller and the

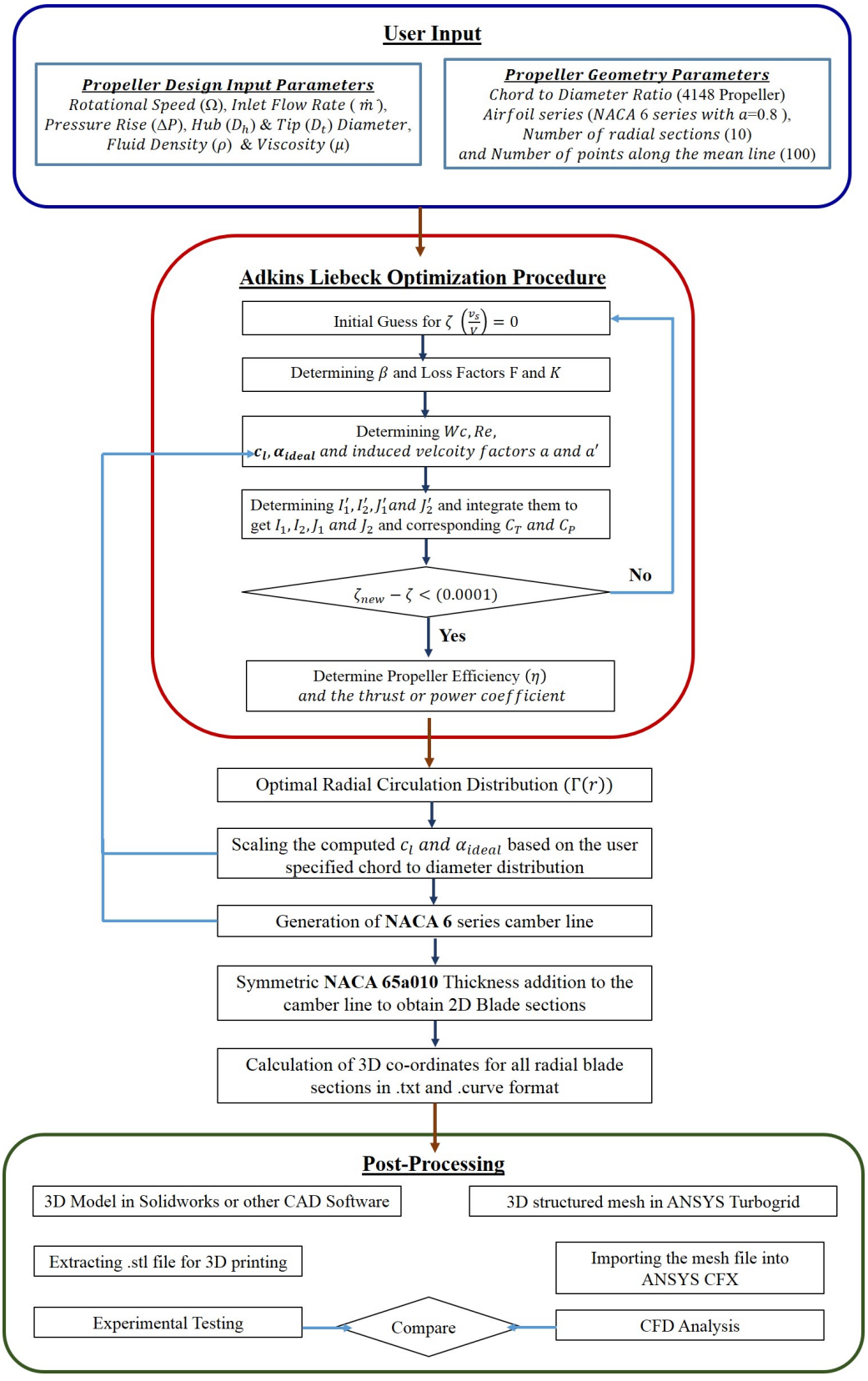

Figure 5.6: Propeller Design Framework

thickness and chord distribution along the radial has been adopted from Kravitz who used it for contra-rotating marine propellers and was also adopted by Miclea-Bleiziffer et al. for axial flow blood pumps [99, 100]. Both Kravitz et al. and Miclea-Bleiziffer et al. modified the tip thickness to increase the strength of the propeller tip. The 4148 Naval propeller geometrical properties is shown in Appendix A. If the user doesn't specify the radial chord distribution, then the optimum chord distribution obtained from the Betz-Prandtl-Goldstein theory will be used.

This concludes the method to generate and optimize a propeller blade design, to achieve the required performance. The next section will focus on verifying the code developed using the discussed Blade Element Momentum Method with the code using Vortex Lattice Method for propeller blade design.

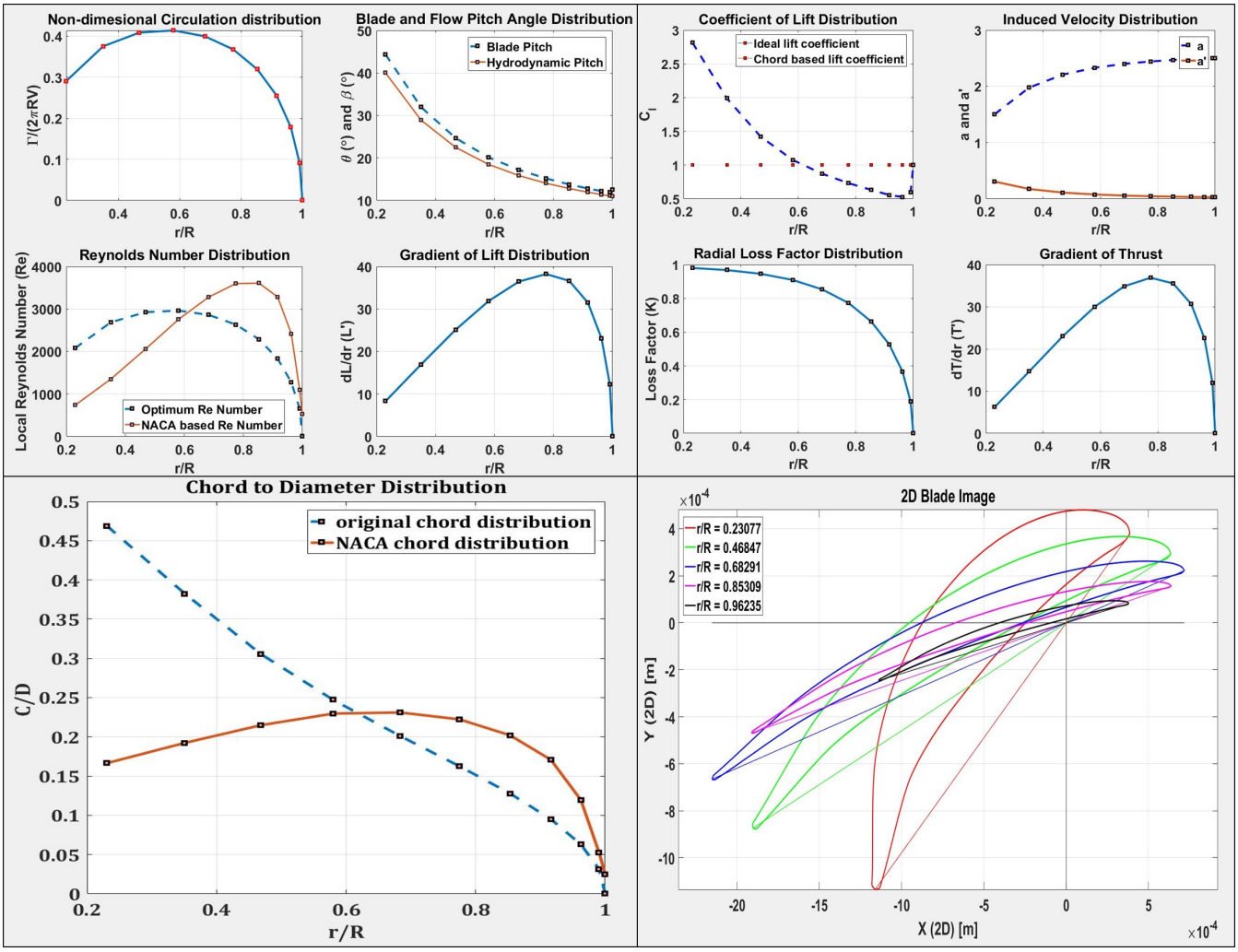

Figure 5.7: Graphical Output from the code showing radial variation of all the computed parameters and the 2D blade section at selected r/R ratios from hub to tip

5.7 Propeller Design Method Verification

Before using the above-discussed code to generate propeller geometries and analyze it using CFD, the code is verified against other propeller design theories. The selected theory for comparison is the most common and widely adopted classical lifting line theory developed independently by Lanchester and Prandtl in 1907 and 1919, which models each airfoil section with a bound vortex and an associated shed vortex sheet from it [13]. The optimization code implementing lifting line theory, called Propeller Vortex Lattice (PVL) was initially developed by Kerwin in 2001, which was later improved by Chung(2007), Stubblefield (2008), Flood (2009) and Epps et al (2009) and is currently known as OPENPROP [101]. The OPENPROP code similar the one discussed in the previous section takes the input from the user and gives the propeller geometry as the output that would provide optimum circulation distribution and have minimum losses due to shed vortices. Epps et. al. provided experimental validation of OPENPROP code and hence a comparison of output from the two methods would give confidence in using the code implementing the Blade Element Theory.

In order to compare the outputs from the two codes, the requirements given as inputs are those required for an IVC (Inferior Vena Cava) propeller. The following are the inputs given to both the propeller codes:

- Inlet Volume flow rate ($\dot{m}$) = $2.82\ l/min$
- Pipe diameter = Diameter of IVC = $14.3\ mm$
- Propeller hub diameter = $3\ mm$
- Propeller tip diameter = $13\ mm$
- Propeller Rotational Speed = $8000\ rpm$
- Desired Pressure Rise = $6\ mm\ Hg$ = $799.934\ Pa$
- Radial Chord to Diameter Distribution = CoD of Naval Propeller 4148
- Radial Thickness Distribution = toD of Naval Propeller 4148
- Thickness Distribution around the Camber Line = NACA 65A010 (Epps modified)
- Camber line = NACA 6 series with a=0.8
- Number of Sections = 10
- Number of camber points = 100
- Density (ρ) = $1050\ kg/m^3$
- Dynamic Viscosity (μ) = $3.5\ mPasec$

The outputs compared from the two codes are the optimum circulation distribution, the hydrodynamic pitch angle, and the lift coefficient distribution along with the computer Propeller efficiency and power coefficient. The outcomes from both the codes are illustrated

in Figure 5.8, which shows a close match in values between the two methods. For the proposed method, the efficiency computed is higher and the subsequently the power coefficient is lower than that obtained from OPENProp code, since ideal value of lift coefficient and angle of attack is considered which is later scaled based on the chord length. This validates that the developed code and successfully proves, that the Blade Element Momentum theory and the Betz-Prandtl condition for minimum losses can be used for designing propellers for VADs.

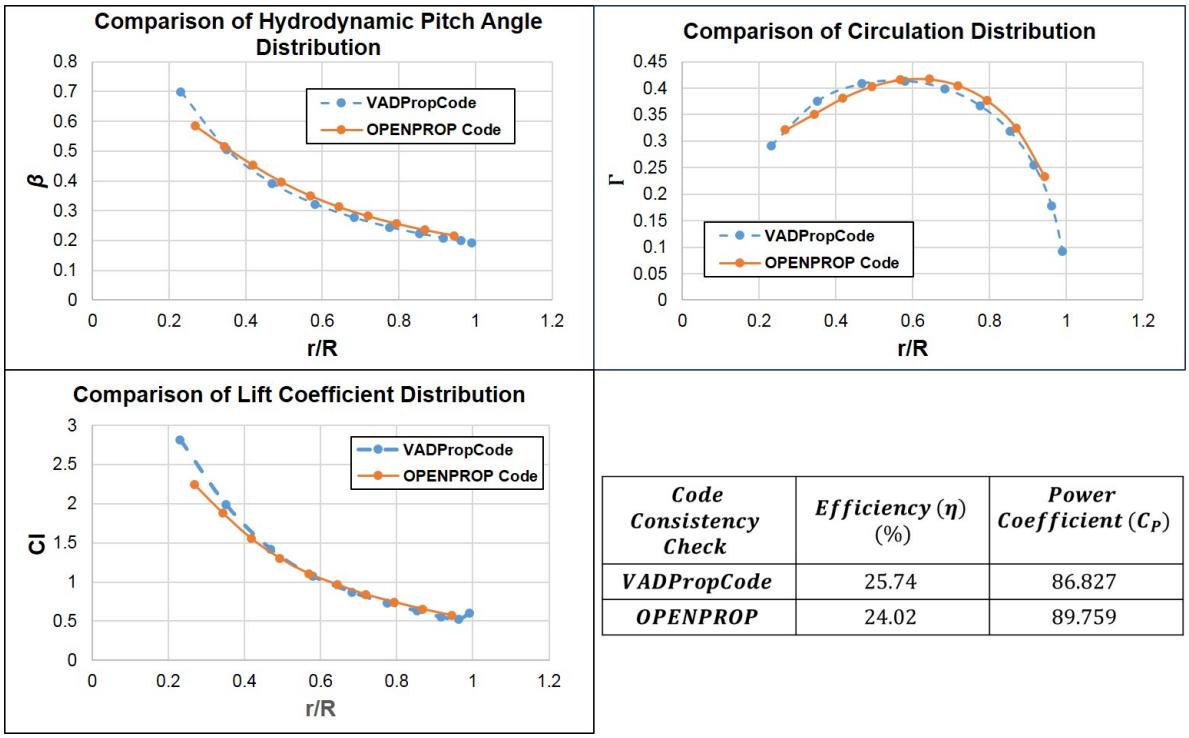

Code Consistency Check	*Efficiency* (η) (%)	*Power Coefficient* (C_P)
VADPropCode	25.74	86.827
OPENPROP	24.02	89.759

Figure 5.8: Comparison of Output from the developed VADProp Code and OPENProp Code for selected r/R ratios from hub to tip

In this chapter, the nomenclature for the propeller blade and the airfoil section was introduced in the first part, followed by the momentum and blade element theory used to determine the induced flow losses and to relate the propeller geometry with its performance. The latter half of the chapter introduced the Betz-Prandtl radial loss model to design optimum propellers followed by a step by step procedure to implement the optimization code. The last part of the chapter showed verification of the proposed code with the Epps's OPEN PROP code to validate the method and use it for designing propellers for different applications like blood pump in this case.

Chapter 6

Selection of Total Cavopulmonary Connection Geometry

It was seen in Chapter 1 that Fontan procedure is widely adopted by the cardiac surgeons to treat patients with single ventricular physiology. The extra-cardiac Fontan procedure has gained a lot of preference since its introduction in 1990 by Dr. de Leval. The distinguishing feature of this surgery is an extra-cardiac graft connecting Inferior Vena Cava (IVC) to one of the pulmonary arteries with the Superior Vena Cava (SVC) sutured directly to the upper side of one of the pulmonary arteries. This artificial connection forming a secondary circulation conduit to unload the single functional ventricle is often called the 'Total Cavopulmonary Connection (TCPC)'. However, as discussed in Chapter 1, the non-physiological flow conditions inside the TCPC results in increased flow losses, reduced cardiac output and elevated systemic venous pressure. These effects, in turn, deteriorate the functioning of vital body organs eventually leading to mortality in Fontan patients. These TCPC-geometry induced complications have inspired various cardiac surgeons and researchers to modify the morphology of TCPC anastomosis site [39–41]. This chapter discusses one such attempt made at studying four different TCPC geometries to select the best performing one, of which two are clinically adopted and the other two are potential candidates. The performance is evaluated based on the fluid power losses, the hindrance to blood flow path and distribution of hepatic fluid from the IVC to both the lungs.

6.1 The Total Cavopulmonary Connection

Four basic surgically constructible geometric configurations of the TCPC were generated and studied to evaluate the hydrodynamic power losses, blood flow pattern, and distribution within them. In order to generate the geometries, the anatomical and physiological parameters for children within 11- 15 years age specified in Chapter 2, Section 2.2 are used. As informed in Chapter 2, the average diameter for the IVC, SVC, LPA, and RPA is taken as

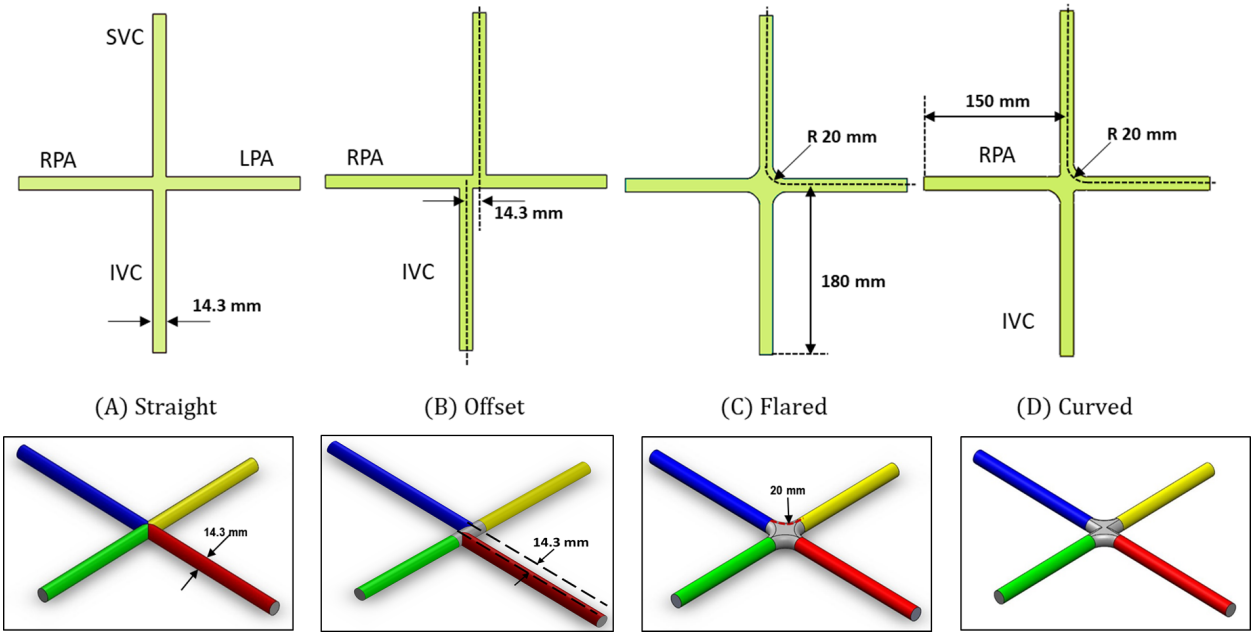

Figure 6.1: Sectional Views of the four TCPC configurations along the coronal plane and their corresponding 3D view

14.3 mm. The length of the IVC and SVC vessel was kept as 180 mm, whereas that of the LPA and RPA was kept equal to 150 mm for the development of the flow before entering the junction. The mid-planar and the three-dimensional view for the four studied geometries are shown in Figure 6.1.

The Straight configuration (A) is a conventional configuration where the IVC and SVC are connected coaxial to each other, thereby forming a cross ('+') structure. The Offset configuration (B), which is lately preferred by surgeons over the straight configuration in the Fontan operations, and in the current case is made by offsetting the IVC from SVC by one diameter distance towards RPA. The Flared configuration (C) is created by assigning a fillet radius of 20 mm along the central axis at the site of anastomosis. The last configuration, i.e. the curved configuration (D), has a curvature of 20 mm radius provided only on one side, with IVC curved towards RPA and SVC towards LPA. Many variations are possible in the TCPC geometry but only these configurations have been selected for the initial hemodynamic study. The best performing geometry will be further analysed to see the effect of its geometrical parameters on its performance. All CAD models were generated using SOLIDWORKS CAD software (Dassault system, Waltham, MA) while Ansys CFX -solver (Ansys Inc., Canonsburg, PA) was used to perform the 3D-CFD simulations to elucidate the flow and velocity patterns inside the connections.

6.2 Hydrodynamic Power Loss

The amount of power loss in each model is calculated using the conservation of energy principle. Since there is no work input or any heat transfer the only energy available is the pressure energy. This pressure energy is composed of static pressure energy and dynamic pressure energy given by the product of pressure and volume flow rate. The difference in the power between the inlet and the outlet is considered as net power loss for any TCPC configuration. This power loss includes the viscous losses, losses due to flow mixing and recirculation, changes in flow direction around the curvature and turnings. Here, the IVC and the SVC acts as the inlet, whereas the LPA and the RPA as the outlet. The power loss equation for the TCPC configurations is given by:

$$\begin{aligned} Power\ loss = Q_{IVC}(P_d + P_s)_{IVC} + Q_{SVC}(P_d + P_s)_{SVC} \\ -Q_{RPA}(P_d + P_s)_{RPA} - Q_{LPA}(P_d + P_s)_{LPA} \end{aligned} \tag{6.1}$$

$$\begin{aligned} \because \quad Q &= Volume\ flow\ rate\ (m^3/sec), \\ P_s &= StaticPressure(N/m^2), \\ and \quad P_d &= Dynamic\ Pressure\ (N/m^2) = \tfrac{1}{2}\rho U^2 \end{aligned}$$

In the equation above, the subscript to the flow rate and pressure terms represents the blood vessel of interest. In the dynamic pressure expression, the variable U represents the area average velocity through a particular cross-section and ρ represents the density of the fluid.

6.3 Flow Simulation Setup

CFD analysis is performed for all the four TCPC geometries in order to understand the detailed three-dimensional flow field existing inside a TCPC. The geometry generated in SOLIDWORKS is imported into the ANSYS Meshing module to generate a fine unstructured computational mesh on which numerical analysis will be performed. The CFD solver used for the analysis was ANSYS CFX (Ansys Inc., Canonsburg, PA), which uses a control volume finite element method.

The setup for the simulation requires a definition of Boundary Conditions and flow properties. The boundary conditions are taken from the physiological parameters defined for a 11-15 years child as shown in Chapter 2, Table 2.1. Recollecting information from Table 2.1, the average cardiac output for the target age group is $4.5\ l/min$ with 63% of the blood flow returning from IVC and the remaining 37% from the SVC. The average values of blood pressure inside the LPA and RPA were found to be around $12.8\ mm\ Hg$. These values represent the flow conditions experienced during major part of the cardiac cycle of a child within the age group of 11-15 years. The walls of the TCPC are considered to be rigid without any compliance and is assumed to have zero slip between the TCPC wall and

the fluid. Blood had to be introduced into the setup as a new user-defined material with the density and dynamic viscosity values of $1050\ kg/m^3$ and $3.5\ centipoise$ respectively. As discussed in Chapter 1, the patients undergoing Fontan surgery are given anti-coagulants to prevent blood clotting at the site of surgery. These anti-coagulants reduces the RBC count in the blood thereby increasing the relative volume of plasma which is mainly composed of water. Moreover, the viscosity of the blood is found to become constant above a vessel tube diameter of 1 mm [61]. For a large diameter tube, more RBCs are concentrated in the tube center while the cell-free plasma is in contact with the wall [61]. Considering these conditions, the blood is modeled as a Newtonian fluid having a constant viscosity. The heart of the patients suffering from single ventricle defect doesn't have enough energy to pump the blood to both the systemic and pulmonary circulation and hence the blood pulsatility is almost negligible by the time the blood returns to the vena cava. As a result, the effect of pulsations on blood flow variations inside the TCPC are neglected and consequently, all the simulations are considered to be steady state. The CFD setup for the Flared TCPC illustrating the inlet and outlet boundary conditions is shown in Figure 6.2, while Table 6.1 shows the boundary conditions applied to the model.

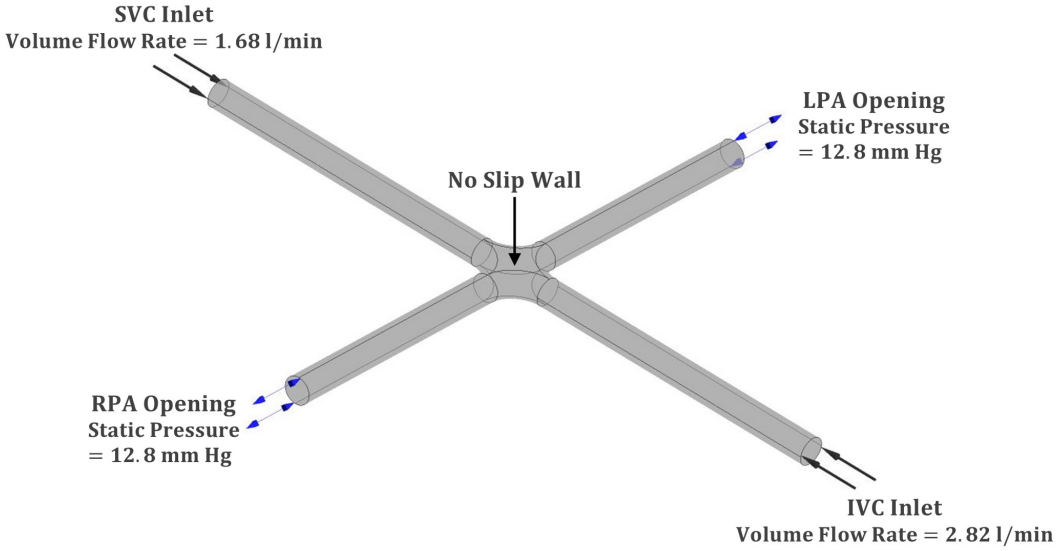

Figure 6.2: CFD setup and Boundary Conditions for the Flared TCPC configuration

The Flow Reynold's number computed at the IVC and SVC inlet with the above-mentioned mass flow rate gives a value of 1255.43 and 747.9169 which is below the laminar to turbulence transition Reynold's number of 2300 for internal flow through a pipe. Thus, the Laminar flow model is selected for all the TCPC alone simulations. In order to achieve higher accuracy, the high-resolution advection scheme is implemented in ANSYS CFX. The convergence criterion is set by making sure that the solution satisfies the following conditions:

- The RMS value of the residuals of the continuity and momentum equation reaches a

Table 6.1: TCPC Boundary Conditions for the simulation

Boundary	Parameter	Value
IVC Inlet	Mass Flow Rate	0.04935 kg/sec
SVC Inlet	Mass Flow Rate	0.0294 kg/sec
LPA Opening	Static Pressure	12.8 mm Hg
RPA Opening	Static Pressure	12.8 mm Hg
TCPC Wall	Wall	No slip wall

value around 10^{-4}.

- Monitor point which in this case is flow energy loss reaches a steady solution with fluctuations within 5% of the mean value.
- The flow domain has imbalances in mass, and the three Cartesian velocity components (u,v, and w) of less than 0.5%.

6.4 Mesh Independence Study

In order to ensure that the power loss computed from the CFD simulations is independent of mesh resolution or the element size, a mesh independence study is performed. The analysis is implemented for Flared TCPC configuration and the final refined mesh element size is used for meshing the other 3 configurations to have a consistency in the mesh. Table 6.2 shows, the element size and number for the three mesh levels analysed. Inflation layers, as shown in Figure 6.3, are provided to each mesh at the TCPC wall in order to capture the development of boundary layer and flow separation near the wall. An unstructured tetrahedral mesh, shown in Figure 6.3 was used for the easy meshing of the complicated central connection geometry. It can be seen from Table 6.2 that the error in the computed power loss value is 30.71% between the medium and coarse mesh which is reduced to 7.37% between the fine and medium mesh indicating an achieved mesh independent solution.

Table 6.2: Flared TCPC Mesh Independence Study

Mesh Level	Maximum Element Size [mm]	Number of Elements [millions]	Power Loss [mW]	Percentage Error [%]
Coarse	1.2	0.7405	6.4738	30.71
Medium	0.8	2.425	9.3436	7.37
Fine	0.6	4.921	10.088	NA

Since the error between the medium and fine mesh is only 7.37%, the former meshing scheme is selected for all the future simulations to save computational time and resources.

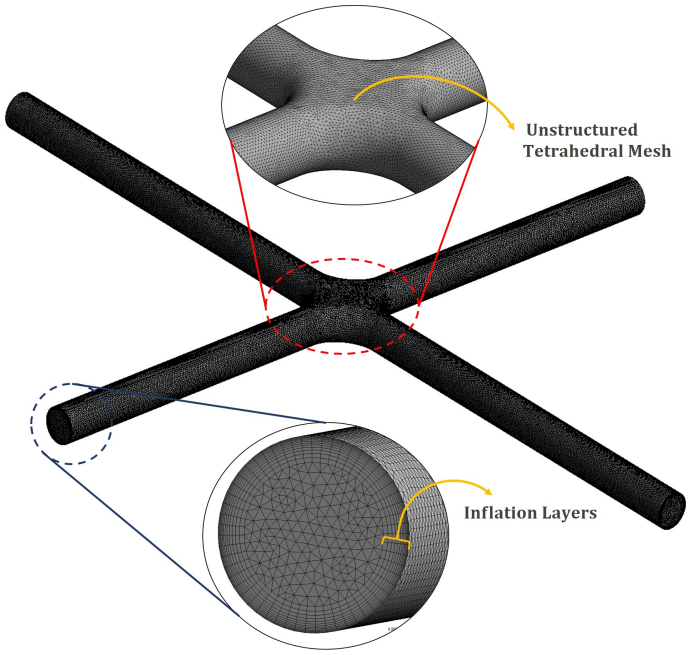

Figure 6.3: Final Refined Mesh for the Flared TCPC showing unstructured tetrahedral mesh elements and inflation layers at the wall in the inset.

6.5 TCPC Configurations Performance Comparison

As discussed earlier, the fluid flow pattern, power loss, and hepatic fluid distribution are the three main criteria used to compare the performance of the considered four TCPC configurations and select the optimal one. Since there are no external mechanical forces or shear stresses acting on the blood particles, Blood Damage Index (BDI) isn't selected as a criterion for comparison.

6.5.1 Pressure and Velocity Contours

The pressure and velocity contours provide a visualization of pressure and velocity variations within the flow domain and hence a better understanding of the underlying flow physics. Pressure and Velocity contours on the Mid-Coronal plane dividing the TCPC into anterior and posterior part are shown for the four TCPC configurations in Figure 6.5 and 6.4.

The gradation of colours along the IVC and SVC walls in the velocity contours shows the development of flow from IVC and SVC inlet in all the four configurations as it approaches the central confluence. The blue regions in the velocity contours are indicative of the flow stagnation, flow separation, and recirculation regions. The blue circular dot visible at the central confluence region, in the Straight and Flared configuration, is indicative of the flow stagnation region generated due to head on impingement of the IVC and SVC flow. This

site of stagnation is slightly above the center owing to the higher IVC flow inertia due to its higher mass flow rate as compared to the SVC flow. The presence of fillet in case of Flared configuration at the site of anastomosis causes the IVC flow to be detached at the corners as pointed by the arrows.

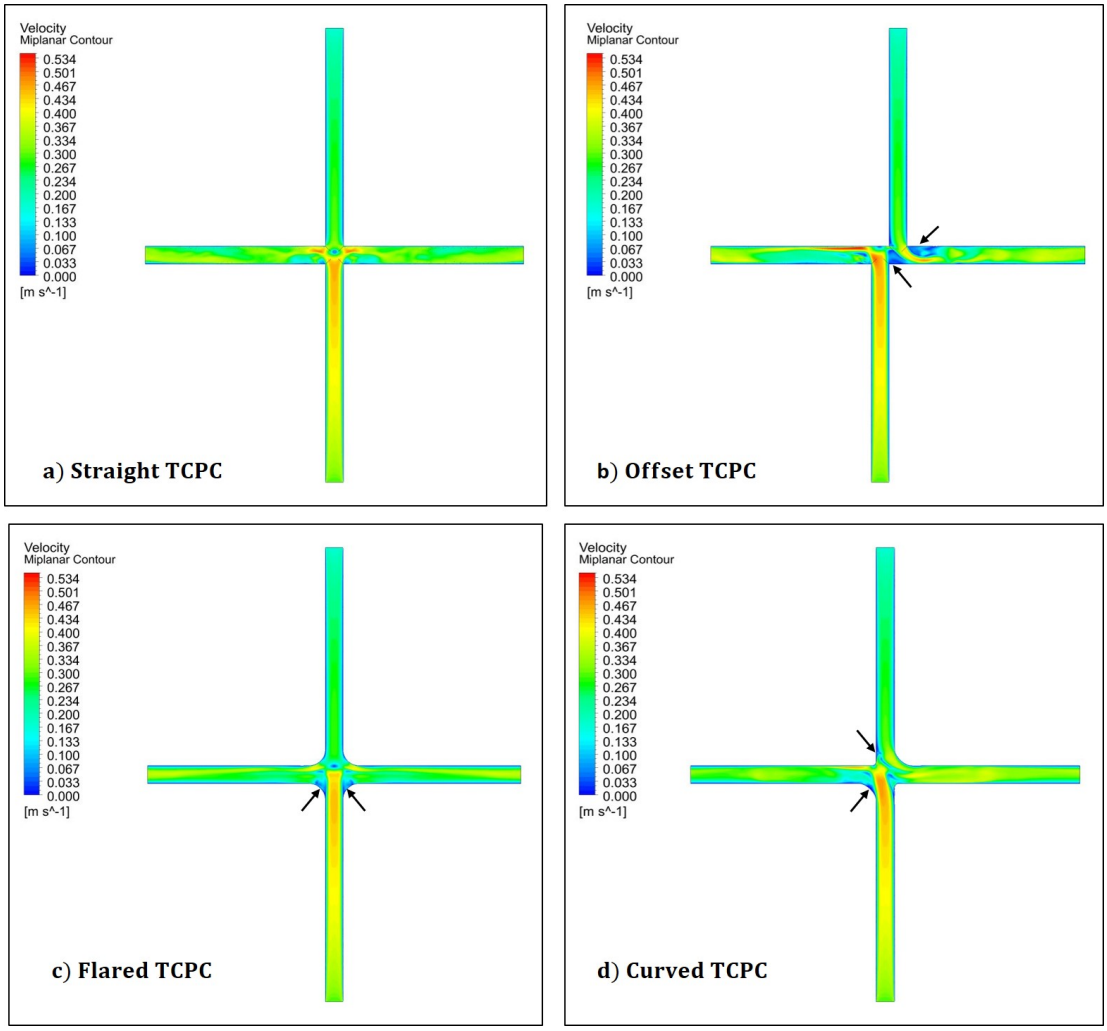

Figure 6.4: Mid-Planar Velocity Contours

The geometrical offset between the IVC and SVC vessels causes the flows to impinge on the wall creating a flow stagnation zone on one side of the PA wall and large flow separation and recirculation regions on the opposite side of the PA wall as indicated by arrows. In contrast to other three configurations, the curved configuration shows minimum evidence of flow separation and flow stagnation regions. This is attributed to its geometry which causes some part of the IVC flow to divert into the RPA and some to collide and mix with the SVC flow. The curvature on one end of the IVC and SVC reduces the intensity of impact and at the same time diverts the flow smoothly into the PAs.

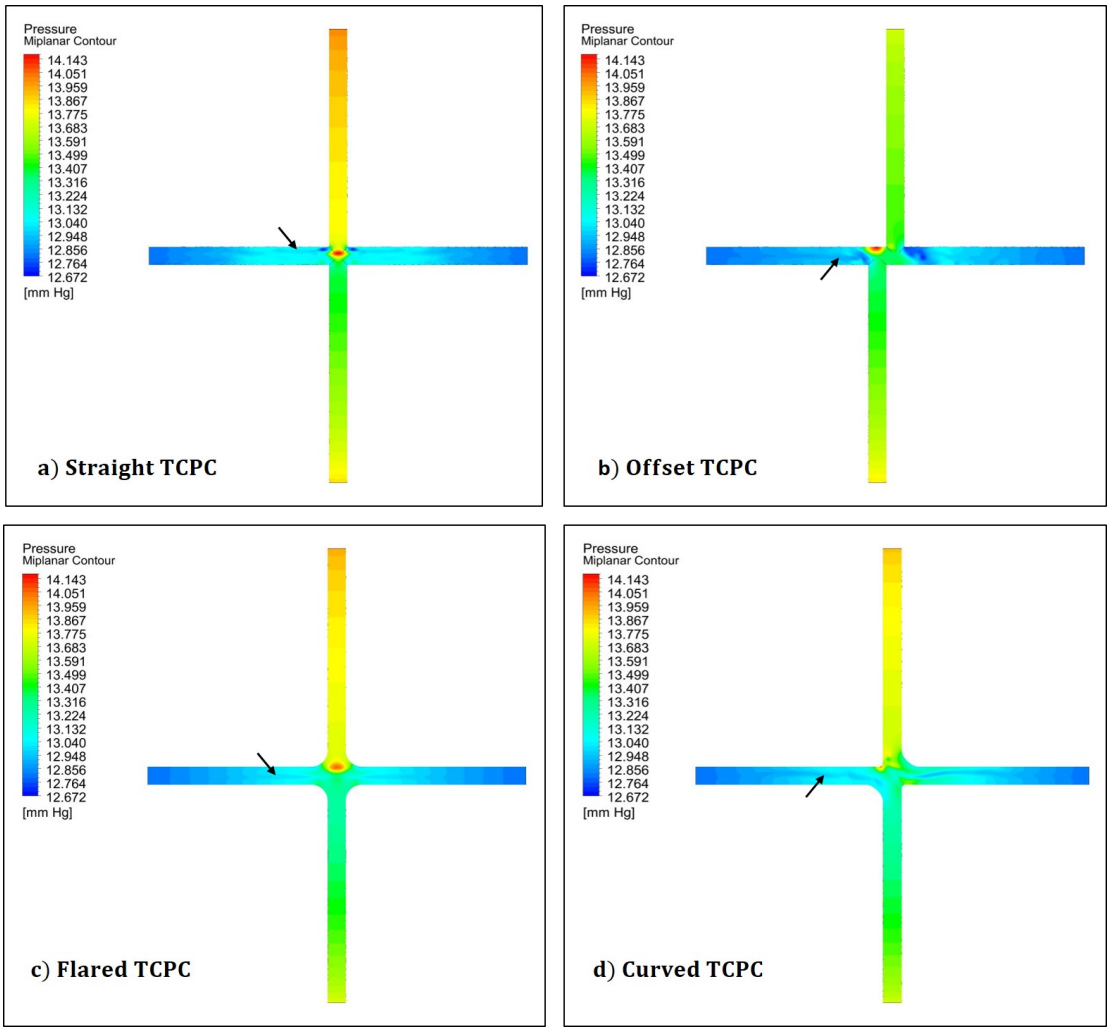

Figure 6.5: Mid-Planar Pressure Contours

It is interesting to see that by the virtue of conversion of kinetic energy into pressure energy, similar to that of a RAM jet, all the stagnation zones in the velocity contour plots correspond to the regions of highest pressure, depicted in red on the pressure contour plots for the TCPC configurations. Another important phenomenon witnessed is the low pressure blue coloured lines running along the lengths of the Pulmonary artery as indicated by black arrows in Figure 6.5. These are representative of the low pressure core of the vortex sheets which are generated after the IVC flow impingement either with the PA wall or the SVC flow. The vortex sheet which isn't visible in velocity contours can be visualized via velocity vectors and streamlines and will be discussed in the upcoming subsection.

6.5.2 Velocity Vectors and Streamlines

In order to visualize the flow splitting and generation of helical vortices in the studied TCPC configurations, 5 transverse planes, 4 at a distance of 15 mm from the central point along the four vessels and one central plane along the IVC axis are generated and tangential velocity vectors are plotted on these planes as shown in Figure 6.6.

The tangential velocity vectors are chosen because they are indicative of the vortex circulations and the flow splitting. In case of the Straight and Flared configuration, the IVC and SVC velocity vectors show almost symmetric behaviour about vertical axis representing equal flow division to the Pulmonary arteries. The LPA and RPA velocity vectors for the straight configuration shows two large vortices and two small vortices. This quadruple vortex flow is also evident from the velocity streamlines. The central confluence vector plot shows the evidence of collision point acting above the center of the LPA pipe (the circle denotes the pipe wall) for both straight and flared configurations. The smaller vortices aren't evident in the LPA and RPA vector plots of the Flared configuration since, in this case, the curvature provided at the corner dissipates the intensity of flow collision and allows the SVC flow to smoothly divert into the PAs as evident in the Flared TCPC velocity streamlines.

In contrast to the IVC and SVC vector plots for the Straight and Flared configuration, the corresponding plots are asymmetric for the Offset and Curved configuration, depicting vena cava flow diverting into the side the vena cava is offset or curved. In case of Offset configuration, an evidence of vortex sheet generation is seen on the RPA branch, which is initiated after the collision of IVC flow with the PA wall. The LPA velocity vectors show evidence of small vortices but are representative of flow recirculation in the separated flow regions as it was observed in the velocity contour. These small recirculations are also evident in the flow streamlines shown in Figure 6.6. Finally, for the curved configuration, the intensity of RPA vortex seems to be low due to the curving of IVC towards RPA, while small recirculation vortices are seen in the LPA side near the bottom wall. In both the offset and curved configuration the flow inside the LPA shows no evidence of vortex sheet. In this way, the flow features that were hidden in the velocity contours are disclosed by velocity vector plots and streamlines.

6.5.3 Hepatic Fluid Distribution

In a normal human circulatory system, the Inferior Vena Cava (IVC) carries the deoxygenated blood from the vital organs like kidney, liver, abdomen, and limbs to the Right Atrium. It has been found that an equal distribution of hepatic fluid to both the lungs is important to prevent pulmonary venous malformation which could be fatal if not cured [37,38]. In case of Fontan patients with Extra-cardiac TCPC, the geometry of the connection governs the distribution of the IVC flow carrying hepatic fluid to the lungs and there has been evidence of PVMs in such patients due to poor hepatic fluid distribution [37, 102, 103]. Considering the ill effect of PVMs in Fontan patients, the four TCPC configurations are evaluated

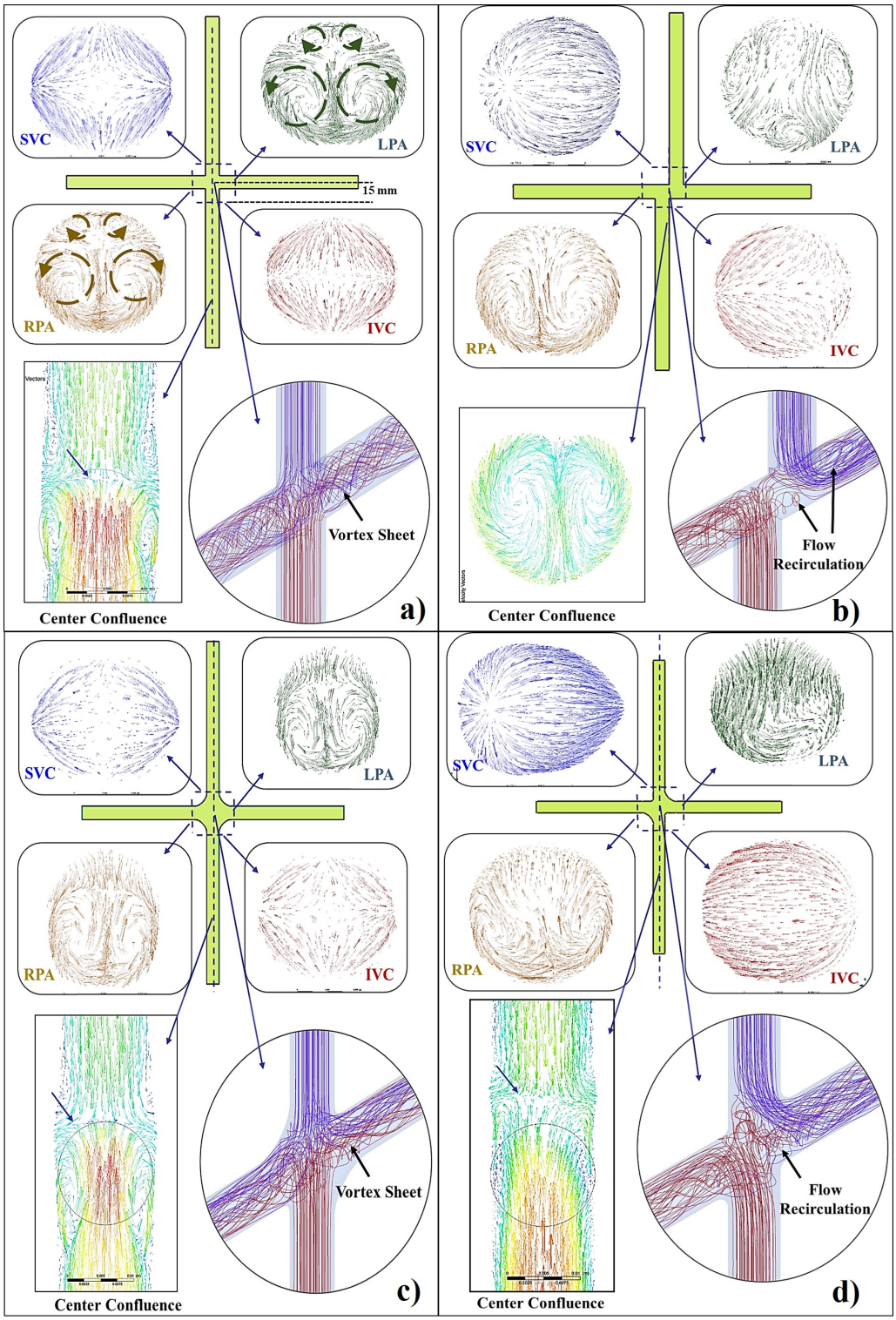

Figure 6.6: Tangential Velocity Vector Plots and Velocity Streamlines for the four TCPC configurations: (a) Straight, (b) Offset, (c) Flared, and (d) Curved

for their IVC flow distribution to LPA and RPA carrying blood to the lungs. In order to do this, Blood Cells are defined as a new material and are injected from the IVC. In Ansys CFX, Lagrangian particle tracking option is used, where the path followed by the blood particles is evaluated using forward Euler integration method. Once the solution is converged, the blood particle tracks could be visualized in the CFX post-processing module. The Blood particles originating from IVC are tracked from the inlet to PA outlets and their corresponding coordinates are exported to Microsoft Excel. In order to determine the IVC flow split, the number of particles reaching the LPA and RPA outlets is determined based on their coordinates and the percentage flow split is evaluated based on the fraction of total particles reaching each outlet. The IVC or Hepatic flow split for the four TCPC configurations is determined by inserting 1000 particles at the inlet and tracking them using the above-described procedure. However, while exporting the track coordinates of all the 1000 particle, a few particles are missed due to Excel's limitation to accommodate more than 104857 rows of data. The number of LPA and RPA particle tracks and the corresponding Hepatic flow distribution is shown in Table 6.3.

Table 6.3: Blood flow split percentage between LPA and RPA for TCPC configurations

TCPC Configuration	**LPA Tracks**	**RPA Tracks**	**Percentage LPA Flow**	**Percentage RPA Flow**
Straight	359	354	50.351	49.649
Offset	182	580	23.885	76.115
Flared	372	344	51.955	48.045
Curved	188	492	27.647	72.353

To justify the hepatic flow split evaluated by tracking the blood flow trajectories for the four TCPC configurations, the 300 Blood flow tracks originating from IVC and reaching the LPA and RPA for four TCPC configurations are visualized and illustrated in Figure 6.7. It could be seen clearly that the IVC flow is distributed almost equally for the Straight and Flared configuration owing to their geometry which allows the IVC and SVC flow to mix at the center and divide equally to the lungs. On the other hand, as seen in Figure 6.7 the Hepatic Fluid from the IVC shows an RPA dominant flow for Offset and Curved configuration since here the IVC is offset or curved towards that side of the PA. This is the first evidence showing that an offset or flaring on one end of the IVC would result in poor hepatic flow split to the lungs and could potentially cause pulmonary venous malformations.

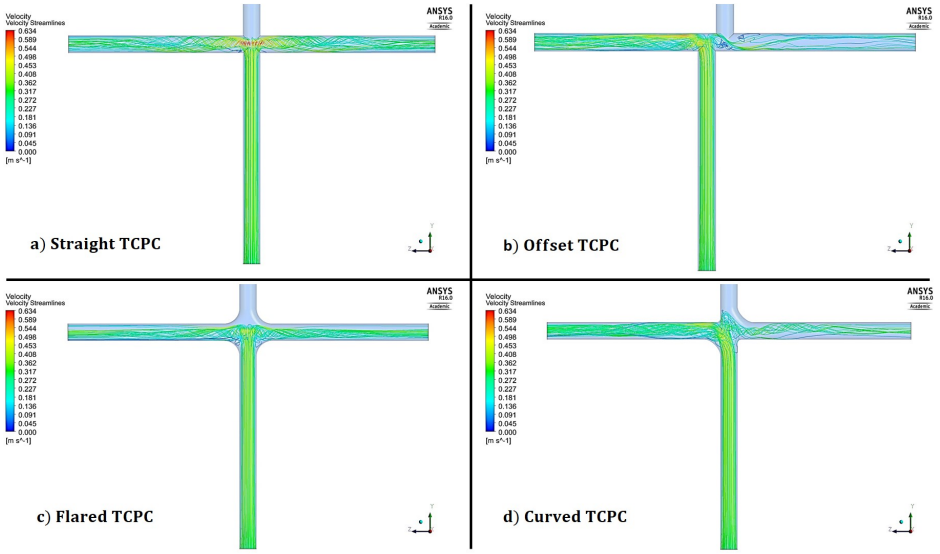

Figure 6.7: Blood particle tracks showing Hepatic fluid (IVC Flow) distribution to the Lungs

6.5.4 Fluid Power Loss

The amount of energy lost by the blood flowing from the IVC and SVC to the LPA and RPA helps to quantify the efficiency of a TCPC configuration to distribute blood to the lungs. The Power loss equation 6.1 is defined in the CFX-Post for all the cases analysed for the four TCPC configurations. Since the power loss expression takes difference of total energy at inlet and outlet, it takes into consideration the losses due to viscosity, flow mixing, recirculation, vortex generation and geometrical hindrances. The power loss in the four TCPC configurations for the normal physiological IVC:SVC flow split of 63:37 and the cardiac output of 4.5 l/min are listed in Table 6.4. As expected the amount of power loss is maximum in the Straight configuration due to direct impingement and central mixing of the IVC and the SVC blood and formation of vortex sheets along the length of LPA and RPA as it was seen in Figure 6.6 resulting in relatively higher energy dissipation. Whereas, the curved configuration shows the minimum amount of power loss due to relatively streamlined flow pattern and lower flow mixing. It could be seen that the power loss in case of Flared and Offset configuration is almost comparable even though the fluid flow has different characteristics. As it was mentioned earlier, in case of Flared configuration the curvature helps to dissipate the intensity of flow impingement and mixing at the center as compared to the Straight configuration since the flow has enough room to select its course before approaching the central confluence which helps to mitigate the losses. Whereas in case of Offset configuration which has least propensity for energy deprecating IVC and SVC flow mixing due to its geometry, the flow losses are introduced due to the impingement of high-velocity IVC flow to the PA wall and the consequent vortex flow generation in RPA arm, in addition, to flow separation and recirculations near the LPA walls as seen in Figures 6.6.

Table 6.4: Power Loss in TCPC configurations at IVC:SVC flow split of 63:37

TCPC Configuration	Power Loss (mW)
Straight	11.8298
Offset	9.6263
Flared	9.34362
Curved	8.8818

IVC:SVC Flow Split Study

The power loss study is further extended to analyse the effect of different IVC to SVC flow split in order to mimic various conditions experienced during a cardiac cycle. The IVC:SVC flow split is also found to vary with age [69] and hence this study could provide an insight as to how a particular TCPC configuration would perform as a Fontan patient grows old. For this study, the LPA and RPA pressures were kept equal to 12.8 mm Hg while the IVC and SVC flow percent was changed from 30% to 70% of the cardiac output and the corresponding results for power loss variation are shown in Figure 6.8. It can be seen that the power loss trend is similar to that found at 63% IVC flow, with the Straight and the Curved configurations showing the maximum and minimum loss trend while the Offset and Flared configurations having almost similar power loss curve which is slightly higher than that of the curved configuration due to the reasons explained in subsection 6.5.4. Besides, all the configurations show a parabolic trend in power loss with minimum losses at equal IVC and SVC flows. This is justified since an equal flow resistance in both the PAs would expect symmetrical IVC-SVC flow for minimum losses and flow equilibrium. The trend in power loss found in this study shows strong agreement with the trend found in various other experimental and numerical studies done by other researchers [38, 39, 104].

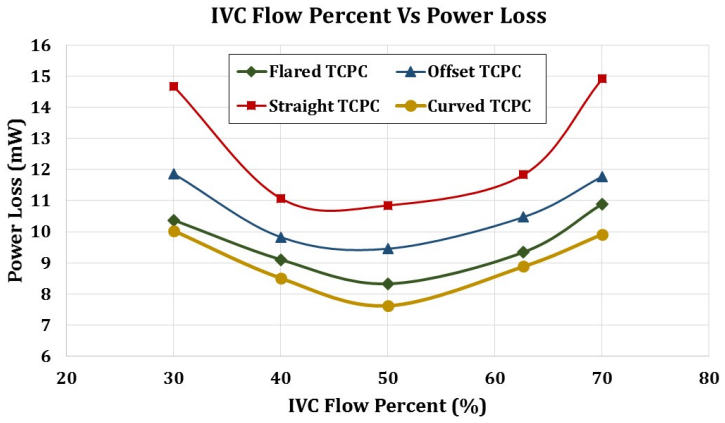

Figure 6.8: Effect of IVC:SVC flow split on power loss in all the four TCPC configurations

RPA:LPA Flow Split Study

It is known that the pulmonary vascular resistance, which affects the blood flow through the LPA and RPA, varies with changes in cardiac output, lung volume, gravity, intravascular pressure and during rest and exercising condition of the human body [68, 70, 105]. Hence a study is done to see the effect of changes in RPA to LPA flow rate on power loss in all the four TCPC configurations. To implement this study, the IVC to SVC flow split was kept equal to the normal physiological value of 63:37 while the RPA flow percentage was varied from 30% to 70% of the cardiac output to simulate different lung resistance ratios. As a result, in the CFD setup, the outlet boundary condition at the LPA and RPA opening was changed from static pressure to mass flow rate. Similar to the IVC-SVC flow split study, it could be seen from Figure 6.9 that the overall power loss is maximum for the Straight configuration and minimum for the Curved configuration. Here, since the Straight and Flared configuration are symmetric about the vertical axis the power loss to RPA flow percent curve is parabolic with minimum power loss occurring for equal flow split to RPA and LPA that is for equal lung resistance. On the contrary, the Offset and Curved configuration power loss curve show a slight tilt towards RPA flows greater than 50%, with minimal losses occurring for 60% RPA flow. This is expected since the IVC flow is greater than the SVC flow, and hence it will experience lower flow losses when it is guided (either via. offsetting or curving) towards the lung or PA with lower resistance, analogous to an electrical network. As a result, doctors and researcher often tend to offset the IVC having higher flow rate towards lung with lower resistance or the lung requiring higher flow rate to reduce flow losses [38]. However, it would give adverse effects if the lung resistance increases or if the IVC flow reduces as it could be seen in Figure 6.9.

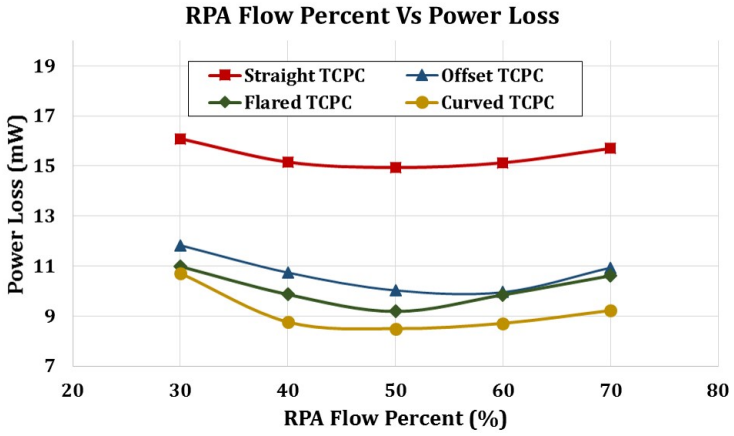

Figure 6.9: Effect of RPA:LPA flow split on power loss in all the four TCPC configurations

Based on the analysis done for the power losses, hepatic flow distribution and flow pattern inside the four studied TCPC configurations, the Flared TCPC gave the best performance considering a tradeoff between power loss and hepatic flow split. As a result, the Flared

TCPC configuration is selected for further studies and as an optimal TCPC graft geometry inside which the dual propeller pump will be inserted.

6.6 Flared TCPC Flow and Geometry Study

Since the Flared TCPC configuration was selected for all the future simulations, it was necessary to determine the effect of curvature radius on power loss and flow pattern inside the TCPC. In order to do so, the curvature radius was changed from 10 mm to 25 mm in steps of 5 mm thereby giving 4 geometries to compare and study. The effect of flaring radius on power loss for the physiological values of IVC:SVC flow split and LPA/RPA pressure is shown in Figure 6.10, where an inverse relation between power loss and radius of curvature is evident.

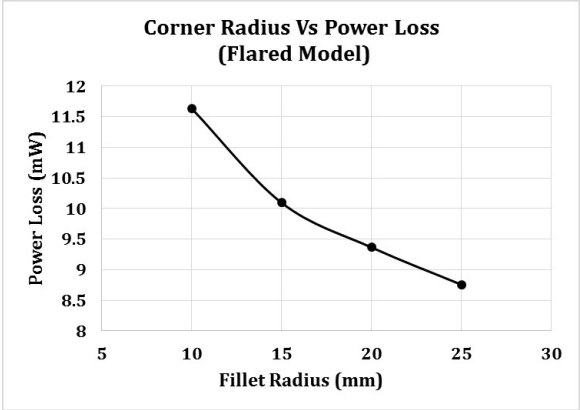

Figure 6.10: The effect of curvature radius on power loss in the Flared TCPC configuration

This is experienced since the intensity of impingement of the IVC and SVC blood flow at the central confluence is reduced as the curvature radius increases. This phenomenon is also seen in pipe flow with a bend where the bend loss coefficient reduces as the radius of bend increases for a constant pipe diameter. For a very small radius of curvature, the effect will be similar to that of the Straight TCPC with large vortex sheet developed immediately downstream of the site of collision as seen from the velocity streamlines for flared TCPC in Figure 6.11a. This can also be witnessed from the pressure contours for the studied four radii configurations shown in Figure 6.11b, where a prominent low pressure region at the center of the LPA and RPA arms indicating the core of the vortex sheet is evident in the 10 mm radius geometry.

As one would expect, as the radius of curvature is increased, the flow is guided along the curvature and is distributed to both the lungs more smoothly. This helps to set the fluid path before reaching the central confluence and hence to reduce the intensity of mixing and the intensity of generated vortex sheet. This is evident from the pressure contour where the

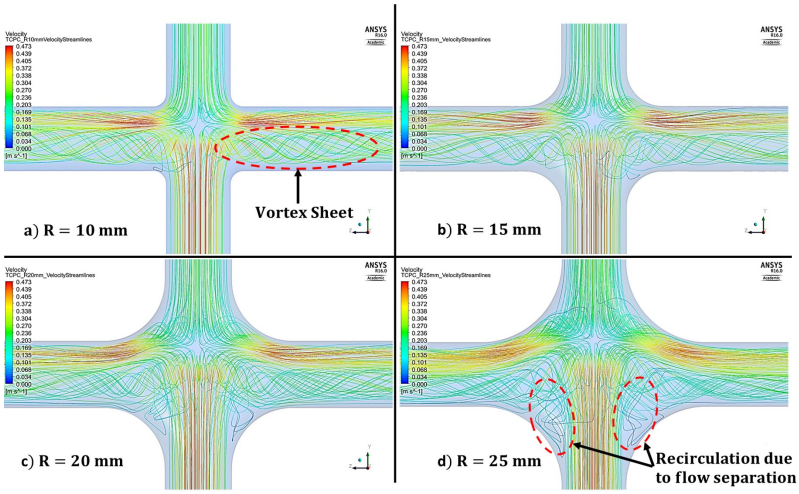

(a) Velocity Streamlines

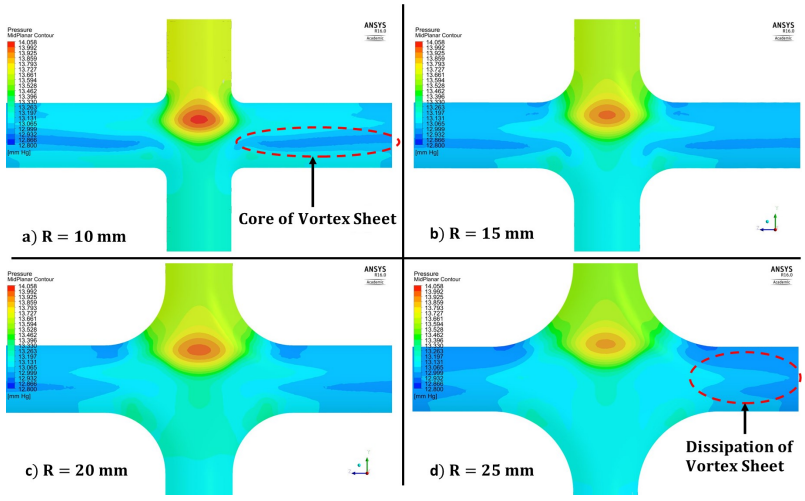

(b) Mid-Planar Pressure Contours

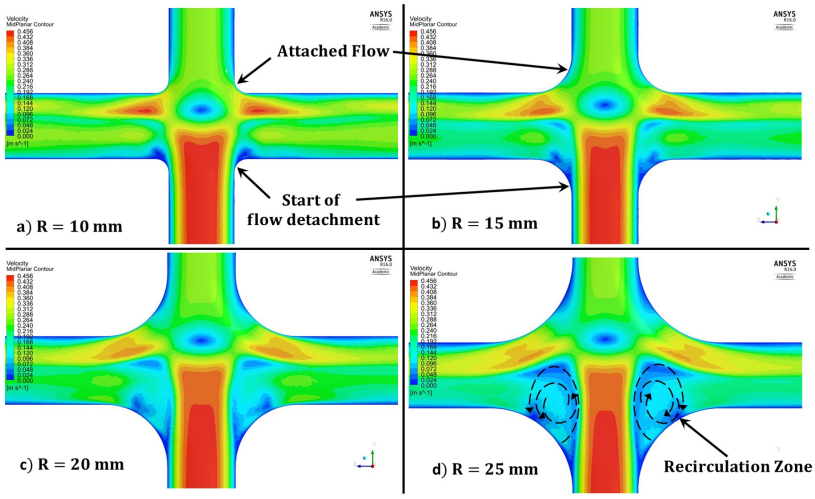

(c) Mid-Planar Velocity Contours

Figure 6.11: Flared TCPC Radius of Curvature Study

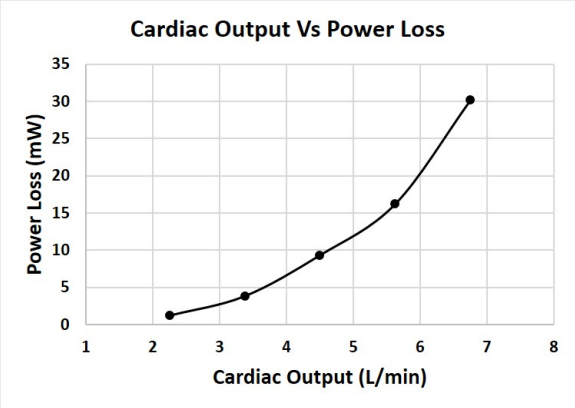

Figure 6.12: Variation in power loss with the cardiac output in the Flared TCPC configuration with R=20 mm

central blue line depicting the vortex core, recedes away from the center with an increase in flaring radius until it vanishes completely for the 25 mm geometry. However, the chances of flow separation and recirculation were seen to increase with the increase in the radius of curvature. This can be observed in Figure 6.11a, where the velocity streamlines show significant recirculation at the site of curvature on the IVC side for 25 mm geometry. A certain amount of recirculation is also evident in 20 mm geometry near the IVC curvature site. This is more clearly illustrated in Figure 6.11c showing mid-planar velocity contours for all the radius of curvatures. It can be seen, that the start point of flow detachment on the IVC side is moving upstream with the increase in curvature radius with the low velocity SVC flow detachment becoming evident for 25 mm configuration. The large curvature radius introduces sites of flow recirculation, having very low velocity, which increases the blood particle residence time and poses a high risk of blood clotting or thrombosis. Considering the side effects of too large fillet radius and its advantages in terms of streamlined flow with reduced power losses, the 20 mm curvature radius geometry is selected as the optimal Flared TCPC geometry and will be used for all the TCPC-propeller simulations henceforth in this thesis.

6.6.1 Effect of Flared TCPC geometry on Power Loss at different Cardiac Outputs

The last physiological parameter analysed is the cardiac output which varies during exercise, heavy breathing and during anxiety and it is important to study how the proposed flared configuration with 20 mm fillet radius performs under changing cardiac output conditions. In order to simulate these conditions, the cardiac output is increased from $2.25\ l/min$ to $6.75\ l/min$ in the steps of $1.125\ l/min$. The IVC to SVC flow split is still maintained at $63:37$ for all the studied cardiac outputs with the LPA and RPA pressure of $12.8\ mm\ Hg$ at the outlets. It is known that for a constant diameter tube, the frictional losses increase with

an increase in velocity or the flow rate. A similar behavior was observed for this study, as shown in Figure 6.12, where the power loss is increasing with an increase in cardiac output, due to higher viscous losses experienced at higher flow rates.

6.7 Experimental Testing and Validation

In order to validate the results obtained for the selected Flared TCPC configuration study, an experimental test rig was constructed as shown in Figure 6.16. The optimal Flared TCPC model with the flaring radius of 20 mm was selected for testing. The test setup was used to determine the TCPC performance in terms of power loss for different IVC to SVC flow splits and for different cardiac outputs. The results obtained from the test setup are compared with the corresponding numerical results obtained from CFD analysis to validate the computational model.

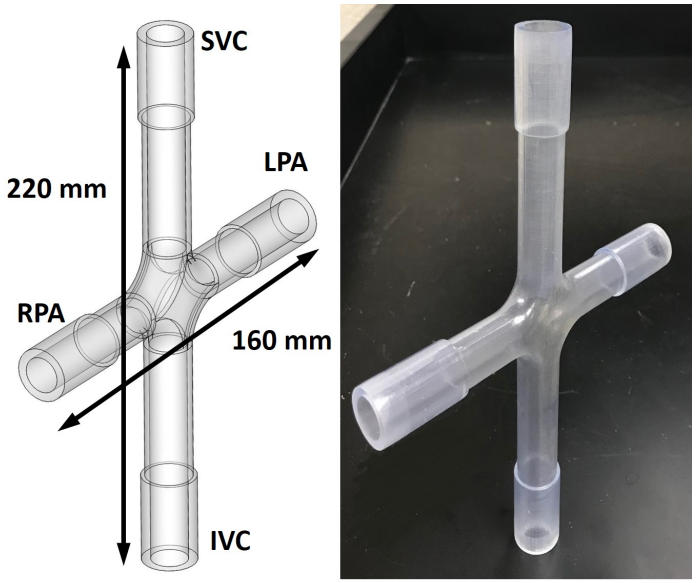

Figure 6.13: Flared TCPC CAD Model and the corresponding SLA based 3D printed TCPC Model

6.7.1 Methods and Materials

The to scale Flared TCPC model shown in Figure 6.13 was manufactured using stereolithography (SLA) additive manufacturing technique having a resolution of 0.005" in Z and 0.020" in XY direction by Stratasys Ltd. (MN, USA). To facilitate clear visibility of the fluid flow inside the TCPC as well as that of the pump to be inserted, the Somos Watershed XC 11122 seethrough material is selected. This material is widely used for manufacturing intricate designs requiring a smooth finish and high water resistance, however, since the part was printed

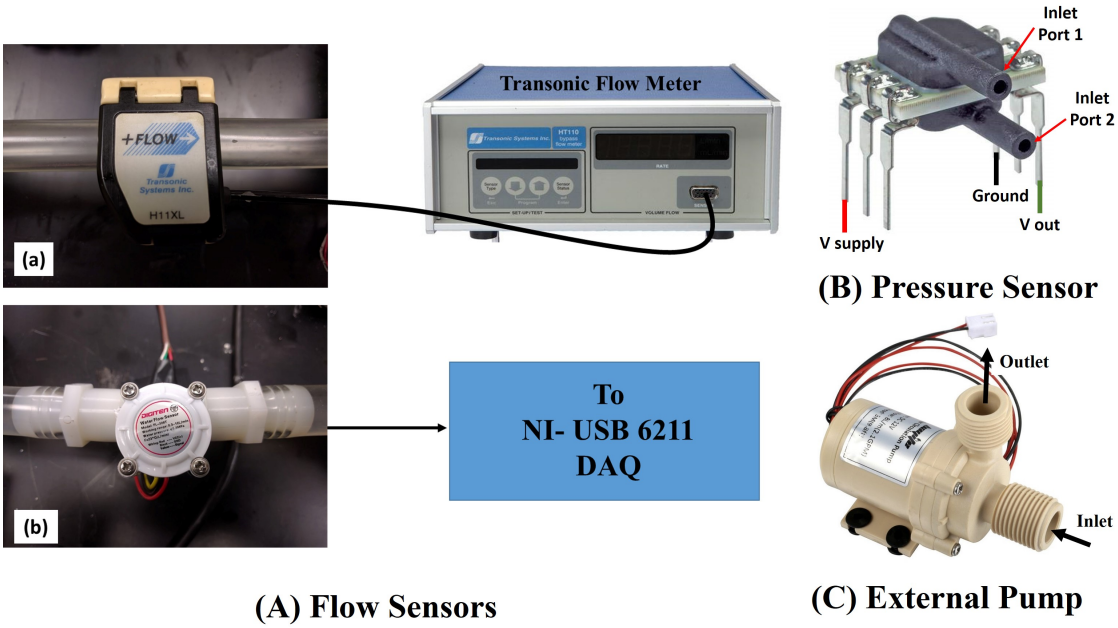

Figure 6.14: (A) Flow sesnsors; (a) Transonic, and (b) Digiten; (B) Pressure Sensor and (C) External Circulatory Pump used in the test setup

in a single piece, it wasn't possible to provide any finishing or surface treatment on the inner side of the TCPC which rendered less than 100% transparency with a hint of bluish hue. In order to save on the printing cost and the limited availability of space on the printing tray, the length of the printed TCPC was kept 220 mm along the IVC-SVC branch and 160 mm along the LPA-RPA conduit.

For this preliminary proof of concept testing, the experiments were conducted with water ($\rho = 998\ kg/m^3$ and $\mu = 8.9 \times 10^{-4}\ Pa - sec$) and in future, the tests could be performed with a water-glycerine mixture having same density and viscosity as that of the blood to better mimic the physiological setting. The flow inside the network was maintained using an external circulatory pump, (Bayite BYT-7A006 DC Centrifugal Pump), shown in Figure 6.14, having a maximum flow inducing capacity of 8 l/min. A 4 channel, linear DC power supply, GW-Instek GPE-4323 (New Taipei City 236, Taiwan), was used to control the DC voltage across the external pump to control the flow through the system.

Two high accuracy, pre-calibrated, non-contact Transonic H11XL (Transonic Systems Inc, Ithaca, NY, USA) sterile tubing flow sensors were used to accurately determine the flow rate through the IVC and SVC branches. These flow sensors are widely used for blood flow measurements due to their ultra-sound volume flow measurement technology allowing contact-less sensing without hindering the flow path. The sensors were pre-calibrated by Transonic for water and glycerine-water mixture by testing in conjunction with Tygon tubing having 5/8" outside diameter. The signals sensed by the H11XL sensors are sent to and read continuously by Transonic HT110 Bypass flow meter shown in Figure 6.14 to display

the instantaneous mean volume flow through the tube. In order to determine the distribution of fluid into the LPA and RPA branches, two Digiten FL-308T flow meters detecting the frequency via embedded hall sensors are used. These sensors have low accuracy at low flow rates and provide resistance to the flow due to its rotary paddle wheel. These flow sensors were calibrated in a closed flow loop using the Transonic flow sensor in series, however, during flow measurements, the accuracy of these sensors was low with errors ranging from 5% -10%. As a result, it was decided to measure the frequency output from these sensors, take their ratio and multiply it with the total inflow from IVC and SVC branches to determine the flow split to LPA and RPA based on mass conservation. Four ball valves, two for controlling the flow split through the IVC and SVC branches, and other two for controlling the flow resistance through LPA and RPA branches, are used.

To measure the static pressure inside the four major branches of the TCPC, four Honeywell's (Honeywell Inc, Morris Plains, NJ, USA) piezoresistive ABP series DJJT001PGAA5 board mount gauge pressure sensors are used, with two located at a distance of 180 mm on the IVC and SVC pipe and the other two at a distance of 150 mm on the LPA and RPA pipe from the center. The sensor locations were selected to match the inlets and outlets locations in the numerical TCPC model. The pressure range of these sensors is 0 to 1 psi [51.715 mm Hg] requiring a supply voltage of 5 V DC. These sensors can be used for either gauge or differential pressure measurement and give analog voltage as the output signal which is updated at $1\ kHz$ frequency. The high accuracy of $\pm\ 0.25\%$ of the full-scale span of the measured values makes these sensors suitable for blood pressure measurement applications. These sensors are pre-calibrated over an operating temperature range of $0°C$ to $50°C$. The transfer function defining the relation between the sensor voltage output and the applied pressure is given by Equation 6.2.

$$Output(V) = \frac{0.8 \times V_{supply}}{P_{max} - P_{min}} \times (P_{applied} - P_{min}) + 0.10 \times V_{supply} \tag{6.2}$$

In the above equation, the supply voltage was kept at a constant value of 5 V, with the minimum and maximum pressure values of $0\ mm\ Hg$ and $51.175\ mm\ Hg$. The pressure sensors are supplied with the working fluid via a 1/8" clear polyurethane tube connecting the barbed tube fitting at the pipe wall to the barbless in-port of the pressure sensors. The tube lengths are kept equal for all the sensors to have equal flow losses and thereby remove any bias. The pressure sensors are soldered to two circuit boards, one accommodating the IVC and RPA sensors and the other accommodating the SVC and LPA sensors which are kept at the same ground level.

Since the diameter (=14.3 mm) of the TCPC lumen (inner diameter) was non-standard, the next closest standard pipe size available was selected to complete the flow network. This next closest size was found for 1/2" PVC pipes having an I.D. of 15.291 mm. As shown in Figure 6.16, 1/2" Schedule 40 Clear PVC pipes were used to facilitate flow visualization and locating section with trapped bubbles. In order to center the pipes with respect to the Flared TCPC, three PLA based 3D printed mounts were used.

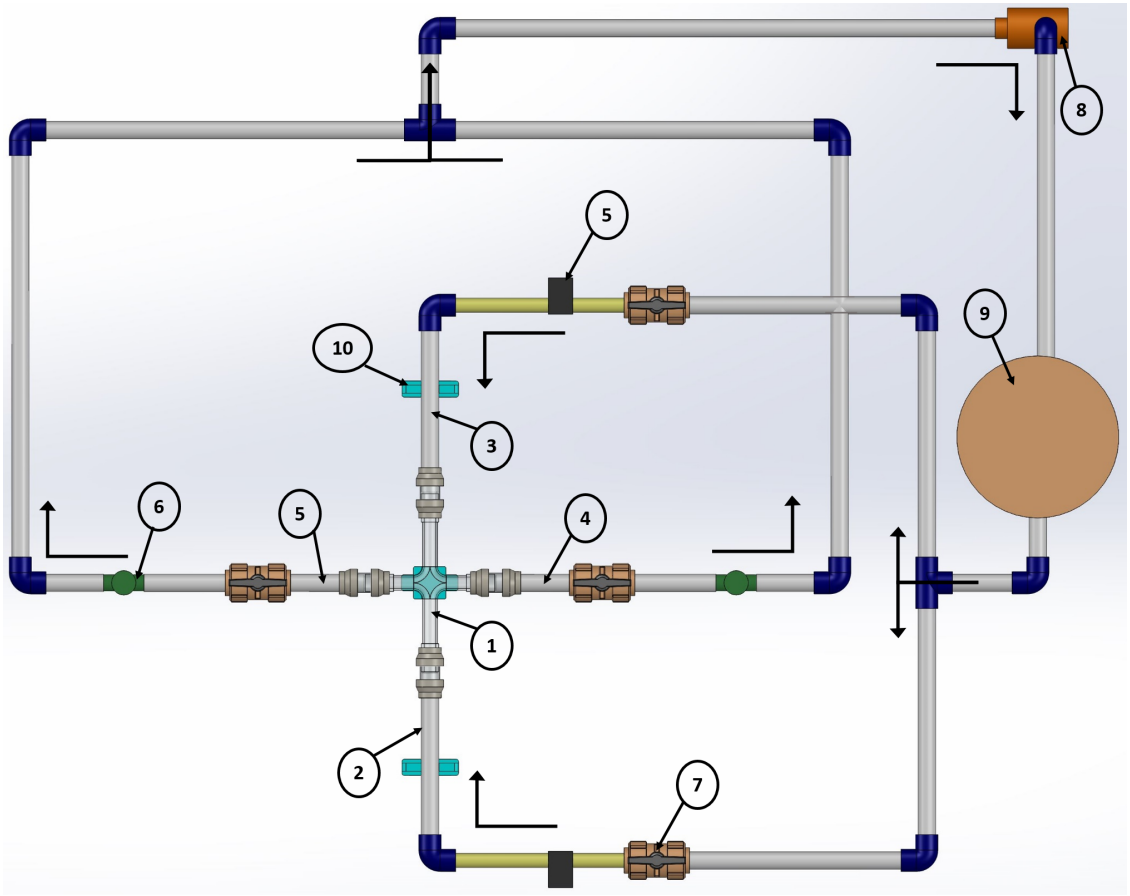

Figure 6.15: Schematic Network Model of Flared TCPC Experimental Test Setup

In the current case, the flow Reynolds number ($\rho V D/\mu$), computed with water as the working fluid, at the IVC inlet and SVC inlet for the physiological flow rates of 2.82 l/min and 1.68 l/min comes out to be 4389 and 2614 respectively, indicating that the flow will be in transitional to turbulent regime when using water. The ideal length required for the flow to be fully developed in case of turbulent flows is given by:

$$L_{entrance_{turbulent}} = 5.3 \cdot Re^{0.12} \cdot D \tag{6.3}$$

Using the above equations the entrance lengths for the IVC and SVC pipes comes out to be around 200 - 220 mm and hence a conservative value of 250 mm was used for the IVC and SVC pipe lengths connecting the TCPC model. However, if the flow were Laminar as in case of blood the entrance length would drastically increase to around 1.2 m using the equation given below:

$$L_{entrance_{laminar}} = 0.06 \cdot Re \cdot D \tag{6.4}$$

Thus in future, while working with blood and if there is a need for a fully developed flow profile, a larger entrance pipe length would be needed, however, this would be difficult to incorporate given the amount of space required on each side. A workaround would be to rather use a flow straightener and a converging tube to remove flow disturbances and non-uniformity in the flow, similar to ones used in wind and water tunnels.

As seen in the setup schematic diagram, the flow coming from the single reservoir is split exactly halfway using a T-connector to avoid any inherent bias of flow to one of the vena cava branch. Similarly, the flow returning from the left and right pulmonary arteries is made to travel equal pipe lengths before meeting another T-connector from where the flow is sucked by the circulation pump and supplied back to the reservoir. Such a pipe connection network helps to remove any bias of flow split between the inlets and outlets for completely open valves. Furthermore, the storage container was kept open to the atmosphere making this setup an open loop circuit. This is not a matter of concern since this setup was used for evaluating the power loss which is calculated by taking the difference in pressure and flow rate at inlet and outlet which helps to cancels out the common reference atmospheric pressure values read. To facilitate this, the pressure sensors are used as gauge sensors by keeping the lower port open to the atmosphere. However, the setup needs to be closed if we require actual physiological absolute pressure values to be maintained at the inlets and outlets of the TCPC. In that case, additional four reservoirs would be required at each inlet and outlet having a fixed level of liquid column to exert the required inlet and outlet static pressures. This could be implemented into the current test rig in the future making some modifications.

Finally, in order to make the flow network modular, all the pipes are connected using Push-On slip couplings which could be easily removed using a slip fitting pipe removal tool.

6.7.2 Data Collection

The flow and pressure sensor output signals are read by the NI USB 6211 Data Acquisition device shown in Figure 6.17. The outputs from pressure sensors are connected to 4 of the 16 Analog Input channels while those from Digiten Flow sensors are connected to the 2 Counter Input channels. The voltage and frequency signals received by the DAQ are read and converted into corresponding pressure and flow rate values using LabVIEW (National Instruments Corp, Austin, TX), a data collection and post-processing software.

The front panel of the developed virtual user interface is displayed in Figure 6.17. The program allows the user to select the channel corresponding to the sensor type and also allows the user to specify the sensor properties like, input voltage, peak pressure of the pressure sensor, sampling rate and number of samples to display on the graphical output and the type of pressure input mode i.e either reference single ended (to measure gauge pressure) or differential mode. The default values assigned are shown in Table 6.5. Besides, the ON/OFF switches on the panel provide a provision to turn off a particular sensor channel. The capture button is provided to instantaneously capture the values. In order to remove the

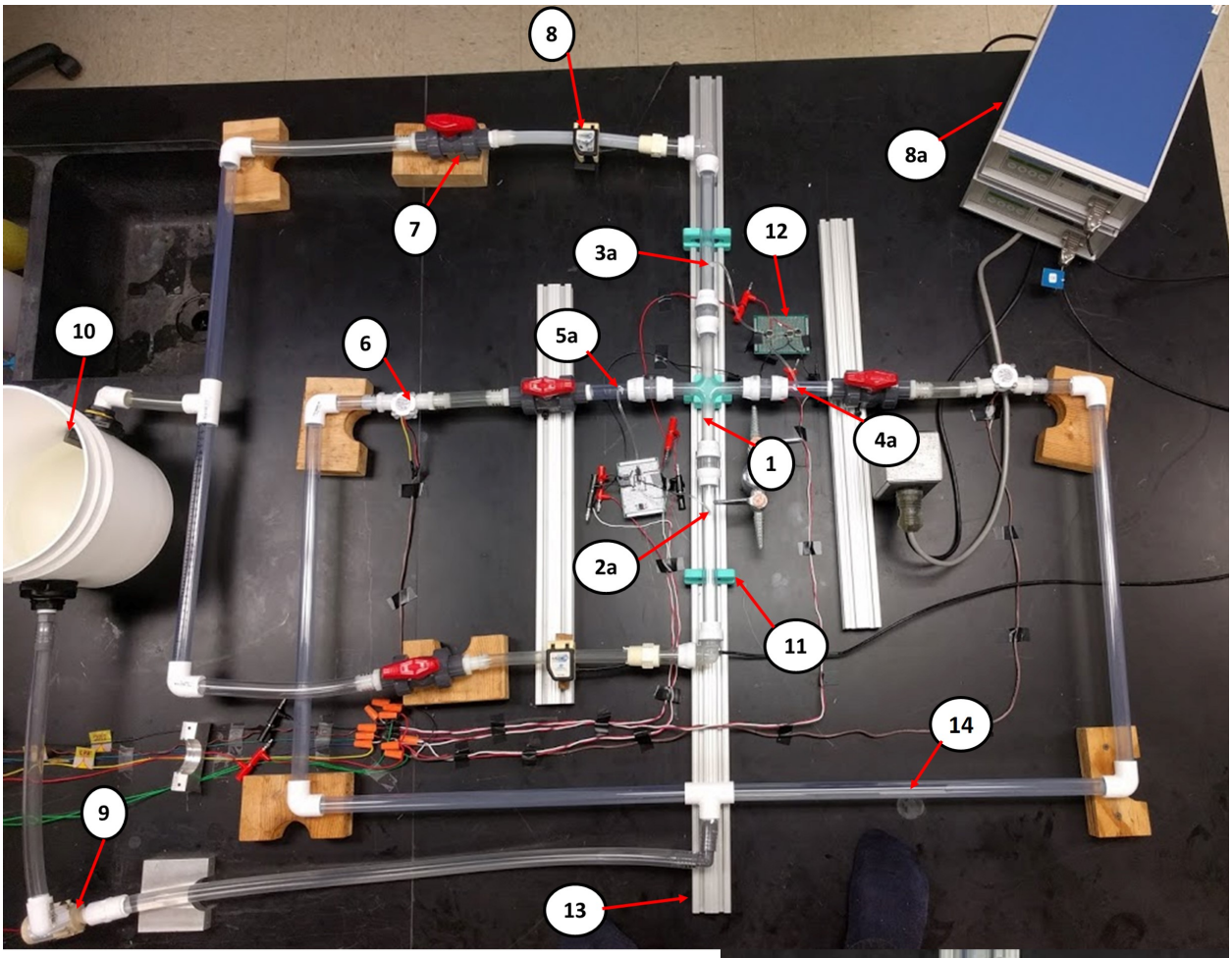

Components of Test Rig:
1) 3D Printed Flared TCPC
2) IVC Duct (2a) IVC pressure tap)
3) SVC Duct (3a) SVC pressure tap)
4) LPA Duct (4a) LPA pressure tap)
5) RPA Duct (5a) RPA pressure tap)
6) Digiten Flow Sensor
7) Ball Valve
8) Transonic Flow Sensor
8a) Transonic Flow Meter
9) External Centrifugal circulatory Pump
10) Storage Tank or Reservoir
11) 3D Printed Pipe Support Mount
12) Board Mount Pressure Sensors
13) T-Slotted Aluminium Frame
14) 1/2" Clear Schedule 40 PVC Pipe

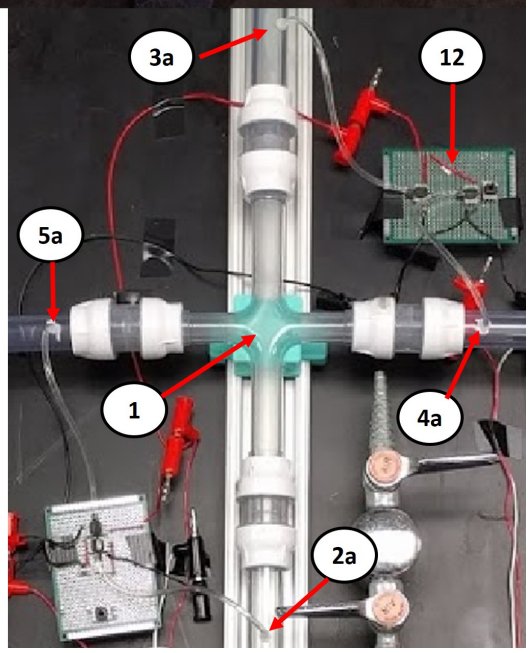

Figure 6.16: Top View of the Flared TCPC Test Setup, with the zoomed in view of the TCPC in the inset along with the component annotations listed on the bottom left

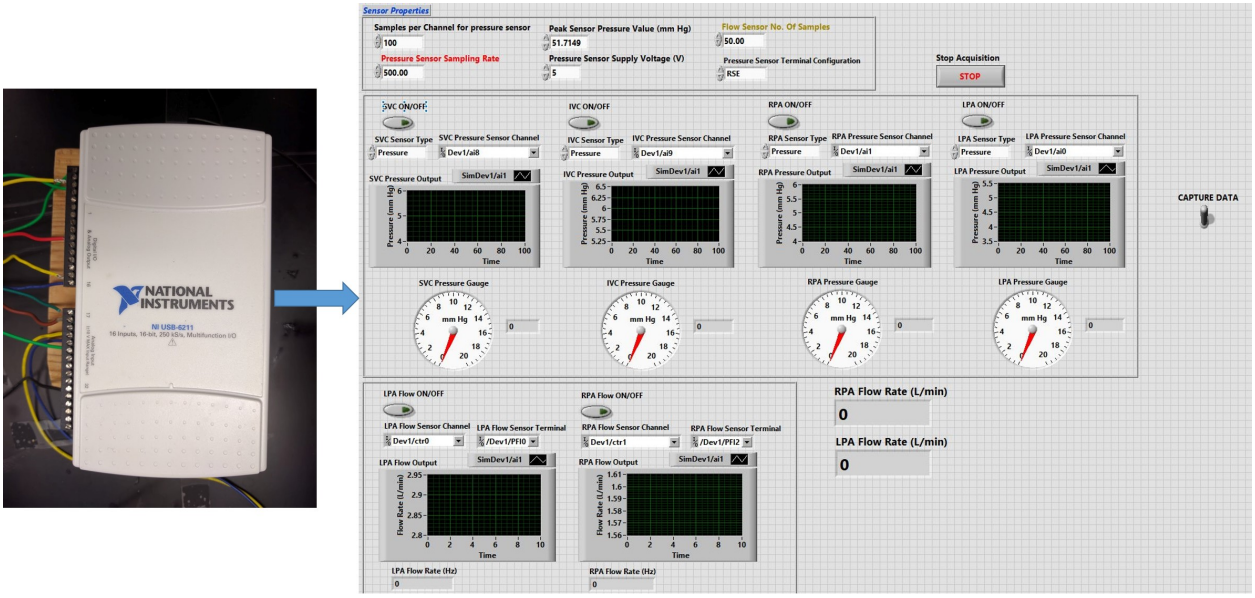

Figure 6.17: NI USB-6211 DAQ and LabVIEW Front Panel for measuring flow rate and pressures in the TCPC arms

noises and filter the signals, the RMS value of the 100 read samples is taken per second and displayed on the Pressure gauge and Flow Rate Output box.

6.7.3 Experimental Results

The first part of the experimental test was to evaluate the TCPC performance for IVC flow percentage ranging from 10% to 90% of the cardiac output or the total flow rate of 4.5 l/min. The flow rate was set by changing the external pump voltage until the required total of 4.5 l/min for the IVC and SVC flow rate shown by the Transonic flow meters is reached. Whereas, the IVC and SVC flow split was achieved using the ball valves attached to the corresponding flow conduits. For each of the cases tested, four readings were taken and a mean of the four values is presented. The power loss was evaluated for each reading using the Power loss equation 6.1, where the dynamic pressure is determined by evaluating the area average velocity from the inlet and outlet flow rate values. To simulate the flow conditions for various test cases, a series of CFD analysis were conducted for the selected Flared TCPC model by changing the working fluid in the CFD setup from blood to water. The corresponding results for both the studies are shown in Figure 6.18.

The results presented for the IVC flow split have a maximum and minimum error of 40% and 3.5% at the IVC flow of 10% and 80% respectively. It could be seen that the experimental and CFD power loss trend curve starts to deviate for lower IVC percentage flows giving maximum errors for those readings. The drifting of minima from 50% to 40% cannot be justified but could be speculated to be due to the presence of flow turbulence. Similarly,

Table 6.5: LabVIEW Default Settings and Properties of Pressure and Flow Sensors

Sensor Properties/Settings	Values
Pressure Sensor Sampling Rate	500 Hz
Pressure and Flow Sensor Supply Voltage	5 V
Pressure Sensor Peak Pressure	51.7149 mm Hg
Pressure and Flow sensor:	
Number of samples to display	100
Pressure sensor terminal mode	RSE

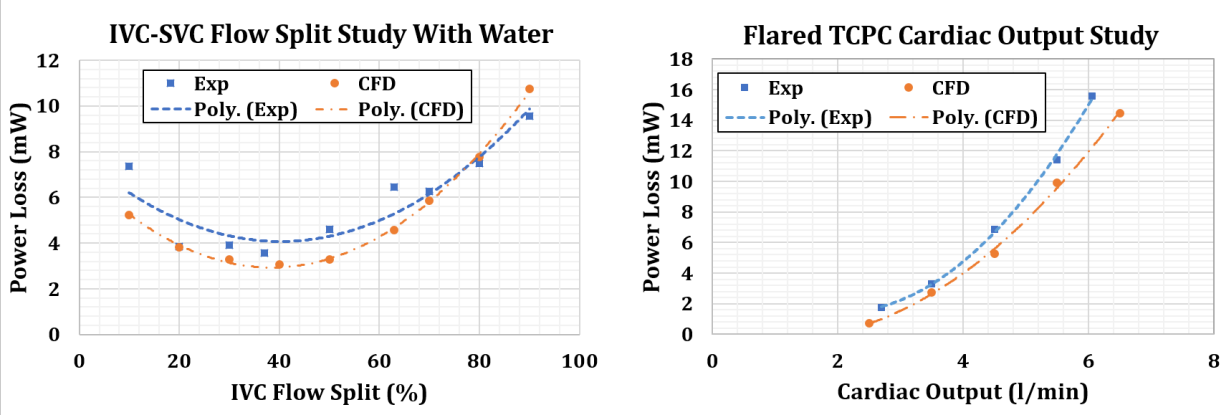

Figure 6.18: Comparison between CFD and experiemntal results for (a) IVC-SVC flow split study, and (b) Cardiac Output Study

the power loss results from the cardiac output study show a positive correlation with that observed for the numerical study with blood in section 6.6.1. For the cardiac output study, the maximum and minimum percentage error between the numerical and experimental results were found to be 23% and 13% respectively. It could be noticed that the deviation in results increased with an increase in cardiac output.

The numerical model isn't able to capture all the loses since the TCPC model used is a simplified one without incorporating any pipe diameter changes or inclusion of pipe couplings which changes the flow domain. Also, the simulation assumes a uniform flow at the inlet which would not be in case of experiments. The discrepancy visible in the comparison results between experiment and CFD is indicative of the above-mentioned losses. Moreover, the similarity in power curve trend acts as a verification for the design and at the same time serves as validation for the computational model to some extent.

This chapter illustrated the comparison and selection of optimal TCPC geometry for minimum power loss and equal IVC or hepatic flow split to both the lungs. The last part of the chapter explained the experimental setup and methodology along with verification and validation of the Flared TCPC CFD model.

Chapter 7

Design and Analysis of Percutaneous Dual Propeller Pump

The two commercially available percutaneous axial flow pumps, Abiomed Impella RP (Figure 1.9) and the Cardiobridge Reitan Catheter pump (Figure 1.10) have respectively shown promising results to assist patients with right and left ventricular dysfunction, as it was discussed in Chapter 1. However, the clinical trials of these pumps in Fontan patients showed low success given their design made for meeting different requirements rather than those of a Fontan. The dual-propeller pump design was hypothesised as a potential solution to provide a short to long-term assistance to such patients. As illustrated in Figure 7.1, the design procedure of this pump is bifurcated to first consider each component individually followed by the final assembly analysis. Since blood flow losses and distribution are one of the main concerns in traditional extra-cardiac TCPC, the author proposes to use a Flared graft at the center to connect the IVC, SVC, LPA, and RPA. The design and analysis of this was shown in Chapter 6. The Flared TCPC graft constitutes the first part of the pump design since it will be used while surgeons perform the Extra-Cardiac Fontan procedure. This chapter concerns with the design and analysis of remaining components of the dual propeller pump which will be inserted at a later stage in a patient with the Extra-Cardiac Flared TCPC.

7.1 Design and Analysis of Vena Cava Propellers

In this section, the analysis of the most critical part of the pump, i.e. blades, is performed. As introduced in Chapter 5, an inverse design methodology implementing the Blade Element Momentum theory in conjunction with the Radial Loss approximations is utilized to design the propeller blades. As shown by Miclea-Bleiziffer et al. [60], the inverse design method requires a correlation between the actual (flow through the propeller disk) and the desired flow rate (free-stream inflow at the inlet), which without any experimental data is not possible to predict. The existence of flow recirculation near the propeller blade makes it difficult to

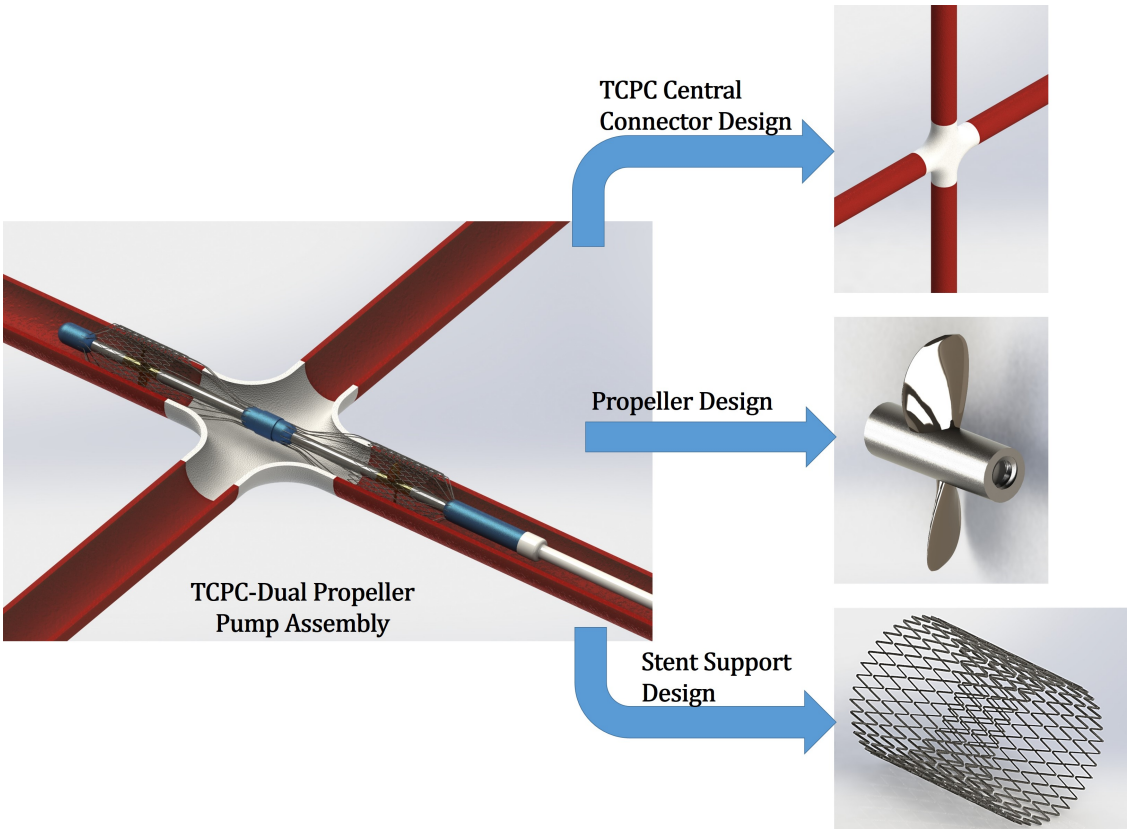

Figure 7.1: Dual Propeller Pump Assembly and its corresponding components

predict the actual flow through the propeller and requires some preliminary simulations. The initial analysis part involves iterating through the inflow rate until the required pressure rise is achieved. The iterations are initially performed only for the IVC propeller and the corresponding correlation between the propeller through flow and the free stream flow rate is applied for designing the SVC propeller.

7.1.1 IVC Propeller Analysis

Before discussing the propeller through-flow analysis results, the CFD simulation setup and mesh independence study for the selected final IVC propeller blade design is described to show the analysis procedure.

The design inputs to the VADProp code for the IVC propeller are shown in Table 7.1. It could be seen that the actual inlet flow rate through the propeller came out to be 3 times that of the desired inflow rate ($2.82\ l/min$). The desired thrust was determined from the propeller disk area ($A_d = 132.733\ mm^2$) and the required pressure rise ($5.5\ mm\ Hg$) across the propeller disk. The hub diameter was kept equal to 3 mm.

Table 7.1: Input parameters to the VADProp Code

Design Parameter	**Value**
Inflow Rate(Q_∞)	$8.4\ l/min$
Inflow(Free stream) Velocity (V_∞)	$0.8717\ m/sec$
Pressure Rise (ΔP)	$5.5\ mm\ Hg$ [$733.273\ Pa$]
Desried Thrust (T)	$0.1\ N$
Hub Diameter (D_h)	$3\ mm$
Tip Diameter (D_t)	$13\ mm$
Rotational Speed (N)	$8000\ rpm$
Fluid Density (ρ)	$1050\ kg/m^3$
Fluid Dynamic Viscoisty (μ)	$3.5\ cP$
Number of Blades (B)	2
Chord to Diameter Distribution (CoD)	CoD of 4148 Propeller $\times 1.3$
Radial Thickness Distribution (toD)	toD of 4148 Propeller with tip modifications
Airfoil Camber line profile	NACA 6 series with $a\ = 0.8$
Airfoil thickness profile	NACA 65A010 (Epps modified)

As discussed in Chapter 5, the most suitable marine airfoil series, NACA 65, was selected for the mean line or the camber line representation. In order to facilitate easy blade manufacturing, Epps et al. had modified the mean line distribution around the blade trailing edge to make it circular [101]. It was seen in Chapter 5 that the mean line was dependent on chord length, which is usually specified for a propeller series in terms of CoD (Chord to Diameter) ratio at different radial sections. The chord to diameter and maximum thickness to chord distribution is readily available for the 4148 Naval Propeller and has been previously used successfully by Kravitz to design AUV [100] and by Miclea-Bleiziffer et al. for VAD design [60]. Considering this, 4148 is used as the base propeller and its corresponding radial thickness and chord distribution are implemented for propeller design in this thesis. As shown in Figure 7.2, the local flow Reynolds number evaluated at the blade surface, for the propeller design with given 4148 propeller chord distribution shows most of the blade sections lying in the laminar flow region (Re < 2300). In order to ensure that the propeller has minimal part of the blade lying in the laminar flow region, the blade chord is increased by 30%. This is done as suggested in the thesis of Miclea-Bleiziffer et al. since it is known that drag losses are higher for laminar as compared to turbulent flows. Moreover, the only parameter to control the flow Reynolds number ($Re = \rho W c/\mu$) at propeller blade surface is the chord length since the inflow velocity (V_∞) and hence the resultant velocity (W) is fixed for the design point. The modified CoD and the Re number distribution obtained from the VADProp Code for the above-mentioned inputs is shown in Figure 7.2. It could be seen that around 80% the propeller blade ($\xi = 0.38\ to\ \xi = 0.98$) lies above the transitional flow Re number, with the laminar flow region existing near the hub and the tip of the blade. These

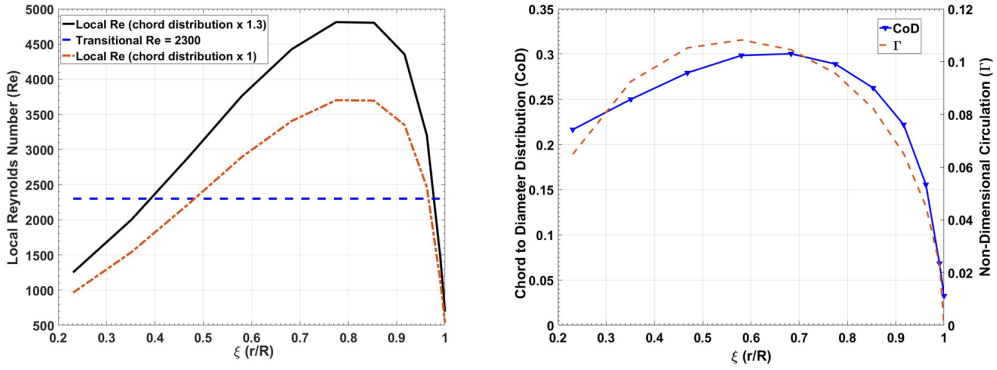

Figure 7.2: Local Reynolds Number and Circulation Distribution along Radial Direction from hub to tip of the IVC propeller

regions will, however, act as a penalty on propeller's performance. Moreover, the chord length is also decided by the availability of space within the catheter sheath to ensure blade foldability while insertion. It is known that the ideal blade circulation distribution, due to bound vortices, is parabolic along the radial direction with maxima at the center, which is also depicted in Figure 7.2 for the current IVC propeller design.

Propeller Mesh Generation

The '.curve' file generated from the VADProp code contains the coordinates of the specified number of radial sections from hub to tip as shown in Figure 7.3.

These curve files are imported into ANSYS TurboGrid which is widely used for Turbomachinery Blade Meshing. Two additional curve files are specified for the hub and the shroud which represents the bounding walls of the blade. The upstream and downstream interface surfaces are specified at a distance of 5 mm from the propeller blade. In the current case, the clearance between the blade and the shroud (IVC wall) is 0.65 mm (10% propeller radius) which is relatively high for an axial flow pump with a shroud. It was seen that using 14.3 mm as the diameter of the shroud wall resulted in negative volume and highly skewed elements in the clearance region between the blade tip and the shroud wall. However, by setting the shroud wall diameter equal to the blade tip diameter (13 mm), the regions with negative elements or elements with high aspect ratio and skewness were eliminated. Thus, it was decided to model and mesh the propeller domain in Turbogrid with shroud wall in contact with the blade tip and the annular clearance region using Ansys Design Modeler and Mesher. The geometrical representation of propeller blade in TurboGrid is done by lofting the imported blade curves in the spanwise direction. Bspline option is selected for the curve type since it results in a smooth curve by interpolating the points specified in the curve file. The same option is used for surface modeling to facilitate smooth interpolation. ATM Optimized Topology placement option is selected to create high-quality hexahedral meshes

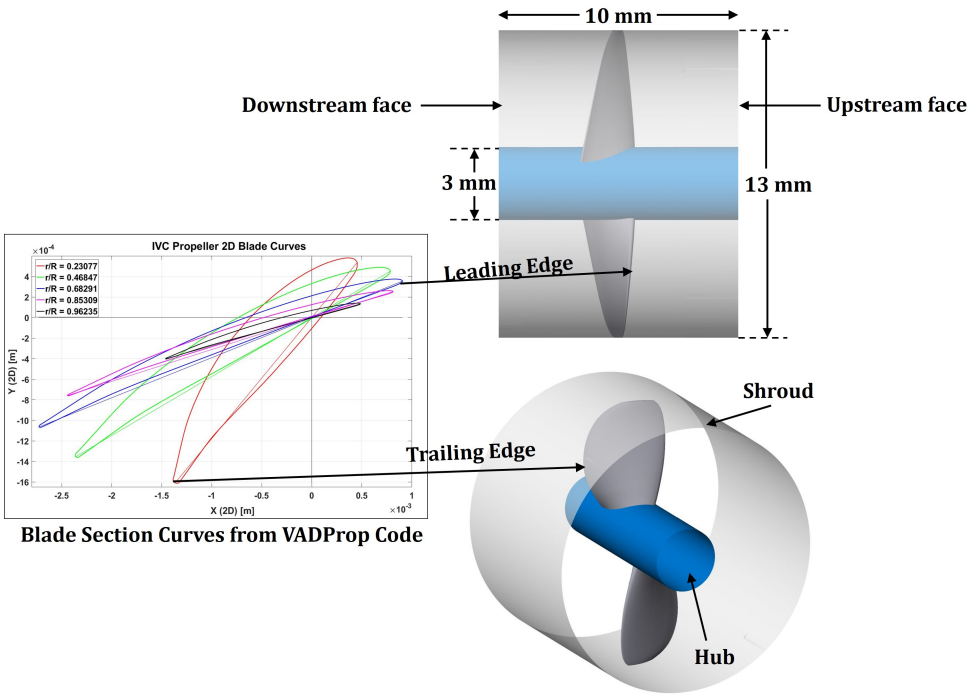

Figure 7.3: Propeller Geometry Modelled by ANSYS TurboGrid using the blade section curves obtained from VADProp Code

without any requirement for manual control.

Once the geometry is modeled and the topology is placed along different radial sections, the Mesh data is defined. As a reference for the readers, for the refined mesh used in this Thesis, the global size factor defining the element refinement was set equal to 1.5 with a Factor Ratio of 0.8 for boundary layer refinement. TurboGrid's y+ method which is dependent on the flow Reynold's number was used for specifying the near wall element size. Since the Reynolds number in this case (with rotational speed = 8000 rpm) varies from 1,130 to 21,235 (from hub to tip) a mean value of 10,000 was specified. The number of elements in the flow passage along the spanwise direction was selected by using Boundary layer method such that the estimated y+ value is <10. The resulting refined mesh had around 1 million elements and is shown in Figure 7.4.

7.1.2 CFD Setup

In order to numerically resolve the flow behaviour around the propeller and to evaluate its performance, RANS based ANSYS CFX solver was used. The CFD setup of the IVC propeller placed inside a duct with a diameter equal to that of the IVC vessel is shown in Figure 7.5. Here the inlet mass flow and outlet opening pressure are equal to the physiological values described in Chapter 2. Unlike TCPC CFD setup, the propeller setup has a rotating

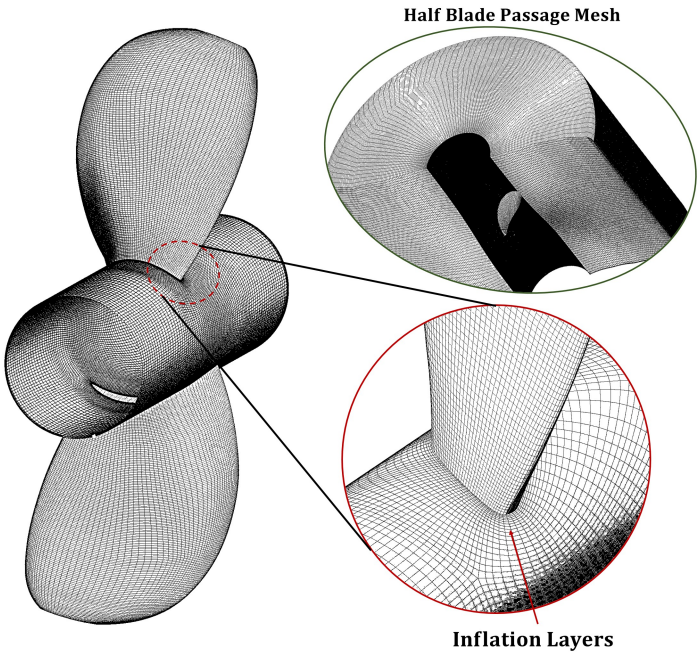

Figure 7.4: Refined Mesh for the IVC Propeller used for simulations, Inset: (bottom) Grid showing inflation layers near the blade boundary, (top) Refined mesh for half blade passage volume

part in the flow domain which requires the domain to be divided into 2 parts: a stationary domain (inlet and outlet duct) and a rotating domain (propeller and shroud). It is assumed that the propeller is attached to a rotating shaft of 3 mm diameter extending upstream and downstream of it as shown in the setup. The grids for the inlet duct, the outlet duct, and the shroud are generated using ANSYS Meshing Module. The meshes at the interface of two domains are connected using GGI (General Grid Interface) connection which is used for establishing a connection between two dissimilar meshes.

The interface between the propeller upstream, downstream wall and the inlet, outlet duct is modeled using Frozen Rotor model which connects the two a rotating and a stationary domain such as to have a relatively fixed position throughout the simulation. Since the entire upstream, downstream and shroud surface of the propeller (rotating) domain is in contact with the corresponding inlet, outlet duct and the clearance domain inner wall, a pitch angle of 360° is specified at the interface. The length of the inlet and the outlet duct is kept equal to 100 mm. Since the maximum flow Reynolds number (evaluated at the tip) is 21,235, which is $< 10^5$, the flow isn't in the turbulence regime, however, the turbulence is expected to be introduced downstream of the propeller. As discussed in Chapter 4, the SST turbulence model with automatic wall function is used to resolve the flow boundary layer near the wall and free shear flow near the core and have been widely adopted by VAD designers as mentioned in the review study done by Fraser at al. [89]. The CFD setup parameters and the corresponding boundary conditions are listed in Table 7.2.

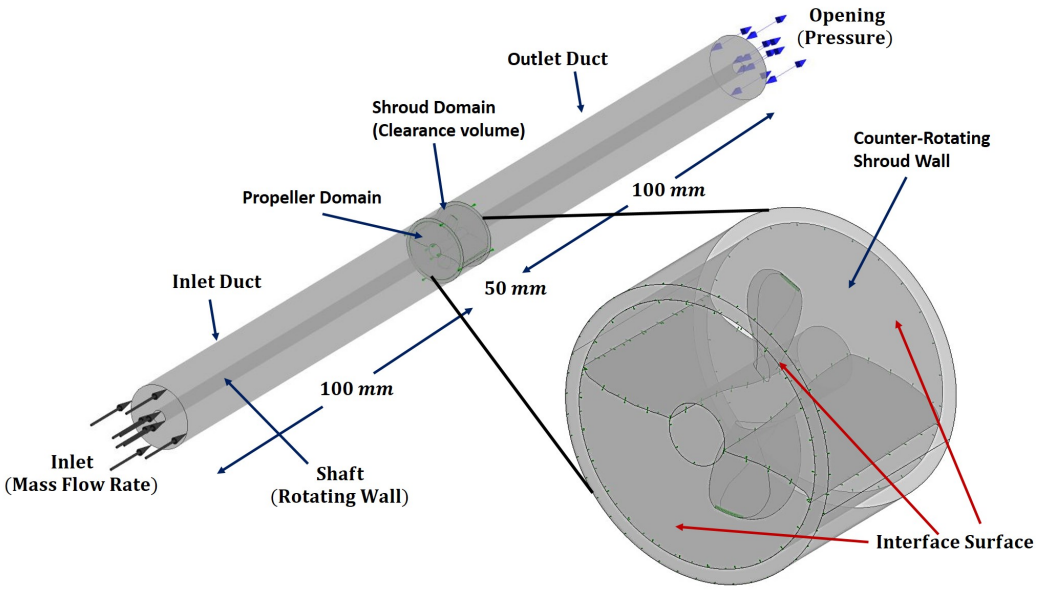

Figure 7.5: IVC Propeller CFX Setup

Here, since the shroud domain outer wall is stationary but is included in the rotating domain, a counter-rotating wall boundary condition is specified at that location. In order to achieve higher numerical accuracy, a high-resolution advection scheme is used to solve for the advection term $(u.\nabla)$ in the RANS equation. The convergence of the solution is monitored according to the criteria set for TCPC simulation mentioned in section 6.3. However, in this case, the monitor points are the pressure rise and the blade torque instead of power loss.

Table 7.2: IVC Propeller CFD Setup Boundary Conditions

Boundary	Boundary Condition	Parameter Value
Inlet Duct Inlet	Inlet: Mass Flow Rate	0.04935 kg/sec
Outlet Duct Outlet	Opening: Pressure	12.8 mm Hg
Inlet Outlet Duct Wall	No Slip Wall	
Propeller Blade, Hub Wall	No Slip Wall	
Shroud Wall	Counter Rotating Wall	
Shaft Wall	Rotating Wall	8000 rpm

7.1.3 Grid Independence Study

In order to ensure that the results obtained from the CFX solver are independent of the propeller mesh element size or the grid size, a mesh independence study was conducted. As mentioned above the convergence criteria for the RMS of the residuals was set to 10^{-4} while

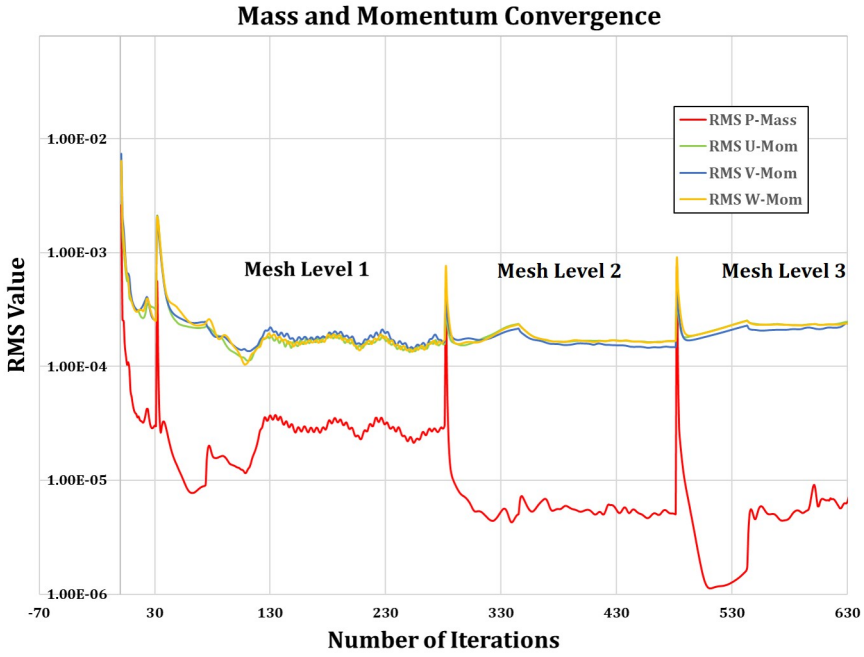

Figure 7.6: Mesh Convergence Monitor showing convergence of mass and momentum solution residuals

ensuring the monitoring points: Pressure Rise (ΔP) and the Blade Torque (Q) approach a constant value with fluctuations less than 5% of the mean value. Table 7.3 shows the rotor grid elements and the corresponding propeller performance parameters. The percentage error in the values for pressure rise and blade torque between the fine and medium mesh is only 0.737% and 0.86% respectively confirming an independent mesh solution. It is worth noting that, the RMS values of mass and momentum residuals failed to reach the value of 10^{-4} as depicted in Figure 7.6, instead, they reached a constant plateau between 10^{-3} and 10^{-4} with minor fluctuations signifying a converged solution.

Table 7.3: IVC Propeller Mesh Convergence Study

Global Size Factor	**Number of Elements in Blade Passage**	**Pressure Rise (ΔP) [mm Hg]**	**Blade Torque (Q)**
1.3	303200	5.6461	0.21
1.5	993960	5.467	0.20466
1.8	2399320	5.427	0.2029

It was previously shown that the maximum Reynold's number existing within the flow domain is less than the transitional value to consider the flow to be fully turbulent and hence SST turbulence model was used. As discussed in Chapter 4, the mesh y^+ value is a critical

parameter determining the size of the nearest element to the wall which is used by the solver to decide whether to solve for the boundary layer flow or approximate it using the law of wall. In order to achieve an accurate solution, it is necessary to resolve the boundary layer and hence have a y^+ value of at most equal to 10. As shown in Figure 7.7, the y^+ contour on the IVC propeller and the shroud wall evaluated in CFX-Post has a maximum value of only 7.926 at the shroud wall and 4.616 at the propeller blade wall near the tip of the leading edge. This is expected since the highest velocity gradients are experienced at the blade tip and leading edge. This ensures that the mesh has adequately fine elements near the wall to resolve the boundary flow and provide good accuracy of results.

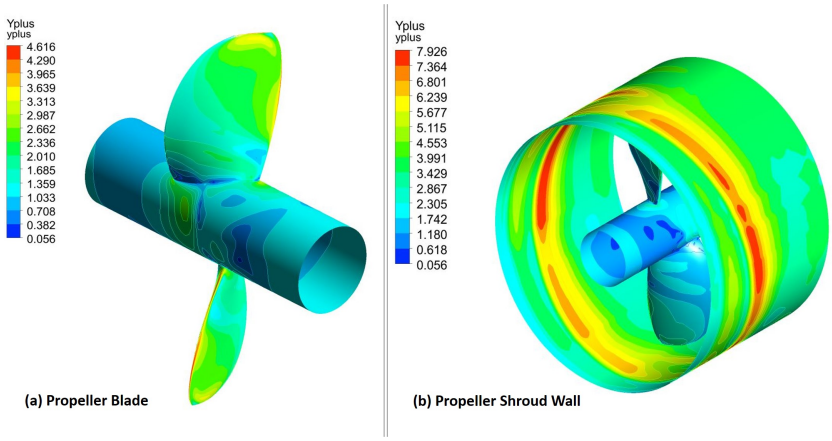

Figure 7.7: IVC propeller blade and shroud y^+ contour for the final refined mesh

IVC Propeller Through Flow Analysis

It was seen in Chapter 5 that the thrust developed by the propeller is given by the product of mass flow through the propeller and the change in momentum between the inlet and the outlet. This mass flow rate through the propeller is dependent on the inflow velocity by an axial interference factor 'a'. However, it is difficult to predict the actual value of inflow velocity to be given to the VADProp code without pre-knowing the relation between free stream and propeller through flow velocity. Thus an initial design was done with the same input parameters as those mentioned in Table 7.1, by changing the inflow rate to the physiological value of $2.82\ l/min$. The corresponding inlet flow velocity is computed by dividing the flow rate with the area of the duct (with 14.3 mm diameter). The pressure rise obtained for this design was 518 Pa [3.885 mm Hg] which was less than the desired pressure rise of 5.5 mm Hg. Now, in order to determine the flow through the propeller blade, a circular plane perpendicular to the flow is constructed along the rotational plane of the blade as shown in Figure 7.8. According to Miclea-Bleiziffer et al. [99], the through-flow rate is determined by applying the $massFlowAveAbs$ function in CFX-Post on the axial flow velocity and then multiplying the determined value with the blade circular disk area (with diameter = 13

Table 7.4: Performance of IVC propeller models designed using different inlet flow rate design inputs to the VADProp code

IVC Propeller Model	**Inflow Rate input to VAD Prop code [l/min]**	**Through Flow Rate from CFX [l/min]**	**Pressure Rise ΔP [mm Hg]**
Initial Model	2.82	6.99	3.885
Model 2	5.64	7.4959	3.946
Model 3	8.4	7.455	5.47
Model 4	10	7.936	6.477
Model 5	14	8.148	7.884

mm). The corresponding value obtained for this initial design was $6.99\ l/min$ suggesting to increase the inlet flow rate in the propeller design code to nearby or higher than the obtained value. In order to evaluate this effect, a study was done for four different inlet flow rates specification to the VADProp code to design four propellers. The CFD setup and boundary conditions are kept same as that described in section 6.3. The specified through-flow rate and the corresponding pressure rise between the inlet and the outlet for the four propeller models along with the initial design is shown in Table 7.4. It could be seen that the flow rate across the propeller disk is almost constant varying between $7\ l/min$ to $8\ l/min$, while the pressure rise is increasing with the flow rate. This is obvious given the thrust and hence the pressure rise is proportional to the through-flow rate. It could be seen that the Model 3 (highlighted in blue), with an input flow rate of $8.4\ l/min$ to the VADProp code, the designed propeller was able to give the desired pressure rise ($\approx\ 5.5\ mm\ Hg$) which corresponds to an increment factor of 3 with respect to the free stream flow rate ($2.82\ l/min$). In this way, $8.4\ l/min$ was determined as the final inlet flow rate (or inlet velocity) input to be given to the VADProp code for designing the IVC propeller. Using the same increment factor gives an inlet flow rate of $5\ l/min$ for designing the SVC propeller with the other design parameters same as those mentioned in Table 7.1.

The reduction in the through-flow rate across the IVC propeller could be attributed to the flow recirculation occurring around the blade hub and tip region as shown in Figure 7.8. These recirculations increase as the through flow rate and hence the pressure rise across the propeller blade increases. Note that the axial velocity vectors depicted in the figure are projected from the through flow plane circumscribing the propeller blades and hence the flow recirculation experienced in the clearance region between the blade tip and the shroud(or pipe) wall is not captured. This is the reason why it is difficult to predict the actual flow rate across the propeller without doing the preliminary analysis, the recirculating flow behaviour will be explained in detail in the following section while analysing the performance or the head characteristics of the IVC and SVC propellers.

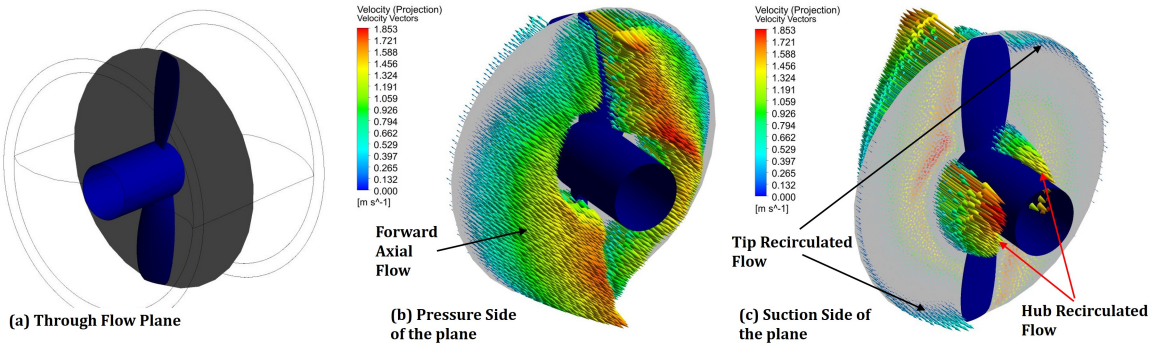

Figure 7.8: Through flow plane constructed along the rotational plane of the IVC propeller with the hub and tip recirculation visible on suction side and forward flow on the pressure side of the plane

7.1.4 Propeller Performance Characteristics

The final IVC and SVC propeller blade curves generated using the inlet flow rates obtained in the previous section are shown in Figure 7.9. The IVC propeller is seen to have a higher twist as compared to the SVC propeller (compared by looking at the coordinates of the leading and trailing edge of the two propellers) since it has to generate same pressure but at a higher flow rate (2.82 l/min as compared to 1.68 l/min in case of SVC propeller).

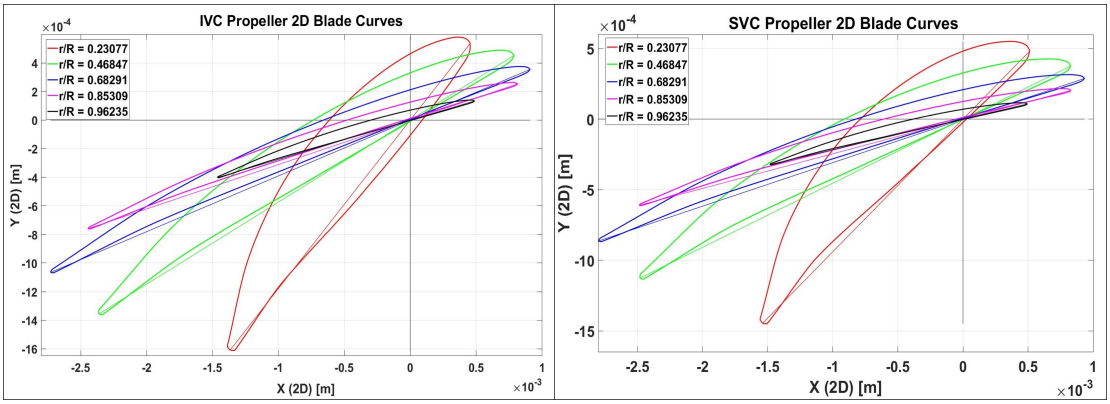

Figure 7.9: IVC and SVC Propeller Radial Sectional Blade Curves

As discussed in Chapter 5, the parameters defining the propeller performance are the Thrust coefficient (C_T), Power Coefficient (C_P), the advance ratio ($J = V/nD$) and the propeller efficiency ($\eta = J(C_T/C_P)$). All these parameters are related to the amount of pressure generated by the propeller at a particular flow rate and rotational speed. In the current case, in order to determine the hydraulic performance of the propellers, the inlet flow rate and the propeller rotational speed is varied from 1-7 l/min and 6000-12000 rpm respectively in the CFD setup described in section 7.1.2. The output parameters evaluated were the pressure

rise (ΔP) between the inlet and the outlet and the blade torque (Q_b). The efficiency is then determined using the formula:

$$\eta = \frac{\Delta P Q}{Q_b\, \omega} \times 100 \tag{7.1}$$

In the above expression, Q refers to the volume flow rate specified at the inlet. It can be seen from Figure 7.10 that the hydraulic performance of the IVC and SVC propeller is similar to an axial flow pump showing an inverse relationship between the flow rate and the pressure rise.

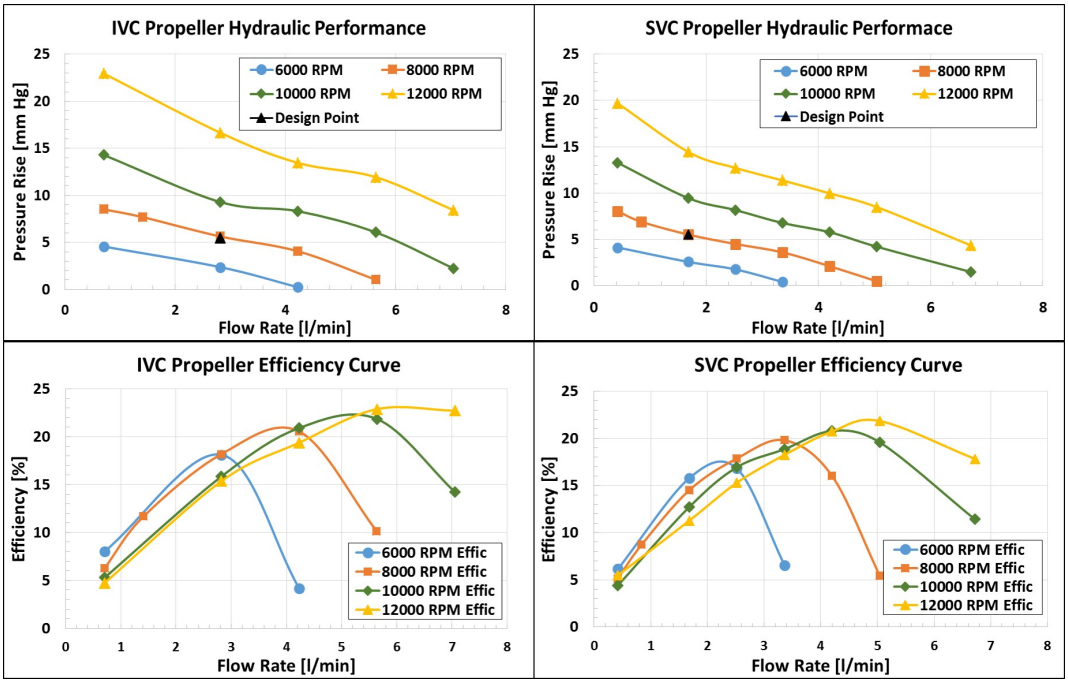

Figure 7.10: IVC and SVC Propeller Hydraulic Characteristics

Both IVC and SVC propellers are seen to provide the pressure rise as that specified for the design point. An important phenomenon to notice here is that the pump efficiency is too low, with a maximum of only 23% for IVC propeller and 22% for SVC propeller. This can be attributed to the small propeller size which causes the viscous effects to overpower the inertial effects. In marine propellers, the blade size is large enough to induce enough inertial forces in the liquid to overcome the viscous losses. Moreover, the parabolic variation of efficiency curves is also commonly seen in axial flow pumps. This behaviour is due to the higher dissipative losses at higher flow rates and higher recirculation losses at lower flow rates. To understand this, a comparison is done between the velocity streamlines of IVC propeller rotating at 8000 rpm and operating at a flow rate of 0.705 l/min and 5.64 l/min. As illustrated in Figure 7.11, the high suction created upstream of the propeller at low flow rate engulfs the incoming flow causing the streamtube to condense into a conical tube. The high

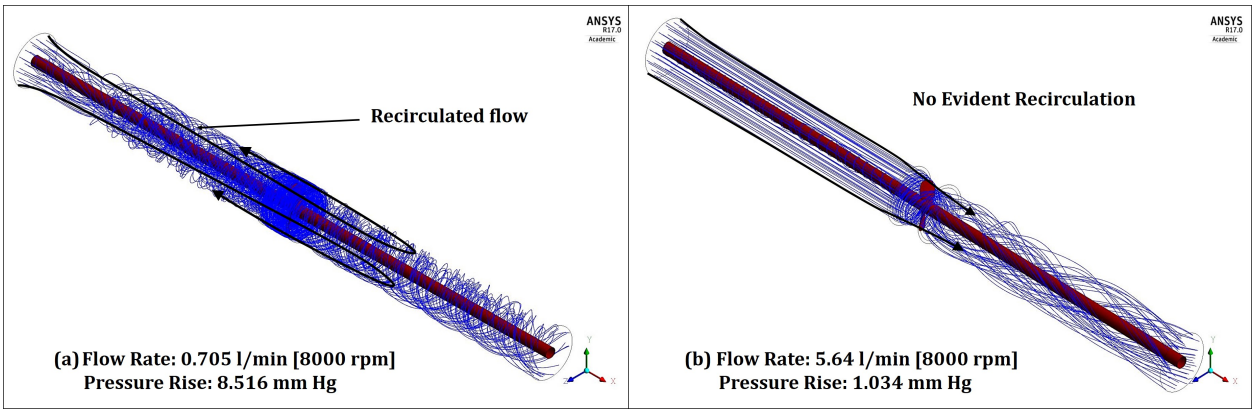

Figure 7.11: IVC Propeller velocity streamlines with evidence of recirculation at 0.705 l/min, and no evidence of reciculations at 5.64 l/min (at design speed of 8000 rpm)

pressure gradient across the propeller blade and the natural tendency of any fluid to flow from higher to lower pressure region forces some part of the flow to move in the backward direction. The hub and the tip of the propeller are the target zone for the flow recirculation since they have the least amount of lift generating capability due to the low circulation in those areas as it was depicted in Figure 7.11. As a result, the propeller has to spend more energy to maintain the required flow rate and pressure rise. In contrast to this, at higher flow rates the pressure gradient across the propeller is too low to condense the streamtube which converges upstream into the propeller only once it reaches within the vicinity of propeller blades as shown in Figure reffig:ivcpropellerstreamlinesrecirculations. Here, the propeller has to do less work due to minor recirculation, however, a large amount of energy will be expelled by the propeller on working against the viscous (frictional) losses which are significant at higher flow rates. In this way, the IVC and SVC propeller pumps are able to provide a pressure rise of around 1 to 22 mm Hg for a flow rate ranging from 0.4 to 7 l/min while rotating at 6000 to 12000 rpm.

The variation in pressure at the design point for SVC propeller is shown in Figure 7.12 in terms of a contour plot on the longitudinal plane. The pressure variation along the axial direction, computed by taking area average pressure at 10 sections from the inlet to the outlet, illustrates the jump in pressure across the propeller disk as that experienced in actuator disk. Similar behaviour was also observed for the IVC propeller.

Before proceeding forward, it is worth highlighting the effect of blade pitch and blade number on propeller performance. In order to study this, an addition was made to the VADProp code to change the blade pitch to a desired value by rotating all the blade sections equally in either positive (away from the inflow) or negative (towards the inflow) direction. For the pitch study, the pitch angle for the IVC propeller was varied from -10° to 20° in steps of 10° whereas, for the blade number study, IVC propeller with 2, 3, and 4 blades were analysed. All the analysis were done at the physiological inlet flow rate and at a design speed of 8000 rpm. The corresponding results are shown in Table 7.5 and 7.6. It can be seen that increas-

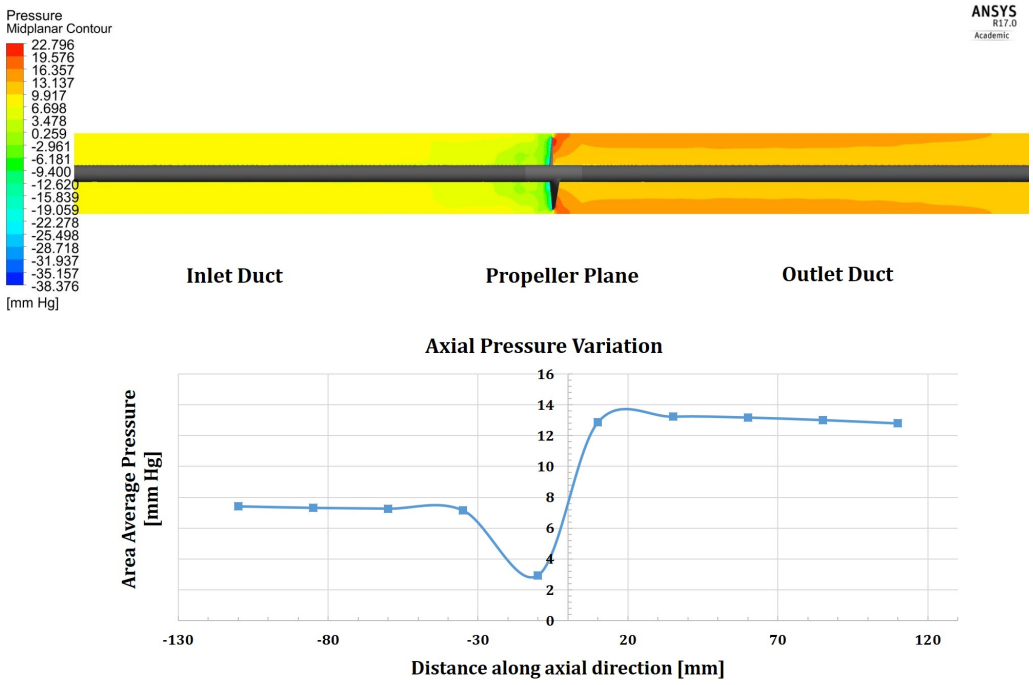

Figure 7.12: Pressure variation in SVC propeller at design point along on logitudinal plane and along axial flow direction

ing the pitch angle with respect to the base model increases the pressure rise, however, the efficiency is maximum for the bade angles computed initially at the design point using the Blade element momentum theory [for the Base Model], showing that increasing the pitch angle and diverting from the design point might increase the pressure rise but at an expense of operating efficiency. The study performed to evaluate the effect of the number of blades showed that increasing the blade number increased the propeller performance. This is observed since the blade solidity increase as the blade number is increased and it approaches closer towards the actuator disk with an infinite number of blades thereby producing higher thrust and pressure rise. Although this parametric study is not of any relevance for this thesis, it is a good source of information for readers interested in designing a controllable pitch propeller based VAD.

7.2 Experimental Setup and Testing

In order to gain confidence in the propeller design and reliably acknowledge its performance obtained from the numerical simulations, a series of experimental tests evaluating the propeller performance characteristics are conducted. An experimental test rig constructed to test the IVC and SVC propeller prototype is shown in Figure 7.13. This setup, like the one

Table 7.5: IVC Propeller Pitch Change Study

Angle of Rotation of the Blade [degrees]	**Pressure Rise [mm Hg]**	**Efficiency [%]**
-10	0.911	14.897
0 [Base Model]	5.47	17.329
10	10.06	15.694
20	11.435	10.066

Table 7.6: IVC Propeller Blade Number Study

Number of Blades	**Pressure Rise [mm Hg]**	**Efficiency [%]**
2 [Base Model]	5.47	17.329
3	6.382	21.4748
4	6.848	21.994

constructed for testing TCPC, is made by connecting the Clear 1/2" Schedule 40 PVC pipes with push on slip couplings for easy assembly and modifications.

7.2.1 Materials and Methods

The IVC and SVC propellers prototypes to be tested are manufactured to scale using the Formlabs Form 2 Stereolithography (SLA) 3D printer. The Formlabs Photopolymer Tough Resin (FLTOTL04) is used for printing the propellers. The propellers printed using the curve file obtained for the design inputs shown in table 7.1 created blade sections that were too thin to withstand the pressures acting on the blade. The fragile nature led to breaking of the blade at its hub which experiences the maximum bending stress. To increase the blade strength, the propeller blade thickness was increased over the original thickness distribution available for 4148 Naval Propeller (Listed in Appendix A) while providing a fillet at its base (or hub-blade interface) as shown in Figure 7.14. An increase in thickness acts as a penalty on propeller's performance due to higher flow losses. Hence a study was done to evaluate the reduction in pressure rise with an increased propeller blade thickness. The three blade thickness values considered were 1.2, 1.6 and 2 times the original thickness distribution. It was found that the pressure reduced by approximately 50 Pa (or 0.375 mm Hg) for a twice thick blade and by around 25 Pa (or 0.1875 mm Hg) for 1.6 times thick propeller blade. For 1.2 times blade thickness, the propeller gave almost the similar performance with around 5 Pa (or 0.0375 mm Hg) pressure reduction. Considering the insignificant amount of losses and the need for strengthening the propeller at high rotational speeds a mid value of 1.6 was considered as an incremental factor for the blade thickness.

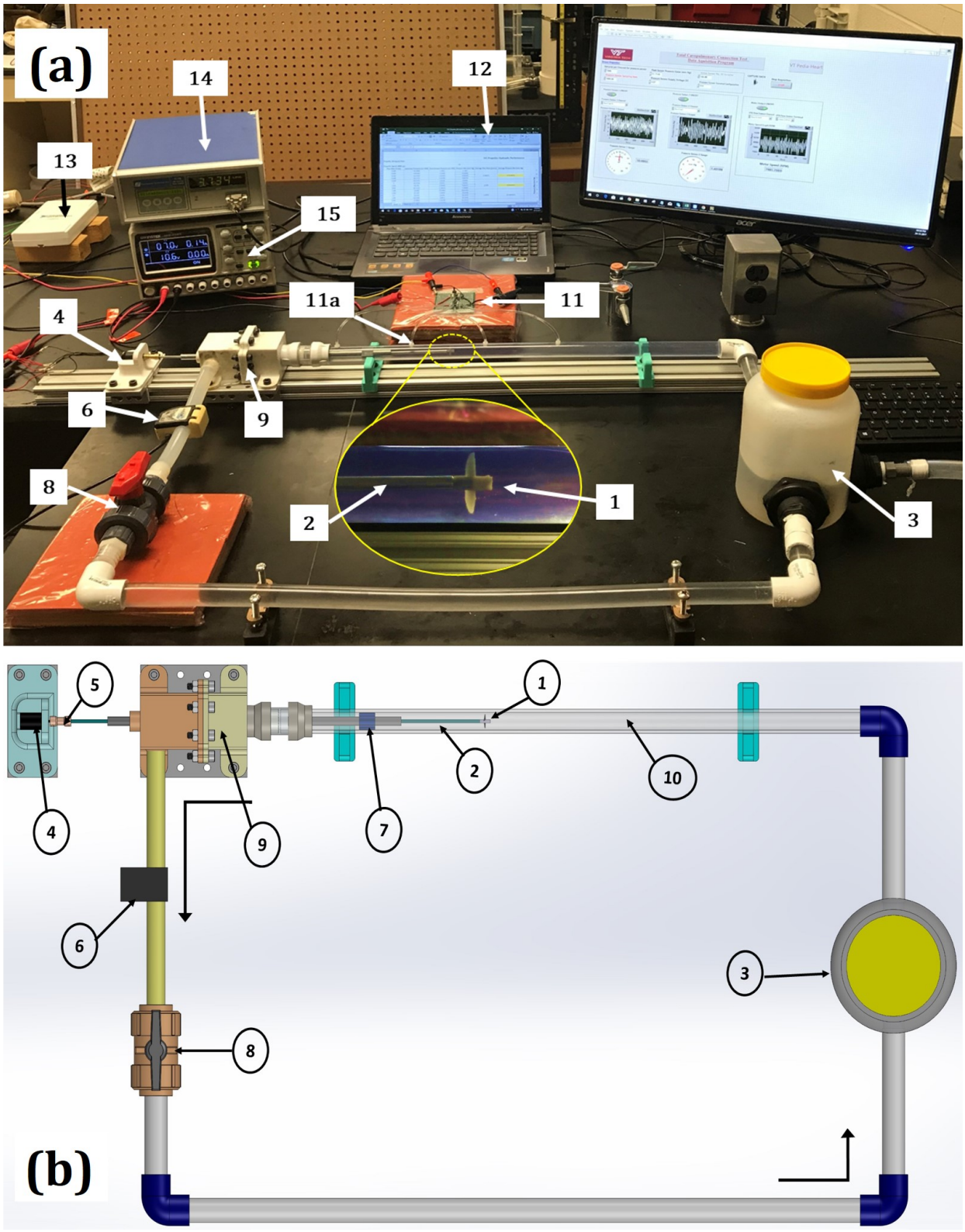

Figure 7.13: (a) Experimental Test Setup for single propeller hydraulic testing, and (b) a schematic diagram for the same

Table 7.7: Component corresponding to the annotation number in test setup

Components of Test Setup	
Annotation No.	**Component**
1	Propeller
2	Propeller Shaft
3	Liquid Storage Container
4	BLDC Motor
5	Motor-Shaft Coupler
6	Transonic Flow Sensor
7	Flow Straightner
8	Valve
9	Settling Chamber Assembly
10	1/2" Clear PVC Pipe
11	Board Mount Pressure Sensor
11a	Pressure tap
12	Data Visualization and Recording
13	NI DAQ
14	Transonic Flow Meter
15	DC Power Source

To mount the propellers on the rotary shaft, M2 right-handed female threads were incorporated in the design as shown in Figure 7.14. This was done since cutting threads into a 3D printed propeller had a high risk of shattering the resin which is brittle. The 3D printed IVC propeller along with its corresponding 3D model compared in Figure 7.14, shows that the quality of the 3D printed propellers wasn't the best with some irregularities at the blade tip and blade edges. These are the points where the support structures added to facilitate the printing process are attached. These support structures leave a small bead of material at the point of contact which needs to be delicately filed or removed to smoothen the blade surface.

A 400 mm long stainless steel shaft of 3 mm diameter, same as that of the propeller hub diameter, was machined at one end to add male M2 threading to mount the propeller onto it. The shaft was supported inside a hollow tube or a stainless steel shaft sleeve having an inner and outer diameter of 4 mm and 8 mm respectively. The propeller shaft is supported inside the shaft tube with the help of 2 radial stainless steel ball bearings, each press-fitted at each end of the tube. The other end of the shaft was coupled to the BLDC motor with a rigid coupler shown in Figure 7.15. The primary driver selected for the propeller was a 12 V 1525U012BRC Brushless D.C. motor (Faulhaber Inc, Micromo, Clearwater, Fl, USA) having a speed range of 1,000-16,000 rpm and maximum torque of 1.8 mNm. The motor is integrated with a built-in speed controller which gives frequency output to monitor the motor speed. The motor sends three pulses per revolution, which can be used to determine

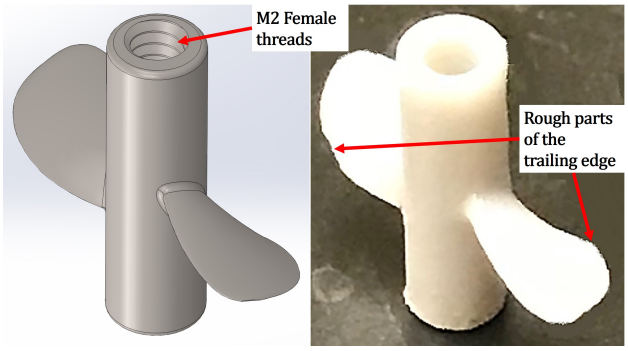

Figure 7.14: 3D CAD model and the corresponding 3D printed resin model of the IVC Propeller

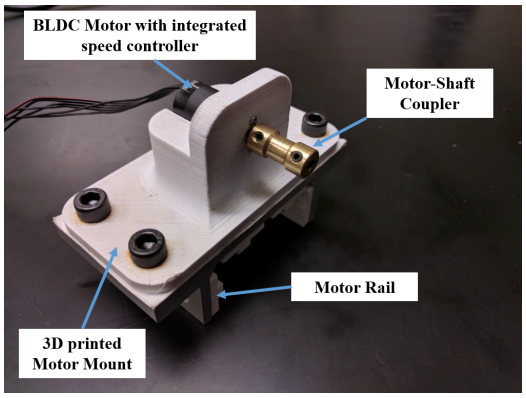

Figure 7.15: BLDC Motor with rigid shaft coupler housed in a 3D printed mount

the relationship between frequency and rpm as given by:

$$Motor\ Speed\ (RPM) = \frac{Frequency\ Output \times 60}{3} \tag{7.2}$$

In order to align the motor and the propeller shaft, a PLA based motor mount, shown in Figure 7.15, having its axis aligned with the pipe axis is 3D printed using the Fused Deposition Modeling (FDM) additive manufacturing technique. The mount was printed fairly accurate to house the motor and mount itself on the rail which slides on the T-slotted aluminum frame displayed in the test setup picture. The additional adjustments in height were achieved using thin plastic shims that helped raise the mount until the required height was achieved. Similar minor adjustments in the lateral direction were made possible by using a lever and a bolt to laterally push the railing on either side.

In order to have minimal obstruction to the flow downstream and upstream of the propeller, the propeller was located away from the shaft tube as shown in Figure 7.13. Keeping the propeller close to the shaft sleeve (having an outer diameter of 8mm) would change the flow physics and also block the propeller flow since it would cover half of the blade span. As a result, it was decided to extend the propeller shaft away from the shaft tube. The length of

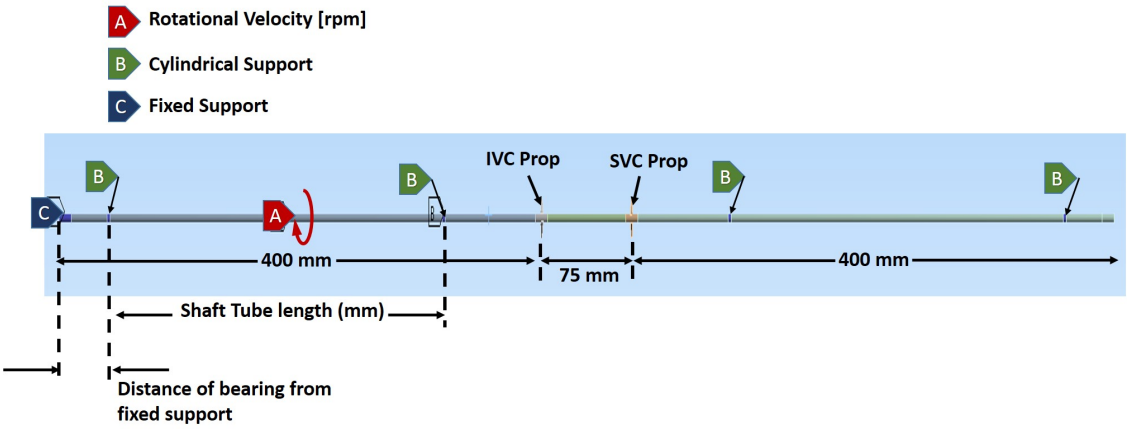

Figure 7.16: Dual Propeller Shaft system modal analysis setup in ANSYS APDL

the overhanging part of the shaft and the part inside the shaft tube was computed so as to avoid any resonant vibrations at the design speed or close to the design shaft speed of 8000 rpm.

The evaluation was done by keeping in mind that the same shaft and tube arrangement will be used for the dual propeller configuration with an additional central shaft connecting the two propellers. Since the hollow tube and propeller shaft has to be long enough to locate the propeller close to the middle of the test section, it would potentially create long segments of shaft either between the two bearings inside the sleeve or for the part extending outside the sleeve into the test section. To analyse the natural frequency for different shaft-tube length combinations, a parametric Modal analysis was performed in ANSYS APDL. The boundary conditions given were a fixed support to the part connected to the motor and cylindrical support to the four surfaces in contact with the bearings, with the stainless steel material properties assigned to the shaft. The analysis was performed at rotational speeds varying from 2000 rpm to 14000 rpm with an increment of 2000 rpm. The input parameters defined for the study were the length of the shaft between motor and the tube and the shaft tube length. The length of the central shaft was kept equal to 65 mm. The aim was to achieve the 1st natural frequency of the system above and away at least $\pm 20\%$ of 8000 rpm while also ensuring the propeller is kept away from the shaft tube. The output of this study is shown in Figure 7.17. It could be seen that the maximum 1st mode natural frequency was achieved for three different values of shaft-motor segment length but for the same tube length of 280 mm. The shaft-motor section length of 40 mm was selected since that allowed a maximum propeller overhang of 80 mm (given the total shaft length is 400 mm). The analysis was also performed for the configuration with a single propeller and it was found that the same amount of overhang and tube length gave the same 1st mode frequency thereby allowing us to operate safely, without any vibrations, at 8000 rpm.

The presence of curvatures, fittings, baffles, valves, and sensors in the flow loop tends to make the flow nonuniform and chaotic before it reaches the test section, thereby preventing

	A	B	C	D	E	F
1	Name	Update Order	P1 - Bearing2_Plane1.FD1	P2 - Shaft_Tube_Length	P3 - Mode-1	P4 - Mode-2
2	Units		mm	mm	rev min^-1	rev min^-1
3	DP 0	1	40	300	9020	9020
4	DP 1	2	40	180	3172.1	3175.7
5	DP 2	3	40	200	3885.9	3889.9
6	DP 3	4	40	220	4881	4885.4
7	DP 4	5	40	240	6330.7	6335.6
8	DP 5	6	40	260	8561.8	8567.1
9	DP 6 (Current)	7	40	280	10377	10377
10	DP 7	8	20	300	9020.4	9020.5
11	DP 8	9	30	300	9020.4	9020.5
12	DP 9	10	60	300	9020	9020
13	DP 10	11	20	280	8561.8	8567.1
14	DP 11	12	30	280	10157	10163
15	DP 12	13	60	280	10377	10377
16	DP 13	14	40	290	9663	9663
17	DP 14	15	40	270	10157	10163
18	DP 15	16	55	280	10377	10377
19	DP 16	17	65	280	10378	10378

Figure 7.17: Dual Propeller Shaft Parametric Modal Analysis Results for studied candidate design points with the selected point highlighted in red.

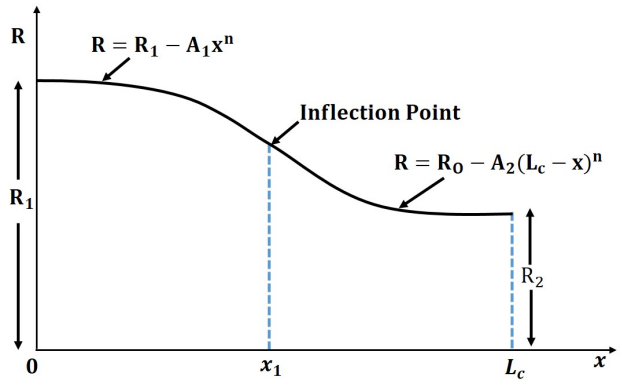

Figure 7.18: Converging Cone wall contour notation and empirical relation

observation of good quality readings from the tests. To improve the flow quality, a settling chamber consisting of a Honeycomb structure, and a converging cone or nozzle depicted as two rectangular flanges are incorporated in the test setup. The honeycomb structure removes the inflow swirls and acts as a flow straightener while the converging tube helps to make the flow uniform while accelerating and aligning the flow along the axis of the tube. The honeycomb structure and the converging tube were designed according to the guidelines listed by Barlow et al. and Watmuff et. al. [106, 107]. In order to fit the settling chamber and the contraction cone on the 100 mm rail, the length of both the blocks was kept equal to 50 mm. The length of the Honeycomb mesh inside the settling chamber was kept equal to half of the settling chamber length with the honeycomb hexagon cell size determined by using the length of the honeycomb mesh to cell size ratio of 7. The recommended value for minimum losses was between 6 to 8 and hence a mid value was selected for this case [106, 107].

Similarly, the converging cone having the length to inlet diameter ratio of 0.5 was designed with the radius of curvature for the concave and convex part defined by equations given by Watnuff et. al. as illustrated in Figure 7.18. Here R_1 represents the inlet radius to the cone which was same as that of the length of the cone (=17.5 mm). The inflection point was selected to lie at the midway of the cone and the outer radius (R_o) was kept equal to the 1/2" pipe diameter (=15.29 mm) into which the cone will be opening. The terms A_1 and A_2 represents the circular sectional area at the inlet and the outlet. Watmuff et al. found that for n = 3, in the curvature radius equation, the cone provided minimum adverse pressure gradient and hence minimum chances of flow separation and as a result, the same value of n was used for the designing the cone curvature in this case.

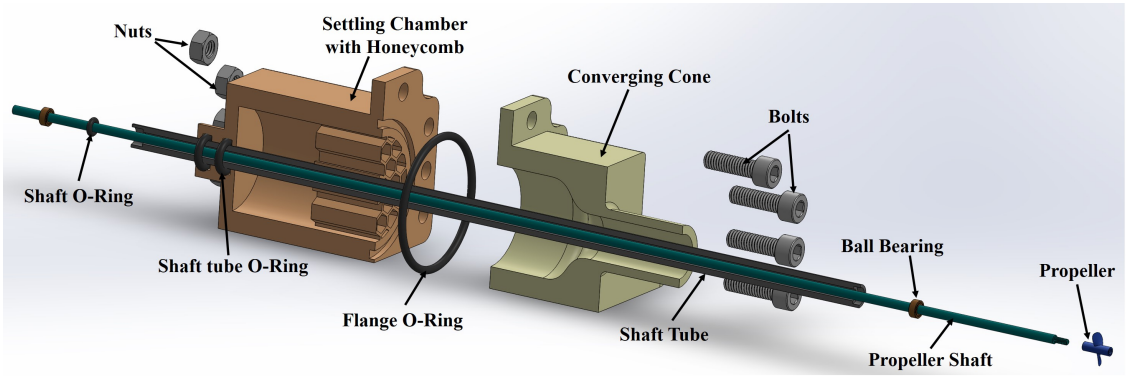

Figure 7.19: Longitudinal cross section of the exploded view of the Settling chamber-Convergence cone Propeller shaft tube assembly

The settling chamber with honeycomb and the converging cone shown in Figure 7.13 were 3D printed via FDM method using PETG (Polyethylene Terephthalate) material which is which is widely used for applications requiring to hold liquid. Its properties like low porosity, high strength, and rigidity as compared to PLA and ABS makes it suitable for such applications. To avoid any leakage between the two flanges a groove is provided on the settling chamber flange face to accommodate a 2 mm wide Buna-N O-Ring with 41 mm ID. Two other smaller O-Rings are housed inside the two grooves provided at the back end of the settling chamber to prevent any leakage between the shaft tube and the chamber. To better understand the assembly, an exploded view illustrating all the components is shown in Figure 7.19. It is worth mentioning that even though PETG has good water holding capacity it requires a coating of Petroleum Jelly or Epoxy (Loctite EA E-20 HP) to prevent any water from oozing out of the walls under high pressure conditions.

Even though honeycomb structure has its own advantages of streamlining the flow and reducing the flow turbulence, it was giving large flow hindrance given a low pressure and flow inducing capacity of the pump. As a result, the honeycomb structure was removed from the design of the settling chamber as shown in Figure 7.20. Instead, a 15 mm long flow straightener with six vanes, depicted in blue, was added downstream of the contraction cone and placed at a distance of 25 mm from the end of the shaft tube. The flow straightener was

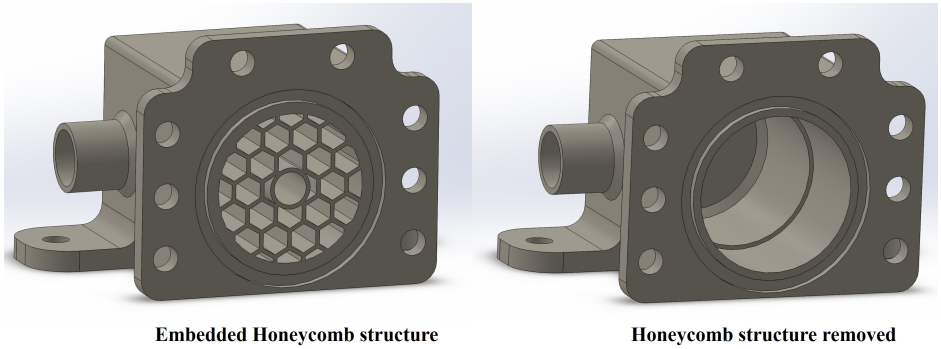

Figure 7.20: Settling Chamber with and without honeycomb structure embedded

designed to have a transitional fit with the shaft tube wall while the outer walls of the vanes were made to touch the inner wall of the pipe. In this way, the flow straightener served to center the propeller shaft with respect to the pipe wall while simultaneously straightening the flow.

Two 3D printed pipe support mounts similar to those used for Flared TCPC testing were used to accurately position the pipe at the center of the slotted frame and in line with the motor mount. Single Transonic flow sensor H11XL was used to measure the flow with a ball valve used to control the flow through the test section. As shown in Figure 7.13 (a), the static pressure was measured at a distance of 50 mm upstream and downstream of the propeller using the Honeywell ABP series board mount differential pressure sensors.

It was observed in section 6.7 that with working fluid as water, the inflow Reynolds number is greater than 2300 making the flow at the inlet turbulent. The entrance length of pipe required for the flow to be fully developed in that case was calculated to be around 220 mm and to be on a safer side the pipe length was kept equal to 380 mm in front of the propeller. The remaining length of the pipe behind the propeller was kept equal to 200 mm.

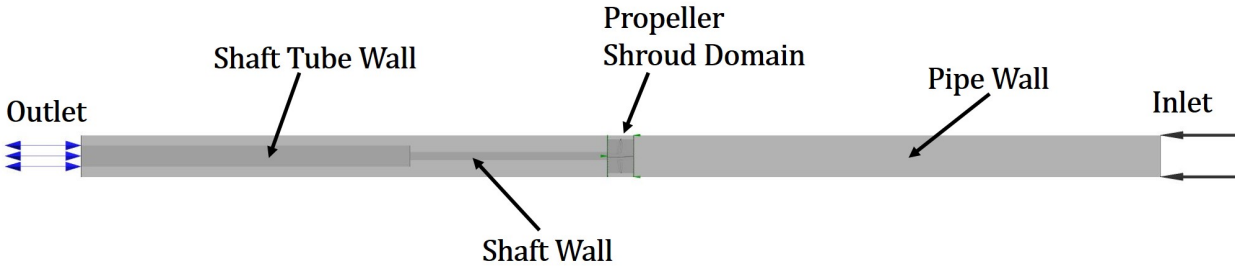

Figure 7.21: CFD Setup of IVC Propeller representing geometry similar to the experimental setup

Since the CFD setup (Figure 7.5) used for evaluation of propeller performance in blood is significantly different as compared to the experimental test setup, a new CFD setup representing the experimental test rig is modeled as shown in Figure 7.21. For this case, the

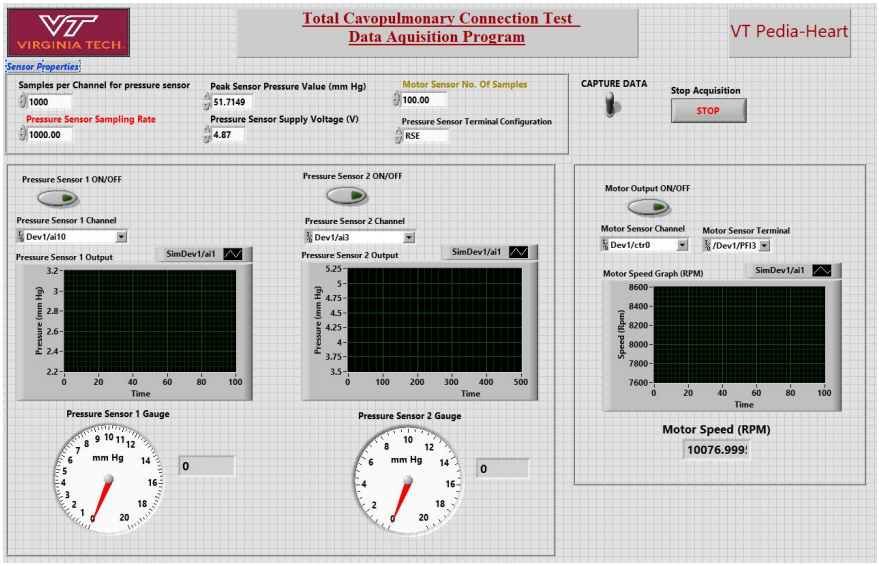

Figure 7.22: LabView front panel for measuring characteristic performance of the propeller pump

working fluid is changed from blood to water and the pressure rise is evaluated at 50 mm sections upstream and downstream of the propeller to mimic the experimental settings.

7.2.2 Data Collection and Results

The LabVIEW code used for the Flared TCPC performance testing was modified by removing the PA flow sensor channels and adding a counter channel to sense the motor speed as displayed on the front panel shown in Figure 7.22.

The initial tests were performed with propeller blade suction side facing the convergence tube and the pressure side towards the storage container. Even though propeller was able to induce the flow through the loop, the losses at the settling chamber section were too high to get the required flow rate and pressure rise. As a result, it was decided to face the suction side of the propeller blade towards the storage tank having minimum flow resistance path. This setting helped the propeller to draw more fluid and propel it into the settling chamber from where the flow returned back into the container flowing through the long return duct show in Figure 7.13. The storage container lid was closed to ensure a closed loop flow condition.

The IVC and SVC propellers were tested for an inflow rate ranging from 0.5 to 3 l/min and 0.25 l/min to 2.5 l/min respectively while rotating at a speed of 7000-10000 rpm. For each test case, four readings were taken of the RMS pressure and the instantaneous flow rate and the mean of those four values was used to evaluate the pump characteristics at each test case. The hydraulic performance or the head flow characteristics of the IVC and SVC propellers determined experimentally shows a similar trend as the numerical results. It could be noticed that the test values are deviating for the IVC propeller at flow rates below 1 l/min

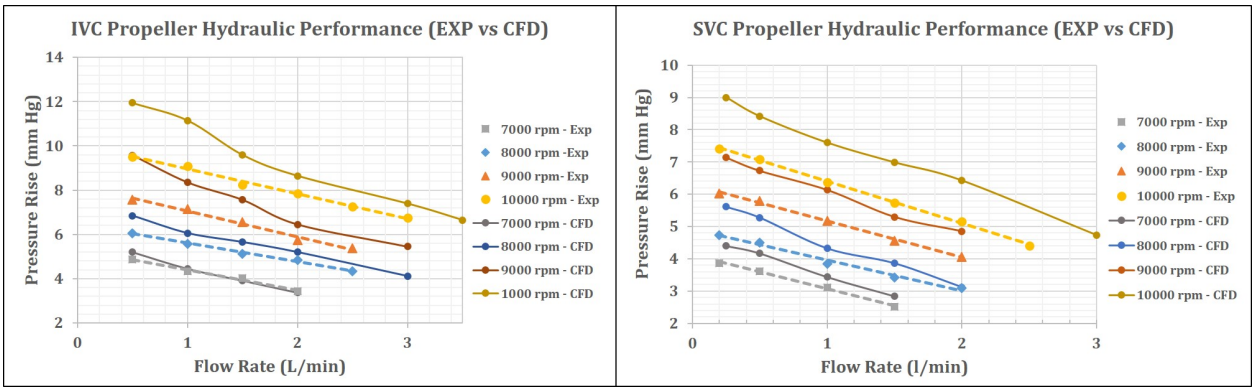

Figure 7.23: IVC and SVC Hydraulic Performance comparison for Experimental testing and CFD analysis

and speeds above 8000 rpm in comparison to the CFD results. This is mainly due to the slight clearance between the shaft and the inner bearing race which is unable to hold the high pressure generated by the propeller at those points leading to minor leakages from the bearing side exposed to the atmosphere. This contributed towards pressure losses which can be seen by a fair divergence of the performance curve at higher rpm and lower flow rates with good overlapping results at higher flow rates and lower speeds giving a maximum and minimum error of 20.85% and 1.6% for IVC propeller and 19.67% and 0.68% for SVC propeller respectively. Since SVC propeller generates lower pressure, there were no leakages experienced and as a result, the percentage error is slightly lower than that seen for IVC propeller. The percentage errors obtained are however considerable with those witnessed during experimental VAD testing by other researchers [99, 108]. Other sources of error are introduced due to the propeller profile which is not as accurate as the CAD model. To hold the fluid, an oil seal fitting in front of the bearing is required, however, since there are no standard oil seals available of such small size, a custom oil seal needs to be designed to meet the requirements. As a temporary solution, an o-ring was introduced behind the bearing as illustrated (as shaft o-ring) in the exploded view (Figure 7.19) which helped to reduce the leakage temporarily.

Neglecting the effect of leakage at very high pressures, the numerical predictions from the CFD shows a good agreement with the experimental results inferring a successful verification of the propeller design method and validation of the CFD numerical model.

7.3 Single IVC propeller inside TCPC

The previous section verified that the IVC and SVC propellers would provide the required pressure augmentation at the design point. Before moving forward and introducing the results of the dual propeller pump study, the effect of inserting and placing a single propeller inside the IVC is briefly evaluated in this section. This is mainly done to draw attention

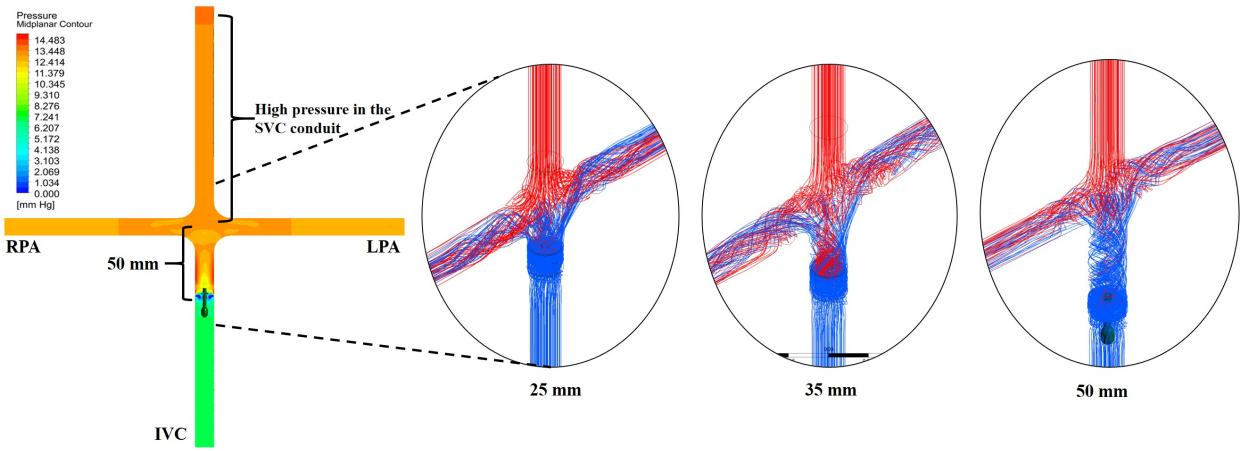

Figure 7.24: Mid-coronal plane pressure contour for 50 mm configuration and the flow streamlines for the propeller distance of 25 mm, 35 mm and 50 mm.

towards the drawback of assisting a Fontan Patient with a pump augmenting the flow only in one branch of the vena cava. In order to perform this study, an IVC propeller is placed at a distance of 25 mm, 35 mm and 50 mm from the center of the TCPC. This is done in particular to visualize the effect of the propeller on the flow behaviour and losses with the change in placement of the device. In this study, the catheter and the surrounding stent are not modeled for simplifying the geometry and flow setup.

The CFD setup for this includes a rotating propeller domain placed at different lengths along the IVC from the TCPC center. The boundary conditions are similar to the physiological flow conditions existing inside a TCPC [listed in Table 6.1]. Whereas, the interface setting between the IVC propeller and the IVC duct upstream and downstream faces is similar to that mentioned in the propeller hydraulic performance CFD setup (Figure 7.5). Similar to IVC - SVC single propeller study, the SST turbulence model is used with automatic wall function to simulate the flow inside the TCPC embedded with a single propeller pump.

The variation of pressure within the TCPC domain for the 50 mm configuration is shown in Figure 7.24 with the velocity streamlines for the three propeller positions depicted in the inset. It could be seen that the IVC propeller helps to reduce the blood pressure upstream of the propeller to normal physiological values, however, the blood pressure inside the SVC conduit is elevated to around 13 mm Hg which is about 3 times the normal physiological central venous pressure values. This is one of the main causes of hypertension in vena cava for Fontan patients who are supported by a cavopulomary assist device placed either on the IVC or SVC side as reported by Dr. Rodefeld [45]. The velocity streamlines depicted in Figure 7.24 illustrate the flow agitation at the central confluence which reduces as the distance of the propeller from the center increases. Increasing the distance provides a longer path for the flow to dissipate its energy before reaching the central confluence and in turn, reduces the intensity of flow mixing and hence the energy losses. However, placing a cavopulmonary device too far isn't advantageous since then there will be higher viscous losses incurred by

the flow downstream of the propeller and the overall pressure rise between the pulmonary artery outlet and the IVC inlet would reduce. It could be observed from Table 7.8 that the gradient of pressure rise or energy imparted reduces as the propeller recedes away from the center. Another important thing to notice is that the IVC inlet pressure reduces while the SVC inlet pressure increases as the propeller is moved away from the center.

Table 7.8: IVC Propeller performance at different distance inside the IVC from center of the TCPC

IVC Propeller Distance [mm]	**IVC Inlet Pressure [mm Hg]**	**SVC Pressure [mm Hg]**	**Power Imparted [mW]**
25	7.559	13.326	34.499
35	7.413	13.398	35.189
50	7.337	13.513	35.263

Thus, it could be concluded that just having a single flow augmentation device in one of the vena cava is not enough to correct the abnormal flow dynamics in Fontan patients and that a need for a dual pumping mechanism is required to bring the patient closer to normal physiology.

7.3.1 Experimental Verification

To demonstrate and verify the effect of having a VAD inserted on one side of the vena cava, a series of experimental tests were conducted on Flared TCPC test setup by replacing the elbow joint on one end of one of the vena cava duct with the single propeller settling chamber assembly as shown in Figure 7.25. For sake of comparison with the study performed in the previous section, the IVC propeller was chosen to augment the flow inside the Inferior Vena Cava. Similar to the TCPC test setup, an external circulation pump is used to maintain the required physiological cardiac output of 4.5 l/min within the system. The location of the pressure ports and the flow sensors was kept unchanged. The first part of the study concentrates on comparing the flow losses induced by a non operational propeller placed at a distance of 25 mm, 37.5 mm and 50 mm from the center. The same study is then extended to determine the amount of energy imparted or power gained by the fluid when the propeller is operated at design speed at the same three locations. The last part of the experimental testing concentrates on determining the hydraulic performance of the IVC propeller pump at the three distances and observing the corresponding relative pressures in the SVC duct.

For the first part of the study, an equal flow split between the IVC and SVC was maintained by the valves while keeping the propeller pump stationary inside the Inferior Vena Cava. Similar to TCPC test procedure, four sets of readings were taken from the four pressure sensors and flow sensors and an average of the four readings is considered and presented in Figure 7.26(a). As displayed in the power loss plot, the propeller provides the least hindrance when placed farthest from the center when not operating.

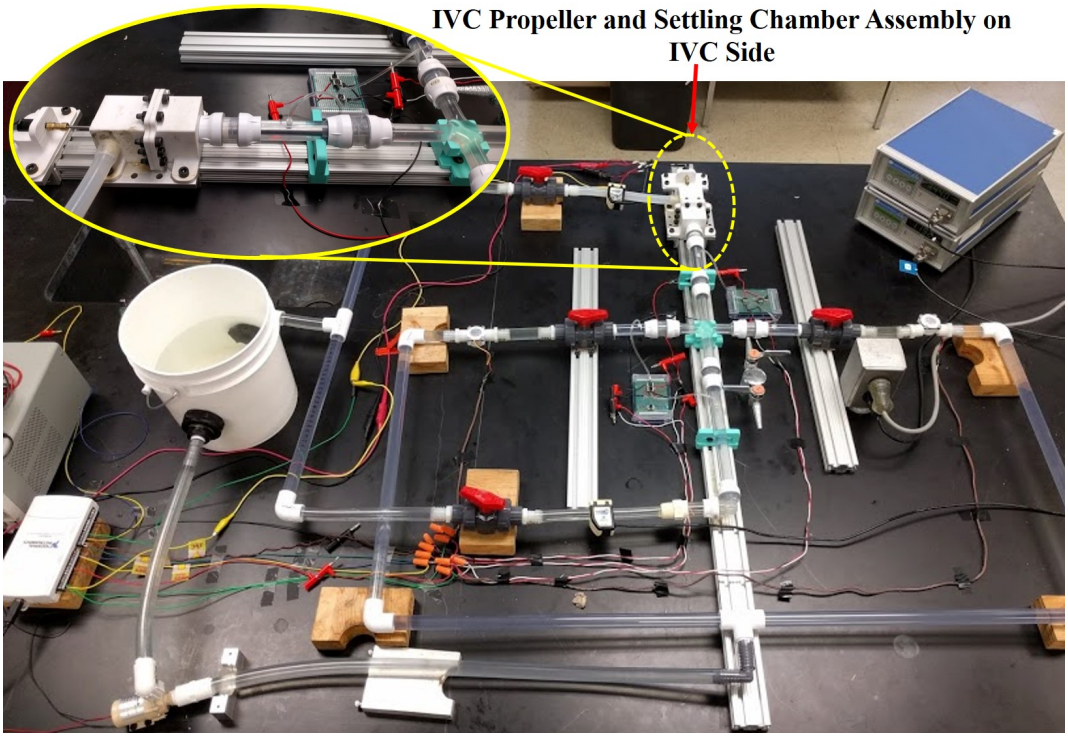

Figure 7.25: Experimental Setup of Flared TCPC incorporating the IVC Propeller Settling Chamber Assembly on the IVC side

However, when the propeller is turned on and rotated at 8000 rpm, the flow rate increases to $3.5 \pm 0.093\ l/min$ for all the three cases. Since the flow rate induced was same for the three cases, the valve adjustment was left undisturbed and the readings were taken once the flow rate and pressure values had settled to a steady value after starting the pump. The power gain and pressure rise curves for the three pump configurations are shown in Figure 7.26(a) on the same graphical plot. The curve shows that the maximum gain in power and pressure is achieved when the propeller is placed midway between 25 mm and 50 mm. The magnitude of the percentage difference of power loss between the 25 mm and 37.5 mm distance and that between 37.5 mm and 100 mm distance is 15.77% and 5.34% agreeing with the trend observed in the numerical analysis of the Single IVC propeller working in blood. The CFD simulations had shown that the propeller had the least losses for 50 mm distance, however, the growth in power gain was reducing with distance showing an imminent drop at a larger distance. Moreover, the flow is within laminar to transitional zone when dealing with blood, while the turbulent nature of the flow in case of water magnifies the losses and wouldn't give the same behaviour as that with blood. Another reason for experiencing higher losses at 50 mm propeller placement was that the pipe connector, connecting the TCPC and the IVC pipe was closest to the propeller at this distance, which imposed higher flow resistance and losses.

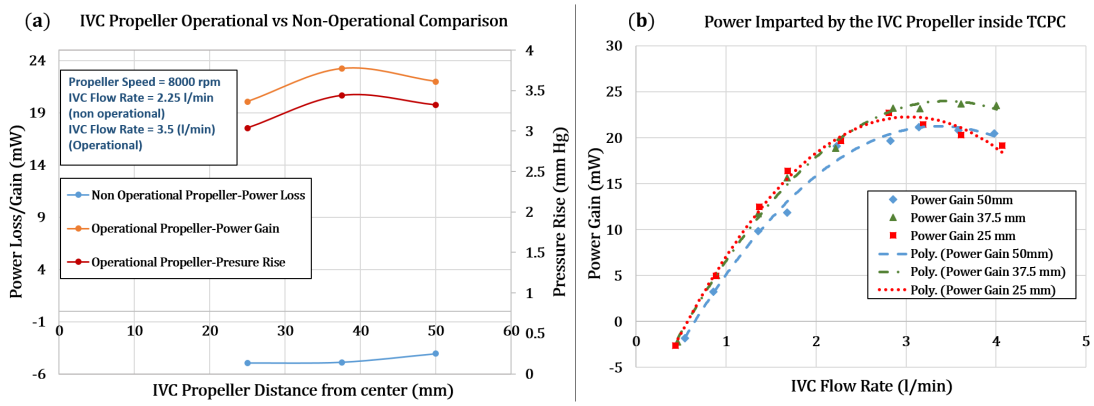

Figure 7.26: IVC Propeller Performance in terms of: (a) power loss and gain when non operational and operating at design speed, and (b) power imparted to the fluid at 50 mm, 37.5 mm and 25 mm IVC propeller distance from the center

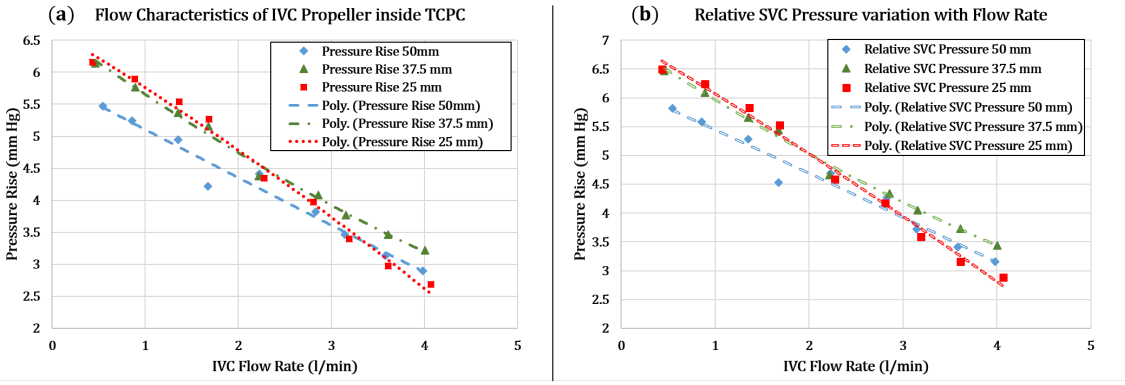

Figure 7.27: (a) IVC Propeller Hydraulic Performance inside Flared TCPC when placed at 25 mm, 37.5 mm and 50 mm from the center, and (b) Relative pressure rise in the SVC branch due to flow induced by the IVC propeller operating at the same three axial distances from the center.

The hydraulic performance of the IVC propeller at three distances shown in Figure 7.27 illustrates that a pressure rise of around 4 mm Hg is achieved at the design flow rate of 2.82 l/min which is lower than the expected value by 1 to 1.5 mm Hg mainly due to the high flow resistance provided by the settling chamber as well as the turbulent flow loses. As discussed in the single propeller hydraulic performance testing section, the quality of the 3D printed propeller isn't the best with irregularities existing near the blade tip and edge which could also penalize the propeller performance. In the absence of flow augmenting device inside the SVC branch, the IVC propeller does the work of pressuring the SVC duct along with the LPA and RPA duct. As a result, the pressure rise was determined by taking a difference between the average of pressure measured at the LPA, RPA, and SVC and that at the IVC. The relative SVC pressure with respect to IVC for the three propeller distance showed the same trend as the pressure rise, with an average value of 0.4 mm Hg higher

than that measured at the LPA and RPA. This is an important phenomenon demonstrating how a single propeller placed in the IVC would result in the cross flow of blood into the SVC causing the latter to become pressurized and hypertensive as it was observed in case of numerical simulations performed with blood. Also, it could be seen that mid propeller distance provided the best performance in terms of power gain and pressure rise, while the propeller at 50 mm distance shows minimum pressure rise for lower flow rates given the large distance available for the flow to dissipate energy before exiting through the LPA and RPA branches. This wasn't seen in case of blood due to laminar nature of the flow having lower dissipative losses as compared to a turbulent flow.

In this way, the modified Flared TCPC model helped to verify the expected behaviour of a single ventricular assist device of creating a hypertensive vena cava when explicitly used to augment the cavopulmonary flow in one of the vena cava of the Fontan patients.

7.4 Dual Propeller Pump Analysis

The drawbacks of augmenting the flow with a single propeller pump inside the vena cava led to the development of the dual propeller pump concept [Figure 7.1]. As discussed in Chapter 1, to facilitate an easy and single percutaneous insertion from the femoral vein, the IVC and SVC propellers are mounted on the same shaft, such that, while rotating at the design speed of 8000 rpm, they would generate an equal pressure rise for an IVC to SVC flow split of 63:37. The goal is to distribute the blood to the lungs effectively, by generating the required lung perfusion pressure and unloading the single functional ventricle. The analysis of this device is performed by including the IVC propeller, SVC propeller and central shaft inside the Flared TCPC and studying the blood flow pattern, IVC and SVC pressure reduction (or pressure rise between vena cava and pulmonary arteries) and the power or energy transferred to the fluid. Similar to the single propeller study, the stent and catheter aren't included in the model for simplification and its effect would be studied at a later stage.

The CFD setup for this device is shown in Figure 7.28, where the entire domain is divided into three parts namely, the stationary domain consisting of the IVC, SVC, LPA, RPA and the central confluence region and two rotating domains for the IVC and SVC propeller and shroud clearance domain. The central shaft connecting the IVC and SVC propeller is given the same rotational speed as the rotating domain. Here, the boundary conditions are same as those used for TCPC physiological model [listed in Table 6.1], while the connection between the rotating and stationary grid is achieved using General Grid Interface (GGI) setting same as that used for the propeller hydraulic performance flow setup. The SST turbulence model with automatic wall function is used to model the flow. The final mesh settings obtained from the grid independence study for the Flared TCPC and the propellers are used.

In order to determine the optimal separation distance between the two propellers, a study was done to examine the effect of axial distance between them on the blood flow pattern and pressure augmentation. For this study, the propellers were placed symmetrically from

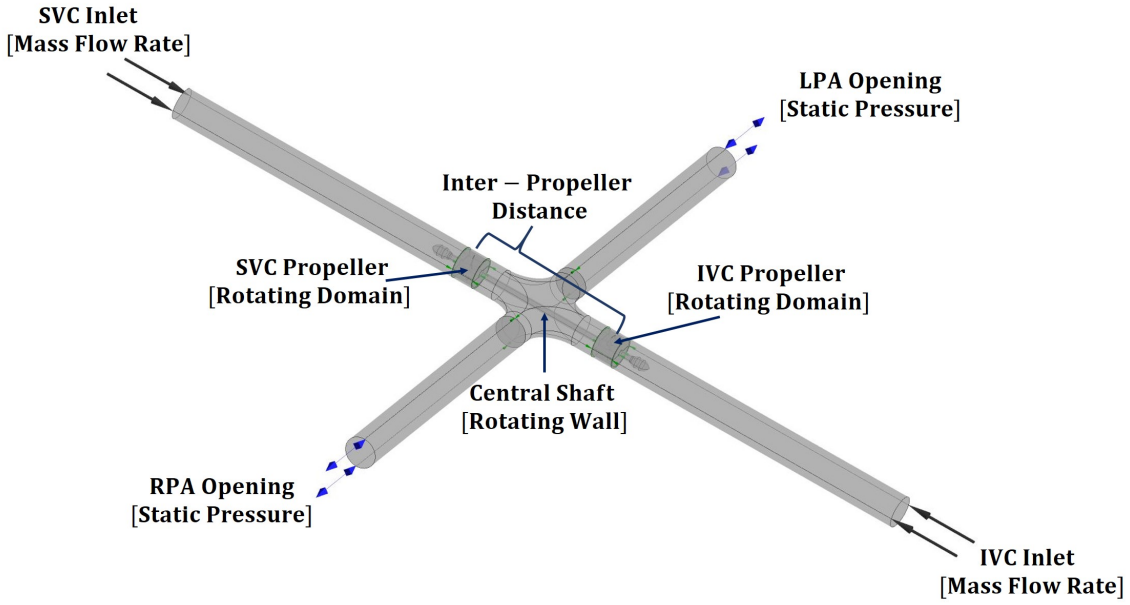

Figure 7.28: CFD Setup for Dual Propeller Pump placed inside the Flared TCPC

the center with inter-propeller distance chosen as 50 mm, 75 mm, and 100 mm. The reason for not exceeding above 100 mm is the space constraint inside the SVC tract, having a mean length of $71 \pm 14\ mm$ as measured using a central venous catheter (CVC) [109]. The results of this study are displayed in Figure 7.29 with (a), (b) and (c) showing the velocity streamlines, the mid-coronal plane pressure contour and the variation in area average pressure along the IVC-SVC conduit. Both, pressure contour and vena cava pressure variation graph confirm that irrespective of the inter-propeller distance, the device has the potential to reduce the vena cava pressure to the normal physiological level of around $6 - 7\ mm\ Hg$ while fulfilling the pressure requirements at the pulmonary artery ends (of around 13 mm Hg).

A contrary behaviour, as compared to the single propeller analysis inside the TCPC, is observed for the power gain, where, for the close placement of the two propellers, the device produces higher power output and performs more efficiently. Since the difference between the efficiency values or power output values aren't significant for the three studied inter-propeller distances, the deciding factor to select the optimal configuration will be the blood damage induced by them and will be discussed in the following section.

7.5 Blood Damage Estimation

In the previous sections, the propeller pump was evaluated only on the basis of its hydraulic performance to verify if it provided the required pressure rise at a given inflow rate. However, any heart assist device has to primarily ensure that it isn't damaging the Red Blood

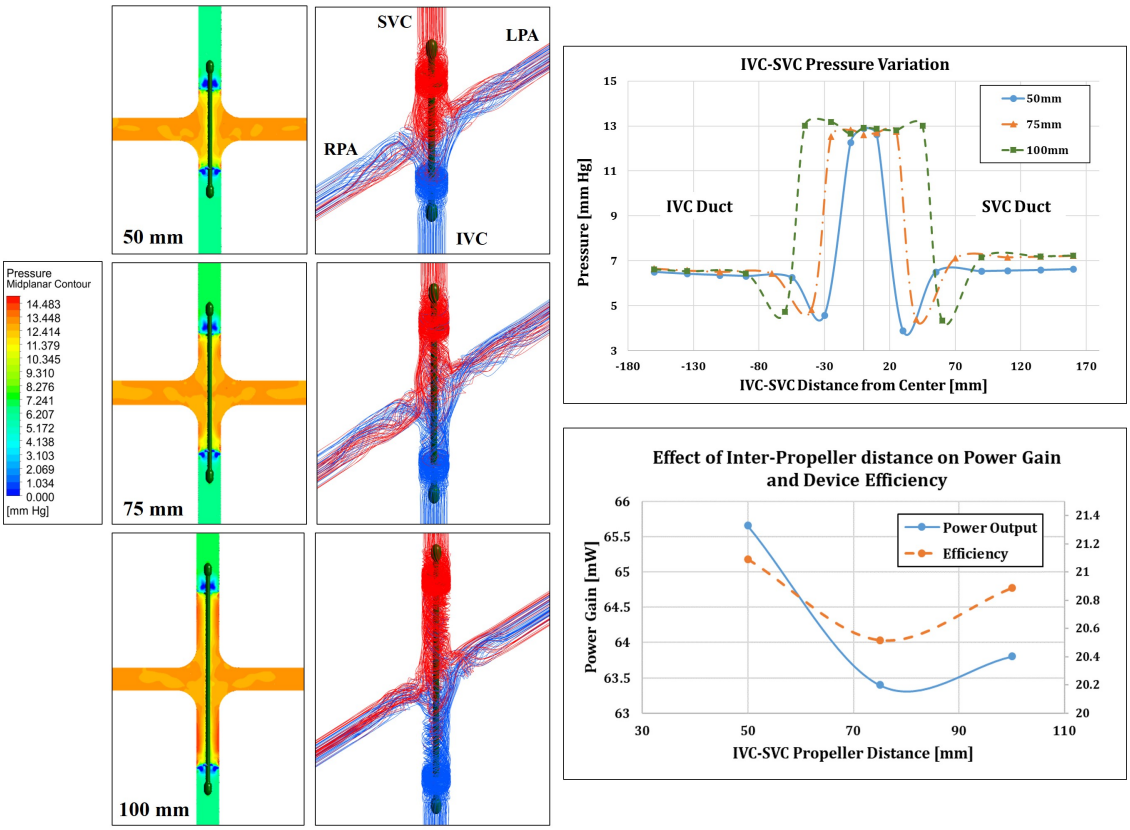

Figure 7.29: Mid-Coronal Plane Pressure Contour, Velocity streamlines and variation of fluid power augmentation with inter-propeller distance inside the Flared TCPC

Cells. The reduction in the RBC count due to their rupture under high shear stress is referred to Hemolysis and is one of the major factors leading to Blood Damage as it was introduced in Chapter 3. As it was discussed there, the two most commonly used Blood Damage Estimation methods are the Eulerian approach, solving the blood damage scalar transport equation for the entire domain and the Lagrangian approach, which evaluates the blood damage history of a particle track to determine the cumulative destruction to Red Blood Cells. Taskin et al. [76] and Fraser et al. [65], evaluated the blood damage potential of a number of mechanical circulatory support devices and concluded that both Eulerian and Lagrangian methods overestimated the blood damage values as compared to experimentally evaluated hematocrit reduction [a measure of blood damage]. However, these methods are a good analysis tool for comparing different devices or designs for optimization study to select the one with least potential for blood damage.

As it was concluded in Chapter 3, the Lagrangian Particle Tracking method in conjunction with the modified power law model proposed by Grigioni et al. is implemented in this thesis to predict the relative hemolysis between different designs. Recollecting the power law model, the blood damage index of a device is directly proportional to the amount of scalar

shear stress induced and the time of exposure of RBCs to those stresses. The Scalar Shear Stress (SSS) equation introduced by Bludszuweit et al. 3.14 is used to determine the stress acting on a particle during a single time step.

7.5.1 CFD Setup for Blood Damage Modelling

In order to estimate the blood damage using ANSYS CFX, a new material representing the red blood cells is introduced in the CFD setup alongside the already introduced blood, for all the TCPC and propeller models discussed earlier. The material properties of the blood cells are adapted from those used by Miclea-Bleiziffer et. al., and are listed in Table 7.9.

Table 7.9: Red Blood Cell Material Properties

Properties/Settings	**Values**
Material Group	Particle Solids
Molar Mass	67000 $[g/mol]$
Density	1094.1 $[kg/m^3]$
Reference Temperature	25 $[^{\circ}C]$
Reference Pressure	0 atm
Diameter	0.0075 $[mm]$

Since we have solid red blood cell particles introduced into the fluid (blood) domain, this becomes a two-phase flow problem. However, since the mass of a red blood cell is negligible in comparison to the surrounding blood, a One-Way particle coupling method is used. This means that blood cells won't influence the blood flow, and instead, the blood cell particle path will be affected by the flow field. The particles are introduced at the inlet duct inlet when studying a single propeller characteristic or at the IVC and SVC inlet when studying the TCPC-Dual propeller characteristics. The particle injection settings at an inlet (specified inside fluid values in CFX) are shown in Table 7.10.

In this way, 1000 particles are inserted at the inlet and in order to allow the solver to track these particles from inlet to the outlet, 30000 integration steps are specified as particle termination control criteria (increased from a default value of 10000).This would prevent the particle tracks from terminating before exiting from the outlet.

Once the solution is obtained from the CFX solver, the 1000 particle tracks from each inlet (in case of multiple inlets) can be visualized and the corresponding values of particle time and scalar shear stress at each integration point (or node) along the particle trajectory is exported as a .csv file from ANSYS CFD Post-Processing module. The exported excel sheet is read by a MATLAB code, which segregates the particles and determines the damage sustained by each particle by implementing the modified power law model. Depending on the size of the domain, the complexity of flow, number of particles, number of integration

Table 7.10: Particle Injection Boundary Condition at Inlet

Particle Behaviour Settings	**Values**
Mass and Momentum	Zero Slip Velocity
Particle Position	Uniform Injection
Particle Locations	Equally Spaced
Number of Positions	Direct Specification: 1000
Particle Mass Flow:	
IVC Inlet	0.007191 [kg/sec]
SVC Inlet	0.004284 [kg/sec]

steps, and the excel limitation on the number of rows (1,048,576), the number of particles actually exported and read by the Matlab code are usually less than 1000.

7.5.2 Scalar Shear Stress Comparison

One of the two main factors affecting the Blood Damage Index, the Scalar Shear Stress (SSS), is analyzed for different propeller pump configurations using contour plots, iso-volume and volume histogram. According to Taskin and Fraser et al., the regions with high SSS values above 50 Pa are mainly responsible for shearing and rupturing the blood cells. This volume is dominant around the propeller blade surface where the maximum shearing occurs as shown in Figure 7.30.

It could be seen that the SSS volume (for $\sigma > 50\ Pa$) is higher for the IVC and SVC propeller evaluated inside the TCPC in Dual Propeller configuration as compared to that evaluated individually in a straight duct. The additional high shear stress region is witnessed within the shroud clearance area and is speculated to be due to the flow mixing and hindrance at the center of the TCPC (as shown in Figure 7.29) which agitates the flow around the propeller blade tip clearance. In both the configurations, it could be seen that the IVC propeller has higher SSS volume than the SVC propeller especially near the hub (as highlighted in the black dotted circle). It is known that the resultant velocity of the fluid approaching the blade increases from hub to tip and so does the velocity gradient between the wall surface and the first fluid layer. The Scalar Shear Stress which is a function of velocity gradient is thereby seen to have very low values at the hub and high values at the tip with highest values at the leading edge where the fluid first comes in contact as highlighted by a black dotted circle in Figure 7.30.

In order to compare the propeller pumps, the percentage of the SSS volume corresponding to $\sigma > 50\ Pa$ within the propeller domain is computed and is shown in Figure 7.31. It could be seen that the percentage of high SSS volume in dual propeller pumps is almost 1.5 times that seen for the individually operated IVC and SVC propellers thereby complying with the

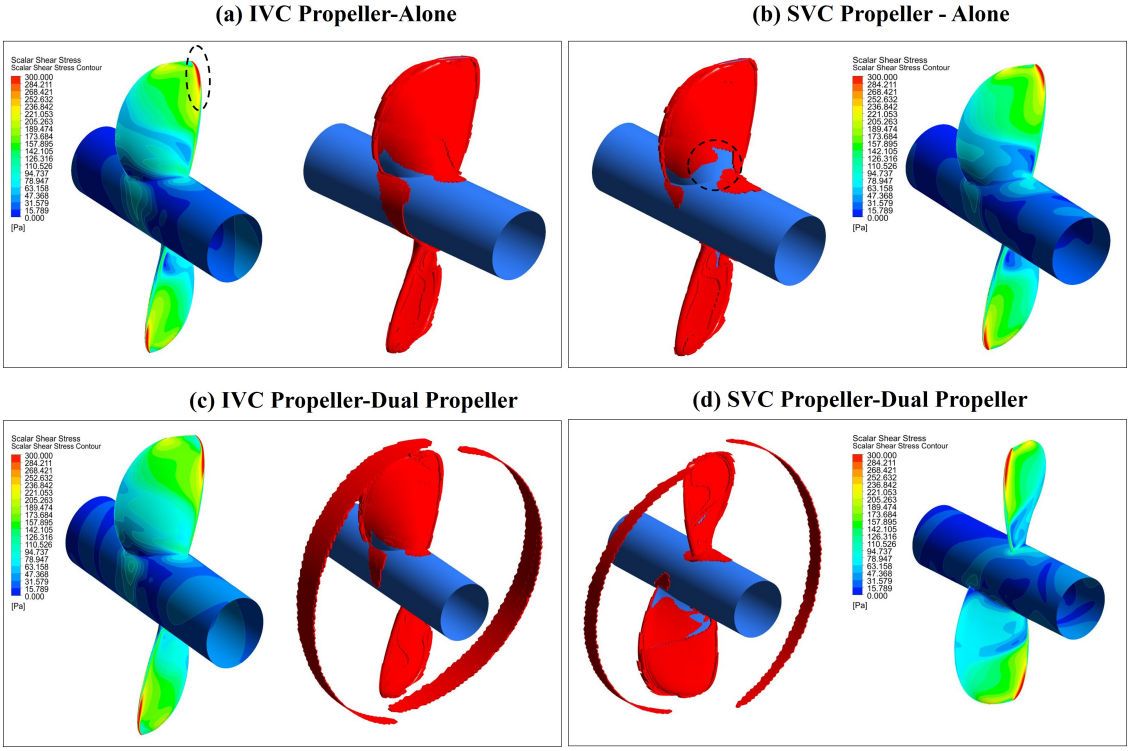

Figure 7.30: SSS Volume and SSS contour on the blade surface for the IVC and SVC propeller in stand alone and dual-propeller configuration

SSS volume distribution seen in Figure 7.30. The Inter-Propeller distance has a little effect on the variation of SSS with distance, with a difference of only 0.01% and 0.005% between 75 mm - 50 mm and 100 mm - 75 mm configurations.

As described by Fraser et al., the scalar shear stresses exerted on the blood cells could be grouped based on their impact on blood damage. The very low values of SSS, less than 1 Pa, are considered to be very safe for the blood cells and in fact, the blood cells wouldn't undergo any rupture even for the low values of stress ($1\ Pa < \sigma < 9\ Pa$). The mid stress level ($10\ Pa < \sigma < 49\ Pa$) is the region where the blood cell membrane starts to weaken while experiencing stretching of its membrane, and for higher stress levels above ($> 50Pa$) there is very high potential for membrane rupture and hemoglobin leakage into plasma, indicating the start of Hemolysis. Inferring from this, it is ideal to have a maximum percentage of the volume lying in very low and low regions of SSS. This is actually visible from the histogram plot of the percentage SSS volume within the fluid domain divided into groups based on the SSS values discussed above. For single propeller configuration (Figure 7.32a), it could be seen that SVC propeller has significantly higher SSS volume in the very low region as compared to the IVC propeller, thereby suggesting probability for lower blood damage potential. On the other hand, the dual propeller configuration shows a decreasing trend in volume in very low SSS region and an increasing trend in low SSS region with the

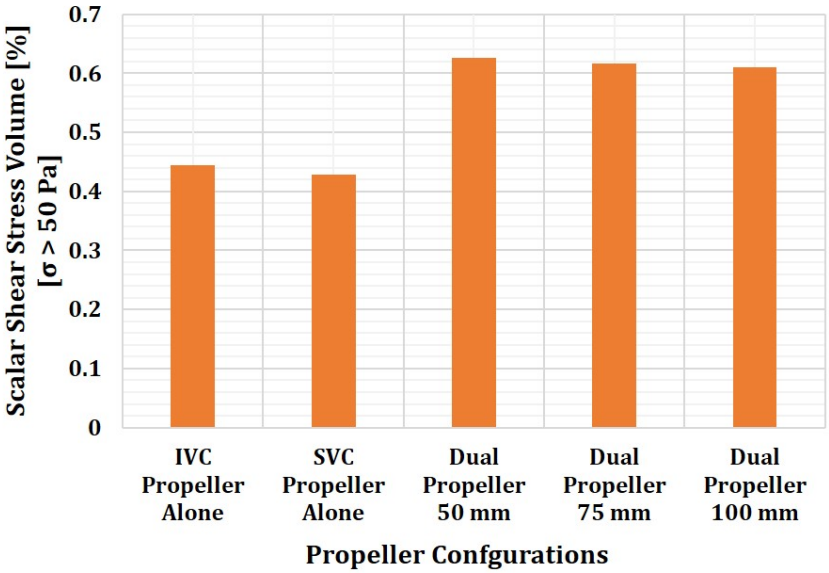

Figure 7.31: Critical SSS Volume for 5 propeller configurations

increase in inter propeller distance. However, the differences aren't as significant as those seen between the single IVC and SVC propellers to make any relative guesses on the blood damage potential for the three configurations.

7.5.3 Blood Damage Index and Particle Residence Time

The MATLAB code output for BDI particle distribution computed for the investigated IVC and SVC propeller pumps is presented in Figure 7.33. It could be seen that the maximum number of particles have a BDI of less than 0.002% with very few going up to 0.01%. The particle exposure time, denoting the time required by an injected particle to exist the flow domain, is exported from the CFD results and is presented in Histogram form to illustrate its distribution. It could be seen that the maximum number of particles have an exposure or residence time within 1 second, with a few recirculating particles exceeding 1 sec. The average value of Blood Damage Index and Particle Residence time for the IVC and SVC propeller when operating individually are shown in Table 7.11.

Table 7.11: BDI and Particle Residence time in IVC and SVC propellers

	Blood Damage Index [%]	**Particle Residence Time [Sec]**
IVC Propeller	3.14e-04	0.195
SVC Propeller	4.56E-04	0.329

The contradictory BDI results are seen for SVC propellers in comparison to those seen for

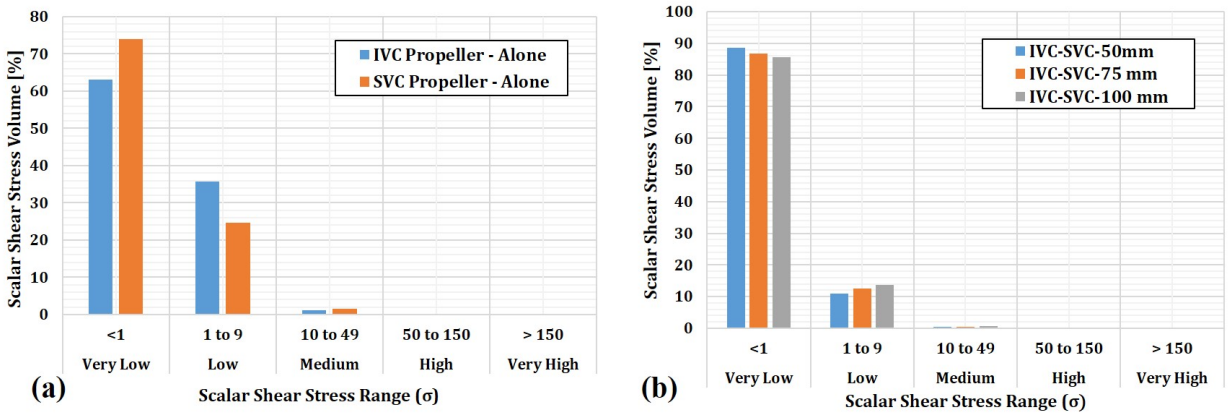

Figure 7.32: Scalar Shear Stress Volume Distribution for different propeller configurations

the SSS volume distribution. Even though the volume of high SSS is low in SVC propeller in comparison to IVC propeller, the average particle residence time is around 0.12 sec more than that in IVC propeller, causing the particles to be exposed to low stress values for a longer time thereby building the blood damage potential. The longer particle travel time in SVC propeller can be attributed to higher recirculating particles from the shroud clearance region as depicted in Figure 7.34. For better comparison the particle tracks are visualized in terms of their particle travel time, for which SVC propeller shows more red and yellow trajectories (denoting higher values of travel time) as compared to the IVC propeller, thereby explaining the cause of higher BDI.

A similar comparison of BDI and Particle residence time is done for the three Dual Propeller pump configurations developed based on the inter-propeller separation distance. For this case, the BDI for particles injected from the IVC and SVC is evaluated separately. It can be observed that the particles injected from SVC side take a longer time to exit, with the 50 mm inter-propeller distance showing maximum residence time and 100 mm showing minimum as depicted in Figure 7.35. In terms of BDI, the 75 mm configuration outperformed the other two for both IVC and SVC injected particles. Based on the previous results, the 75 mm configurations showed slightly lower performance in terms of power output and efficiency in comparison to other two inter propeller distances, however, the differences were very low. This relatively lower generation of pressure resulted in lower shearing of the blood cells and hence a lower overall blood damage for the 75 mm configuration. Therefore, considering the advantage of low Blood Damage potential a midway distance of 75 mm distance is selected for the future analysis of dual propeller final assembly with the stent support.

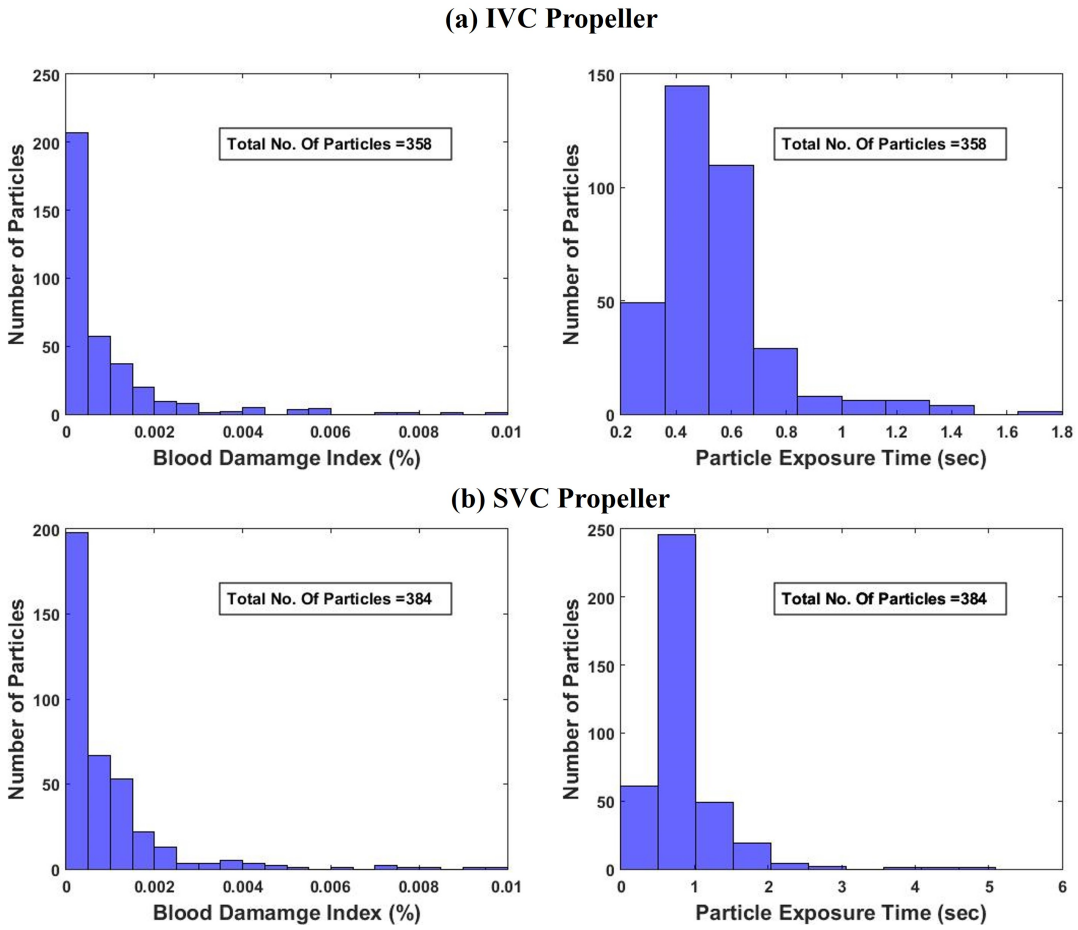

Figure 7.33: BDI and Particle residence time distribution for the particle population studied for IVC and SVC propeller

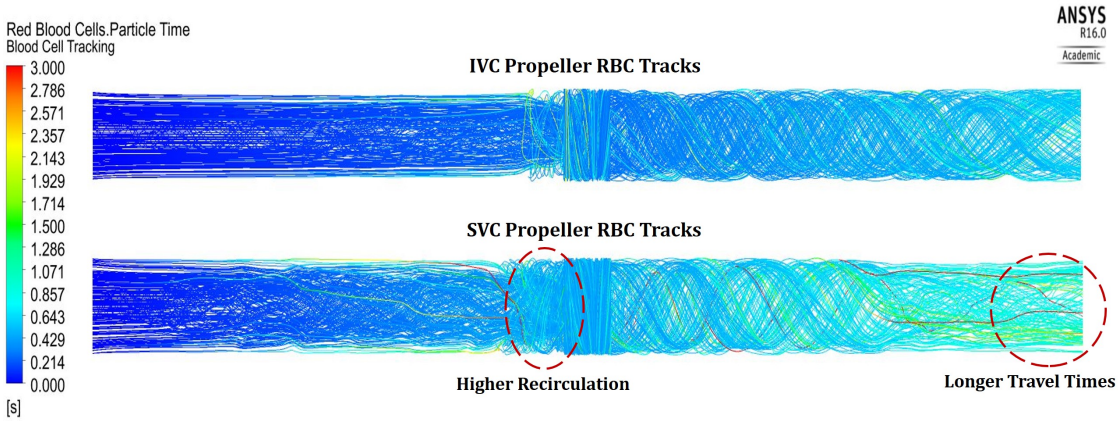

Figure 7.34: 200 Red Blood Cell Tracks flowing past the IVC and SVC propeller

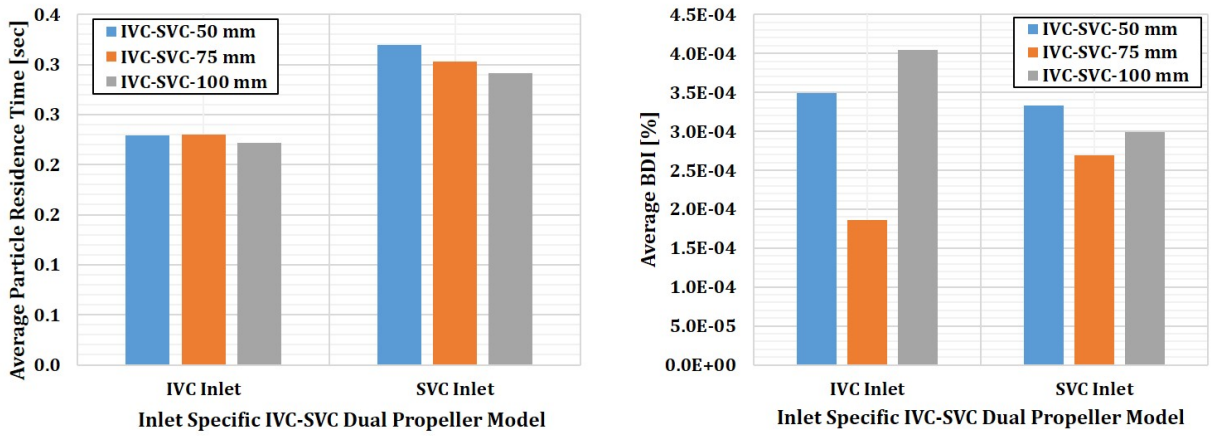

Figure 7.35: Comparison of Average Particle Residence Time and Average BDI for different IVC-SVC inter-propeller distance

7.6 Stent Design and Analysis for Hemodynamics and Blood Damage

In the present section, the key design parameters of a stent used to support the studied propeller pump are investigated for their effect on hemodynamic efficiency (or pressure rise) and blood damage. A generic parametric model of Stent, shown in Figure 7.36, was generated in SOLIDWORKS using the design guidelines listed in the Open Stent Design Document developed by Nitinol Devices & Components Inc. [110]. The parameters that were studied included the stent length, strut thickness, strut width, number of struts and number of columns or rings of struts. As depicted in Figure 7.36, the solid model of the stent was subtracted from the annular region with an outer and inner diameter equal to vena cava vessel wall diameter and propeller shroud diameter respectively to obtain the corresponding stent fluid domain. It is assumed that the outer wall of the stent is conforming to the inner wall of the IVC and SVC blood vessel. The length and width of the bridge connecting two strut columns were kept as 0.2 mm, while the radius of the gap between the adjacent struts was kept equal to half of the strut width for all the studied designs. In the stent design terminology, a strut refers to a single basic element, shown between the black dotted lines, which is repeated circumferentially and longitudinally to make a meshed structure of the stent. Various combinations of strut design and placement could result in different stent designs, however, the design shown in Figure 7.36 represents the most basic one to avoid complexity in the computational model.

To perform the numerical analysis with stent inclusion around the pump, the only change in CFD setup required in comparison to the single propeller analysis setup include the replacement of propeller clearance shroud domain with the annular stent domain as represented in Figure 7.37, with rest of the settings remaining the same. The goal of this study is to analyze

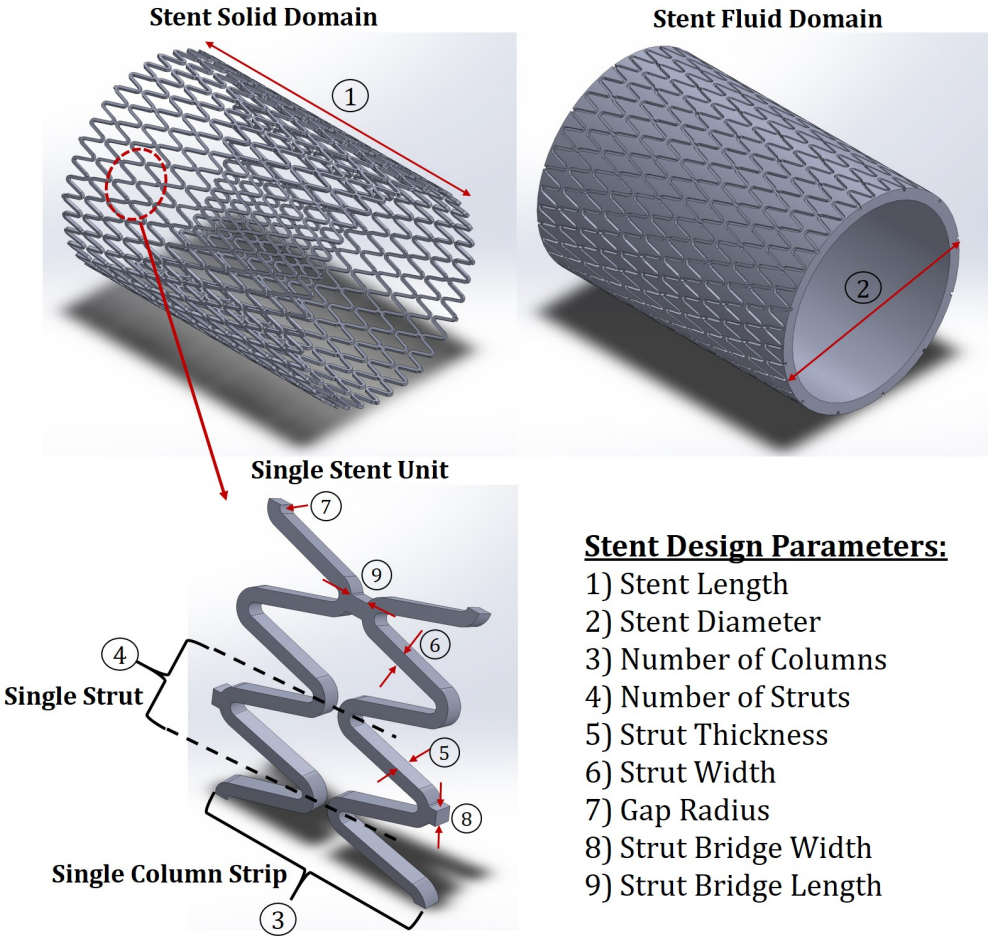

Figure 7.36: Stent Design Parmeters

the effect of stent parameters on BDI and hydraulic performance of IVC propeller and select the optimal design for the final dual propeller configuration.

A baseline stent model with parameters highlighted in blue in Table 7.12 was initially generated to analyse and compare the effect of the stent on the performance of the pump. A grid sensitivity analysis was performed on this stent model to ensure that the results obtained for the pressure rise are not affected by the stent grid. The final refined mesh for the base stent model had elements around 27 million. The same mesh setting is then used for all the studied designs. In order to perform the parametric study, the value of each parameter listed in the design matrix is independently varied by keeping all other design parameters same as that of the base design model. Thus each design parameter had a maximum, a minimum, a mid and a base value giving a total of 16 design points that were analyzed numerically and compared using ANSYS CFX. It should be noted that for the length change study, for each value of length, the corresponding stent column number listed in the design matrix is used to keep the strut length same or in other words to keep the stent length to column number ratio

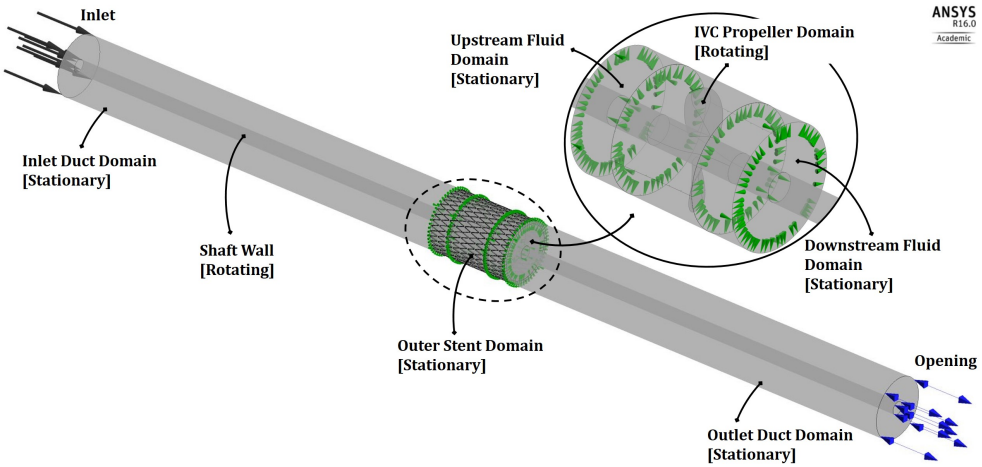

Figure 7.37: CFD Setup for Stent Base Model along with the IVC propeller

constant and equal to 5:3.

Table 7.12: Stent Design Matrix with the baseline model design parameters highlighted in blue

Design Parameters	Minimum Value	Mid - Value 1	Mid - Vaue 2	Maximum Value
Length of the stent [mm]	10	15	20	30
Thickness of the stent [mm]	0.1	0.15	0.2	0.3
Number of Columns	6	9	12	18
Number of Struts	12	24	36	45
Width of the Strut [mm]	0.1	0.13	0.17	0.2

7.6.1 In-Stent Restenosis and Wall Shear Stress

Before analyzing and comparing different stent designs a brief study is done on the potential for In-Stent Restenosis in patients with stent implants and with stent supported ventricular assist device like in the current case. Nitinol based stents are widely used for opening up arteries blocked by plaque. A restenosed artery is one in which the plaque rebuilds around the stent thereby blocking the blood passage through the blood vessel again. Investigations have revealed that the low Wall Shear Stress (WSS) levels ($< 0.5\ Pa$) within the stent struts is one of the major causes of this problem [50,111,112]. In order to study this effect, the wall shear stress acting at the stent - artery wall interface is evaluated for a stented IVC and a stent-supported-propeller pump assisted IVC. The Wall Shear Stress Contours for both the designs are shown in Figure 7.38. It can be clearly seen that in the stented vena cava without any propeller assistance, there is a predominance of low Wall Shear Stress Regions, especially

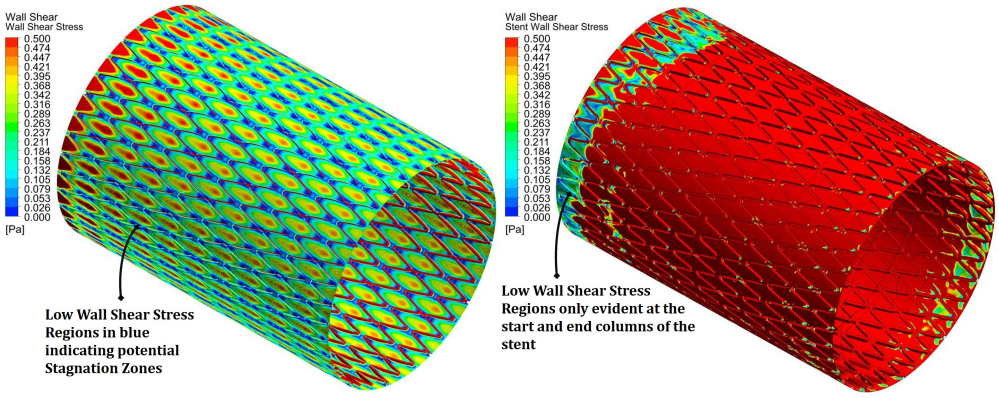

Figure 7.38: Wall Shear Stress Contour in Stented IVC (left), and in IVC fitted with propeller blood pump surrounded with stent support (right)

around the strut walls. An almost parabolic distribution of low WSS is seen for the fluid domain within a strut. These low WSS regions are potential locations of flow stagnation and mini flow vortices and recirculation zones. These flow stagnation and recirculation zones developed due to strut imposed boundary flow hindrance induces flow irregularities and increases the residence time of the blood particles in the stented region. This prolonged exposure of blood particles in the vicinity of stent wall increases the chances of thrombosis which results in restenosis. In contrast, in case of VADs supported with stent the rotational flow induced by the pump increases the velocity gradient at the stent wall and hence the local wall shear stress as seen in Figure 7.38. However, at far upstream and downstream regions of the stent, away from the propeller, one could witness small pockets of struts with low WSS regions, which are negligible in contrast to those seen in a stented artery. This suggests that longer stent supports around the propeller pump would still face the issue of restenosis at the end strut columns, thereby implying usage of shorter stents for pump support. Thus, to conclude, a stented artery embedded with a VAD would have very low chances of restenosis due to the existence of flow turbulence around the pump, keeping low WSS regions at bay.

7.6.2 Stent Hemodynamic Analysis

The baseline stent model designed using the design parameters listed in Mid-Value 2 column in Table 7.12 was initially studied to investigate the effect of the introduction of a stent on blood flow and hemodynamics. Table 7.13 shows the comparison of this base model in four configurations namely: an IVC duct without stent, IVC duct with stent, IVC propeller without stent and IVC propeller with stent.

It could be seen that the effect of stent addition is to increase the Blood Damage Index, Scalar Shear Stress Volume and Particle Residence Time along with increasing the pressure losses due to imposed flow hindrance. The higher values of SSS volume can be attributed to the additional regions located near the Stent column in the immediate vicinity of the propeller

Table 7.13: Stent base model Hemodynamic comparison

Model	**Pressure Drop or Pressure Rise [mm Hg]**	**BDI [%]**	**Scalar Shear Stress Volume** $[\sigma > 50\ Pa]$ $[mm^3]$	**Particle Residence Time [sec]**
IVC Duct	0.616	7.75E-06	NA	0.3937
Stented IVC Vessel	0.620	2.65E-05	NA	0.4342
IVC Propeller without stent	5.47	3.14E-04	6.781	0.195
IVC Propeller with stent	4.462	1.69E-03	11.36	0.38433

blade as depicted in Figure 7.39, which also shows how the circumferential blood particle tracks within the clearance region are trapped inside the mid-stent area thereby increasing the average time required by them to exit the flow domain.

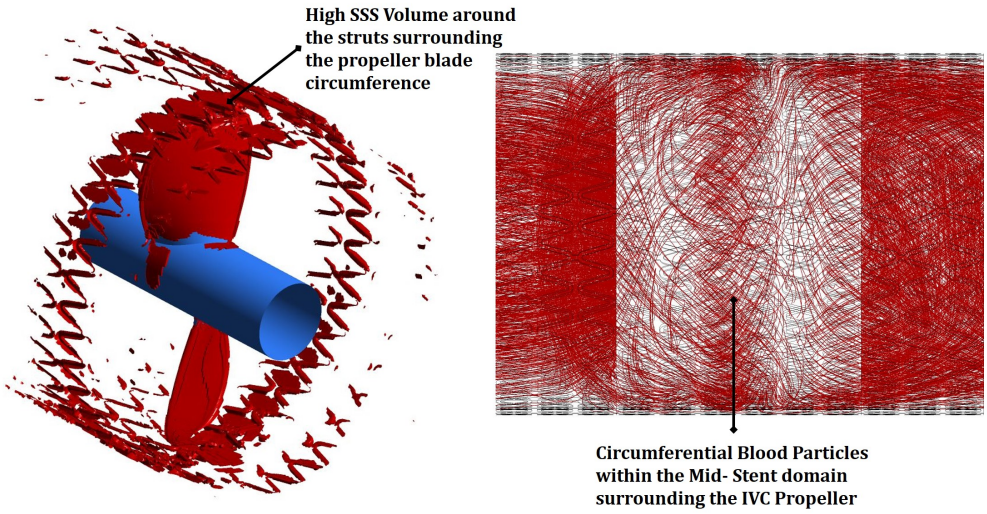

Figure 7.39: Scalar Shear Stress Volume distribution around a stented IVC propeller (left) and Blood Particle tracks within the stent propeller shroud annular region (right)

Thus, it can be concluded that stent addition has a negative impact on propeller performance as well as on blood damage and the objective is to develop a stent design that will have low pressure losses and Blood Damage Index. The analysis done above for the base model is repeated for all the remaining 15 design points whose results are graphically shown in Figure fig:stentparametricstudyresults, where the black marker denotes the results obtained for the base stent design.

One critical inference that can be made from the plots is that for all the design parameters except for strut number, the Blood Damage Index is correlated with Pressure Rise. Meaning higher the pressure rise, higher the blood shear stress and hence higher chances of RBC rupture.

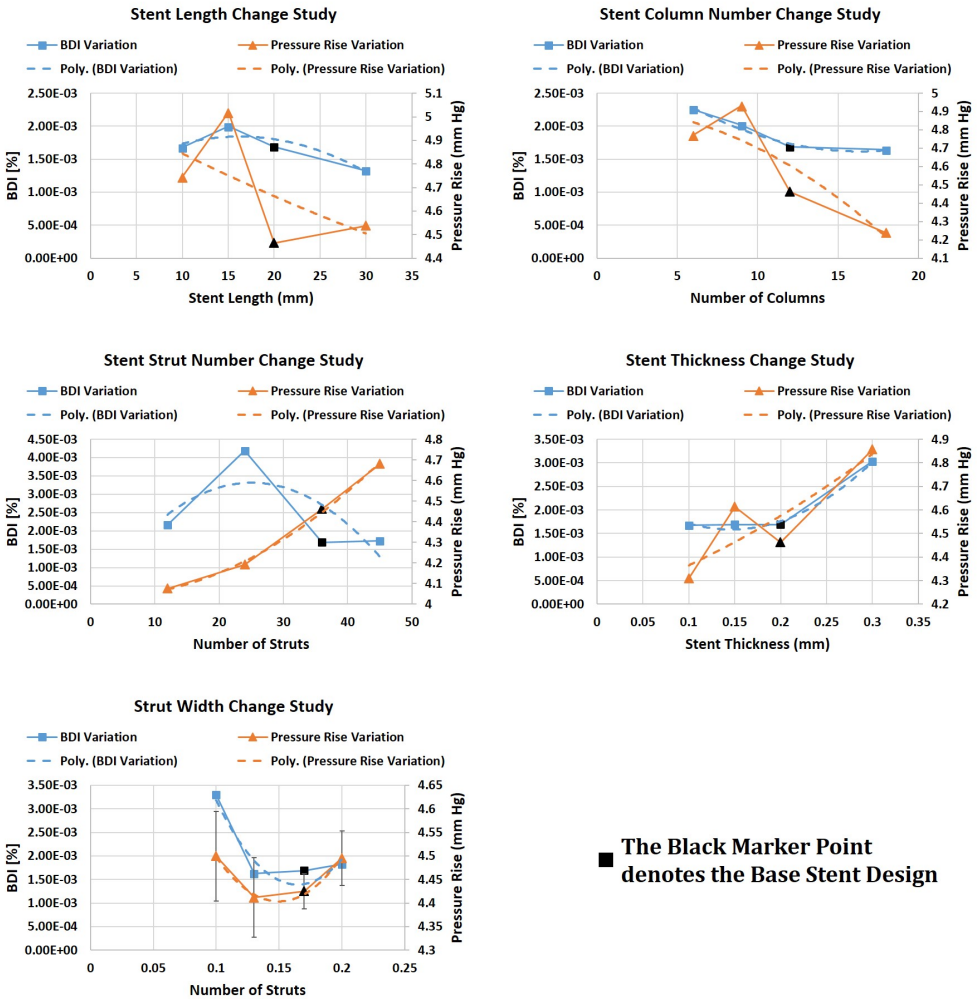

Figure 7.40: Stent Parametric Study Results

The trend lines for the BDI and Pressure Rise variation with each design parameter shows that stent length and column change have a negative impact on blood damage and pressure rise. An increase in Length and Column Number is analogous to increasing hindrance along the flow path thereby contributing to higher flow losses. Similarly, an increase in stent thickness shows an increasing trend in pressure rise and Blood Damage since a thicker stent would occupy a greater portion of the annular area between the propeller blade tip and the vessel wall. This reduces the blade tip clearance and hence the pressure losses due to a reduction in tip flow recirculation as it is witnessed in an axial flow device with high blade tip clearance. In case of strut number change study, an increase in the number of struts would produce a denser stent mesh with more frequent but smaller gaps between the struts. Thus an increase in strut number would mean an approach towards a more smoother stent wall with lesser flow irregularities. This would help to reduce flow hindrance and at the same time reduce

the particle residence time, thereby reducing the blood damage. For the final design parameter, i.e. the stent width, there is no explanation to describe the observed inverse parabolic behaviour of pressure rise and blood damage.

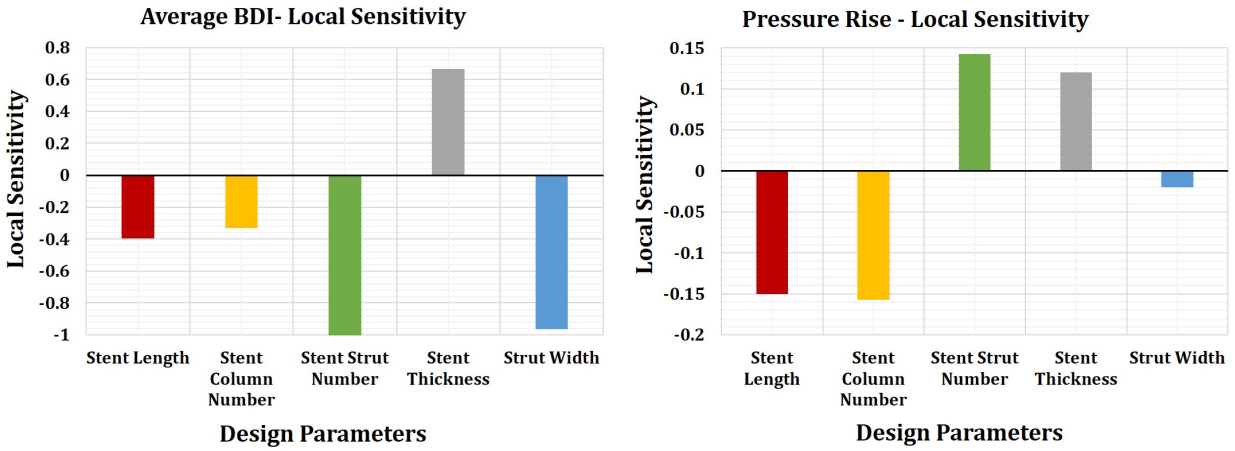

Figure 7.41: Local Sensitivity of BDI and Pressure rise to Stent Design Parameters

The magnitude of the effect of the 5 design parameters on Average BDI and Pressure Rise can be represented in terms of Local Sensitivity Plots obtained from ANSYS Workbench Response Surface Analysis. The results obtained for the parametric study done earlier are given as input to the Response Surface Optimization Module In Ansys and a non-parametric regression method was selected to obtain the local sensitivity plots. The Local Sensitivity chart is a powerful tool which allows the user to see the weight of the different input parameters on each output. It calculates the change of the output based on the change of each input independently, at the current value of each input parameter defined in the project [113]. The sensitivity chart at base design input point shows the trend for each parameter explained in detail in the parametric study. It could be seen that strut width has a negligible effect on pressure rise but helps to reduce the blood damage, thus inferring allowance to high values of strut width. Similarly, it is preferable to have more struts since it reduces the damage potential and increases the pressure rise. Similar inferences could be made for different design parameters. However, instead of manually analyzing each design parameter, the ANSYS Multi-Objective Genetic Algorithm (MOGA) optimization method is used to determine the optimal design point that fulfills the objective of minimum blood damage and maximum pressure rise. The values of design parameters obtained for the optimal candidate point are shown in Table 7.14. These values are then used to design the optimal stent model which is analyzed to determine the actual Blood Damage and Pressure Rise values which are listed in Table 7.14. The target was to achieve a stent design with BDI less than 2e-3 % and a Pressure Rise of greater than or equal to 5 mm Hg which is the physiological demand in the studied Fontan patients and it could be seen that the evaluated design meets those requirements and hence is selected for the final dual propeller assembly analysis. The results for the average BDI and pressure rise obtained from the optimization study are evaluated for a long straight

IVC duct shown in Fig. 7.37, however, these values are not indicative of the pressure rise and the blood damage that would be incurred for the stented dual propeller pump configuration and hence they are significant from comparison point of view to select an optimal stent design.

Table 7.14: Design Parameters of Stent at Optimal Point

Design Parameters	**Value**
Stent Length [mm]	15
Stent Column Number	11
Number of Struts	39
Stent Thickness [mm]	0.2
Stent Width [mm]	0.16
Performance Parmaeters	**Value**
Blood Damge Index [%]	1.91e-03
Pressure Rise [mm Hg]	5.002

7.7 Final Dual Propeller Assembly Analysis

Having analyzed various components of the percutaneous cavopulmonary pump and selected the most suitable one for the current application, a final dual propeller assembly can be evaluated numerically by adding all the components to the CFD setup. The final design (shown in Figure 7.1) and the corresponding CFD setup model shown in Figure 7.42 consists of the IVC and SVC propeller separated at a distance of 37.5 mm from the center and supported by a stent body modeled using the optimal parameters determined in the previous section. The central confluence of the TCPC is made Flared with a curvature radius of 20 mm to comply with outcomes obtained from the TCPC geometry study. The IVC and SVC stent body is connected to the central and end shaft support bearing housings which are part of the stationary domain. The long tube extending inside the IVC represents the catheter carrying wires to supply power to the motor mounted inside the housing seen on the upstream side of the IVC propeller.

The final dual propeller assembly was numerically investigated using CFD analysis at the design point for the net power gain, the amount of blood damage induced and the pressure reduction inside IVC and SVC branches. The corresponding results are displayed in Table 7.15 which compares the dual propeller assembly without stent and catheter evaluated in the previous section with the final assembly. As one would expect, the addition of stent increases the Blood Damage Index for the IVC and SVC blood particles by almost 2 times, which is supported by a visible increase in SSS volume and blood particle residence time in comparison to the pump without the stent. The increased value of BDI to around 5.5e-04 %

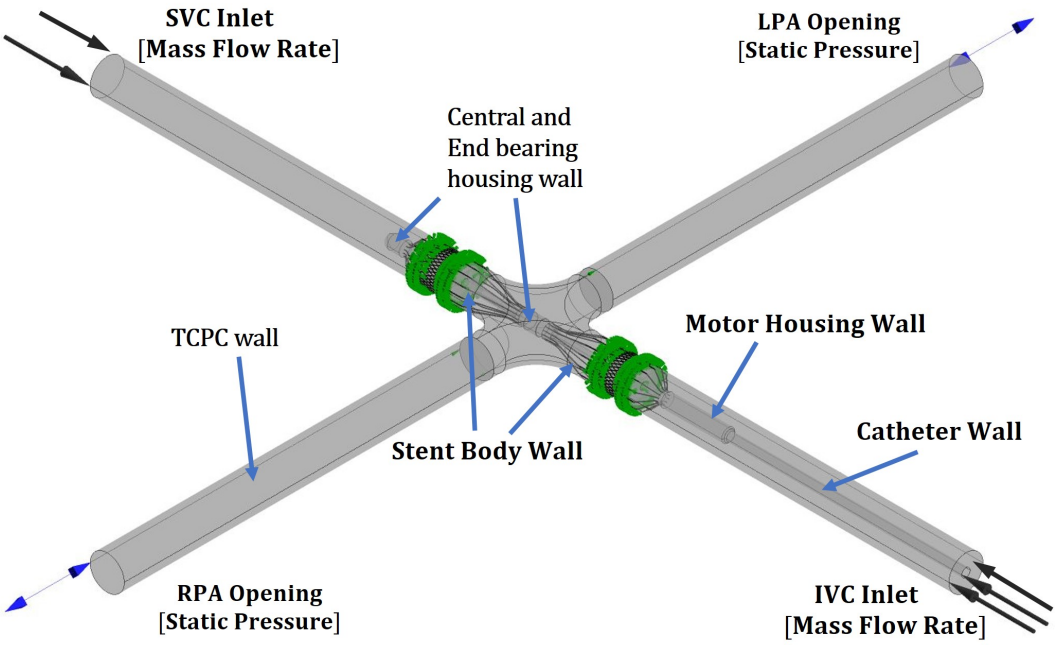

Figure 7.42: CFD Setup of the Final Dual Propeller Pump Assembly

for the stent covered pump shouldn't be a matter of concern because comparable BDI values were found for the comprehensive hemolysis index analysis study performed by Fraser et al. on similar sized three axial flow ventricular assist devices. The values of BDI found by Fraser et al. for the evaluated three axial flow pumps ranged from 5e-04 % to 6.2e04 %. Also, it is worth mentioning that the axial flow pumps didn't have a stent body surrounding the pumps and that the high values of HI were witnessed since they were used for left ventricular assistance which requires higher pressure rise across the pump explaining the large values of BDI in their case. The effect of stent is also visible on power gain and IVC-SVC inlet pressure which is decreased and increased respectively as compared to the base model effectively resulting in an IVC-PA and SVC-PA pressure rise of 5.594 mm Hg and 5.55 mm Hg respectively. Even though the addition of stent reduces the propeller performance, it is a necessary component to be introduced without which there are no other means to support the pump and prevent the pump blades from contacting the vena cava wall. Moreover, the hepatic fluid split from IVC was found to be 51% and 49% to the left and right lung suggesting that the pump is able to reach the required target of reducing the pressures inside the vena cava to physiological values while augmenting and equally distributing blood to both the lungs.

The final analysis is done to evaluate the hindrance imposed by the stationary pump body to blood flowing through the cavopulmonary connection in the event of power outage or mechanical failure, by comparing the increase in power loss between the Flared TCPC model and the one embedded with dual propeller pump. The CFD setup was same as the one used for the analysis done above with the difference of defining everything within the stationary

Table 7.15: Dual Propeller Pump Performance Comparison for model with and without stent-catheter assembly

	Pump Model	
Comparison Parameters	**Dual Propeller with Stent and Catheter**	**Dual Propeller withtout stent**
Power Gain [mW]	47.047	63.398
Blood Damage Index [%]:		
IVC Inlet	2.96E-04	1.86E-04
SVC Inlet	5.41E-04	2.69E-04
Critical Scalar Shear Stress Volume [mm^3] [$\sigma > 50\ Pa$]:	23.59	18.80
Particle Residence Time [sec]		
IVC Inlet	0.61	0.574
SVC Inlet	0.88	0.80
Vena Cava Pressure [mm Hg]		
IVC Inlet	7.21	6.81
SVC Inlet	7.25	7.10
Pressure Rise [mm Hg]		
IVC Propeller	5.59	5.99
SVC Propeller	5.55	5.71

domain. The results for this comparison are shown in table 7.16. It could be seen that an event of propeller stoppage or breakdown would increase the fluid power loss by 60.83 % over that found for blood flow through TCPC without a pump. The blockage in blood flow passage by the stationary dual propeller pump increases blood particle travel time only by 0.05 sec in the inferior vena cava tract, however, it slows down the particles in SVC tract by almost 0.2 sec. It is obvious that the particles traveling from SVC would take longer time given the additional flow resistance at the central confluence imposed by high inertia blood flowing from the IVC.

The blood particle flow paths, shown in Figure 7.43, comparing the IVC and SVC cavopulmonary flow for the two configurations confirms that the pump wouldn't block blood flow even in the event of a breakdown. The pressure inside the IVC and SVC tract is increased only by 6.357% and 0.5% thereby negligibly increasing the chances of hypertension inside the vena cava in comparison with the conditions existing in a Flared TCPC without a pump. Even though the pump body doesn't affect the flow path, it surely does increase the amount of work required by the single ventricle to push the flow past the pump into the lungs. Thus

Table 7.16: Flared TCPC with and without Dual Propeller Pump Assembly Performance Comparison

Comparison Parameters	**Stationary Dual Propeller with stent**	**Flared TCPC without pump**
Power Loss [mW]:	15.0287	9.344
Particle Residence Time [sec]:		
IVC Inlet	0.6757	0.62994
SVC Inlet	1.004	0.8388
Pressure [mm Hg]:		
IVC Inlet	14.620	13.757
SVC Inlet	14.04	13.97

under such circumstances, it would be advisable to remove the catheter-based pump out of the vena cava by first covering it with a catheter sheath and then pulling it out.

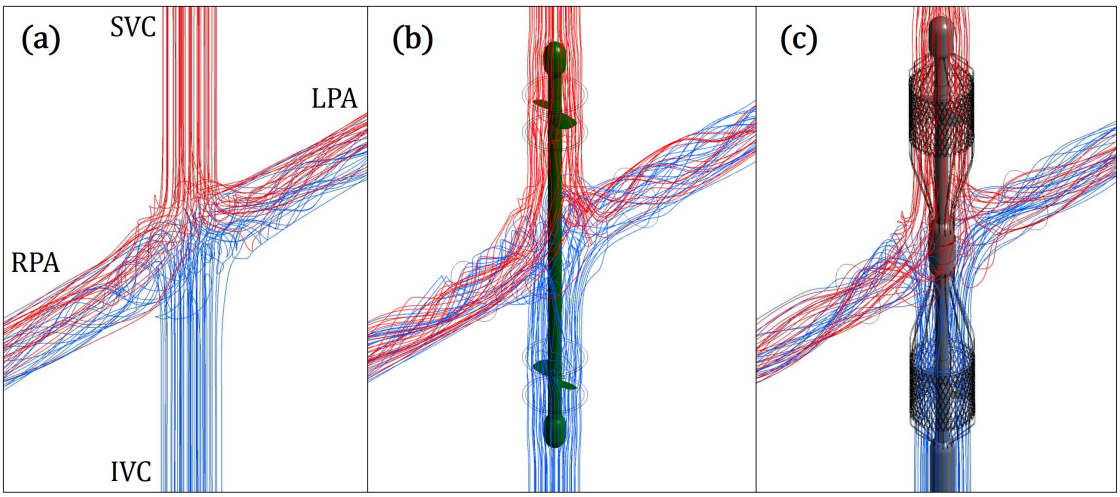

Figure 7.43: Comaprison of IVC and SVC blood flow streamlines and Power Loss for: (a) Flared TCPC, (b) Dual Propeller Pump without stent and catheter, and (c) Dual Propeller Pump with stent and catheter

7.8 Potential Conceptual Dual Propeller Stand-Alone Pump

Before concluding this chapter, the author wants to illustrate a potential design for the future which could have superior behaviour in terms of pump's performance to unload the single

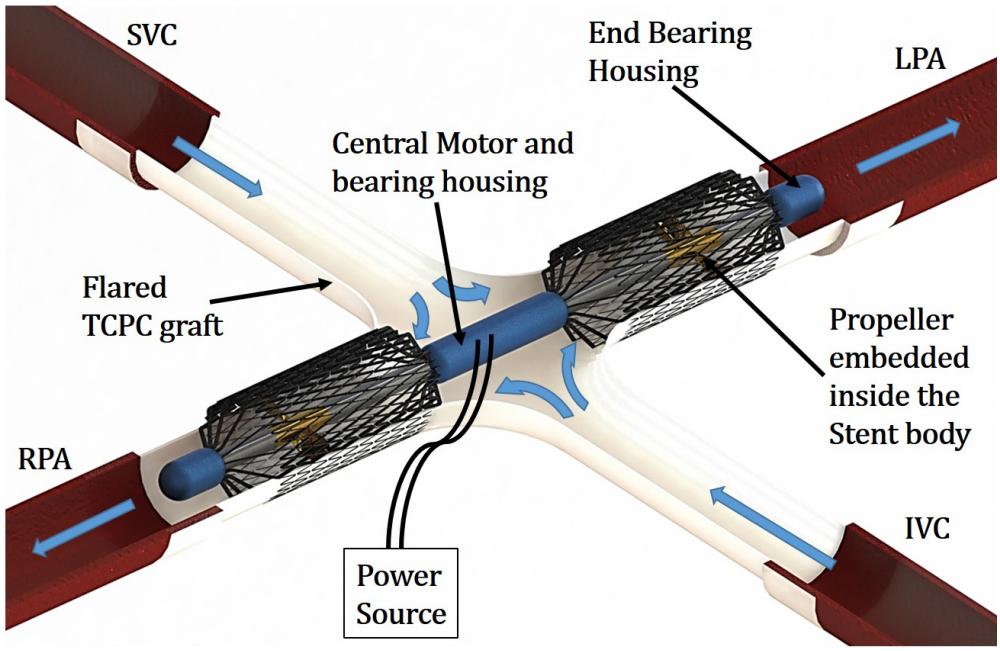

Figure 7.44: Stand alone dual propeller pump configuration

functional ventricle. It was seen in the previous study that the introduction of catheter and motor housing to the final pump assembly led to an increase in pressure inside the IVC tract resulting in a reduction in pressure rise across the pump. As a workaround to this problem, the author visualizes a stand-alone dual propeller pump design having the motor mounted at the center and the propellers located inside the left and right pulmonary arteries with the suction side of the blade facing the center and pressure side facing the lungs as shown in Figure 7.44. The motor is not wired to an external power source but to an internally or externally harvested energy source. Such an energy source can be energized with the help of piezoelectric crystals attached to the body parts or to an internal organ like the heart which is continuously pulsating thereby generating energy by the virtue of its motion. As displayed in the Figure 7.44, the stent body will be embedded within the central Dacron or Teflon graft similar to commercially available Gore Stent Grafts. A dual shaft motor with coupler and bearings will be housed inside the central housing which will provide same motion and speed to the propellers attached to the motor shafts.

The main distinguishing factors of this design as compared to the catheter-based design are that the propellers are placed inside the pulmonary arteries instead of venae cavae (singular vena cava) and that there is no need to design two propellers for different inlet conditions since both the pumps will have same inflow rate given that the flared TCPC geometry equally distributes the blood to both the pulmonary arteries. Since the IVC propeller was designed for higher pressure augmentation, it has been used for the preliminary analysis of this stand-alone device. For the same physiological boundary conditions as those used for dual propeller assembly, the comparison of the two dual propeller configurations could be

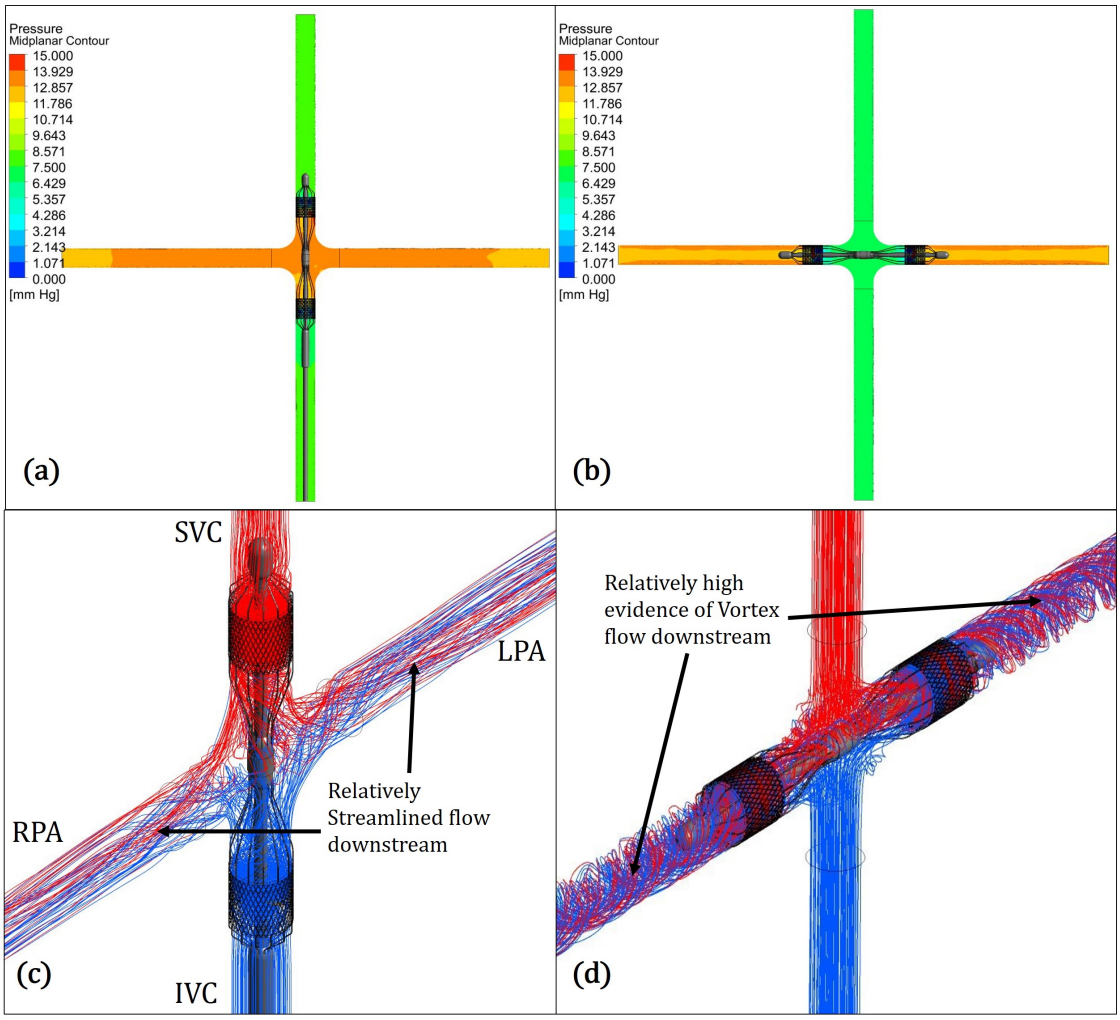

Figure 7.45: Comparison of Catheter Based Dual Propeller Pump (a and c) and Horizintal Stand Alone Pump (b and d) in terms of pressure contour and velocity streamlines

shown as in Figure 7.45 which displays how a streamlined flow developed upto the central motor housing in case of stand-alone pump is converted into helical streams downstream of the propeller whereas the central motor housing in case of catheter pump reduces the intensity of flow mixing at the center thereby targeting the source of vortex flow generation downstream inside the pulmonary arteries. The comparison of pressure contours between the two configurations depicts that the blood pressure is reduced for the entire length of vena cava blood vessel in case of horizontally placed propellers and the pressures at the inferior and superior vena cava inlet are lower than those found for the catheter-based dual propeller assembly by 0.97 mm Hg and 0.613 mm Hg which even though negligible, significantly improves the lung perfusion and left ventricular filling. However, the increased pressure rise and the induced vortex flow downstream of the propellers inside the pulmonary arteries

leads to an increase in blood damage index and the corresponding critical scalar shear stress volume [$\sigma > 50\ Pa$] for the stand-alone pump over the catheter-based pump by almost 40% and 15% respectively.

Inferring from the results, it could be concluded that the stand-alone configuration could provide promising hydraulic performance improvement at the cost of blood cell trauma. However, the drawback of increased particle damage could be reduced by optimizing the pump design.

This chapter illustrated how each component of a VAD pump was designed and analysed for flow hemodynamics, blood damage potential and hydraulic performance to decide the optimal design characteristics for the pump. The experimental and numerical results discussed in this chapter confirmed that the proposed dual propeller pump design would potentially help to reduce the single ventricle overload while ensuring the blood damage to be under control. Even though the number of parameters and design points evaluated was handful, it provides a good initial base for future optimization studies to potential researchers designing percutaneous assist device for Fontan patients.

Chapter 8

Conclusion and Future Scope

The current thesis outlined in detail the step by step methodology to design and develop a novel percutaneous dual propeller pump. The objective was to develop a pump which could assist the single functional ventricle of Fontan patients by generating a modest pressure rise of 5-6 mm Hg to augment the flow from the Superior and Inferior Vena Cava to the lungs. The main objective of this thesis was to introduce an ideal cavopulmonary assist device for patients with single ventricular physiology and the current thesis demonstrated the potential of the proposed dual-propeller assist device to fulfill the set objective. This chapter briefly summarizes the outcomes of research and discusses the limitations and potential improvements and additions to the design of the pump and test setup.

8.1 Summary of Research Outcomes

As a starting point in any product development process, the current thesis defined the need of an assist device by introducing the congenital heart defect (CHD) of ventricle hypoplasia or single functional ventricle and discussing how a patient diagnosed with such defects are treated to unload the single functional ventricle. As it was discussed in Chapter 1, the three-stage palliation procedure including the Fontan Completion, is often adopted to treat such patients with single functional ventricle, however, the resulting extra-cardiac total cavopulmonary connection led to decreased cardiac output, non-physiologic flow pattern, hypertensive vena cava, lower lung perfusion, and left ventricular filling. The long-term existence of these non-physiologic conditions was shown to impair the single functional ventricle and increase the risk of mortality in Fontan patients.

Keeping the deficiencies of the Fontan Completion outcome in mind, a novel concept of percutaneous dual propeller pump was introduced to augment the flow from vena cava to the lungs and assist the Fontan patients and was investigated numerically, and experimentally in this thesis.

The first part of the thesis concentrated on the selection of an optimal Total Cavopulmonary Connection (TCPC) that will help to reduce flow losses and load acting on the single ventricle. The preliminary analysis of four different TCPC geometries showed how flaring or providing a moderate radius of curvature at the site of anastomosis of the IVC, SVC, LPA, and RPA could help to reduce the flow losses and provide equal distribution of hepatic fluid from the IVC to both the lungs. The Flared TCPC configuration ensured that there was a minimal bias of blood flowing to the lungs which would prevent the development of pathological condition like arterio-venous malformation. The numerical CFD model of the selected Flared TCPC model was validated by comparing the results for power losses at different IVC:SVC flow split and cardiac outputs with the experimental results as it was shown in Chapter 6.

This thesis demonstrated that an inverse design method implementing the classical Rankine-Froude's blade element momentum theory along with the Goldstein's radial momentum loss function could successfully be used to generate blade profiles fulfilling the pressure requirements inside the cavopulmonary tract. The last part of Chapter 5 verified the propeller performance output from the code developed by the author by comparing it with that obtained from the MIT researchers' developed vortex-lattice method based OPEN Prop code for the same design inputs. The Adkins-Liebeck proposed optimization method based on above-mentioned theories was originally developed for designing marine propellers and hence was not completely applicable to generate a propeller that could be used for ventricular assistance and that an initial study had to be performed for determining the relation between the free stream flow and the actual flow through the propeller blade disk. This had to be done keeping in mind the propensity of blood recirculation from downstream of the propeller to upstream from the large radial clearance between the blade tip and the vena cava wall. However, once the approximate though flow relation is know, which in this case came out to be three times the free stream flow, the IVC and SVC propellers were able to provide the required pressure augmentation of 5-6 mm Hg at the physiological IVC to SVC flow split of 63:37 while rotating at 8000 rpm as evaluated using CFD analysis. The hydraulic performance of the IVC and SVC propeller pumps showed a downward sloping but relatively flat pressure profile with the flow rate. The performance curves confirmed that the pump has a capability of generating pressures up to 20 mm Hg for flow rates and operating speeds ranging from 0.5 to 7 l/min and 6000 - 12000 rpm respectively. The confidence in the CFD based numerical results for the performance of the IVC and SVC propellers operating in water was increased by the experimental validation and verification which demonstrated a good agreement with a maximum of 20% error which was introduced due to the flow losses in settling chamber and minute leakages from the bearing race.

The Section 7.3 of Chapter 7 briefly highlighted and confirmed, the drawbacks of single vena cava flow assistance by a placing a single circulatory support device inside the IVC, both numerically and experimentally. The flow simulations, as well as the pressure readings from the experiment, proved the development of high pressures in the SVC tract demonstrating the cause of vena cava hypertension for the case of single vena cava assistance.

In response, the Dual Propeller configuration having propellers symmetrically placed inside

the IVC and SVC tract from the center of the TCPC helped to reduce the vena cava pressure to normal physiological values of around 6-8 mm Hg while increasing the lung perfusion pressure and equally distributing the flow to the pulmonary arteries. It was observed in Chapter 7 and Section 7.4 that the propeller placement from the center played an important factor in terms of pressure losses and blood damage with smaller separation distances indicating a higher relative occurrence of vena cava cross flow and mixing at the center and higher pressure generation which reduces as the propellers are moved away from the center.

Chapter 3 of this thesis explained how scalar shear stress imposed by a blood pump and blood particle residence time causes red blood cell rupture and how this rupture induced blood damage by an assist device could be predicted using mathematical models. The Blood Damage Index code developed using Grigioni's modified power law model and the Heuser-Optiz's model constants were used throughout this thesis for Hemolysis prediction. It was observed that factors like high pressure, large recirculation, central flow mixing and agitation increased the chances of RBC rupture due either the existence of high critical scalar shear stress volume ($>$ 50 Pa) or prolonged exposure to moderate shear stresses. The employed Lagrangian particle tracking method in the numerical studies to determine the blood particle tracks in conjunction with the mathematical model was used to determine the BDI. The average BDI of 3e-04% to 4e-04% was observed for the single and dual propeller configuration which was found to be acceptable based on the previous research and findings for similar sized axial flow blood pumps. This finding proved that the dual propeller pump configuration could be used for cavopulmonary assistance without any potential issue of blood damage.

The thesis also highlighted the first ever attempt made to comprehensively study the effect of stent support system on cavopulmonary assist device's performance while considering the effect of blood damage. The findings showed that an optimal stent design should have a low thickness, smaller lengths, lesser number of strut columns while it is favorable to have a large number of struts with moderate width to obtain low blood damage and pressure losses.

In this way, the current thesis provided a comprehensive outline of the design methodology, numerical analysis, and experimental validation supporting the novel idea of utilizing a minimally invasive single shaft dual propeller pump that could potentially assist a Fontan patient without any risk of blood damage.

8.2 Limitations and Future Scope

As discussed in the summary, the proposed method for cavopulmonary pump blade design and optimization was originally developed for large-scale applications like marine propellers mainly for applications having flow Reynolds number to be higher than 10^5. However, this is not the case for blood pumps and hence the propellers designed with such a method would experience higher viscous losses, consequently resulting in lower efficiencies as it was demonstrated in this thesis. The problem could, however, be tackled by adopting the open

source code like XFOIL (developed for low Reynold's number flows) which pre-investigates different airfoil profiles in its directory for the given design inputs to select the suitable airfoil series that would give minimal drag and maximum lift for the flow Reynold's numbers experienced for a blood pump. This airfoil series could then be used to decide on the blade camber, chord and thickness distribution and can as the input to the VADProp code to generate a propeller blade suitable for blood pumping application. Furthermore, a detailed study on Turbulence models could be performed in order to see its effect on flow convergence and performance parameters of the blood pump.

The flow simulations were performed in steady state without considering the effect of small pulsations experienced by the blood flowing into the cavopulmonary tract. In addition to this, the numerical analysis neglected the blood vessel and lung compliance which would change the flow resistance inside venae cavae and pulmonary arteries. These could be analysed by defining the inlet flow rate and outlet pressures as a function of time and performing transient flow simulations to better mimic the flow physiology actually experienced inside the cavopulmonary tract.

In this thesis all the experimental studies were done with water which gave the preliminary validation of the proposed design, however, they didn't demonstrate the pumps performance with blood as the working fluid and the amount of blood damage induced. This could be performed in stages with first set of experiments conducted with 60:40 mixture of water and glycerine having same density and viscosity as that of blood. Following the successful results obtained from the first test, the next test, which is an in-vitro test, would be performed with blood bag where fresh bovine blood would be circulated inside the test rig and the corresponding relative increase in plasma free hemoglobin content would be determined to provide a more realistic estimation of blood trauma or Hemolysis Index. In order to obtain more accurate results, it is necessary to 3D print the propeller blades using DMLS (Direct Metal Laser Sintering) technique which will precisely capture and manufacture all the blade intricacies and at the same time increase the blade strength. Besides, the settling chamber part of the experimental test setup needs to be modified to induce lower flow resistance.

Experimental setup could be modified to incorporate Particle Image Velocimetry (PIV) or Laser Doppler Anemometry (LDA) testing methods to visualize the flow path, velocity profile, flow gradients along the pipe wall and blade surface to accurately predict the wall shear stress.

The stent design analysis performed in this thesis didn't consider the effect of design parameters on its strength which could be analysed by implementing fluid-structure interaction (FSI) studies where the pressure exerted by the fluid in contact with the stent body computed from CFD solver is transferred to the Finite Element solver for deformation and critical stress calculations.

Finally, The design of the central motor or bearing housing in the final dual propeller assembly needs to be optimized to have minimum cross flow and mixing of blood at the center to effectively increase the augmented pressure and improve blood distribution to the lungs.

8.3 Research Significance and Conclusion

The current research demonstrated the development of a novel dual propeller pump which was the first ever attempt of its kind to have two propeller pumps mounted on a single shaft to assist patients with single ventricular physiology or patients born with hypoplastic right ventricle. Currently, there is no device existing in the market specifically developed to assist Fontan patients. The attempts of using the available percutaneous and implantable assist devices have shown limited success for long-term assistance with a number of post-implantation complications such as bleeding and thromboembolism along with elevated central venous pressure, and flow obstruction due to the need for an occlusive mechanism was evident from the clinical studies performed with these devices as it was mentioned in Chapter 1. Heart transplantation is the best available option to provide definitive therapy to such patients, however, the lack of availability of donor hearts, the unique physiological needs of each patient, and the mismatch of heart sizes between the donor and recipient results in a long waiting period for the Fontan patients. During the long waiting period, the physiological condition of the functional ventricle and other vital organs deteriorates and ultimately increases the chances of mortality in such patients.

The current research targeted this problem and aimed at developing an assist device which could assist the Fontan patients during their waiting period by keeping in mind that the pump provides a modest pressure rise to bring the flow conditions closer to that experienced by a normal person. The ideal pump design is required to be small in size, have less number of parts for minimal exposure of the foreign material to blood, pose a minimal obstruction to the blood flow in case of power outage or mechanical failure and be easily inserted and supported inside the total cavopulmonary connection. This thesis, which showed the preliminary attempt to design such a pump, met most of the ideal cavopulmonary pump requirements by using only two propeller blades for the IVC and SVC pumps, making the pump blades and the stent support foldable (by making them out of Nitinol), using single shaft embedded with two propellers to facilitate the use of a single motor, had lower number of parts while allowing for a single minimally invasive percutaneous insertion. All these features make the current proposed device unique and an ideal candidate for a cavopulmonary assistance. Besides, from performance and blood damage point of view, the current thesis demonstrated the capability of the propeller pumps both numerically and experimentally to generate a modest pressure rise of 5-6 mm Hg at the design speed of 8000 rpm and at the physiological flow rates experienced within the IVC and SVC. Moreover, the blood damage index calculations showed a superior performance of the proposed pump with the average Blood Damage Index less than $10^{-3}\%$ for all the evaluated designs, which was less than or comparable to that experienced during clinical trials for axial flow blood pumps by other researchers.

The present thesis acts as the first step of the design process of the proposed device and acts as a stepping stone for future developments targetting the limitations and shortcomings of this thesis that were discussed in Section 8.2. The above-mentioned points and the outcomes discussed in this thesis show that the proposed percutaneous dual propeller cavopulmonary

assist pump could potentially provide assistance to Fontan patients by unloading the single functional ventricle thereby acting as a bridge to transplantation and recovery.

Bibliography

[1] "normal heart circulation diagram." https://organanatomy.com/tag/normal-heart-circulation-diagram/.

[2] "Tricuspid atresia." https://www.rch.org.au/cardiology/heart_defects/Tricuspid_Atresia/.

[3] "Pulmonary atresia with vsd." https://www.rch.org.au/cardiology/heart_defects/Pulmonary_Atresia_with_VSD/.

[4] "Hypoplastic left heart syndrome hd." https://www.rch.org.au/cardiology/heart_defects/Hypoplastic_Left_Heart_Syndrome_HD/.

[5] "Double inlet left ventricle dilv." https://www.rch.org.au/cardiology/heart_defects/Double_Inlet_Left_Ventricle_DILV/.

[6] "Double outlet right ventricle." https://www.rch.org.au/cardiology/heart_defects/Double_Outlet_Right_Ventricle/.

[7] "Information for patients and parents about the fontan operation." https://www.rch.org.au/cardiology/parent_info/Information_for_patients_and_parents_about_the_Fontan_Operation/.

[8] The Berlin Heart Inc., The Woodlands, Texas, *EXCOR Pediatric VAD: Instructions for Use*, 8th ed., 2016.

[9] https://www.heartware.com/resources.

[10] http://www.abiomed.com/impella/impella-rp.

[11] http://www.cardiobridge.com/product/reitan-catheter-pump-10f/.

[12] R. Whitemore, "Rheology of the circulation,(1968)," *Received June*, vol. 12, 1975.

[13] J. Carlton, *Marine propellers and propulsion*. Butterworth-Heinemann, 2012.

[14] D. R. Francis, "Why do death rates decline?." http://www.nber.org/digest/mar02/w8556.html.

[15] H. Nichols, "The top 10 leading causes of death in the united states," 23 February 2017 2017. https://www.medicalnewstoday.com/articles/282929.php.

[16] K. Tanner, N. Sabrine, and C. Wren, "Cardiovascular malformations among preterm infants," *Pediatrics*, vol. 116, no. 6, pp. e833–e838, 2005.

[17] S. M. Gilboa, O. J. Devine, J. E. Kucik, M. E. Oster, T. Riehle-Colarusso, W. N. Nembhard, P. Xu, A. Correa, K. Jenkins, and A. J. Marelli, "Congenital heart defects in the united states: Estimating the magnitude of the affected population in 2010," *Circulation*, vol. 134, no. 2, p. 101, 2016.

[18] J. H. Moller, K. A. Taubert, H. D. Allen, E. B. Clark, and R. M. Lauer, "Cardiovascular health and disease in children: current status. a special writing group from the task force on children and youth, american heart association.," *Circulation*, vol. 89, no. 2, pp. 923–930, 1994.

[19] "Single ventricle defect."

[20] J. Beckeman, "Anatomy and circulation of the heart."

[21] M. Gewillig and D. E. Boshoff, "Missing a sub-pulmonary ventricle: the fontan circulation," in *The right ventricle in health and disease*, pp. 135–157, Springer, 2015.

[22] F. Fontan and E. Baudet, "Surgical repair of tricuspid atresia," *Thorax*, vol. 26, no. 3, pp. 240–248, 1971.

[23] F. Fontan, J. W. Kirklin, G. Fernandez, F. Costa, D. C. Naftel, F. Tritto, and E. H. Blackstone, "Outcome after a" perfect" fontan operation.," *Circulation*, vol. 81, no. 5, pp. 1520–1536, 1990.

[24] M. R. de Leval, "The fontan circulation: What have we learned? what to expect?," *Pediatric cardiology*, vol. 19, no. 4, pp. 316–320, 1998.

[25] Y. Kotani, S. Kasahara, Y. Fujii, K. Yoshizumi, Y. Oshima, S.-i. Otsuki, T. Akagi, and S. Sano, "Clinical outcome of the fontan operation in patients with impaired ventricular function," *European Journal of Cardio-Thoracic Surgery*, vol. 36, no. 4, pp. 683–687, 2009.

[26] M. Gewillig, "The fontan circulation," *Heart*, vol. 91, no. 6, pp. 839–846, 2005.

[27] P. Khairy, S. M. Fernandes, J. E. Mayer, J. K. Triedman, E. P. Walsh, J. E. Lock, and M. J. Landzberg, "Long-term survival, modes of death, and predictors of mortality in patients with fontan surgery," *Circulation*, vol. 117, no. 1, pp. 85–92, 2008.

[28] K. N. Pundi, J. N. Johnson, J. A. Dearani, K. N. Pundi, Z. Li, C. A. Hinck, S. H. Dahl, B. C. Cannon, P. W. O'Leary, D. J. Driscoll, *et al.*, "40-year follow-up after the fontan operation: long-term outcomes of 1,052 patients," *Journal of the American College of Cardiology*, vol. 66, no. 15, pp. 1700–1710, 2015.

[29] J. Rychik, "Protein-losing enteropathy after fontan operation," *Congenital heart disease*, vol. 2, no. 5, pp. 288–300, 2007.

[30] P. Rao, "Protein-losing enteropathy following the fontan operation.," *The Journal of invasive cardiology*, vol. 19, no. 10, p. 447, 2007.

[31] J. Rychik, D. Goldberg, and K. Dodds, "Long-term results and consequences of single ventricle palliation," *Progress in Pediatric cardiology*, vol. 29, no. 1, pp. 19–23, 2010.

[32] K. Pundi, K. N. Pundi, P. S. Kamath, F. Cetta, Z. Li, J. T. Poterucha, D. J. Driscoll, and J. N. Johnson, "Liver disease in patients after the fontan operation," *The American journal of cardiology*, vol. 117, no. 3, pp. 456–460, 2016.

[33] I. Lindsay, J. Johnson, M. D. Everitt, J. Hoffman, and A. T. Yetman, "Impact of liver disease after the fontan operation," *The American journal of cardiology*, vol. 115, no. 2, pp. 249–252, 2015.

[34] B. W. Duncan, J. M. Kneebone, E. Y. Chi, V. Hraska, F. F. Isik, G. L. Rosenthal, T. K. Jones, S. L. Starnes, and F. M. Lupinetti, "A detailed histologic analysis of pulmonary arteriovenous malformations in children with cyanotic congenital heart disease," *The Journal of thoracic and cardiovascular surgery*, vol. 117, no. 5, pp. 931–938, 1999.

[35] M. N. Kavarana, J. A. Jones, R. E. Stroud, S. M. Bradley, J. S. Ikonomidis, and R. Mukherjee, "Pulmonary arteriovenous malformations after the superior cavopulmonary shunt: mechanisms and clinical implications," *Expert review of cardiovascular therapy*, vol. 12, no. 6, pp. 703–713, 2014.

[36] D. J. Schneider, A. Banerjee, A. M. Mendelsohn, and W. I. Norwood, "Hepatic venous malformation after modified fontan procedure with partial hepatic vein exclusion," *The Annals of thoracic surgery*, vol. 63, no. 4, pp. 1177–1179, 1997.

[37] M. J. Shah, J. Rychik, M. A. Fogel, J. D. Murphy, and M. L. Jacobs, "Pulmonary av malformations after superior cavopulmonary connection: resolution after inclusion of hepatic veins in the pulmonary circulation," *The Annals of thoracic surgery*, vol. 63, no. 4, pp. 960–963, 1997.

[38] P. G. Walker, G. F. Oweis, and K. G. Watterson, "Distribution of hepatic venous blood in the total cavo pulmonary connection: an in vitro study into the effects of connection geometry," *Journal of biomechanical engineering*, vol. 123, no. 6, pp. 558–564, 2001.

[39] S. Sharma, A. Ensley, G. Chatzimavroudis, A. Fontaine, and A. Yoganathan, "Does the addition of curvature at the total cavopulmonary connection (tcpc) site reduce power losses?," in *Journal of the American College of Cardiology*, vol. 29, pp. 4359–4359, Elsevier Science Inc, 655 Avenues of the Americas, New York, NY 10010, 1997.

[40] S. Sharma, S. Goudy, P. Walker, S. Panchal, A. Ensley, K. Kanter, V. Tam, D. Fyfe, and A. Yoganathan, "In vitro flow experiments for determination of optimal geometry of total cavopulmonary connection for surgical repair of children with functional single ventricle," *Journal of the American College of Cardiology*, vol. 27, no. 5, pp. 1264–1269, 1996.

[41] D. D. Soerensen, K. Pekkan, D. de Zélicourt, S. Sharma, K. Kanter, M. Fogel, and A. P. Yoganathan, "Introduction of a new optimized total cavopulmonary connection," *The Annals of thoracic surgery*, vol. 83, no. 6, pp. 2182–2190, 2007.

[42] F. Zafar, C. Castleberry, M. S. Khan, V. Mehta, R. Bryant, A. Lorts, I. Wilmot, J. L. Jefferies, C. Chin, and D. L. Morales, "Pediatric heart transplant waiting list mortality in the era of ventricular assist devices," *The Journal of Heart and Lung Transplantation*, vol. 34, no. 1, pp. 82–88, 2015.

[43] G. A. Giridharan, S. C. Koenig, J. Kennington, M. A. Sobieski, J. Chen, S. H. Frankel, and M. D. Rodefeld, "Performance evaluation of a pediatric viscous impeller pump for fontan cavopulmonary assist," *The Journal of thoracic and cardiovascular surgery*, vol. 145, no. 1, pp. 249–257, 2013.

[44] M. D. Rodefeld, J. H. Boyd, C. D. Myers, B. J. LaLone, A. J. Bezruczko, A. W. Potter, and J. W. Brown, "Cavopulmonary assist: circulatory support for the univentricular fontan circulation," *The Annals of thoracic surgery*, vol. 76, no. 6, pp. 1911–1916, 2003.

[45] M. D. Rodefeld, S. H. Frankel, and G. A. Giridharan, "Cavopulmonary assist:(em) powering the univentricular fontan circulation," in *Seminars in Thoracic and Cardiovascular Surgery: Pediatric Cardiac Surgery Annual*, vol. 14, pp. 45–54, Elsevier, 2011.

[46] A. L. Throckmorton, K. K. Ballman, C. D. Myers, K. N. Litwak, S. H. Frankel, and M. D. Rodefeld, "Mechanical cavopulmonary assist for the univentricular fontan circulation using a novel folding propeller blood pump," *ASAIO Journal*, vol. 53, no. 6, pp. 734–741, 2007.

[47] A. L. Throckmorton, S. Lopez-Isaza, E. A. Downs, S. G. Chopski, J. J. Gangemi, and W. Moskowitz, "A viable therapeutic option: mechanical circulatory support of the failing fontan physiology," *Pediatric cardiology*, vol. 34, no. 6, pp. 1357–1365, 2013.

[48] J. Zhu, H. Kato, Y. Y. Fu, L. Zhao, C. Foreman, L. Davey, R. D. Weisel, G. S. Van Arsdell, and O. Honjo, "Cavopulmonary support with a microaxial pump for the failing fontan physiology," *ASAIO Journal*, vol. 61, no. 1, pp. 49–54, 2015.

[49] R. K. Riemer, G. Amir, S. H. Reichenbach, and O. Reinhartz, "Mechanical support of total cavopulmonary connection with an axial flow pump," *The Journal of thoracic and cardiovascular surgery*, vol. 130, no. 2, pp. 351–354, 2005.

[50] J. W. Rossano, R. K. Woods, S. Berger, J. W. Gaynor, N. Ghanayem, D. L. Morales, C. Ravishankar, M. E. Mitchell, T. K. Shah, C. Mahr, *et al.*, "Mechanical support as failure intervention in patients with cavopulmonary shunts (mfics): rationale and aims of a new registry of mechanical circulatory support in single ventricle patients," *Congenital heart disease*, vol. 8, no. 3, pp. 182–186, 2013.

[51] S. Weinstein, R. Bello, C. Pizarro, F. Fynn-Thompson, J. Kirklin, K. Guleserian, R. Woods, C. Tjossem, R. Kroslowitz, P. Friedmann, *et al.*, "The use of the berlin heart excor in patients with functional single ventricle," *The Journal of thoracic and cardiovascular surgery*, vol. 147, no. 2, pp. 697–705, 2014.

[52] `https://www.heartware.com/products-technology`.

[53] B. R. Imielski, R. A. Niebler, S. J. Kindel, and R. K. Woods, "Heartware ventricular assist device implantation in patients with fontan physiology," *Artificial organs*, vol. 41, no. 1, pp. 40–46, 2017.

[54] G. J. Arnaoutakis, D. Blitzer, S. Fuller, A. W. Eckhauser, L. M. Montenegro, J. W. Rossano, and J. W. Gaynor, "Mechanical circulatory support as bridge to transplantation for the failing single ventricle," *The Annals of thoracic surgery*, vol. 103, no. 1, pp. 193–197, 2017.

[55] C. M. Haggerty, F. Fynn-Thompson, D. B. McElhinney, A. M. Valente, N. Saikrishnan, J. Pedro, and A. P. Yoganathan, "Experimental and numeric investigation of impella pumps as cavopulmonary assistance for a failing fontan," *The Journal of thoracic and cardiovascular surgery*, vol. 144, no. 3, pp. 563–569, 2012.

[56] B. H. Morray, V. V. Dimas, S. Lim, D. T. Balzer, D. R. Parekh, N. M. Van Mieghem, P. Ewert, D. W. Kim, H. Justino, D. B. McElhinney, *et al.*, "Circulatory support using the impella device in fontan patients with systemic ventricular dysfunction: A multicenter experience," *Catheterization and Cardiovascular Interventions*, 2017.

[57] O. Reitan, "Catheter pump," May 12 1998. US Patent 5,749,855 A.

[58] Ö. Reitan, J. Sternby, and H. Öhlin, "Hydrodynamic properties of a new percutaneous intra-aortic axial flow pump," *Asaio Journal*, vol. 46, no. 3, pp. 323–329, 2000.

[59] E. J. Smith, O. Reitan, T. Keeble, K. Dixon, and M. T. Rothman, "A first-in-man study of the reitan catheter pump for circulatory support in patients undergoing high-risk percutaneous coronary intervention," *Catheterization and Cardiovascular Interventions*, vol. 73, no. 7, pp. 859–865, 2009.

[60] M. Miclea-Bleiziffer, A. Untaroiu, and A. Delgado, "Development of a novel design method for marine propellers by computing the exact lift of arbitrary hydrofoils in cascades," *Ocean Engineering*, vol. 83, pp. 87–98, 2014.

[61] K. B. Chandran, S. E. Rittgers, and A. P. Yoganathan, *Biofluid mechanics: the human circulation*. CRC press, 2012.

[62] G. R. Cokelet, "Experimental determination of the average hematocrit of blood flowing in a vessel," *Microvascular research*, vol. 7, no. 3, pp. 382–384, 1974.

[63] G. R. Cokelet, "Rheology and hemodynamics," *Annual Review of Physiology*, vol. 42, no. 1, pp. 311–322, 1980.

[64] "Anticoagulation and congenital heart defects," September 2017.

[65] K. H. Fraser, T. Zhang, M. E. Taskin, B. P. Griffith, and Z. J. Wu, "A quantitative comparison of mechanical blood damage parameters in rotary ventricular assist devices: shear stress, exposure time and hemolysis index," *Journal of biomechanical engineering*, vol. 134, no. 8, p. 081002, 2012.

[66] Z. Knobel, C. J. Kellenberger, T. Kaiser, M. Albisetti, E. Bergsträsser, and E. R. V. Buechel, "Geometry and dimensions of the pulmonary artery bifurcation in children

and adolescents: assessment in vivo by contrast-enhanced mr-angiography," *The international journal of cardiovascular imaging*, vol. 27, no. 3, pp. 385–396, 2011.

[67] S. Kutty, L. Li, R. Hasan, Q. Peng, S. Rangamani, and D. A. Danford, "Systemic venous diameters, collapsibility indices, and right atrial measurements in normal pediatric subjects," *Journal of the American Society of Echocardiography*, vol. 27, no. 2, pp. 155–162, 2014.

[68] C. P. Cheng, R. J. Herfkens, C. A. Taylor, and J. A. Feinstein, "Proximal pulmonary artery blood flow characteristics in healthy subjects measured in an upright posture using mri: the effects of exercise and age," *Journal of Magnetic Resonance Imaging*, vol. 21, no. 6, pp. 752–758, 2005.

[69] M. A. Salim, T. G. DiSessa, K. L. Arheart, and B. S. Alpert, "Contribution of superior vena caval flow to total cardiac output in children," *Circulation*, vol. 92, no. 7, pp. 1860–1865, 1995.

[70] G. Kovacs, A. Berghold, S. Scheidl, and H. Olschewski, "Pulmonary arterial pressure during rest and exercise in healthy subjects: a systematic review," *European Respiratory Journal*, vol. 34, no. 4, pp. 888–894, 2009.

[71] L. Krovetz, T. McLoughlin, M. Mitchell, and G. Schiebler, "Hemodynamic findings in normal children," *Pediatric research*, vol. 1, no. 2, pp. 122–130, 1967.

[72] S. Masutani, C. Kurishima, A. Yana, S. Kuwata, Y. Iwamoto, H. Saiki, H. Ishido, and H. Senzaki, "Assessment of central venous physiology of fontan circulation using peripheral venous pressure," *The Journal of thoracic and cardiovascular surgery*, vol. 153, no. 4, pp. 912–920, 2017.

[73] S. L. Dixon and C. Hall, *Fluid mechanics and thermodynamics of turbomachinery*. Butterworth-Heinemann, 2013.

[74] M. Grigioni, U. Morbiducci, G. D'Avenio, G. Di Benedetto, and C. Del Gaudio, "A novel formulation for blood trauma prediction by a modified power-law mathematical model," *Biomechanics and Modeling in Mechanobiology*, vol. 4, no. 4, pp. 249–260, 2005.

[75] J. D. Hellums, "1993 whitaker lecture: biorheology in thrombosis research," *Annals of biomedical engineering*, vol. 22, no. 5, pp. 445–455, 1994.

[76] M. E. Taskin, K. H. Fraser, T. Zhang, C. Wu, B. P. Griffith, and Z. J. Wu, "Evaluation of eulerian and lagrangian models for hemolysis estimation," *ASAIO journal*, vol. 58, no. 4, pp. 363–372, 2012.

[77] M. Giersiepen, L. Wurzinger, R. Opitz, and H. Reul, "Estimation of shear stress-related blood damage in heart valve prostheses–in vitro comparison of 25 aortic valves.," *The International journal of artificial organs*, vol. 13, no. 5, pp. 300–306, 1990.

[78] P. L. Blackshear Jr, F. D. Dorman, and J. H. Steinbach, "Some mechanical effects that influence hemolysis.," 1965.

[79] J. Apel, R. Paul, S. Klaus, T. Siess, and H. Reul, "Assessment of hemolysis related quantities in a microaxial blood pump by computational fluid dynamics," *Artificial Organs*, vol. 25, no. 5, pp. 341–347, 2001.

[80] L. Ge, L. P. Dasi, F. Sotiropoulos, and A. P. Yoganathan, "Characterization of hemodynamic forces induced by mechanical heart valves: Reynolds vs. viscous stresses," *Annals of Biomedical Engineering*, vol. 36, no. 2, pp. 276–297, 2008.

[81] C. Bludszuweit, "Model for a general mechanical blood damage prediction," *Artificial Organs*, vol. 19, no. 7, pp. 583–589, 1995.

[82] K. K. Yeleswarapu, J. F. Antaki, M. V. Kameneva, and K. R. Rajagopal, "A mathematical model for shear-induced hemolysis," *Artificial Organs*, vol. 19, no. 7, pp. 576–582, 1995.

[83] F. G. Schmitt, "About boussinesq's turbulent viscosity hypothesis: historical remarks and a direct evaluation of its validity," *Comptes Rendus Mécanique*, vol. 335, no. 9-10, pp. 617–627, 2007.

[84] A. CFX, "Solver theory guide. ansys," *Inc., Canonsburg, PA*, 2011.

[85] B. E. Launder and D. B. Spalding, "The numerical computation of turbulent flows," *Computer methods in applied mechanics and engineering*, vol. 3, no. 2, pp. 269–289, 1974.

[86] D. C. Wilcox *et al.*, *Turbulence modeling for CFD*, vol. 2. DCW industries La Canada, CA, 1998.

[87] F. Menter, "Multiscale model for turbulent flows," in *24th Fluid Dynamics Conference, Orlando, FL, July*, pp. 6–9, 1993.

[88] J. Bardina, P. Huang, and T. Coakley, "Turbulence modeling validation," *AIAA paper*, vol. 2121, p. 1997, 1997.

[89] K. H. Fraser, M. E. Taskin, B. P. Griffith, and Z. J. Wu, "The use of computational fluid dynamics in the development of ventricular assist devices," *Medical engineering & physics*, vol. 33, no. 3, pp. 263–280, 2011.

[90] I. H. Abbott and A. E. Von Doenhoff, *Theory of wing sections, including a summary of airfoil data*. Courier Corporation, 1959.

[91] J. E. Kerwin, "Hydrofoils and propellers," *Lecture Notes, Massachusetts Inst. Technology, Boston, MA*, 2001.

[92] H. Glauert, *The elements of aerofoil and airscrew theory*. Cambridge University Press, 1983.

[93] L. Prandtl, "The generation of vortices in fluids of small viscosity," *The Aeronautical Journal*, vol. 31, no. 200, pp. 718–741, 1927.

[94] A. Betz, "Schraubenpropeller mit geringstem energieverlust. mit einem zusatz von l. prandtl," *Nachrichten von der Gesellschaft der Wissenschaften zu Göttingen, Mathematisch-Physikalische Klasse*, vol. 1919, pp. 193–217, 1919.

[95] T. Theodorsen *et al.*, "The theory of propellers," 1948.

[96] C. N. Adkins and R. H. Liebeck, "Design of optimum propellers," *Journal of Propulsion and Power*, vol. 10, no. 5, pp. 676–682, 1994.

[97] S. Goldstein, "On the vortex theory of screw propellers," *Proceedings of the Royal Society of London. Series A, Containing Papers of a Mathematical and Physical Character*, vol. 123, no. 792, pp. 440–465, 1929.

[98] W. Batten, A. Bahaj, A. Molland, and J. Chaplin, "The prediction of the hydrodynamic performance of marine current turbines," *Renewable energy*, vol. 33, no. 5, pp. 1085–1096, 2008.

[99] M. Bleiziffer, "Development of an inverse design method for propellers with application on left ventricular devices."

[100] K. Eyal, "Analysis and experiments for conta-rotating propeller," 2011.

[101] B. Epps, "Openprop v2. 4 theory document," *MIT Department of Mechanical Engineering Technical Report, Cambridge, MA. Available at: http://openprop. mit. edu. Accessed December*, vol. 15, p. 2010, 2010.

[102] K. Graham, H. Sondheimer, and M. Schaffer, "Resolution of cavopulmonary shunt-associated pulmonary arteriovenous malformation after heart transplantation.," *The Journal of heart and lung transplantation: the official publication of the International Society for Heart Transplantation*, vol. 16, no. 12, pp. 1271–1274, 1997.

[103] D. Srivastava, T. Preminger, J. E. Lock, V. Mandell, J. F. Keane, J. E. Mayer, H. Kozakewich, and P. J. Spevak, "Hepatic venous blood and the development of pulmonary arteriovenous malformations in congenital heart disease," *Circulation*, vol. 92, no. 5, pp. 1217–1222, 1995.

[104] A. Gerdes, J. Kunze, G. Pfister, and H.-H. Sievers, "Addition of a small curvature reduces power losses across total cavopulmonary connections," *The Annals of thoracic surgery*, vol. 67, no. 6, pp. 1760–1764, 1999.

[105] C. P. Cheng, R. J. Herfkens, A. L. Lightner, C. A. Taylor, and J. A. Feinstein, "Blood flow conditions in the proximal pulmonary arteries and vena cavae: healthy children during upright cycling exercise," *American Journal of Physiology-Heart and Circulatory Physiology*, vol. 287, no. 2, pp. H921–H926, 2004.

[106] J. B. Barlow, W. Rae, and A. Pope, "Low-speed wind tunnel testing, 1999," *Jhon Wiley&Sons, Canada*.

[107] J. Watmuff, "Wind tunnel contraction design," in *Proceedings of 9th Australian Fluid Mechanics Conference*, pp. 82–89, 1986.

[108] A. L. Throckmorton, K. K. Ballman, C. D. Myers, S. H. Frankel, J. W. Brown, and M. D. Rodefeld, "Performance of a 3-bladed propeller pump to provide cavopulmonary assist in the failing fontan circulation," *The Annals of thoracic surgery*, vol. 86, no. 4, pp. 1343–1347, 2008.

[109] S. K. Sonavane, D. M. Milner, S. P. Singh, A. K. Abdel Aal, K. S. Shahir, and A. Chaturvedi, "Comprehensive imaging review of the superior vena cava," *Radiographics*, vol. 35, no. 7, pp. 1873–1892, 2015.

[110] C. Bonsignore, "Open stent design," *ed: Fermont, CA: Nitinol Devices and Components, Inc*, 2011.

[111] K. C. Koskinas, Y. S. Chatzizisis, A. P. Antoniadis, and G. D. Giannoglou, "Role of endothelial shear stress in stent restenosis and thrombosis: pathophysiologic mechanisms and implications for clinical translation," *Journal of the American College of Cardiology*, vol. 59, no. 15, pp. 1337–1349, 2012.

[112] M. Stiehm, M. Brede, D. Quosdorf, H. Martin, and A. Leder, "A sensitivity analysis of stent design parameters using cfd," *Biomedical Engineering/Biomedizinische Technik*, 2013.

[113] A. Workbench, "V13. 0 user's manual," *Ansys Inc*.

Appendix A

4148 Naval Propeller Properties

The table below lists the distribution of chord to diameter distribution (c/D) ratio, maximum sectional thickness to diameter (t/D) ratio, and the maximum sectional thickness to chord (t/c) ratio at different radial sections from hub to tip. The blade tip thickness and chord length modifications were made same way as that done by Kravitz et. al. [100] to facilitate the printing of the 3D printed propellers and to improve the blade tip strength.

	4148 Naval Propeller Characteristics		
r/R	**c/D**	**t/D**	**t/c**
0.2	0.16	0.0329	0.2056
0.3	0.1812	0.0281	0.1551
0.4	0.2024	0.0239	0.1181
0.5	0.2196	0.0198	0.0902
0.6	0.2305	0.0160	0.0694
0.7	0.2311	0.0125	0.0541
0.8	0.2173	0.0091	0.0419
0.9	0.1807	0.0060	0.0332
0.95	0.1388	0.0045	0.0324
1	0.001	0.0000	0
	Modified Tip		
1	0.025	0.0029	0.1143

Appendix B

Blood Damage Index Code

```
                    %%%%%%%%%%%%%%%%%%%%%%%%%%%%%%%%%%%%%%
                    %%% Blood Damage Index Calculation %%%
                    %%% Code Developed by:             %%%
                    %%%            Jakin Jagani        %%%
                    %%% M.S. in Mechanical Engineering %%%
                    %%%        Virginia Tech           %%%
                    %%%%%%%%%%%%%%%%%%%%%%%%%%%%%%%%%%%%%%

clc;
clear all;
close all;

%% Getting Data from the User

%%%%%%%%% Getting User Inputs %%%%%%%%%

% Enter the number of particles that were inserted at the inlet for ...
   the CFD
% simulation in ANSYS CFX and specify the number of domains that were ...
   used
% because ANSYS gives particle tracks for each domain separately and ...
   hence
% the particle tracks should be exported separately for each defined ...
   domain
% in CFX post processing


prompt1 = {'Enter number of particles inserted at the Inlet:','Enter ...
   number of Domains in the setup:'};
dlg_title = 'User Input';
num_lines = 1;
defaultans = {'1000','2'};
prompt1_ans = inputdlg(prompt1,dlg_title,num_lines,defaultans);
```

```
29
30 tot_part = str2double(char(prompt1_ans(1)));  % Number of particles
31 n_domain = str2double(char(prompt1_ans(2)));  % Number of domains
32
33 %%%%%%%%% Getting the User Selected CFX Exported Excel Sheet %%%%%%%%%
34
35 % If there is a stationary and rotating domain, then always select the
36 % excel or .csv file exported for the particle tracks within stationary
37 % domain first
38
39 %%%%%% OR %%%%%%
40
41 % If there are multiple domains then always select the particles exported
42 % for the largest domain first since they will have maximum number of
43 % tracking points
44
45
46 for p = 1:n_domain
47
48 [filename,filepath]=uigetfile({'*.csv';'*.xlsx'},'Select the Exported ...
       Excel Sheet from CFX');
49 dir_filename = strcat(filepath,filename);
50 [Import_File(p).Excel_File,Import_File(p).cell] = xlsread(dir_filename);
51 Import_File(p).filename = filename;
52 fprintf('Domain %d associated with filename: %s is Read ...
       \n',p,Import_File(p).filename);
53 end
54
55 %% Determining Column in which the Particle Time and Scalar Shear ...
       Stress Belongs
56
57 % This part of the code determines the column in which the particle ...
       travel
58 % time and scalar shear stress is located in the read .csv or .xlsx file
59
60
61 [a,b] = size(Import_File(p).cell);
62
63 for c = 1:b
64 if ~isempty(find(not(cellfun('isempty', ...
       strfind(Import_File(p).cell(:,c), 'Stress'))))) || ...
65 ~isempty(find(not(cellfun('isempty', ...
       strfind(Import_File(p).cell(:,c), 'stress'))))) || ...
66 ~isempty(find(not(cellfun('isempty', ...
       strfind(Import_File(p).cell(:,c), 'Scalar'))))) || ...
67 ~isempty(find(not(cellfun('isempty', ...
       strfind(Import_File(p).cell(:,c), 'scalar')))))
68 Import_File(p).col_stress = c;
69 else if ~isempty(find(not(cellfun('isempty', ...
       strfind(Import_File(p).cell(:,c), 'Time')))))
70 Import_File(p).col_time = c;
```

```
71 end
72 end
73 end
74
75
76 %% Input Data from User
77
78 % Blood Damamge Equation Constants (HO constants)
79 % The user is free to replace the constant values found from the ...
      literature
80 % or determined experimentally from the couette viscometer blood shearing
81 % test and regression analysis
82
83 C      = 1.8e-6;
84 alpha  = 0.7650;
85 beta   = 1.9910;
86
87
88
89 %% Determinig Break Points for the Blood Particles
90
91 for d = 1:n_domain
92
93 % Determining the break points based on peaks of time value to segregate
94 % different blood particles
95
96 [~,Import_File(d).Break_Point]=findpeaks(Import_File(d).Excel_File...
97                                          (:,Import_File(p).col_time));
98
99
100 % Assigning the last read row in the Excel sheet as a break point
101
102 Import_File(d).Break_Point(length(Import_File(d).Break_Point)+1) = ...
      length(Import_File(d).Excel_File(:,Import_File(p).col_time));
103
104 % Determining number of particles leaving the system based on the ...
      number of break
105 % points
106
107 Import_File(d).N_particles = length(Import_File(d).Break_Point);
108
109 % Determining the position of next particle based on the end point of
110 % previous particle
111
112 Import_File(d).Start_Point = [1;Import_File(d).Break_Point(1:end-1)+1];
113
114
115 fprintf('Break Points Determined for domain %d: ...
      %d\n',d,Import_File(d).N_particles);
116
117
```

```
%% Assigning Shear Stress and Particle time values to blood particles in
% main domain


if d == 1

for i = 1:length(Import_File(d).Break_Point)
% Will be used when there are no Secondary Domains
Import_File(d).n_int_m(i)=(Import_File(d).Break_Point(i)-...
                              Import_File(d).Start_Point(i));
Import_File(d).n_int(i)=Import_File(d).n_int_m(i);
Import_File(d).Main_Domain_Blood_Particles...
(1:(Import_File(d).Break_Point(i)-Import_File(d).Start_Point(i)+1)...
,1,i)= 1:Import_File(d).Break_Point(i)-Import_File(d).Start_Point(i)+1;

Import_File(d).Main_Domain_Blood_Particles...
(1:(Import_File(d).Break_Point(i)-Import_File(d).Start_Point(i)+1),2,i)...
= Import_File(d).Excel_File(Import_File(d).Start_Point(i):...
Import_File(d).Break_Point(i),Import_File(p).col_stress);

Import_File(d).Main_Domain_Blood_Particles...
(1:(Import_File(d).Break_Point(i)-Import_File(d).Start_Point(i)+1),3,i)...
= Import_File(d).Excel_File(Import_File(d).Start_Point(i):...
Import_File(d).Break_Point(i),Import_File(p).col_time);

Import_File(d).Main_Domain_Blood_Particles...
(1:(Import_File(d).Break_Point(i)-Import_File(d).Start_Point(i)+1),4,i)...
= Import_File(d).Excel_File(Import_File(d).Start_Point(i):...
Import_File(d).Break_Point(i),1);

Import_File(d).Main_Domain_Blood_Particles...
(1:(Import_File(d).Break_Point(i)-Import_File(d).Start_Point(i)+1),5,i)...
= Import_File(d).Excel_File(Import_File(d).Start_Point(i):...
Import_File(d).Break_Point(i),2);

Import_File(d).Main_Domain_Blood_Particles...
(1:(Import_File(d).Break_Point(i)-Import_File(d).Start_Point(i)+1),6,i)...
= Import_File(d).Excel_File(Import_File(d).Start_Point(i):...
Import_File(d).Break_Point(i),3);

Import_File(1).X_md(1:(Import_File(d).Break_Point(i)...
-Import_File(d).Start_Point(i)+1),i)= ...
    Import_File(d).Main_Domain_Blood_Particles...
(1:(Import_File(d).Break_Point(i)-...
Import_File(d).Start_Point(i)+1),4,i);

Import_File(1).Y_md(1:(Import_File(d).Break_Point(i)...
-Import_File(d).Start_Point(i)+1),i)= ...
    Import_File(d).Main_Domain_Blood_Particles...
(1:(Import_File(d).Break_Point(i)-Import_File(d).Start_Point(i)+1),5,i);

```

```
167 Import_File(1).Z_md(1:(Import_File(d).Break_Point(i)...
168 -Import_File(d).Start_Point(i)+1),i)= ...
        Import_File(d).Main_Domain_Blood_Particles...
169 (1:(Import_File(d).Break_Point(i)-Import_File(d).Start_Point(i)+1),6,i);
170
171 [Import_File(1).max_diff(i),Import_File(1).max_diff_index(i)] =...
172 max(diff(Import_File(d).Excel_File(Import_File(d).Start_Point(i):...
173 Import_File(d).Break_Point(i),Import_File(p).col_time)));
174
175 end
176
177 % Import_File.N_particles = length(main_domain_indices);
178 fprintf('Primary Domain Particle Values Assigned \n');
179
180 %% Determining locations of particles starting from secondary domain and
181 % assigning corresponding shear stress and time values
182
183 else
184 if ~isempty(Import_File(d).Break_Point)
185
186 if length(Import_File(d).Break_Point) <= ...
        length(Import_File(1).Break_Point)
187
188 for i = 1:length(Import_File(d).Break_Point)
189
190 [Import_File(d).Domain_Break_Point,Import_File(d).Main_Domain_Particle_Index]...
191 =find(Import_File(1).Main_Domain_Blood_Particles(:,3,:)==...
192 Import_File(d).Excel_File(Import_File(d).Start_Point(i),Import_File(p).col_time));
193
194 if ~isempty(Import_File(d).Main_Domain_Particle_Index)
195 for g = length(Import_File(d).Main_Domain_Particle_Index)
196
197 j = Import_File(d).Main_Domain_Particle_Index(g);
198 Import_File(d).Secondary_Domain_Blood_Particles...
199 (1:(Import_File(d).Break_Point(i)-Import_File(d).Start_Point(i)+1),1,i)...
200 = 1:Import_File(d).Break_Point(i)-Import_File(d).Start_Point(i)+1;
201
202 Import_File(d).Secondary_Domain_Blood_Particles...
203 (1:(Import_File(d).Break_Point(i)-Import_File(d).Start_Point(i)+1),2,i)...
204 =Import_File(d).Excel_File(Import_File(d).Start_Point(i)...
205 :Import_File(d).Break_Point(i),Import_File(p).col_stress);
206
207 Import_File(d).Secondary_Domain_Blood_Particles...
208 (1:(Import_File(d).Break_Point(i)-Import_File(d).Start_Point(i)+1),3,i)...
209 =Import_File(d).Excel_File(Import_File(d).Start_Point(i)...
210 :Import_File(d).Break_Point(i),Import_File(p).col_time);
211
212 Import_File(d).Secondary_Domain_Blood_Particles...
213 (1:(Import_File(d).Break_Point(i)-Import_File(d).Start_Point(i)+1),4,i)...
214 =Import_File(d).Excel_File(Import_File(d).Start_Point(i)...
215 :Import_File(d).Break_Point(i),1);
```

```
216
217 Import_File(d).Secondary_Domain_Blood_Particles...
218 (1:(Import_File(d).Break_Point(i)-Import_File(d).Start_Point(i)+1),5,i)...
219 =Import_File(d).Excel_File(Import_File(d).Start_Point(i)...
220 :Import_File(d).Break_Point(i),2);
221
222 Import_File(d).Secondary_Domain_Blood_Particles...
223 (1:(Import_File(d).Break_Point(i)-Import_File(d).Start_Point(i)+1),6,i)...
224 =Import_File(d).Excel_File(Import_File(d).Start_Point(i)...
225 :Import_File(d).Break_Point(i),3);
226
227 Import_File(d).n_int_s(i) =  (Import_File(d).Break_Point(i)...
228 -Import_File(d).Start_Point(i));
229
230 Import_File(1).n_int(j) = (Import_File(1).Break_Point(i)...
231 -Import_File(1).Start_Point(i)) + (Import_File(d).Break_Point(i)...
232 -Import_File(d).Start_Point(i))+1;
233
234 Import_File(1).Main_Domain_Blood_Particles...
235 (1:Import_File(1).n_int(j)+1,:,j) = ...
       [Import_File(1).Main_Domain_Blood_Particles...
236 (1:Import_File(1).n_int_m(i)+1,:,j);
237
238 Import_File(d).Secondary_Domain_Blood_Particles...
239 (1:Import_File(d).n_int_s(i)+1,:,i)];
240
241 end
242 end
243 end
244
245 else
246
247 for i = 1:length(Import_File(1).Break_Point)
248
249 [Import_File(d).Domain_Break_Point,Import_File(d).Main_Domain_Particle_Index]...
250 =find(Import_File(1).Main_Domain_Blood_Particles(:,3,:)...
251 ==Import_File(d).Excel_File(Import_File(d).Start_Point(i),...
252 Import_File(p).col_time));
253
254 if ~isempty(Import_File(d).Main_Domain_Particle_Index)
255
256 for g = length(Import_File(d).Main_Domain_Particle_Index)
257 j = Import_File(d).Main_Domain_Particle_Index(g);
258
259 Import_File(d).Secondary_Domain_Blood_Particles...
260 (1:(Import_File(d).Break_Point(i)-Import_File(d).Start_Point(i)+1),1,i)...
261 =1:Import_File(d).Break_Point(i)-Import_File(d).Start_Point(i)+1;
262
263 Import_File(d).Secondary_Domain_Blood_Particles...
264 (1:(Import_File(d).Break_Point(i)-Import_File(d).Start_Point(i)+1),2,i)...
265 =Import_File(d).Excel_File(Import_File(d).Start_Point(i)...
```

```
:Import_File(d).Break_Point(i),Import_File(p).col_stress);

Import_File(d).Secondary_Domain_Blood_Particles...
(1:(Import_File(d).Break_Point(i)-Import_File(d).Start_Point(i)+1),3,i)...
=Import_File(d).Excel_File(Import_File(d).Start_Point(i)...
:Import_File(d).Break_Point(i),Import_File(p).col_time);

Import_File(d).Secondary_Domain_Blood_Particles...
(1:(Import_File(d).Break_Point(i)-Import_File(d).Start_Point(i)+1),4,i)...
=Import_File(d).Excel_File(Import_File(d).Start_Point(i)...
:Import_File(d).Break_Point(i),1);

Import_File(d).Secondary_Domain_Blood_Particles...
(1:(Import_File(d).Break_Point(i)-Import_File(d).Start_Point(i)+1),5,i)...
=Import_File(d).Excel_File(Import_File(d).Start_Point(i)...
:Import_File(d).Break_Point(i),2);

Import_File(d).Secondary_Domain_Blood_Particles...
(1:(Import_File(d).Break_Point(i)-Import_File(d).Start_Point(i)+1),6,i)...
=Import_File(d).Excel_File(Import_File(d).Start_Point(i)...
:Import_File(d).Break_Point(i),3);

Import_File(d).n_int_s(i) =  (Import_File(d).Break_Point(i)...
-Import_File(d).Start_Point(i));

Import_File(1).n_int(j) = (Import_File(1).Break_Point(i)...
-Import_File(1).Start_Point(i)) + (Import_File(d).Break_Point(i)...
-Import_File(d).Start_Point(i))+1;

Import_File(1).Main_Domain_Blood_Particles(1:Import_File(1).n_int(j)+1,:,j) ...
    = [Import_File(1).Main_Domain_Blood_Particles...
(1:Import_File(1).n_int_m(i)+1,:,j);

Import_File(d).Secondary_Domain_Blood_Particles(1...
:Import_File(d).n_int_s(i)+1,:,i)];

end
end
end
end
end
end

fprintf('Secondary Domain Particle Values Assigned \n');


end
%% Sorting the Particles

for i = 1:length(Import_File(1).Break_Point)

```

```
316 temp_bp = Import_File(1).Main_Domain_Blood_Particles(:,:,i);
317 [m_o,n_o]=size(temp_bp);
318 temp_bp(~any(temp_bp,2),:) = [];
319 temp_bp = sortrows(temp_bp,3);
320 [m,n] = size(temp_bp);
321 temp_bp(m+1:m_o,:) = 0;
322 Import_File(1).blood_particle(:,:,i) = temp_bp;
323 end
324
325 fprintf('Sorting of Particles Completed \n');
326
327
328 %% Getting Particle Co-ordinates
329
330 Import_File(1).X(:,:) = Import_File(1).blood_particle(:,4,:);
331 Import_File(1).Y(:,:) = Import_File(1).blood_particle(:,5,:);
332 Import_File(1).Z(:,:) = Import_File(1).blood_particle(:,6,:);
333
334 %% Variable Initialization/ Space Allocation
335
336 % Elemental Contribution to Blood Damage
337 Import_File(1).delta_BDI = zeros(max(Import_File(1).n_int),tot_part);
338
339 % Constant Shear Stress for each elemental interval
340 Import_File(1).tau_j     = zeros(max(Import_File(1).n_int),tot_part);
341
342 % time at the end of each elemental interval
343 Import_File(1).t_j       = zeros(max(Import_File(1).n_int),tot_part);
344
345 % Time interval between two nodal intervals
346 Import_File(1).delta_t   = zeros(max(Import_File(1).n_int),tot_part);
347
348 % Mechanical Dose for each elemental interval
349 Import_File(1).delta_D_j = zeros(max(Import_File(1).n_int),tot_part);
350
351 % Total Mechanical Dose for a particle till current interval/ time period
352 Import_File(1).D_j       = zeros(max(Import_File(1).n_int),tot_part);
353
354 % Total Blood Damage for a particle till current interval/ time period
355 Import_File(1).BDI       = zeros(max(Import_File(1).n_int),tot_part);
356
357 %% Calculation of Elemntal and nodal Blood Damage Index for each ...
       blood particle inside each domain
358
359 Import_File(1).Total_BDI = 0;
360
361 for i = 1:length(Import_File(1).Break_Point)
362
363 for j = 1:Import_File(1).n_int(i)
364
```

```
365 Import_File(1).delta_t(j,i)     = ...
       Import_File(1).blood_particle(j+1,3,i)-...
366                                    Import_File(1).blood_particle(j,3,i);
367 Import_File(1).tau_j(j,i)       = Import_File(1).blood_particle(j+1,2,i);
368 Import_File(1).t_j(j,i)         = Import_File(1).blood_particle(j+1,3,i);
369 Import_File(1).delta_D_j(j,i)   = ...
       Import_File(1).tau_j(j,i)^(beta/alpha)*Import_File(1).delta_t(j,i);
370 Import_File(1).D_j(j,i)         = sum(Import_File(1).delta_D_j(1:j,i));
371 Import_File(1).delta_BDI(j,i)   = ...
       C*alpha*Import_File(1).D_j(j,i)^(alpha-1)...
372                                     *Import_File(1).delta_D_j(j,i);
373 Import_File(1).BDI(j,i)         = sum(Import_File(1).delta_BDI(1:j,i));
374
375 end
376
377 end
378
379 fprintf('BDI Calculation Completed \n');
380
381 %% Computing Particle Travel Time
382
383 Import_File(1).Particle_Travel_Time = max(Import_File(1).t_j(:,:));
384
385 % Computing average particle travel time
386
387 Import_File(1).Average_Particle_Time = ...
       mean(Import_File(1).Particle_Travel_Time);
388
389
390 %% Calculation for Total Blood Damage sustained by each particle
391
392 Total_BDI = zeros(tot_part,1);
393
394 for k = 1:length(Import_File(1).n_int)
395
396 if Import_File(1).n_int(k) ~= 0
397
398 Total_BDI(k) = Total_BDI(k) + ...
       Import_File(1).BDI(Import_File(1).n_int(k),k);
399
400 end
401
402 end
403
404 % Note the value of BDI computed here is not in percentage and will be
405 % converted to percentage later by multiplying it by 100
406
407 % Average BDI for all the particles determined by taking mean of BDI ...
       of all
408 % the particles
409
```

```
410 Average_BDI = mean(Total_BDI(:));
411
412 fprintf('Average BDI for the Entire domain: %d \n',Average_BDI);
413 fprintf('Average BDI for particles in terms of percentage: %d ...
       \n',Average_BDI*100);
414
415 % Similarly the average particle travel time or residence time or ...
       exposure
416 % time is determined
417
418 Average_Particle_Time = Import_File(1).Average_Particle_Time;
419
420 fprintf('Average Particle Travel Time for the Entire domain: %d ...
       \n',Average_Particle_Time);
421
422
423 %% Plotting BDI [%] and Particle Exposure Time [sec] Histogram
424
425 % Getting total number of particles in each domain
426
427 for d = 1:n_domain
428 N_particles(d) = Import_File(d).N_particles;
429 end
430
431 %% Plotting BDI Histogram
432
433 dim = [.4 .3 .5 .5];
434 str = strcat('Total No. Of Particles =',num2str(N_particles(1)));
435 figure(1);
436 bdi_edges = [0:0.0005:0.01,0.01:0.1:0.1];
437 h1 = histogram(Total_BDI(1:N_particles(1))*100,bdi_edges); % Average ...
       BDI multiplied by 100 to get % BDI
438 set(h1,'facecolor','b');
439 xlabel('Blood Damamge Index (%)','FontSize',16,'FontWeight','bold');
440 ylabel('Number of Particles','FontSize',16,'FontWeight','bold');
441 title(' Average Total BDI vs Number of Particle ...
       Distribution','FontSize',16,'FontWeight','bold');
442 set(gca,'Fontsize',12,'FontWeight','bold');
443 a = annotation('textbox',dim,'String',str,'FitBoxToText','on');
444 a.FontSize = 12;
445 a.FontWeight = 'bold';
446 a.LineWidth = 1;
447 figure1_jpg_name = 'BDI_Distribution.jpeg';
448 figure1_mfig_name = 'BDI_Distribution.fig';
449 dir1_Fig1 = strcat(filepath,figure1_jpg_name);
450 dir1_Fig2 = strcat(filepath,figure1_mfig_name);
451 savefig(dir1_Fig2);
452 saveas(figure(1),dir1_Fig1);
453
454 %%  Plotting Particle Travel Time Histogram
455
```

```
456 figure(2);
457 time_edges = [0:0.1:1,1:1:5];
458 h2 = histogram(Import_File(1).Particle_Travel_Time(1:N_particles(1)),10);
459 set(h2,'facecolor','b');
460 xlabel('Particle Exposure Time (sec)','FontSize',16,'FontWeight','bold');
461 ylabel('Number of Particles','FontSize',16,'FontWeight','bold');
462 title(' Particle Residence Time vs Number of Particle ...
        Distribution','FontSize',16,'FontWeight','bold');
463 set(gca,'Fontsize',12,'FontWeight','bold');
464 a = annotation('textbox',dim,'String',str,'FitBoxToText','on');
465 a.FontSize = 12;
466 a.FontWeight = 'bold';
467 a.LineWidth = 1;
468 figure2_jpg_name = 'Particle_Exposure_Time.jpeg';
469 figure2_mfig_name = 'Particle_Exposure_Time.fig';
470 dir1_Fig3 = strcat(filepath,figure2_jpg_name);
471 dir1_Fig4 = strcat(filepath,figure2_mfig_name);
472 savefig(dir1_Fig4);
473 saveas(figure(2),dir1_Fig3);
474
475
476 %% Writing BDI Study Results in Text File
477
478 fileIDname = strcat(filepath,'BDI_Study.txt');
479 fileID = fopen(fileIDname,'w');
480
481 fprintf(fileID,'Information Regarding Particles exported from file: ...
        %s \n',Import_File.filename);
482 fprintf(fileID,'Total Number of Particles: %d ...
        \n',Import_File.N_particles);
483 fprintf(fileID,'Average BDI for the Entire domain in percentage: %d ...
        \n',Average_BDI*100);
484 fprintf(fileID,'Average Particle Travel Time for the Entire domain: ...
        %d \n',Average_Particle_Time);
485 fclose(fileID);
```